



# Super-Resolution Techniques and Waveform Design for Radar and Dual-Function Radar and Communication Systems

By

Muge Bekar

A thesis submitted to  
the University of Birmingham  
for the degree of  
DOCTOR OF PHILOSOPHY

School of Engineering  
College of Engineering and Physical Sciences  
University of Birmingham  
January 2024

UNIVERSITY OF  
BIRMINGHAM

**University of Birmingham Research Archive**

**e-theses repository**

This unpublished thesis/dissertation is copyright of the author and/or third parties. The intellectual property rights of the author or third parties in respect of this work are as defined by The Copyright Designs and Patents Act 1988 or as modified by any successor legislation.

Any use made of information contained in this thesis/dissertation must be in accordance with that legislation and must be properly acknowledged. Further distribution or reproduction in any format is prohibited without the permission of the copyright holder.

# Abstract

Modern vehicles are densely equipped with sensors, and the space available for these sensors is restricted. In this thesis, firstly, novel waveforms that enable simultaneous radar sensing and communication using a single chipset are designed with the aim of not only reducing the quantity of sensor components and the amount of sensor space on the vehicles but also enhancing the spectrum efficiency by utilising the same frequency for both systems. Such waveforms are subsequently utilised for radar sensing with multiple input multiple output (MIMO) beamforming, resulting in better angular resolutions and higher data rates. The validation of the proposed waveforms for both radar and communication is carried out through simulations and experimentation.

Second focus of this thesis is on the antenna design and autoregressive methods. It is known that high angular resolutions are required in automotive radars to extract detailed information about the scene, which can be fulfilled by using large antennas/arrays but may restrict its suitability for applications in vehicle infrastructure. With the purpose of achieving high angular resolutions yet with reduced number of total antenna elements, sparse MIMO antennas are designed using optimisation techniques. Although sparse MIMO arrays are a solution to reduce the cost and weight of the antenna, it requires the same physical size of the antenna as conventional MIMO arrays. With the aim of attaining high angular resolution while keeping the size of the physical antenna compact as well as reducing the number of total antenna elements, the extrapolation and interpolation approach using autoregressive Burg algorithm is developed here to design virtual array elements towards both azimuth and elevation directions. Finally, to achieve further improvement in angular resolutions, motion of the MIMO radar

platform is exploited through Doppler beam sharpening (DBS) technique. This thesis proposes a technique that applies the Burg algorithm to MIMO radar data collected by motion of the radar platform to enhance the cross-range resolution in both on- and off-boresight directions. The performance of the proposed methods is evaluated through both simulations and experiments at 77 GHz.



*To my lovely son, Göktuğ Bekar*

# Acknowledgements

First and foremost, I would like to express my sincere gratitude to my supervisors, Prof. Marina Gashinova and Prof. Chris Baker, for their constant guidance, encouragement, motivation, and support throughout every stage of my PhD journey.

I would like to thank the Republic of Türkiye, Ministry of National Education for funding and sponsoring my PhD project and making this opportunity possible.

I would like to express my heartfelt thanks to Dr. Ali, my beloved husband, soul mate, and colleague, for always supporting me, being a patient and a very good companion, and for believing in me.

I would like to thank my colleagues, Dr. Anum, Dr. Shahrzad, Dr. Ana, Dr. Yang, Dr. Fatemeh, Xiaofei, Dillon, and the rest of the MISL team, for their friendship and creating a cheerful research environment.

I would like to extend my thanks to my parents, Emine and Hasan, my sister, Figen, my brothers, Emre and Hüseyin, my mother-in-law, Filiz, and other members of my extended family for their endless support and unconditional love.

Last but not least, I would like to express my special thanks to my amazing son, Göktuğ Bekar, for his love and joy and for motivating me with his cheerful smiles, even during the most stressful moments.

# Table of Contents

Abstract.....	i
Acknowledgements .....	iv
List of Figures.....	ix
List of Tables .....	xvii
Abbreviation List.....	xviii
Chapter 1 - Introduction .....	1
1.1    Motivations.....	1
1.2    Contributions .....	9
1.3    Thesis Outline.....	11
Chapter 2 – Background .....	14
2.1    Radar.....	14
2.1.1    Radar Basics .....	15
2.1.2    Radar Waveforms .....	17
2.1.3    Ambiguity Function.....	29
2.1.4    MIMO Radar .....	31
2.1.5    Automotive Radars .....	43

2.2	Communication Basics .....	46
2.2.1	Communication Waveforms.....	48
2.2.2	Multiple Access Schemes in Communication .....	55
2.3	Summary.....	57
Chapter 3 - Waveform Design for Joint RadCom Systems.....		58
3.1	Introduction .....	58
3.2	State of the Art.....	60
3.3	Proposed Techniques.....	63
3.3.1	Time Division Multiplexing (TDM) .....	64
3.3.2	Code Division Multiplexing (CDM) .....	69
3.4	System Parameters Based On BER .....	72
3.5	Simulation Results.....	73
3.6	Experimental Results.....	79
3.6.1	SISO Case.....	80
3.6.2	MIMO Case .....	82
3.6.3	Doppler Effect .....	88
3.7	Conclusion.....	90
Chapter 4 – Sparse MIMO Antenna Designs .....		91
4.1	Introduction .....	91
4.2	State of the Art.....	93
4.3	Thinned MIMO Array .....	97

4.3.1	Thinned 1-D MIMO Array .....	97
4.3.2	Thinned 2-D MIMO Array .....	99
4.4	Optimisation Algorithms .....	102
4.4.1	Simulated Annealing .....	102
4.4.2	Genetic Algorithm .....	105
4.5	Simulation Results.....	110
4.5.1	Optimisation results of 1-D Thinned MIMO.....	110
4.5.2	Optimisation results of 2-D Thinned MIMO.....	116
4.6	Summary.....	124
Chapter 5 Burg-Aided MIMO Array Extrapolation for Improved Spatial Resolution .....		125
5.1	Introduction .....	125
5.2	State-of-the-art.....	127
5.3	MIMO Antenna .....	130
5.4	The Burg Algorithm .....	131
5.5	Burg-Aided MIMO.....	133
5.6	Simulation Results.....	135
5.6.1	Burg-Aided 1-D MIMO .....	135
5.6.2	Burg-Aided 2-D MIMO .....	141
5.7	Experimental Setup and Results .....	151
5.8	Conclusion .....	159
Chapter 6 – Burg-aided MIMO-DBS .....		161

6.1	Introduction .....	161
6.2	State of the Art.....	162
6.3	Background.....	165
6.3.1	Doppler Beam Sharpening.....	165
6.3.2	MIMO-DBS.....	169
6.4	Proposed Algorithm and Simulation Results.....	171
6.5	Experimental Results .....	176
6.6	Conclusion.....	183
Chapter 7 – Conclusion and Future Work .....		184
7.1	Summary and Outcomes.....	184
7.2	Future Work.....	187
References .....		189

# List of Figures

Figure 1.1: Driving automation levels of SAE J3016 [3].	3
Figure 2.1: The basic principle of radar [23].	15
Figure 2.2: (a) Upchirp LFM (b) Downchirp LFM (c) and (d) real and imaginary parts of the upchirp and downchirp, respectively.	19
Figure 2.3: The steps of matched filtering in frequency domain.	22
Figure 2.4: Range profile of a stationary target.	23
Figure 2.5: (a) 13 bits Barker code sequence, (b) simple pulse waveform with a rectangular envelope and 13-bit Barker code modulated RF waveform.	25
Figure 2.6: (a) Tapped delay line of 13-bit Barker code, (b) auto-correlation function of 13-bit Barker code, (c) auto-correlation function of the code in dB unit.	26
Figure 2.7: Block diagram of the 31-bit m-sequence generator.	28
Figure 2.8: Steps of generating the 31-bit m-sequence, and at the final, the achieved bit sequence.	28
Figure 2.9: (a) The zero-Doppler cut of the LFM waveform, (b) the zero-delay cut of the LFM waveform.	31
Figure 2.10: The ambiguity function of the LFM waveform.	31
Figure 2.11: An example of a 1-D MIMO array with 2 Tx and 5 Rx.	35
Figure 2.12: The configuration of MIMO virtual array for 2 Tx and 5 Rx.	36

Figure 2.13: Radiation pattern of 2 Tx x 5 Rx 1-D MIMO array.....	37
Figure 2.14: Demonstration of L-shaped MIMO in spherical coordinate system. Rectangular shapes represent transmitters whereas circle shapes are for receiver elements.....	41
Figure 2.15: L-shaped 2-D MIMO array and its virtual array elements.....	42
Figure 2.16: Automotive radar applications [42]. ....	45
Figure 2.17: Digital communication system [47].....	47
Figure 2.18: (a) The encoded binary data, (b) ASK modulated waveform, (c) FSK modulated waveform, (d) BPSK modulated waveform. ....	49
Figure 2.19: Constellation diagram of (a) BPSK, (b) QPSK.....	51
Figure 2.20: Block diagram of modulation and demodulation of BPSK. ....	52
Figure 2.21: (a) The transmitted binary data at point A, (b) transmitted BPSK waveform at point B, (c) received signal at point C, (d) waveform after mixer – at point D, (e) waveform after the integrator – at E, (f) the received data after thresholding – at point F.....	53
Figure 2.22: Bit error rate performance of BPSK, QPSK, 8-PSK and 16-PSK [50]. ....	54
Figure 2.23: Multiple access schemes [51]. ....	55
Figure 3.1: The proposed joint radar and communication scenario. ....	64
Figure 3.2: (a) The demonstration of dividing sweep time into multiple sub-units and (b) an example of embedded data into the radar signal. ....	65
Figure 3.3: An example of embedded data into LFM signal by using 7-bit m-sequence. ....	70
Figure 3.4: Number of transmitter vs $E_b/N_0$ for different code lengths under a $10^{-6}$ BER or less criterion.....	73
Figure 3.5: Ambiguity function of (a) pure-LFM, (b) BPSK-LFM, (c) 13-bit Barker code and its phase-shifted version, (d) 31-bit m-sequence and its phase-shifted version. ....	75
Figure 3.6: (a) Range-angle map by using BPSK-LFM, (b) range and azimuth angle cuts.....	76



Figure 3.7: (a) Range-angle map by using 31-bit m-sequences, (b) range and azimuth angle cuts.....	77
Figure 3.8: (a) Range-angle map by using 13-bit Barker code and its shifted version, (b) range and azimuth angle cuts. ....	77
Figure 3.9: Simulation result of transmitted data from the first transmitter by using 13-bit Barker code and demodulated data in communication receiver.....	78
Figure 3.10: The configuration of experimental setup. ....	79
Figure 3.11: In SISO case (a) Setup for target detection, (b) communication setup.....	80
Figure 3.12: In radar part, (a) captured reference (BPSK-LFM) and received (BPSK-LFM) signals, (b) zoomed version of (a), (c) range response after matched filtering, (d) zoomed version of the range response. ....	81
Figure 3.13: In communication part, (a) captured reference (LFM) and received (BPSK-LFM) signals, (b) embedded data into radar emission in simulation and received data from communication receiver in the experiment. ....	82
Figure 3.14: MIMO array configuration. ....	83
Figure 3.15: In MIMO case (a) Setup for target detection, (b) communication setup. ....	84
Figure 3.16: Experimental result of BPSK-LFM, (a) Range-azimuth angle map, (b) range and azimuth cuts.....	85
Figure 3.17: Experimental result of 13-bit Barker code, (a) Range-azimuth angle map, (b) range and azimuth cuts. ....	86
Figure 3.18: Experimental result of 31-bit m-sequence, (a) Range-azimuth angle map, (b) range and azimuth cuts. ....	86
Figure 3.19: In experiment (a) transmitted data from the first transmitter by using 13-bit Barker code and demodulated data in communication receiver, (b) transmitted data from the second	

transmitter by using 13-bit Barker code and the demodulated data in communication receiver. .....	87
Figure 3.20: (a) Radar setup for velocity estimation, (b) chirp and frame durations. ....	88
Figure 3.21: (a) Experimental result of range-velocity-angle. (b) Azimuth angle-velocity cut when range is 8.5 m. ....	89
Figure 4.1: (a) An example of thinned 1-D MIMO array configuration, (b) virtual array of (a). .....	98
Figure 4.2: (a) Demonstration of 2-D MIMO in spherical coordinate system, (b) an example of thinned 2-D MIMO antenna configuration, (c) the virtual array of (b).....	101
Figure 4.3: The flow chart of the Simulated Annealing algorithm. ....	106
Figure 4.4: A representation of (a) crossover operator, (b) mutation operator. ....	107
Figure 4.5: The simulated annealing results (a) fitness function response versus number of current solutions, (b) configuration of optimised thinned 1-D MIMO array, (c) the radiation pattern at $0^\circ$ scan angle, (d) radiation pattern at $-30^\circ$ scan angle. ....	112
Figure 4.6: The genetic algorithm results (a) fitness function response versus generation, (b) configuration of optimised thinned 1-D MIMO array, (c) the radiation pattern at $0^\circ$ scan angle, (d) radiation pattern at $10^\circ$ scan angle. ....	114
Figure 4.7: The available areas (a) for two restricted transmit elements, (b) for four restricted receive elements. ....	118
Figure 4.8: The case of 8 Tx and 16 Rx MIMO (a) fitness function response versus number of current solutions, (b) radiation pattern of the thinned 2D MIMO, (c) optimized 2D thinned MIMO array, (d) the corresponding virtual array. ....	119
Figure 4.9: The optimized 2-D thinned MIMO antennas, (a) with 4 Tx and 20 Rx, (b) the pattern of (a) when target is at $(5^\circ, 20^\circ)$ , (c) with 9 Tx and 15 Rx, (d) the pattern of (c) when target is at	

(20°,0°), (e) with 12 Tx and 12 Rx, (f) the pattern of (e) when target is at (20°,-10°) in azimuth and elevation, respectively. ....	120
Figure 4.10: Fitness values and the number of iteration at which the $n^{\text{th}}$ best solution is obtained versus the $n^{\text{th}}$ best solution in the case of 8 Tx x 16 Rx (a) when the Tx's are located at the edges within $\lambda$ margin, (b) Tx's could be anywhere in the planar aperture. ....	123
Figure 5.1: Processing chain of the Burg-aided 1-D MIMO (a), and 2-D MIMO (b). ....	134
Figure 5.3: The azimuth cut at 15 m range in the case of (a) a single target at -15° azimuth angle, (b) two targets at -15° and 0° azimuth angles, (c) targets at 0° and 9° azimuth angles. ....	136
Figure 5.2: (a) MIMO antenna configuration, and its positions of VA elements, (b) the positions of the VA elements when the 6 <sup>th</sup> receiver is missing/failed. ....	136
Figure 5.4: (a) The positions of the multiple targets, (b) the range – azimuth response of 2 Tx and 9 Rx MIMO. ....	138
Figure 5.5: The angular response of the MIMO antenna, Burg-aided MIMO antenna with $\epsilon f = 2$ , and $\epsilon f = 3$ at the range of (a) 21 m, (b) 15 m. ....	139
Figure 5.6: The extrapolated VA element and its angular resolution for 2 Tx and 9 Rx based on (a) $\epsilon f$ is 2, (b) $\epsilon f$ is 3, and the range – azimuth angle response of Burg-aided MIMO with (c) $\epsilon f$ of two, (d) $\epsilon f$ of three. ....	139
Figure 5.7: The angular response of the MIMO antenna, Burg-aided MIMO antenna with $\epsilon f = 2$ , and $\epsilon f = 3$ at the range of (a) 12 m, (b) 18 m, (c) 20 m, (d) 22 m. ....	140
Figure 5.8: The achievable angular resolution versus the aperture length of the Burg-aided VA with $\epsilon f = 2$ in comparison to VA. ....	141
Figure 5.9: (a) The proposed 2-D MIMO array one single transmit/receive element, (b) Virtual array of the antenna configuration of (a), (c) Extrapolated virtual elements via the BA	

(extrapolation along each dimension is shown in red with further extrapolation shown in green).	
.....	143
Figure 5.10: (a) Proposed MIMO with separated Tx and Rx (b) VA of the antenna configuration of (a), (c) Extrapolated virtual elements via the BA.....	144
Figure 5.11: (a) When Tx and Rx packs are separated, (b) VA of the antenna configuration of (a), (c) Extrapolated virtual elements via the BA.....	145
Figure 5.12: The angular response for a boresight target (a) the compact size 2-D MIMO, (b) Burg-aided 2-D MIMO.....	146
Figure 5.13: The angular response for a boresight target (a) the antenna configuration in Figure 5.11(a), (b) Burg-aided 2-D MIMO. ....	146
Figure 5.14: The angular response for multiple targets (a) the compact size 2-D MIMO, (b) Burg-aided 2-D MIMO.....	147
Figure 5.15: The angular response when targets have different RCSs (a) the compact size 2-D MIMO, (b) Burg-aided 2-D MIMO, (c) L-shaped 20 Tx by 20 Rx MIMO radar.....	148
Figure 5.16: (a) The second proposed 2-D MIMO array, (b) Virtual array of the antenna configuration of (a), (c) Extrapolated virtual elements via the BA. ....	149
Figure 5.17: The angular response for a boresight target (a) the second proposed 2-D MIMO, (b) After the BA is applied to the 2 <sup>nd</sup> configuration.....	150
Figure 5.18: The angular response for multi-target scenario (a) the 2 <sup>nd</sup> proposed 2-D MIMO, (b) After the BA is applied to the 2 <sup>nd</sup> configuration.....	150
Figure 5.19: (a) INRAS MIMO radar with 77 GHz frontend, (b) the vertical positioner used with the radar, (c) photograph from the experimental site, (d) two corner reflectors at 2.5 m, (e) three corner reflectors at 3.7 m.....	152

Figure 5.20: The geometrical explanation of the followed direct path of the signal at each transceiver's position.....	153
Figure 5.21:Range – Azimuth angle responses of (a) L-shaped 20x20 MIMO radar, (b) compact size 2-D MIMO radar with 4 Tx and 25 Rx, (c) Burg estimation is applied to compact size 2-D MIMO.....	155
Figure 5.22: The responses of the L-shaped MIMO, compact size MIMO and Burg-aided MIMO for (a) azimuth cut of the corner reflector on the boresight at 1.7 m, (b) elevation cut of the corner reflector on the boresight at 1.7 m.....	156
Figure 5.23: 2-D MIMO azimuth - elevation angle maps of two corner reflectors at 2.5 m (a)L-shaped 20x20 MIMO radar, (b) compact size 2-D MIMO radar, (c)Burg-aided MIMO.....	156
Figure 5.24: 3-D plots of (a) L-shaped 20x20 MIMO radar, (b) compact size 2-D MIMO radar, (c) Burg-aided MIMO. ....	157
Figure 6.1: Geometry of DBS and relative velocity vector of a single stationary point target [175]. ....	165
Figure 6.2: (a) Side looking DBS scenario, (b) improvement in the angular resolution via DBS, (c) forward looking DBS. ....	167
Figure 6.3: Flow chart of the proposed algorithm. ....	171
Figure 6.4: Angular resolutions for DBS, MIMO, MIMO-DBS, Burg-aided MIMO-DBS. .	173
Figure 6.5: (a)Azimuth cut of DBS, MIMO, and MIMO-DBS, (b) azimuth cut of MIMO-DBS and Burg-aided MIMO-DBS. ....	173
Figure 6.6: Range – cross range responses of (a) MIMO, (b) MIMO-DBS, (c) only Doppler data is extrapolated via the BA, (d) only angular data is extrapolated via the BA, (e) the BA is applied towards both azimuth and Doppler dimensions.....	175
Figure 6.7: The lab-based experimental setup.....	176

Figure 6.8: (a) INRAS MIMO radar with 77 GHz frontend, (b) the linear positioner used with the radar, (c) the experimental scenario, (d) collected data points during the experiment.....	177
Figure 6.9:(a) MIMO radar result, (b) MIMO-DBS result, (c) Burg-aided MIMO-DBS result .....	178
Figure 6.10: (a) Experimental setup on the vehicle [175], (b) Photograph of the scene, (c) MIMO result after motion compensation, (d) MIMO-DBS result, (e) results with Burg algorithm applied to both Doppler and angular dimensions (factor 2) to extrapolate the data. ....	182

# List of Tables

Table 2.1: RF and Radar Bands [23] .....	17
Table 2.2: The distances of the path followed by a signal .....	36
Table 2.3: The normalized path difference which is followed by a signal.....	36
Table 2.4: Automotive radar categories [39].....	45
Table 3.1:Radar parameters.....	74
Table 4.1: Optimised 1-D MIMO array using simulated annealing.....	112
Table 4.2: Optimised 1-D MIMO array using genetic algorithm.....	114
Table 5.1: Comparison of L-Shaped MIMO and Burg-aided MIMO in terms of power and positional accuracy of targets .....	158
Table 6.1:Radar parameters in Simulation .....	172
Table 6.2: Radar parameters used in lab-based experiment .....	177
Table 6.3: Radar parameters used in real-world experiment.....	179

# Abbreviation List

1-D: One Dimensional

2-D: Two Dimensional

3-D: Three Dimensional

AF: Ambiguity Function

ACC: Adaptive Cruise Control

ADAS: Advanced Driver Assistance Systems

AM: Amplitude Modulation

AR: Autoregressive

ASK: Amplitude Shift Keying

AWG: Arbitrary Waveform Generator

AWGN: Additive White Gaussian Noise

BA: Burg Algorithm

BER: Bit Error Rate

BPSK: Binary Phase Shift Keying

CDM: Code-Division Multiplexing



CDMA: Code Division Multiple Access

CPI: Coherent Processing Interval

CW: Continuous Wave

DBS: Doppler Beam Sharpening

DPO: Digital Oscilloscope

DSRC: Dedicated Short Range Communications

ETSI: European Telecommunications Standards Institute

FCC: Federal Communication Commission

FDM: Frequency Division Multiplexing

FDMA: Frequency Division Multiple Access

FF: Fitness Function

FFT: Fast Fourier Transform

FIR: Finite Impulse Response

FM: Frequency Modulation

FMCW: Frequency Modulated Continuous Wave

FoV: Field of View

FSK: Frequency Shift Keying

FT: Fourier Transform

GA: Genetic Algorithm

IFT: Inverse of Fourier Transform

ITS: Intelligent Transportation System

LFM: Linear Frequency Modulation

LFSR: Linear Feedback Shift Registers

LIDAR: LIght Detection And Ranging

LRR: Long Range Radar

MF: Matched Filter

MIMO: Multiple Input Multiple Output

MRR: Medium Range Radar

MUSIC: Multiple Signal Classification

OFDM: Orthogonal Frequency Division Multiplexing

OFDMA: Orthogonal Frequency Division Multiple Access

PM: Phase Modulation

PMCW: Phase Modulated Continuous Wave

PN-code: Pseudo-Noise Code

PRI: Pulse Repetition Interval

PSK: Phase Shift Keying

PSLL: Peak-to-Sidelobe Level

QPSK: Quadrature Phase Shift Keying

Radar: RAdio Detection And Ranging

RadCom: Radar and Communication

RCM: Range Cell Migration

RCMC: Range Cell Migration Correction

RCS: Radar Cross Section

RF: Radio Frequency

Rx: Receiver

SA: Simulated Annealing

SAE: Society of Automotive Engineers

SAR: Synthetic Aperture Radar

SDMA: Space Division Multiple Access

SISO: Single Input Single Output

SLL: Sidelobe Level

SNR: Signal to Noise Ratio

SRR: Short Range Radar

TDM: Time Division Multiplexing

TDMA: Time Division Multiple Access

Tx: Transmitter

VA: Virtual Array

V2I: Vehicle-to-Infrastructure

V2V: Vehicle-to-Vehicle

V2X: Vehicle-to-Everything

WAVE: Wireless Access for Vehicular Environment

# Chapter 1 - Introduction

## 1.1 Motivations

Over the last few decades, the number of vehicles on the road has increased dramatically, leading to traffic jams, inefficient energy consumption, loss of time as well as money. More importantly, the number of road accidents has increased resulting in injuries and fatalities. Research described in [1] shows that the main reason of these accidents is human driver errors. In order to reduce driver-based errors and make journeys safer and more comfortable, there is a growing interest towards capable and robust autonomous vehicles. This is because autonomous vehicles can take more optimal and consistent decisions during the journey by gathering information coming from a wide variety of sensors surrounding the vehicle.

According to established standards on levels of automations [2] by Society of Automotive Engineers (SAE levels of automation) historically first vehicles were completely in control by solely the human driver due to absence of sensors of any kind, which is referred as level 0. Later, Advanced Driver Assistance Systems (ADAS) were developed and different types of sensors surrounding the vehicle were proposed such as cameras, acoustic, LIDAR (Light Detection And Ranging) and radar systems (SAE Levels 1-3). For fully autonomous

vehicles where human driver is not required to intervene, it is recognised that a combination of different sensors with redundancy for higher robustness is required. Cameras, for instance, provide a visual picture of the vehicle's surrounding, and classification of objects within a viewed scene is easier using a camera, compared with, say, a radar system. On the other hand, when the weather is foggy or rainy etc., the visibility may not be enough to detect the obstacles with cameras. However, radar is robust to all weather conditions and estimates range, angle and relative speed of the targets. Therefore, automotive radar may be thought of as an essential sensor for autonomous vehicles capable of functioning in all conditions.

As mentioned earlier, the state of the automotive assistance technology were grouped into six levels of autonomy, ranging from Level 0 to Level 5 in 2014 and these were described within SAE J3016 by SAE [3], as shown in Figure 1.1.

Level 0 – no driving automation – driving is totally based on human driver control because there are no warnings, and the human driver performs all actions.


Level 1 is the lowest level of automation and is called “driver assistance”. The human driver is aided with either steering or braking/acceleration support such as adaptive cruise control (ACC) or lane centering.

Level 2 systems – Here, there is partial driving automation, both via steering and braking/acceleration supports provided at the same time to the human driver.

Level 3: The system can autonomously drive under the certain conditions, but still the human driver is required to take control in situations which the vehicle cannot handle.

Level 4 – vehicle can perform autonomous navigation in partial restricted conditions, but driver is required for others.

Level 5 – This is full automation, the human is not required to take over the driving, and a Level 5 system can handle all driving situations and drive autonomously. Currently, Level 2 vehicles dominate the market, and higher levels of autonomy are likely to be seen in the upcoming years.



# SAE J3016™ LEVELS OF DRIVING AUTOMATION™

Learn more here: [sae.org/standards/content/J3016\\_202104](https://sae.org/standards/content/J3016_202104)

Copyright © 2021 SAE International. The summary table may be freely copied and distributed AS-IS provided that SAE International is acknowledged as the source of the content.

<p>What does the human in the driver's seat have to do?</p>	<div>SAE LEVEL 0™</div> <div>SAE LEVEL 1™</div> <div>SAE LEVEL 2™</div> <div>SAE LEVEL 3™</div> <div>SAE LEVEL 4™</div> <div>SAE LEVEL 5™</div>					
	<p>You are driving whenever these driver support features are engaged – even if your feet are off the pedals and you are not steering</p>		<p>You are <b>not</b> driving when these automated driving features are engaged – even if you are seated in “the driver’s seat”</p>		<p>These automated driving features will not require you to take over driving</p>	
	<p>You must constantly supervise these support features; you must steer, brake or accelerate as needed to maintain safety</p>		<p>When the feature requests, you must drive</p>			
<p>What do these features do?</p>	<p>These features are limited to providing warnings and momentary assistance</p>		<p>These features provide steering AND brake/acceleration support to the driver</p>		<p>These features can drive the vehicle under limited conditions and will not operate unless all required conditions are met</p>	
	<p>These features provide steering OR brake/acceleration support to the driver</p>		<p>These features provide steering AND brake/acceleration support to the driver</p>		<p>This feature can drive the vehicle under all conditions</p>	
<p>Example Features</p>	<ul style="list-style-type: none"> <li>• automatic emergency braking</li> <li>• blind spot warning</li> <li>• lane departure warning</li> </ul>		<ul style="list-style-type: none"> <li>• lane centering OR</li> <li>• adaptive cruise control</li> </ul>		<ul style="list-style-type: none"> <li>• traffic jam chauffeur</li> </ul>	
	<ul style="list-style-type: none"> <li>• lane centering AND</li> <li>• adaptive cruise control at the same time</li> </ul>		<ul style="list-style-type: none"> <li>• local driverless taxi</li> <li>• pedals/steering wheel may or may not be installed</li> </ul>		<ul style="list-style-type: none"> <li>• same as level 4, but feature can drive everywhere in all conditions</li> </ul>	

Copyright © 2021 SAE International.

These are driver support features

These are automated driving features

Copyright © 2021 SAE International.

Figure 1.1: Driving automation levels of SAE J3016 [3].

Today's radar sensors are not sufficient for fully autonomous vehicles, and the required technical improvements to enable higher levels of autonomy are listed in [4] as follows:

- Higher angular resolution in both azimuth and elevation directions as well as higher range resolution so that more detailed information about detected objects can be provided. This is crucial to determine objects properties such as height, size and position with respect of the vehicle.
- Enhanced velocity resolution and estimation to be able to detect and potentially classify road users such as pedestrians and cyclists.
- A flexible field of view (FoV) to allow pedestrian detection with a broad FoV as well as highway detection with a narrow FoV.
- Providing reliable detection even in the event of failure of any component and/or environmental influences such as heavy rain.
- Affordable cost and a compact size whilst addressing all the requirements.

It is seen that one of the major challenges related to sensors is that they provide a target's information in a limited range and limited FoV, and this directly limits the safety of autonomous vehicles [5]. It is unrealistic to believe that employing just single radar is sufficient to fulfil all the requirements in an autonomous vehicle. To enhance detection and make autonomous driving more reliable, a large number (six or more) of radar sensors distributed around of each vehicle are needed to provide full assessment of surrounding. Currently, each radar sensor operates individually without additional information from any other sensor. It is obvious that gathering information coming from multiple sensors will improve object detection. For example, in [6], a promising cooperative radar sensor system utilising two radar sensors was presented to increase FoV and its performance under a phase noise was evaluated.



In today's intelligent transportation system (ITS), dedicated short range communications (DSRC) [7] is proposed for vehicular communication which allows exchange of information such as raw sensor data to prevent collision and hence save lives. DSRC is designed for either one-way or two-way communication up to medium range. It is possible to enable vehicle-to-vehicle (V2V), vehicle-to-infrastructure (V2I), and vehicle-to-everything (V2X) communication with DSRC. In this system, for instance, DSRC-equipped vehicles can broadcast their location, speed, destination etc., and other vehicles in the vicinity can adjust their movements and take the required action to avoid a potential collision or provide a hazard warning via these messages [7]. In 1999, the Federal Communication Commission (FCC) in the US licensed a frequency of 5.9 GHz with a 75 MHz bandwidth for DSRC, and the IEEE 802.11p wireless access for vehicular environment (WAVE) standard is used in DSRC [7]. In Europe, the transmission frequency is also 5.9 GHz with a 30 MHz bandwidth, and it has been licensed by the European Telecommunications Standards Institute (ETSI) [8].

The maximum communication range and data rate achieved are 1 km and 27 Mb/s, respectively, in the allocated frequency for DSRC [5], [9]. Nevertheless, this data rate is insufficient for autonomous vehicles especially, in urban areas with traffic congestion. In order to increase data rate, a larger bandwidth is needed, and this is available at mm-wave lengths. However, the electromagnetic spectrum is very dense in the mm-wavelength band [10], [11], and the requests to use these levels are increasing day by day for both radar and communication applications because of the potential high bandwidths available. Therefore, there is a growing interest in sharing a common spectrum for both radar and communication (RadCom) systems as it exploits improvements in spectrum efficiency.

Spectrum sharing methods of RadCom systems can be categorised as *coexistence*, *cooperation* and *codesign* [12]. In *coexistence*, both radar and communication systems have

their own transmitters which utilise the same frequency band, but these systems cannot share their information with each other. Hence, the main challenge with this group is how to eliminate mutual coupling whilst ensuring satisfactory performance in both systems [13]. In the *cooperative* technique, both systems have their own separate hardware, but interference can be mitigated by exploiting the required knowledge between the systems [12]. Therefore, each system is able to effectively reduce interference caused by one to the other. On the other hand, in *codesign*, both RadCom systems are implemented using the same hardware, and the systems use the same waveform. In this way, both systems work simultaneously without considering the interference of one with the other system.

Using one hardware chipset for two different functionalities instead of two separate chipsets is a desired approach in automotive industry. In this way, the cost of hardware and power consumption can be reduced whilst also achieving higher data rates. Moreover, this compact hardware design can help to reduce sensor density on the vehicle, whilst simultaneously reaching the higher levels of automation. However, using a common waveform for both functions can cause significant degradations in their performance because conventional radar and communication waveform characteristics are different and were designed to provide different capabilities. Generally, automotive radars use frequency-modulated continuous-wave (FMCW) whereas communication waveforms are more typically phase coded signals with different kind of multiplexing, such as orthogonal frequency-division multiplexing (OFDM) etc. Therefore, the choice of waveform will have an important impact on the achieved performance, and consequently waveform design must be done very carefully to avoid any degradation.

In the literature, the proposed waveforms to enable both systems can be classified into three groups: *radar-centric* design, *communication-centric* design and *joint design* and

*optimization* [14], [15]. In *radar-centric* waveform designs, the primary function is sensing whereas the communication is implemented as a secondary function as a mode of the radar system. In contrast to radar-centric waveforms, *communication-centric* waveforms are intended to extract radar echo information using a standardized communication system. With regard to the *joint design and optimization* group, they do not favour one to another system and do not have to adhere to any particular standard. The primary objective of the work described in this thesis is to propose new waveforms to enable sensing and connectivity simultaneously for automotive vehicles, using the same chipset without sacrificing radar performance while still reaching high data rates for communications.

Another important parameter in radar performance is angular resolution which is used to differentiate between closely positioned targets. For a given transmission frequency, angular resolution depends on antenna aperture. As the antenna aperture increases, the angular resolution improves [16]. Uniform phased arrays with half-wavelength element spacing are preferred to obtain a desired angular resolution with  $\pm 90^\circ$  FoV. However, the required number of antenna elements can be high and the antenna dimension can be larger than is desirable for automotive radars. To get around this limitation, multiple-input multiple-output (MIMO) antennas can be used to achieve the same angular resolution but with a significantly reduced number of antenna elements and hence a more compact antenna size [17], [18], [19]. For high angular resolution, the total antenna element in a conventional MIMO can still remain very large. Therefore, a further reduction in the number of antenna elements is desired to reduce the cost and weight of MIMO whilst achieving the required beamwidths in both directions. This leads directly to the concept of a sparse MIMO array antenna. If sparsity is to be achieved using a non-uniform placement of antenna elements, this can lead to a configuration with very high sidelobe levels which consequently will limit the radar performance. This means that the

thinning of antenna elements must be done very carefully with the resulting sidelobe levels carefully checked. It should be noted, though, that even if an optimal antenna configuration gives undesired sidelobe levels, sidelobe minimisation techniques can be applied to reduce the overall sidelobe level.

In the literature, the thinning of the total antenna elements in both phased arrays and 1-D MIMO antennas has been studied extensively. However, the thinning of 2-D MIMO antennas has been little explored. Therefore, the second objective of the research described in this thesis is the investigation of the effect of thinning in 2-D MIMO arrays and the design of new antenna configurations.

This second objective also includes obtaining high angular resolution beyond that of the physical MIMO aperture by interpolating and extrapolating the virtual array elements via the Burg algorithm. Furthermore, it is known that high sidelobe levels inherent in MIMO limit the detection and angular resolution becomes worse in the off-the-boresight directions. To overcome these issues, the Burg algorithm is combined with MIMO radar and the Doppler beam sharpening (MIMO-DBS) technique. Performance is tested through simulation and both laboratory-based and real-world experiments.

With these objectives, while enabling joint radar and communication using single chipset, higher angular resolutions can be achieved using the compact sized sensors. As a result, within the confined spaces of vehicles, characterised by increasingly dense sensor packing, the available space for the sensors is optimally utilised. This in turn paves the way for higher levels of automation, strengthening the capabilities of autonomous systems and increasing overall efficiency and safety.

## 1.2 Contributions

The original contributions from the author are as follows:

- The design of new waveforms which help to significantly enhance the radar performance whilst also simultaneously achieving a desired communication performance using the same hardware and same spectral band. Such waveforms are subsequently used for radar sensing with MIMO beamforming, achieving better angular resolutions and higher data rates. The validity of the proposed waveforms is demonstrated through both simulation and experimentation.
- The design of sparse MIMO antenna configurations to reduce the total number of antenna elements whilst also obtaining high angular resolution in both azimuth and elevation directions with acceptable sidelobe levels. To reach this aim, three different methods are followed:
  - Multiple thinned 2-D MIMO antennas using optimization techniques have been designed, and the computational benefits of the predefined initial positions of the array are investigated via simulation.
  - Compact-sized MIMO arrays have been designed, and the virtual array configurations are interpolated and/or extrapolated by applying the Burg algorithm so as to achieve the angular resolution(s) beyond that of the real or virtual aperture.
  - The Burg algorithm has been combined with a MIMO-DBS technique to improve cross-range resolution in both the forward looking and the lateral directions and suppress the sidelobe levels inherent in MIMO.

Based on the above, two journal papers and four conference papers have been published, one journal paper has been recently submitted, and one journal paper is still in preparation as listed below:

- 1- M. Bekar, C. J. Baker, E. G. Hoare and M. Gashinova, "Joint MIMO Radar and Communication System Using a PSK-LFM Waveform With TDM and CDM Approaches," in *IEEE Sensors Journal*, vol. 21, no. 5, pp. 6115-6124, 1 March1, 2021, doi: 10.1109/JSEN.2020.3043085. (The number of citations – 34 on 16/01/2024)
- 2- M. Bekar, C. J. Baker, E. Hoare and M. Gashinova, "Realization of a Joint MIMO Radar and Communication System using a PSK-LFM Waveform," *2020 IEEE Radar Conference (RadarConf20)*, Florence, Italy, 2020, pp. 1-6, doi: 10.1109/RadarConf2043947.2020.9266699.
- 3- M. Bekar, C. J. Baker and M. Gashinova, "Sparse 2D MIMO Antenna Designs using Simulated Annealing," *2023 20th European Radar Conference (EuRAD)*, Berlin, Germany, 2023, pp. 371-374, doi: 10.23919/EuRAD58043.2023.10289537.
- 4- M. Bekar, C. J. Baker and M. Gashinova, "Reconstructed 2D MIMO Using Burg Algorithm," *2023 20th European Radar Conference (EuRAD)*, Berlin, Germany, 2023, pp. 375-378, doi: 10.23919/EuRAD58043.2023.10289589.
- 5- M. Bekar, C. Baker and M. Gashinova, "Enhanced Angular Resolution in Automotive Radar Imagery Using Burg-Aided MIMO-DBS Approach," *2023 20th European Radar Conference (EuRAD)*, Berlin, Germany, 2023, pp. 315-318, doi: 10.23919/EuRAD58043.2023.10289130.
- 6- A. Bekar, M. Bekar, C. J. Baker and M. Antoniou, "Coherent Change Detection for High-Resolution Drone-Borne SAR at 24 GHz," in *IEEE Journal of Selected Topics in Applied Earth Observations and Remote Sensing*, doi: 10.1109/JSTARS.2023.3324570.

- 7- M. Bekar, C. J. Baker and M. Gashinova, "Burg-Aided 2-D MIMO Array Extrapolation for Improved Spatial Resolution," intend to be submitted to *IEEE Transactions on Aerospace and Electronic Systems*.
- 8- M. Bekar, C. J. Baker and M. Gashinova, "Performance Comparison of MIMO-DBS and Back-projection via Burg Algorithm," in preparation, intend to be submitted to *IEEE Transactions on Radar Systems*.

## 1.3 Thesis Outline

- Chapter 2 provides background information that is used throughout the rest of this thesis. In the radar part, fundamentals of radar are presented including radar equation, operating frequencies, radar waveforms, ambiguity function, MIMO radar and automotive radar. In the communication part, communication basics are introduced including communication system types, channel capacity, communication waveforms as well as multiplexing access types.
- Chapter 3 starts with a literature review on joint RadCom systems, and then introduces a novel technique which enables communication data to be embedded into MIMO radar waveforms. A linear frequency modulated (LFM) signal is used for radar sensing, and multiple phase-shift keying (PSK) symbols or bit sequences are embedded into the LFM signal for communications. Such waveforms are subsequently used for radar sensing with MIMO beamforming. Orthogonality between transmitters is ensured using either a time-division multiplexing (TDM) or code-division multiplexing (CDM) approach. The performance of these novel techniques is demonstrated through both simulation and experimentation.

- Chapter 4 starts with a literature review on designing sparse antenna configurations by employing optimization techniques, and it is followed by mathematical explanations of thinned 1-D and 2-D MIMO arrays and fundamentals of genetic algorithm and simulated annealing. Later on, thinned 1-D MIMO arrays that are optimized using either simulated annealing or genetic algorithm are presented. Finally, a methodology of optimizing the positions of the elements of sparse 2-D MIMO array is proposed. This methodology is based on simulated annealing and has the goal of minimizing the sidelobe level (SSL) whilst keeping the beamwidth constant and consistent with the size of the virtual receive array. The computational benefits of predefined initial positions of the array are discussed and results are presented to illustrate performance potential.
- Chapter 5 starts with a literature review on how to achieve higher angular resolutions beyond that of the corresponding antenna. Then, a novel methodology for the extrapolation of 2-D MIMO array using Burg algorithm is proposed with the aim to achieve higher angular resolution beyond that of the corresponding 2-D MIMO virtual array. The main advantage of such an approach is that it allows to dramatically decrease both the physical size and the number of antenna elements of the MIMO array. The performance and limitations of Burg algorithm are examined through both simulation and experimentation at 77 GHz. The experimental methodology used to acquire 3-D data of range, azimuth and elevation information with the 1-D MIMO off-the-shelf radar is described. Using this method, the performance of the proposed array can be tested experimentally, especially at frequencies where it is desired to assess the antenna response prior to fabricating the antenna.
- Chapter 6 starts with a literature review on Doppler beam sharpening (DBS) and combination of MIMO-DBS techniques, then the use of the Burg algorithm combined



with a MIMO-DBS technique, which is a novel technique, is presented to improve cross-range resolution in both the forward looking and the lateral directions. The performance of the proposed method is evaluated through both simulation and lab/real world experiments at 77 GHz.

- Chapter 7 discusses the findings of this thesis and explores potential future works.

# Chapter 2 – Background

## 2.1 Radar

Radar (RAdio Detection And Ranging) is a sensing system used to detect objects in a scene and determine their positions and speeds by measuring their reflected echoes. The history of radar system begins in the last decades of the 19<sup>th</sup> century. Heinrich Hertz, in 1886, experimentally demonstrated that metallic and dielectric bodies could reflect radio waves [20]. In 1897, the Russian scientist Alexander Popov, in his report on radio communication experiments in Baltic Sea, stated he had made a detection of a warship "Lieutenant Il'in" (Лейтенант Ильин in Russian) when it crossed a radio communication link between two other ships, which was the first observation of object detection using radio waves [21]. In 1904, a German engineer, Christian Hülsmeyer, invented the “Telemobiloscope” which was the first patented device using radio waves to detect targets such as ships [20].

Then, early forms of radar devices were developed during Second World War to detect airborne targets and measure their range and speed. They were used for only military purposes. Now, radar is used in many disciplines such as navigation, mapping, weather forecasting, air traffic control, and many, many others. This is because the radar system is able to operate at night and day as well as in all kinds of weather [22].

## 2.1.1 Radar Basics

The basic principle of radar is demonstrated in Figure 2.1. A conventional radar system includes a transmitter, a receiver, an antenna and a display. Basically, the transmitter radiates radio waves into space using an antenna. Reflected echoes coming from objects, typically called as targets, are captured by a receive antenna. In the receiver, there is a processing to detect the presence of a target and to determine the target's position (range, azimuth and elevation) as well as velocity relative to the radar.

A target's range is estimated from the time delay between the transmitted and received signals. If the transmitter and receiver are collocated, the transmitted signal follows the path between transmitter and target, then is reflected from the target and travels back to receiver by the same path to be assessed in radar receiver. Equation (2.1) is used to determine a target's range ( $R$ ) for a generic transmitted pulse:

$$R = \frac{c\tau}{2} \quad (2.1)$$

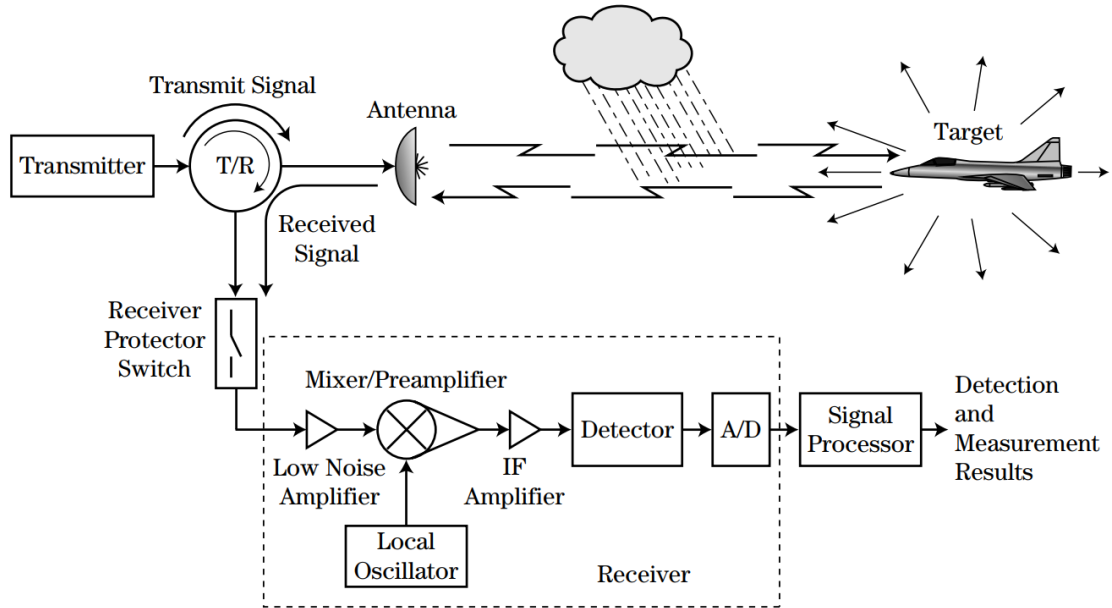


Figure 2.1: The basic principle of radar [23].

where  $\tau$  is the delay time and  $c$  is the speed of light.

The maximum range at which targets can be detected depends on the radar design parameters. Each radar system has a minimum signal to noise ratio ( $SNR$ ) requirement to detect the targets. According to radar equation,  $SNR$  is calculated by [22]

$$SNR = \frac{P_r}{P_n} = \frac{P_t G_t G_r \lambda^2 \sigma}{(4\pi)^3 R^4 k T_o B F L} \quad (2.2)$$

where  $P_t$  and  $P_r$  are transmitted and received power, respectively;  $G_t$  and  $G_r$  are the transmitted and received antenna gains, respectively;  $\lambda$  is the wavelength,  $\sigma$  is the radar cross section of the target,  $k$  is the Boltzmann's constant,  $T_o$  is the noise temperature,  $B$  is its bandwidth,  $F$  is receiver noise figure and  $L$  is used for other losses.  $P_n$  is noise power, calculated as  $P_n = k T_o B F$ .

When a target is located at the maximum detectable range ( $R_{max}$ ),  $P_r$  becomes an allowed minimum ( $P_{r_{min}}$ ), as determined by the required minimum  $SNR$  for the target detection. Hence, the  $R_{max}$  is calculated as in (2.3).

$$R_{max} = \sqrt[4]{\frac{P_t G_t G_r \lambda^2 \sigma}{(4\pi)^3 P_{r_{min}} L}} \quad (2.3)$$

Radars operate over a wide span of transmission frequencies ranging from 3 MHz to 300 GHz. This range is divided into multiple radio frequency (RF) bands and each RF band is named as can be seen in Table 2.1. The table also shows the specific frequency spans allocated for radar applications. When a lower frequency radar is used, the size and weight of the hardware becomes large and heavy due to the longer wavelengths. On the other hand, when higher frequency is preferred, the device becomes more compact and lighter, although it becomes more challenging to generate high powers for long range operation.

Table 2.1: RF and Radar Bands [23]

Band	Frequency Range	ITU Radar Freq.
High frequency (HF)	3–30 MHz	
Very high frequency (VHF)	30–300 MHz	138–144 MHz 216–225 MHz
Ultra high frequency (UHF)	300 MHz–1 GHz	420–450 MHz 890–942 MHz
L	1–2 GHz	1.215–1.400 GHz
S	2–4 GHz	2.3–2.5 GHz 2.7–3.7 GHz
C	4–8 GHz	5.250–5.925 GHz
X	8–12 GHz	8.500–10.680 GHz
Ku (“under” K-band)	12–18 GHz	13.4–14.0 GHz 15.7–17.7 GHz
K	18–27 GHz	24.05–24.25 GHz 24.65–24.75 GHz
Ka (“above” K-band)	27–40 GHz	33.4–36.0 GHz
V	40–75 GHz	59.0–64.0 GHz
W	75–110 GHz	76.0–81.0 GHz 92.0–100.0 GHz
mm	100–300 GHz	126.0–142.0 GHz 144.0–149.0 GHz 231.0–235.0 GHz 238.0–248.0 GHz

## 2.1.2 Radar Waveforms

*Pulse radar* emits its radio waves as a relatively short pulse (typically between a few nano seconds and a few tens of micro seconds) and starts to listen for back-scattered echoes after completing the transmission. The radar signal may be a simple sinusoidal wave with a constant frequency and amplitude. This kind of radar is able to estimate the range of the targets via the time delay of the echoes (scaled by the velocity of light). These radars are commonly designed for well-established long-range applications such as air traffic control and airborne radar.

*Continuous wave (CW) radar* achieves to transmit signals and listen for echoes simultaneously [22]. To avoid too much coupling of the transmitted signal directly into the

receiver, their transmission powers are relatively low and generally much lower than pulsed radars. Therefore, they operate at relatively short ranges but have found wide application such as in automotive radar. CW radars are divided into two groups as described below.

*Unmodulated CW radar:* These radars have a constant frequency, amplitude and phase, and transmit the signal continuously. This kind of radars can be used for velocity estimation of the target, but not for range estimation due to their inherent range ambiguity.

*Modulated CW radar:* The sinusoidal signal modulated in frequency, phase or amplitude can be used to estimate the range of the target, in addition to its radial velocity (i.e., with respect to the radar).

In the following subsections, a brief of linear frequency modulation (LFM) and phase-coded waveforms is given as they are commonly used.

### 2.1.2.1 Linear Frequency Modulation

Among the frequency modulation types, Linear Frequency Modulation (LFM) is one of the most used for radar purposes. This is due to its ease of implementation, its robustness to Doppler shift, and the presence of a useful wideband receiver filtering structure known as stretch processing. Additionally, LFM enables the bandwidth to be independent of the pulse duration. LFM is also known as "chirp" modulation. In an LFM, a sine wave is modulated by increasing (upchirp) or decreasing (downchirp) the frequency of the transmitted signal linearly. The complex form of LFM signals is expressed as

$$s(t) = \text{rect}\left(\frac{t}{T_m}\right) \exp\left(j\left(\varphi + 2\pi f_c t \pm \pi \frac{B}{T_m} t^2\right)\right) \quad -\frac{T_m}{2} \leq t \leq \frac{T_m}{2} \quad (2.4)$$

where  $\varphi$  is the initial phase,  $f_c$  is carrier frequency,  $B$  is bandwidth,  $T_m$  is chirp duration, and  $t$  is time. ‘+’ notation is used for an upchirp whereas ‘-’ notation is used for a downchirp.

Frequency versus time characteristics of baseband upchirp and downchirp LFM signals are shown in Figure 2.2(a) and 2.2(b), respectively. Moreover, real and imaginary parts of upchirp and downchirp LFM signals are illustrated in Figure 2.2(c) and 2.2(d), respectively.

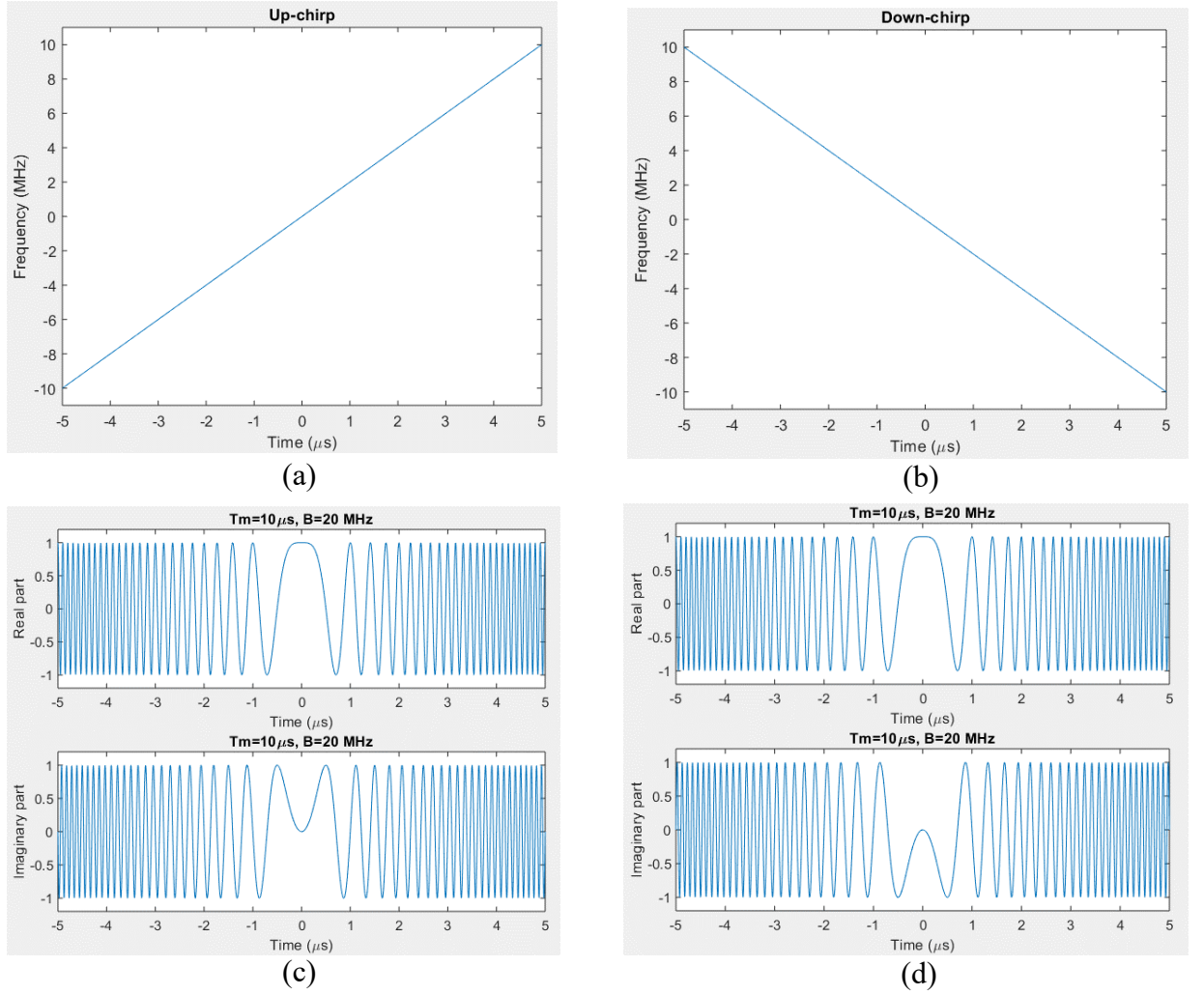


Figure 2.2: (a) Upchirp LFM (b) Downchirp LFM (c) and (d) real and imaginary parts of the upchirp and downchirp, respectively.

### 2.1.2.1.1 Matched Filter

When received signal passes through the matched filter for range compression, the  $SNR$  is maximised at the output of the matched filter [24]. Matched filter (MF) can be applied to the signal in either time domain or frequency domain. In time domain, matched filter can be realised as the convolution of transmitted and received signals:

$$s_{out}(t) = s_r(t) \otimes h(t) \quad (2.5)$$

where  $s_r(t)$  is the received signal, and  $h(t)$  is the impulse response of the MF equal to complex conjugate of the transmitted signal. The received signal is the time delayed version of the transmitted signal, so  $s_r(t)$  and  $h(t)$ , in the case of LFM signal (upchirp), can be written as

$$s_r(t) = \text{rect}\left(\frac{t - \tau}{T_m}\right) \exp\left(j\left(\varphi + 2\pi f_c(t - \tau) + \pi \frac{B}{T_m}(t - \tau)^2\right)\right) \quad (2.6)$$

and

$$h(t) = \text{rect}\left(\frac{t}{T_m}\right) \exp\left(-j\left(\varphi + 2\pi f_c t + \pi \frac{B}{T_m} t^2\right)\right) \quad (2.7)$$

For a stationary target, if constant phase is ignored and centre frequency ( $f_c$ ) is equal to zero (baseband processing),  $s_{out}(t)$  can be written as [25]

$$s_{out}(t) \approx T_m \text{sinc}(B(t - \tau)) \quad (2.8)$$

In frequency domain, the received signal and the complex conjugate of the transmitted signals are multiplied. When the centre frequency is zero, the instantaneous frequency,  $f$ , is given by (2.9), which confirms that the frequency of the LFM signal changes linearly over time, and this agrees with Figure 2.2(a). This is equally applicable to any centre frequency as after derivative the  $f_c$  will only constitute constant and  $f$  will show linear change with time.



$$f = \frac{1}{2\pi} \frac{d(\frac{\pi B t^2}{T_m})}{dt} = \frac{Bt}{T_m} \quad (2.9)$$

In the case of zero centre frequency, Fourier transform (FT) of the upchirp LFM received signal and complex conjugate of the transmitted signal are given by

$$\begin{aligned} S_r(f) &= \int_{-\infty}^{\infty} \text{rect}\left(\frac{t-\tau}{T_m}\right) \exp\left(j\pi \frac{B}{T_m}(t-\tau)^2\right) \exp(-j2\pi f t) dt \\ &= \text{rect}\left(\frac{f}{B}\right) \exp\left(-j\pi \frac{T_m f^2}{B}\right) \exp(-j2\pi f \tau) \end{aligned} \quad (2.10)$$

and transfer function of Matched Filter is

$$\begin{aligned} H(f) &= \int_{-\infty}^{\infty} \text{rect}\left(\frac{t}{T_m}\right) \exp\left(-j\pi \frac{B}{T_m} t^2\right) \exp(-j2\pi f t) dt \\ &= \text{rect}\left(\frac{f}{B}\right) \exp\left(j\pi \frac{T_m f^2}{B}\right) \end{aligned} \quad (2.11)$$

Hence, in the frequency domain, the response of the matched filter is

$$S_{out}(f) = S_r(f)H(f) = \text{rect}\left(\frac{f}{B}\right) \exp(-j2\pi f \tau) \quad (2.12)$$

When inverse of Fourier transform (IFT) of  $S_{out}(f)$  is taken

$$s_{out}(t) = \frac{B}{T_m} T_m \text{sinc}(B(t - \tau)) \quad (2.13)$$

It is clearly seen that only difference between responses of MF in time domain and frequency domain is the constant component ' $\frac{B}{T_m}$ ', which can be ignored. Hence, it can be said that these two methods give the same response. The block diagram of the matched filtering in the frequency domain is demonstrated in Figure 2.3.

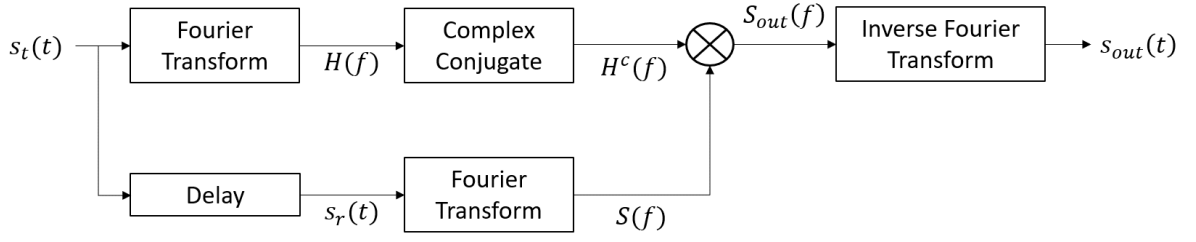


Figure 2.3: The steps of matched filtering in frequency domain.

The pulse compression response of a stationary target is demonstrated in Figure 2.4. The peak point of the main lobe shows the position of the target. Any lobe except the main lobe is called a sidelobe, and the level of the first sidelobe is roughly -13 dB without applying any weightings because the envelope of the transmitted signal is rectangular, and the response of matched filter is sinc function as (2.8) and (2.13). The sinc function, represented as  $\sin(x\pi)/x\pi$ , results in a 13 dB power difference between the main lobe and the first sidelobe levels. In a radar system, it is important to distinguish two or more closely spaced targets. The required minimum separation to resolve two targets when there are two targets in the scene is called as resolution. The detectable minimum distance between targets ( $\Delta R$ ) is called a range resolution, and it depends on the bandwidth of the radiated signal as seen in (2.14). As bandwidth increases, range resolution improves. When the range profile in Figure 2.4 is examined, the range resolution equals to the distance of the half power points, in other words -3 dB power of the main lobe in Figure 2.4. Moreover, the distance between the first null-to-null power points equals to the two times of the range resolution.

$$\Delta R = \kappa \frac{c}{2B} \quad (2.14)$$

where  $\kappa$  is scaling factor used to account for various intentional and unintentional factors that can degrade the range resolution of radar system [23].

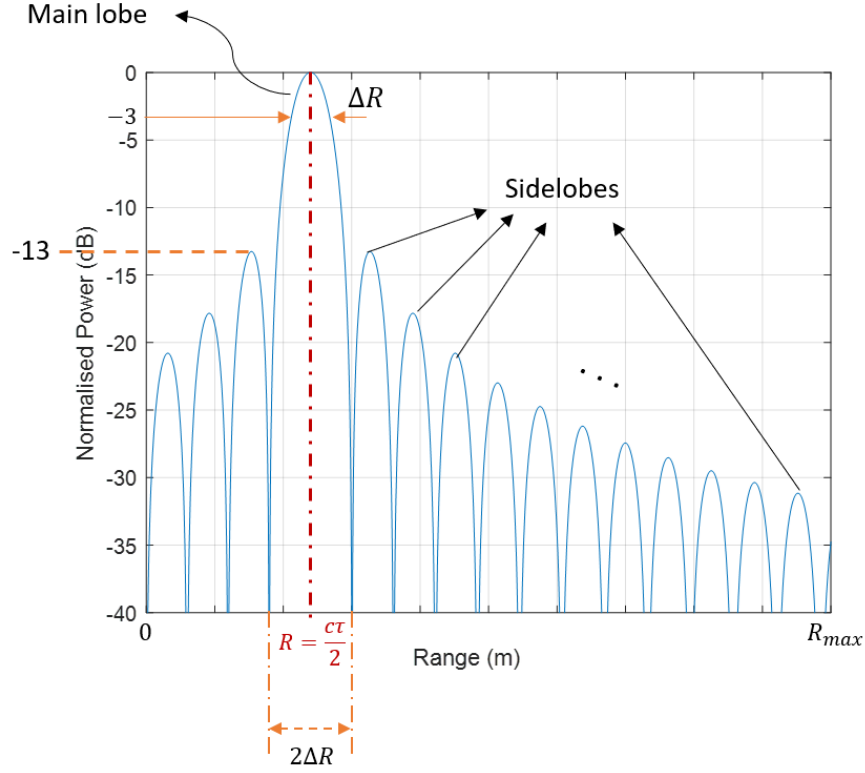


Figure 2.4: Range profile of a stationary target.

### 2.1.2.2 Phase Modulation

In phase modulation (PM), the pulse which has a constant frequency and amplitude is divided into  $N$  sub-pulses, and each sub-pulse is modulated via phase coding using either binary or polyphase coding. The bandwidth is now determined by the modulating rate. The phase modulated signal can be expressed as

$$s_{PM}(t) = \sum_{n=0}^{N-1} a(t) \exp(j(2\pi f_c(t - nt_b) + \varphi_n)) \quad (2.15)$$

where  $a(t)$  is amplitude,  $t_b$  is sub-pulse duration,  $\varphi_n$  is the phase of the  $n$ -th sub-pulse, and  $t$  is time and takes the value of  $0 \leq t \leq T_p$ , where  $T_p$  is the pulse duration.

Binary phase shift keying (BPSK) modulation is commonly used for phase modulation. BPSK uses 0 and  $\pi$  phases, and 0 and  $\pi$  are represented by '+' and '-' signs of amplitude  $a(t)$ . More details are given in Section 2.2.1.1.

The bandwidth of the pulsed radar, which is inversely proportional to the pulse duration ( $B = \frac{1}{T_p}$ ), becomes related to the sub-pulse duration with PM as in (2.16). Hence, higher bandwidth is achieved, and it can be seen from (2.14) that the range resolution improves significantly, compared to pulsed radar.

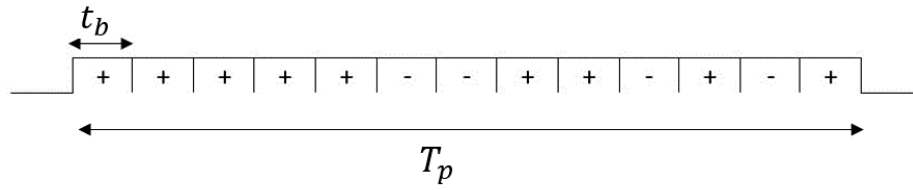
$$B = \frac{1}{t_b} \quad (2.16)$$

There are various codes used in phase modulation, including Barker codes, maximum length shift register sequences (m-sequences), Gold and Kasami sequences. Moreover, each code has multiple sequences which have different code lengths. The aims of all these codes are to provide low sidelobes whilst using pulse compression. In this thesis, Barker codes and m-sequences are used, so brief explanations are given in the upcoming sub-sections.

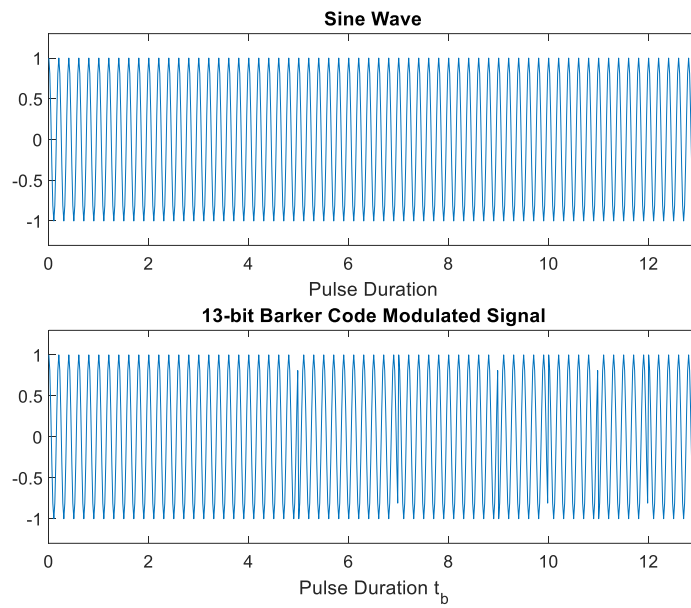
### 2.1.2.2.1 Barker Code

In Barker code, the baseband pulse is divided to multiple sub-pulses (bits or chips in this context), and duration of each sub-pulse is equal, making it a codeword as shown in Figure 2.5(a). The binary phase codes, in other words BPSK, are used for phase modulation. Barker code reduces the sidelobe level (SLL) by changing the phase of the sine wave. There are 7 different Barker codes [22]. As the code length increases, lower sidelobes are achieved. The maximum Barker code length is 13-bits, and its sequence and the phase modulated waveform are shown in Figure 2.5. The received signal passes through delayed tapped line filter which is shown in Figure 2.6(a) where R represents a  $180^\circ$  phase shift. The output of the filter is known

as autocorrelation function, and its response in both linear and dB units are shown in Figure 2.6(b) and 2.6(c), respectively. It is seen from Figure 2.6(c) that 13-bit Barker code gives -22.3 dB sidelobe level whereas LFM gives -13 dB sidelobe level without weightings.



(a)



(b)

Figure 2.5: (a) 13 bits Barker code sequence, (b) simple pulse waveform with a rectangular envelope and 13-bit Barker code modulated RF waveform.

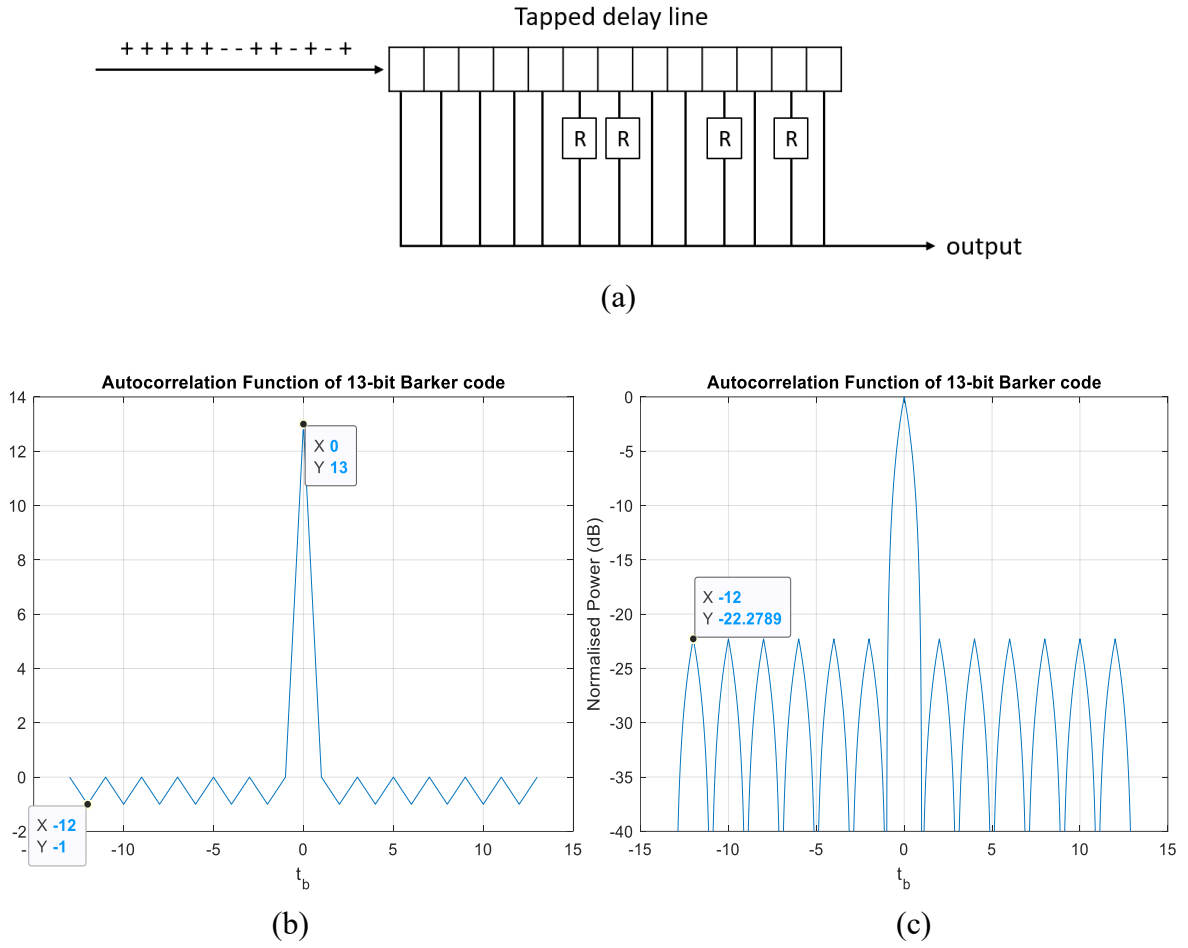


Figure 2.6: (a) Tapped delay line of 13-bit Barker code, (b) auto-correlation function of 13-bit Barker code, (c) auto-correlation function of the code in dB unit.

## 2.1.2.2.2 M-sequences

Maximal length linear feedback shift register sequences, in other words m-sequences, also known as pseudo-random sequences are generated using linear feedback shift registers (LFSR) [26]. A linear function of a number of bits in a shift register determines the input bit of the register. This type of shift register is called a LFSR, and the general equation can be written

as in (2.17). When number of registers is  $n$ , the achieved sequence length is  $2^n - 1$ . The sequence includes only binary values, that is, zeros and ones.

$$f(x) = a_0 + a_1x + a_2x^2 + \cdots + a_nx^n \pmod{2} \quad (2.17)$$

where  $f(x)$  is the next bit in the LFSR sequence,  $a_0, a_1, \dots, a_n$  are the coefficients and can be equal to either 0 or 1, and  $x, x^2, \dots, x^n$  are the current bits in the LFSR.  $n$  shows the degree of the polynomial.

It is worth noting that the primitive polynomial must be used to produce the m-sequences [27], the whole values of initial register state in the polynomial cannot all be equal to zeros. At least one of them must be equal to one in order to produce a sequence. The following is an example of how to create a 31-bit m-sequence.

To generate the 31-bit m-sequence, the polynomial degree must be 5 ( $2^5 - 1 = 31$ ), and the equation of  $f(x) = x^5 + x^3 + 1$  can be used. The block diagram of LFSR used is demonstrated in Figure 2.7. For an initial start with '10000' bit sequence, the obtained output bit is calculated using the block diagram in Figure 2.7, and the result is shown in Figure 2.8. After 31 clock cycle, the register state reaches to the initial state which is '10000'. Therefore, after 31 clock cycle, LFSR starts to produce the same states as expected. With regards to the sequence, it can be generated by combining the first bit of the state at each clock, or second bit of the state, or so on. The sequence shown in Figure 2.8 is generated using the first bit of the register state at each clock.

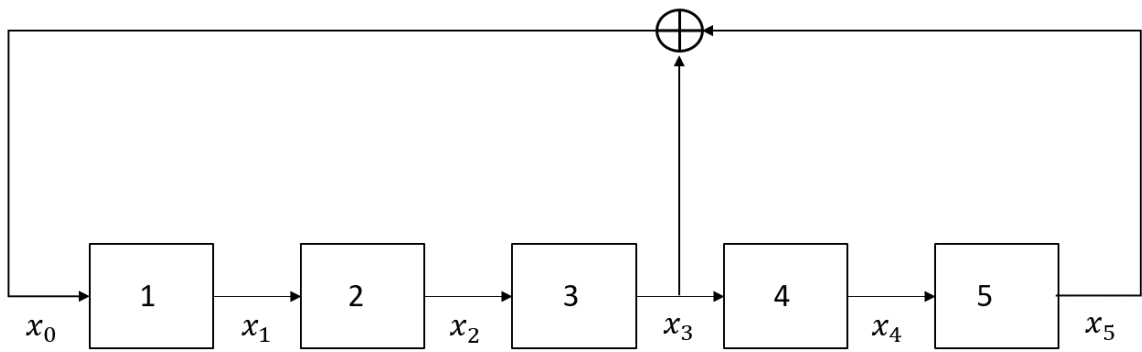


Figure 2.7: Block diagram of the 31-bit m-sequence generator.

Clock Cycle	Register state	Output bit
1	10000	0
2	01000	0
3	00100	1
4	10010	0
5	01001	1
6	10100	1
7	11010	0
8	01101	0
9	00110	1
10	10011	1
11	11001	1
12	11100	1
13	11110	1
14	11111	0
15	01111	0
16	00111	0

Clock Cycle	Register state	Output bit
17	00011	1
18	10001	1
19	11000	0
20	01100	1
21	10110	1
22	11011	1
23	11101	0
24	01110	1
25	10111	0
26	01011	1
27	10101	0
28	01010	0
29	00101	0
30	00010	0
31	00001	1
32	10000	0

initial coefficients

31-bit m-sequence = 1001011001111100011011101010000

Figure 2.8: Steps of generating the 31-bit m-sequence, and at the final, the achieved bit sequence.



### 2.1.3 Ambiguity Function

When a target is moving, it causes a Doppler frequency shift in the received echo signal. The relative motion of the target away from the radar causes a negative frequency shift whereas the motion towards the radar causes a positive shift [22]. The ambiguity function (AF), introduced by Philip Woodward in 1953, is a two-dimensional function which shows the matched filter response of the received signal of the delay time,  $\tau$ , and a Doppler shift,  $f_d$  [28]. One of the forms of AF is given by

$$|\chi(\tau, f_d)| = \left| \int_{-\infty}^{\infty} s(t) s^c(t - \tau) e^{j2\pi f_d t} dt \right| \quad (2.18)$$

where  $s$  is the complex envelope of the signal,  $f_d = \frac{2v}{\lambda}$  where  $v$  is the velocity of the target, and  $(\cdot)^c$  denotes the complex conjugate.

When  $f_d = 0$ , the response of the AF ( $\chi(\tau, 0)$ ) is known as the zero-Doppler cut, and it is equal to the response of the autocorrelation of the waveform (range compressed response). Also, when  $\tau = 0$ , the response of the AF ( $\chi(0, f_d)$ ) is called zero-delay cut, and it is equal to the response of the Fourier transform of the squared modulus of the waveform (velocity response). Each waveform has its own AF response, so it can be used while designing a waveform for a radar application to see the performance of the designed signal.

Here, the AF of the LFM signal will be examined to understand what information can be obtained from an AF plot. It is assumed that the bandwidth of the signal is 200 MHz, and the chirp duration ( $T_m$ ) is equal to the pulse repetition interval (PRI) equal to 50  $\mu$ s. The obtained AF plot using (2.18) is demonstrated in Figure 2.9. The resultant LFM response has a narrow main lobe with low sidelobe levels, though the range and Doppler shift are not entirely independent from each other. Hence, when the target has a velocity, a coupling occurs, so the

target appears at the incorrect range. To understand and compensate for the range – Doppler coupling is vital in applications like tracking and surveillance where precise range estimation of moving targets is critical.

When the zero-Doppler cut of the LFM in Figure 2.10(a) is examined, the positions of the first null-to-null points are equal to  $\pm 0.1$  for  $\frac{\tau_1}{T_m 10^{-3}}$ , so  $\tau_1 = \pm 10^{-4} T_m = \pm 10^{-4} \times 50 \mu s = \pm 5 \times 10^{-9}$ . Also, it is known from (2.1) that if the time delay is known, the range can be estimated, so  $R_1 = \frac{c\tau_1}{2} = \pm 7.5$  cm which equals to the range resolution of the LFM waveform which is given by (2.14), in other words,  $\Delta R = \frac{c}{2B} = \frac{3 \times 10^8}{2 \times 200 \times 10^6} = 7.5$  cm. Hence, it is apparent that the zero-Doppler cut provides the same response as the matched filter of LFM waveform for a stationary target which is detailed in Section 2.1.2.1.1.

When the zero-delay cut of the LFM in Figure 2.10(b) is examined, the positions of the first null-to-null points are equal to  $\pm 1$  for  $f_d \times T_m$ . In other words,  $\frac{2v_1}{\lambda} \times T_m = \pm 1$ , so  $v_1 = \pm \frac{\lambda}{2T_m}$ , and in this case it is assumed that  $T_m = PRI$ , so  $v_1 = \pm \frac{\lambda}{2PRI}$ . Here,  $v_1$  demonstrates the velocity resolution achievable with the designed waveform. Specifically, this indicates that the designed waveform enables the differentiation of two targets positioned at the same range as long as their velocity discrepancy equals or exceeds  $v_1$ . Furthermore, employing multiple chirps enhances the velocity resolution inversely proportional to the number of chirps, as follows:

$$\Delta v = \frac{\lambda}{2nPRI} \quad (2.19)$$

where  $n$  is the number of chirps.

Note that zero-Doppler and zero-delay cuts of the AF defines the achievable resolution in range and velocity of the designed waveform, respectively.

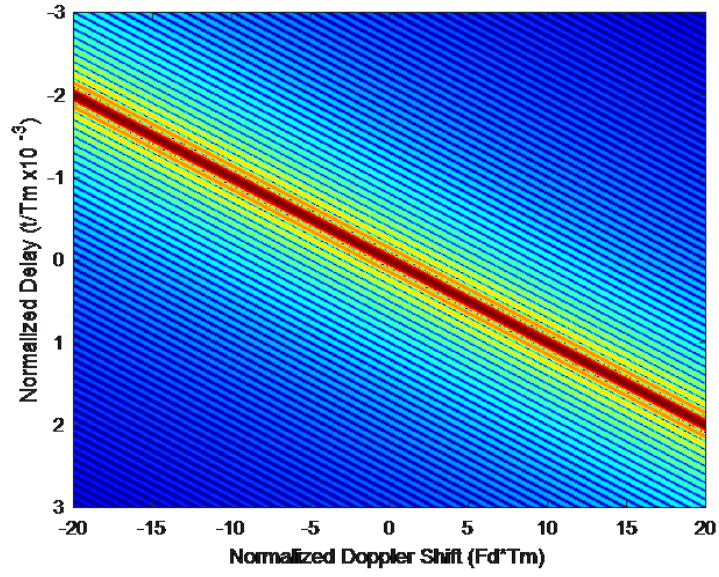


Figure 2.9: The ambiguity function of the LFM waveform.

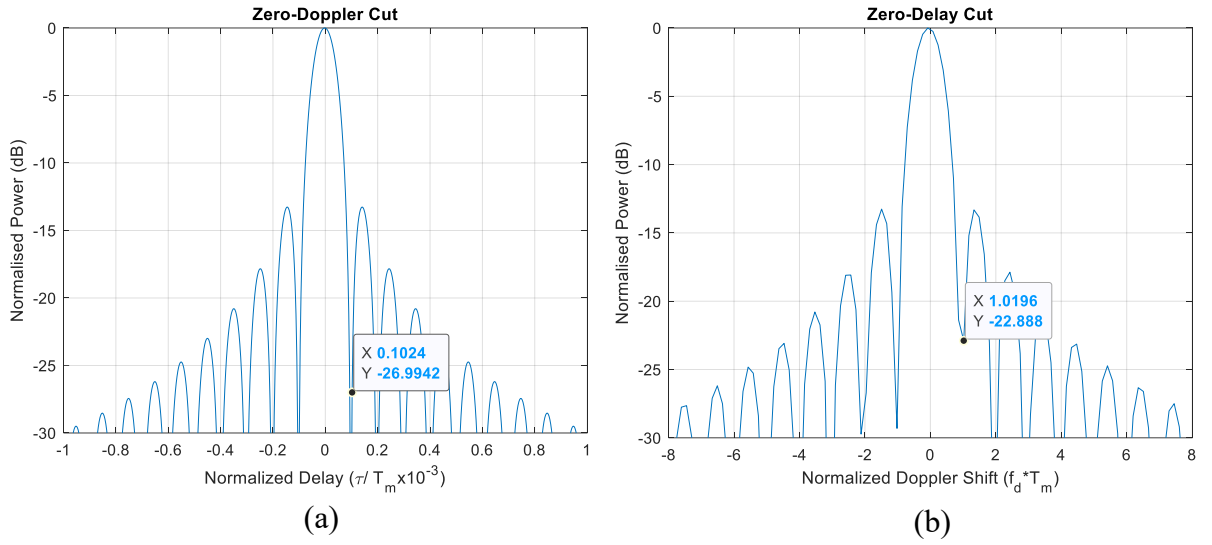


Figure 2.10: (a) The zero-Doppler cut of the LFM waveform, (b) the zero-delay cut of the LFM waveform.

## 2.1.4 MIMO Radar

In addition to range and velocity resolution, another important parameter for a radar application is the estimation of the target's angle, strongly related to the angular resolution. For an angle estimation, two or more antenna elements are needed as a single antenna element does

not meet the requirements for a narrow beamwidth, higher directivity and gain to enable long range operation [16].

The minimum angular difference to distinguish closely positioned targets at the same range is known as the angular resolution, and depends on the antenna length,  $L$ , and wavelength,  $\lambda$ , as follows:

$$\theta_{-3dB} \cong a \frac{\lambda}{L \cos \theta} \quad (2.20)$$

where  $\theta$  is the angle of the target and  $\theta_{-3dB}$  is an angular resolution given in radians.  $a$  is the beamwidth factor and it is 0.88 for a uniformly illuminated rectangular array [22], [23].

Multiple-input multiple-output (MIMO) radar transmits orthogonal waveforms from multiple transmitters and measures reflected echoes with multiple spatially separated receivers. MIMO radar allows transmitters to radiate different waveforms in contrast to phased array radar in which the transmitted signals are just scaled versions of a single waveform design. The received signals pass through a set of matched filters at each receiver to obtain the information from each transmitter-receiver path possible in the MIMO radar. Thanks to the utilisation of orthogonal waveforms, larger virtual arrays compared to physical MIMO aperture are created, enabling the attainment of an angular resolution beyond that of the physical antenna. This enhancement is accomplished with a notably reduced number of antenna elements and a small form factor, compared to a uniform phased array.

In MIMO radar systems, orthogonality must be ensured among the transmitted waveforms in order to prevent interference at the received part [17]. Two waveforms,  $\phi_1$  and  $\phi_2$  are orthogonal in time domain when they fulfil the below requirements (2.21). Thus, when

a matched filter is applied to  $\phi_1$ , the matched filter response does not include any data related to  $\phi_2$ , or vice versa.

$$\int_{-\infty}^{\infty} \phi_1(t) \phi_2^*(t) dt = 0 \quad (2.21)$$

However, orthogonality is challenging because real waveforms are of finite duration and the ideal orthogonal waveform does not exist [29], therefore orthogonality is achieved through multiplexing in different domains. In the literature, there are different categories of MIMO radar waveforms. Full orthogonality is ideal but can be difficult to achieve in practice. Good orthogonality implies a sufficient level of independence for effective radar operation, while moderate orthogonality introduces some interference that must be managed with signal processing techniques.

*Frequency Division Multiplexing (FDM):* The bandwidth of the signal is divided across the number of transmitters [29], [30], [31]. In other words, multiple signals which have slightly different carrier frequency are radiated simultaneously. As there is not a complete separation, in frequency, of the signals, full orthogonality is not possible. However, FDM still provides good orthogonality, but also can cause strong range – azimuth coupling as well as a reduction in the range resolution due to dividing the bandwidth.

*Time Division Multiplexing (TDM):* To ensure the orthogonality, each transmitter is activated at a different time, but all transmitters use the same frequency. Although this method is easy to implement, it causes a latency in the radar response time when there are a high number of transmitters in the MIMO array. This can degrade performance when there is movement in the observed scene.

*Code Division Multiplexing (CDM)*: The transmitted signals are modulated by different phase codes and decoded in receiver part. With CDM, all transmitters are able to be active at the same time whilst using the same transmission frequency. However, it only provides moderate orthogonality, which results in an increase in the range sidelobe level [32].

Depending on the distribution of the antenna elements, MIMO radars are divided into two classes: widely separated (distributed) and colocated MIMO radars [33]. In this work, colocated MIMO radar systems will be focused. In a colocated MIMO radar system, the transmitter and receiver elements are closely located, so the return signals from the target are correlated from element to element, which enables coherent processing across the MIMO array enabling large virtual aperture to be generated, thus enhancing angular resolution [33].

#### 2.1.4.1 Principle of MIMO radar

In a MIMO radar, each transmitted orthogonal waveform follows a slightly different propagation path before arriving at the receiver. These path length differences translate directly into phase differences. These phase differences allow the virtual array to be constructed. If both transmitter and receiver antennas are located in an appropriate way, very long virtual array apertures can be obtained. Hence, narrow antenna beamwidths, in other words high angular resolutions, can be achieved with significantly fewer antenna elements, compared with a conventional phased array radar [34].

Example shown in Figure 2.11 with the MIMO configuration of 2 transmitters (Tx) and 5 receivers (Rx) will be used to demonstrate the MIMO virtual array beamforming principle. The receivers are located uniformly with half-wavelength spacing ( $d_R = \lambda/2$ ) whereas the spacing between transmitters ( $d_T$ ) is  $5\lambda/2$ . The distances of the signal path from the transmitters to the target and from the target to the receivers are calculated from the geometry

in Figure 2.11 by taking the 3<sup>rd</sup> Rx as a reference range and are shown in Table 2.2. The total path followed by the signal is the summation of the distances from transmitters to the target and from the target to the receiver. Table 2.3 is created by normalizing the distances according to total distance from 2<sup>nd</sup> Tx to the target and from the target to 5<sup>th</sup> Rx element. In other words, the whole distances are subtracted from  $2r - 4.5d_R \sin\theta$ . Thus, it can be clearly seen how much extra distance the signal follows until it reaches the receiver elements. Furthermore, equivalent virtual array configuration of this MIMO concept is demonstrated in Figure 2.12. The spacing between the virtual array elements is uniform and equals to  $d_R$ ,  $\lambda/2$  in this example. The equivalent virtual array has identical parametrisation with 10 elements in a uniform linear array with  $d_R$  spacing between elements. Also, the unambiguous field of view (FoV) of this MIMO is determined via (2.22). In this design,  $d_R$  is equal to  $\lambda/2$ , so the FOV is achieved as  $\mp 90^\circ$ .

$$\theta_{FOV} = \mp \sin^{-1} \left( \frac{\lambda}{2d_R} \right) \quad (2.22)$$

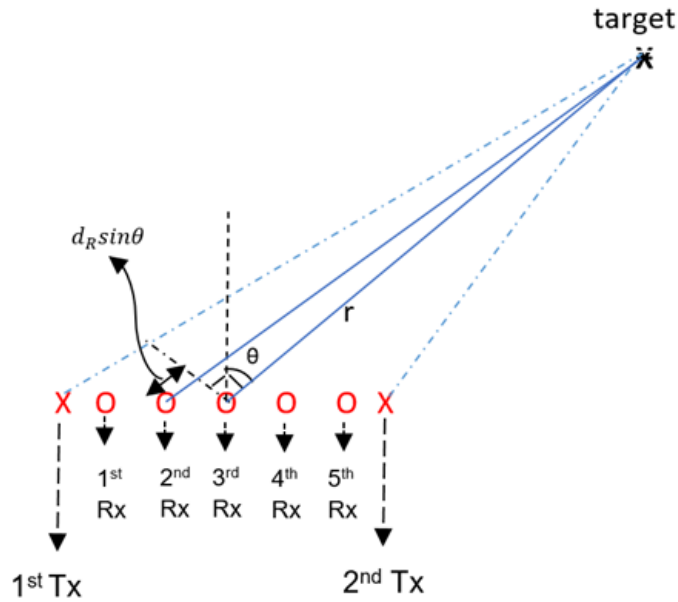


Figure 2.11: An example of a 1-D MIMO array with 2 Tx and 5 Rx.

Table 2.2: The distances of the path followed by a signal

<b><u>Distance:</u></b>	
from 1 <sup>st</sup> $T_x$ to Target	$= r + 2.5d_R \sin\theta$
from 2 <sup>nd</sup> $T_x$ to Target	$= r - 2.5d_R \sin\theta$
from Target to 1 <sup>st</sup> $R_x$	$= r + 2d_R \sin\theta$
from Target to 2 <sup>nd</sup> $R_x$	$= r + d_R \sin\theta$
from Target to 3 <sup>rd</sup> $R_x$	$= r$
from Target to 4 <sup>th</sup> $R_x$	$= r - d_R \sin\theta$
from Target to 5 <sup>th</sup> $R_x$	$= r - 2d_R \sin\theta$

Table 2.3: The normalized path difference which is followed by a signal

	1 <sup>st</sup> $R_x$	2 <sup>nd</sup> $R_x$	3 <sup>rd</sup> $R_x$	4 <sup>th</sup> $R_x$	5 <sup>th</sup> $R_x$
1 <sup>st</sup> $T_x$	$9d_R \sin\theta$	$8d_R \sin\theta$	$7d_R \sin\theta$	$6d_R \sin\theta$	$5d_R \sin\theta$
2 <sup>nd</sup> $T_x$	$4d_R \sin\theta$	$3d_R \sin\theta$	$2d_R \sin\theta$	$d_R \sin\theta$	0

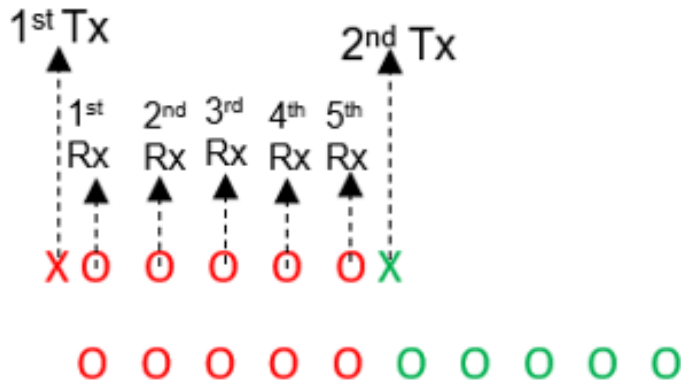


Figure 2.12: The configuration of MIMO virtual array for 2 Tx and 5 Rx.



The radiation pattern of a 2 Tx x 5 Rx MIMO array as well as the radiation patterns of separate transmitter array of 2 elements with  $5\lambda/2$  spacing and receiver array of 5 elements with  $\lambda/2$  spacing, are shown in Figure 2.13. The radiation pattern of the 2 elements transmitters has a narrow beam but shows grating lobes because the separation of elements is bigger than spatial Nyquist criterion,  $\lambda$ , whereas 5 elements receiver has a wide beam, but no grating lobes. What is important that when grating lobes occur in the transmitter's pattern, there is a deep null in the receivers' pattern, so they cancel each other. Thus, a 2 Tx x 5 Rx MIMO array pattern, obtained as a multiplication of two patterns, would have a narrow beam without grating lobes.

More generally, a MIMO consists of  $N_T$  transmitters and  $N_R$  receivers. When the spacing between the transmitters is  $N_R d_R$  and the spacing between the receivers is  $d_R$ , the corresponding virtual array can be represented as a uniform linear array with  $N_T N_R$  elements. Also, when  $d_R$  is equal to  $\lambda/2$  and  $d_T$  is equal to  $N_R d_R$ , a conventional MIMO array is obtained. It is worth noting that a 1-D MIMO array uses number of physical elements equal to  $N_T + N_R$  to

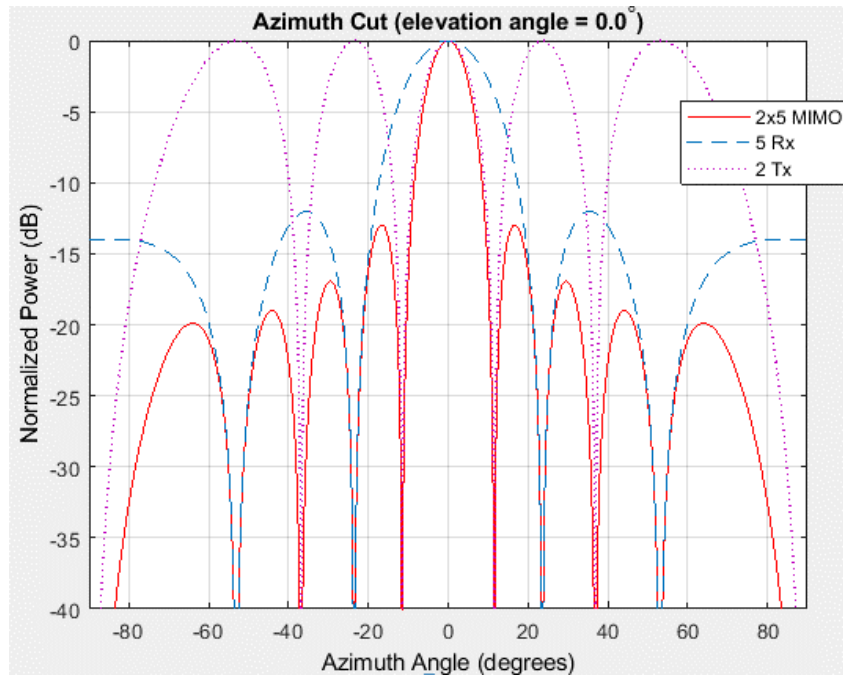


Figure 2.13: Radiation pattern of 2 Tx x 5 Rx 1-D MIMO array.

achieve the same angular resolution as in case of uniform linear array with  $N_T N_R$  elements. Therefore, MIMO can achieve the same angular resolution as the uniform linear array using significantly fewer antenna elements.

#### 2.1.4.2 1-D MIMO Radar Signal Processing

Assuming a conventional 1-D MIMO array consists of  $N_T$  transmit and  $N_R$  receive antenna elements aligned along the  $x$ -axis, the steering vectors of transmit and receive arrays,  $\mathbf{a}_{1-D}(\theta)$  and  $\mathbf{b}_{1-D}(\theta)$  respectively, for a target, positioned in the far field at an azimuth angle  $\theta$  from the boresight, are given by

$$\mathbf{a}_{1-D}(\theta) = [1 \ e^{-jkd_T \sin \theta} \ e^{-j2kd_T \sin \theta} \ \dots \ e^{-j(N_T-1)kd_T \sin \theta}]^T \quad (2.23)$$

and

$$\mathbf{b}_{1-D}(\theta) = [1 \ e^{-jkd_R \sin \theta} \ e^{-j2kd_R \sin \theta} \ \dots \ e^{-j(N_R-1)kd_R \sin \theta}]^T \quad (2.24)$$

where  $k = 2\pi/\lambda$  is the wavenumber,  $[\cdot]^T$  stands for transpose,  $d_T$  and  $d_R$  are the spacing between transmit and receive antenna elements, respectively.

The received data vector can be expressed as [17]

$$\mathbf{x}_{1-D}(t, \tau) = \sum_{l=1}^{L_t} \beta_l(\tau) \mathbf{b}_{1-D}^c(\theta_l) \mathbf{a}_{1-D}^*(\theta_l) \mathbf{s}(t) + \boldsymbol{\epsilon}(t, \tau) \quad (2.25)$$

where  $t$  is the fast time,  $\tau$  is the slow time,  $L_t$  is the number of targets,  $\beta_l(\tau)$  is reflection coefficient of  $l^{th}$  target,  $\mathbf{s}(t) = [s_1(t) \ s_2(t) \ \dots \ s_{N_T}(t)]^T$  is the vector of all transmitted waveforms,  $\theta_l$  expresses the angle of the  $l^{th}$  target,  $\boldsymbol{\epsilon}(t, \tau)$  is zero mean white Gaussian noise,  $(\cdot)^c$  is the operation of complex conjugate,  $(\cdot)^*$  is the operation of conjugate transpose.

At the receiver, received signals are matched filtered with transmitted orthogonal waveforms to obtain a virtual data vector ( $N_T N_R \times 1$ ). The virtual data vector is given by

$$\mathbf{y}_{1-D}(\tau) = \int_0^{T_p} \mathbf{x}_{1-D}(t, \tau) \mathbf{s}^*(t) dt = \sum_{l=1}^{L_t} \beta_l(\tau) [\mathbf{a}_{1-D}(\theta_l) \otimes \mathbf{b}_{1-D}(\theta_l)] + \boldsymbol{\xi}(\tau) \quad (2.26)$$

and

$$\boldsymbol{\xi}(\tau) = \int_0^{T_p} \boldsymbol{\epsilon}(t, \tau) \mathbf{s}^*(t) dt \quad (2.27)$$

where  $T_p$  is pulse width,  $(\cdot)^*$  denotes the conjugate transpose and  $\boldsymbol{\xi}(\tau)$  represents the matched filter output of zero mean white Gaussian noise.

Assuming there is a target at the azimuth angle of  $\theta$ , the steering vector of the whole 1-D virtual array can be written as

$$\mathbf{v}_{1-D}(\theta) = \begin{pmatrix} 1 \\ e^{-jk(d_R)\sin\theta} \\ e^{-jk(2d_R)\sin\theta} \\ \vdots \\ e^{-jk((N_R-1)d_R)\sin\theta} \\ e^{-jk(d_T)\sin\theta} \\ \vdots \\ e^{-jk((N_T-1)d_T + (N_R-1)d_R)\sin\theta} \end{pmatrix}_{N_T N_R \times 1} \quad (2.28)$$

while the positions of the virtual array elements are given by

$$\mathbf{l}_{1-D} = \begin{pmatrix} 0 \\ d_R \\ 2d_R \\ \vdots \\ (N_R - 1)d_R \\ \vdots \\ (N_T - 1)d_T + (N_R - 1)d_R \end{pmatrix}_{N_T N_R \times 1} \quad (2.29)$$

The effective dimension of the virtual array of the 1-D MIMO is calculated as

$$l_x = \max(\mathbf{l}_{1-D}) - \min(\mathbf{l}_{1-D}) = (N_T - 1)d_T + (N_R - 1)d_R \quad (2.30)$$

After taking an fast Fourier transform (FFT) along the virtual array data, the angular response is obtained. The angular resolution defined at the -3 dB points of the MIMO

beamwidth, is determined by the effective length,  $L$ , of virtual array,  $\theta_{3dB} \cong 0.88\lambda/L$ , and, in the case of 1-D MIMO, by the effective dimension of the virtual array,  $l_x$ .

### 2.1.4.3 2-D MIMO Radar Signal Processing

In a 2-D MIMO, the antenna elements might be placed along two orthogonal axes. For example, they may be aligned along horizontal,  $x$ , and vertical,  $z$ , axes in order to obtain the required spatial resolutions in both azimuth and elevation. Assuming that the target is in the far field of the antenna, the angular directions to the target can be assumed to be the same for the colocated MIMO array. If the target is positioned at a point  $(r, \phi, \theta)$ , where  $r$  is the range,  $\phi$  is the azimuth angle, and  $\theta$  is the elevation angle with respect to the MIMO array origin as shown in Figure 2.14. For each pair of transmit and receive elements the path lengths and, therefore, the phase of the signal, arriving from the target differ, thus giving rise to a virtual element.

Assume  $N_T$  transmitters are located on the  $z$ -axis with  $d_T$  spacing and  $N_R$  is the number of receive elements located on the  $x$ -axis with  $d_R$  spacing, as in Figure 2.15. The normalised transmit and receive steering vectors for a single target at  $(r, \phi, \theta)$ , can be written as (2.31) and (2.32), respectively. This type of MIMO antenna can be called L-shaped MIMO.

$$\mathbf{a}_{2-D}(\phi, \theta) = [1 \ e^{jk d_T \cos \theta} \ \dots \ e^{jk(N_T-1)d_T \cos \theta}]^T \quad (2.31)$$

and

$$\mathbf{b}_{2-D}(\phi, \theta) = [1 \ e^{jk d_R \cos \phi} \ \dots \ e^{jk(N_R-1)d_R \cos \phi}]^T \quad (2.32)$$

When  $L_t$  targets are located in the far field of the 2-D MIMO radar, the reflected signals by the targets impinge on the MIMO radar receiver from directions  $(\phi_l, \theta_l)$ ,  $l = 1, \dots, L_t$ . The received data vector can be expressed as in (2.33).

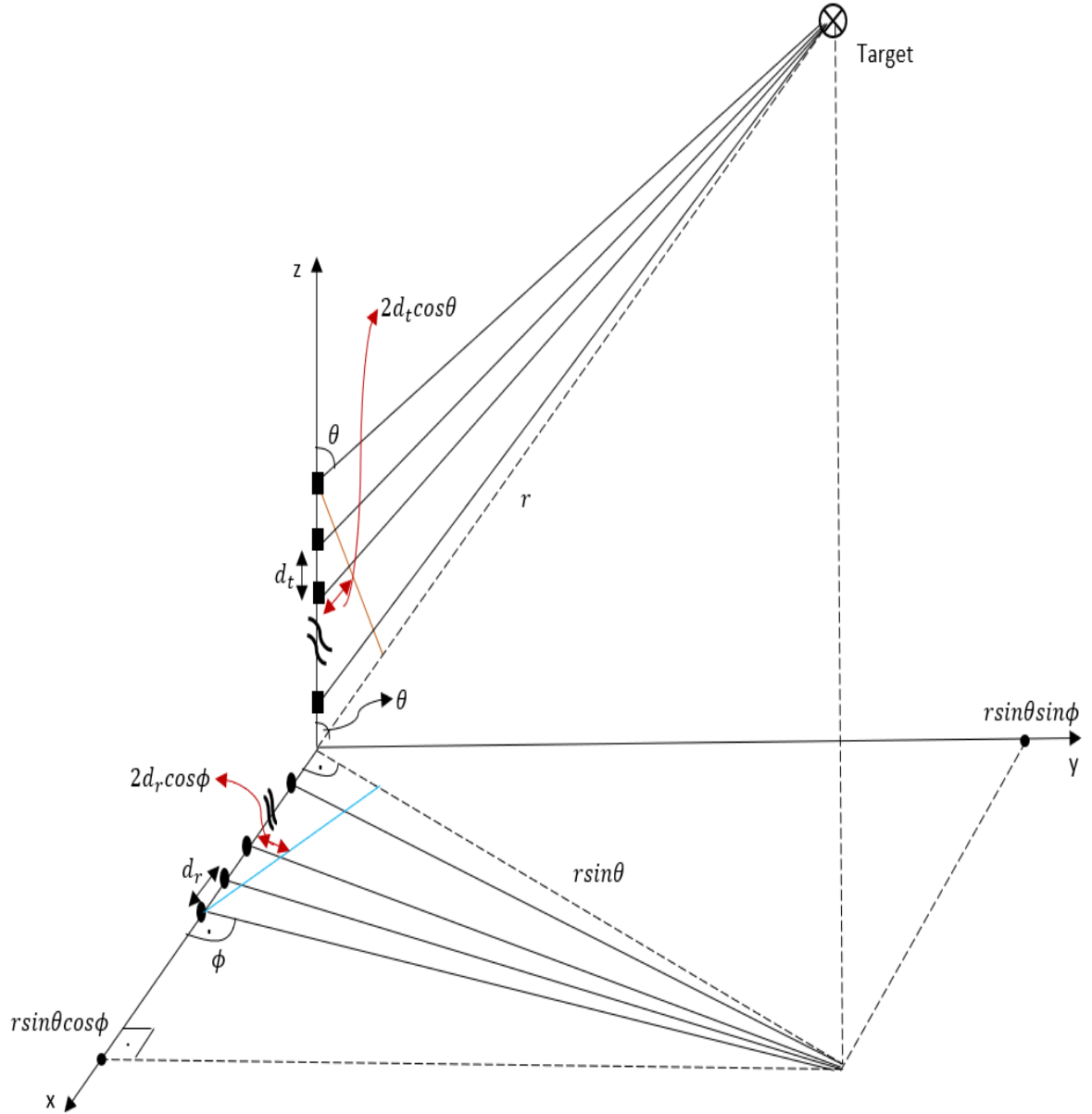


Figure 2.14: Demonstration of L-shaped MIMO in spherical coordinate system. Rectangular shapes represent transmitters whereas circle shapes are for receiver elements.

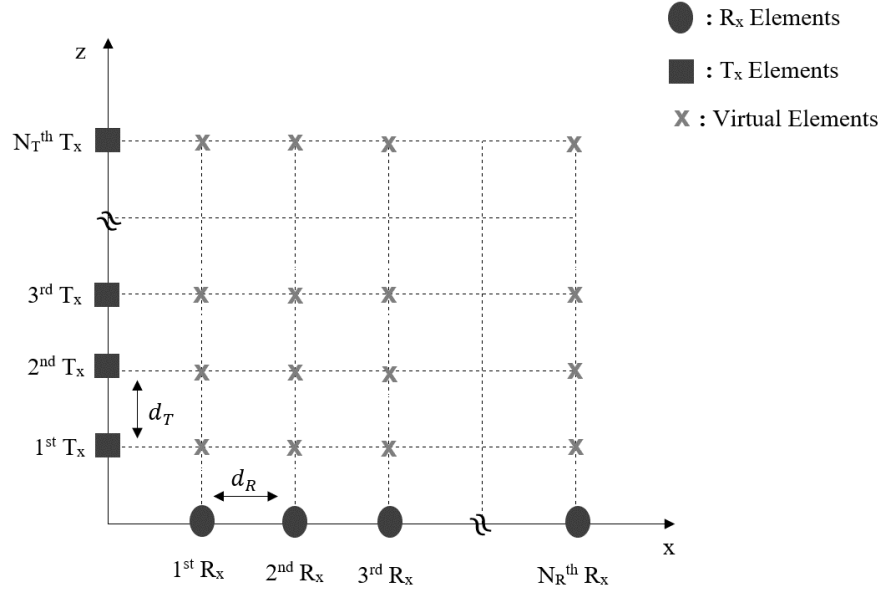


Figure 2.15: L-shaped 2-D MIMO array and its virtual array elements.

$$\mathbf{x}_{2-D}(t, \tau) = \sum_{l=1}^{L_t} \beta_l(\tau) \mathbf{b}_{2-D}^c(\phi_l, \theta_l) \mathbf{a}_{2-D}^*(\phi_l, \theta_l) \mathbf{s}(t) + \boldsymbol{\epsilon}(t, \tau) \quad (2.33)$$

where  $\beta_l(\tau)$  is reflection coefficient of  $l^{th}$  target,  $\mathbf{s}(t)$  is the vector of the orthogonal transmit waveforms,  $\mathbf{s}(t) = [s_1(t) \ s_2(t) \ \dots \ s_{N_T}(t)]^T$ , and  $\boldsymbol{\epsilon}(t, \tau)$  is zero mean white Gaussian noise,  $(\cdot)^c$  is complex conjugate,  $(\cdot)^*$  is conjugate transpose.

At the receiver, the received signals are matched filtered using each transmitted waveform to obtain the virtual data vector for each range bin. The resulting virtual data vector is given by

$$\mathbf{y}_{2-D}(\tau) = \int_0^{T_p} \mathbf{x}_{2-D}(t, \tau) \mathbf{s}^*(t) dt = \sum_{l=1}^{L_t} \beta_l(\tau) \mathbf{a}_{2-D}(\phi, \theta) \otimes \mathbf{b}_{2-D}(\phi_l, \theta_l) + \boldsymbol{\xi}(\tau) \quad (2.34)$$

and

$$\boldsymbol{\xi}(\tau) = \int_0^{T_p} \boldsymbol{\epsilon}(t, \tau) \mathbf{s}^*(t) dt \quad (2.35)$$

where  $T_p$  is pulse width and  $\xi(\tau)$  stands for the matched filter output of zero mean white Gaussian noise.

Assuming there is a target at the  $(r, \phi, \theta)$  coordinates, the steering vector of the 2-D virtual array can be written as

$$\mathbf{v}_{2-D}(\phi, \theta) = \begin{pmatrix} 1 & e^{jkd_R \cos \phi} & \dots & e^{jk(N_R-1)d_R \cos \phi} \\ e^{jkd_T \cos \theta} & e^{jk(d_T \cos \theta + d_R \cos \phi)} & \dots & e^{jk(d_T \cos \theta + (N_R-1)d_R \cos \phi)} \\ \dots & \dots & \dots & \vdots \\ e^{jk(N_T-1)d_T \cos \theta} & e^{jk((N_T-1)d_T \cos \theta + d_R \cos \phi)} & \dots & e^{jk((N_T-1)d_T \cos \theta + (N_R-1)d_R \cos \phi)} \end{pmatrix}_{N_T \times N_R} \quad (2.36)$$

To achieve the angular response of the 2-D MIMO, an FFT is taken along the  $x$ -axis which gives the azimuth information, then second FFT is applied along the  $z$ -axis to obtain the elevation information of the target in the scene.

The positions of the virtual array elements, for an illustrative example, are demonstrated in Figure 2.15. It is seen that the virtual array configuration of the MIMO with  $N_T$  Tx and  $N_R$  Rx physical elements is an equivalent of a  $N_T \times N_R$  rectangular phased array, but using fewer  $N_T + N_R$  antenna elements instead of  $N_T \times N_R$ .

### 2.1.5 Automotive Radars

Automotive radar is an essential sensor in modern vehicles since it can detect and estimate the range, angle and relative velocity of targets in a scene in all-day-and-night and in all-weather conditions. Although the first automotive radar experiments were conducted in the 1950s, intensive development of automotive radars at microwave frequencies only started in the early 1970s [35]. In 1992, in order to understand the impact of radar on traffic accidents, a collision warning system operating at 24 GHz was mounted on more than 4000 trucks and buses

in the USA. This resulted in around a 50% decrease in the number of accidents [36] and has stimulated research and development of vehicular radar systems.

Many different transmission frequencies (such as 10, 17, 24, 35, 49, 60 and 77 GHz) were utilised for early automotive radar applications [35], [36]. However, in current automotive radars, only 24 GHz and 77 GHz are used as carrier frequencies [37], [38], [39], [40]. Until 1<sup>st</sup> of January 2022, the allocated bandwidths for 24 GHz were 250 MHz and 5 GHz. This has been changed and now only the narrowband allocation is available to use [41]. Therefore, the 24 GHz band may not be suitable for automotive radar implementations which require high range resolution. On the other hand, 77 GHz provides enhanced range resolution thanks to its high allocated bandwidth of 5 GHz, which can potentially be used, and consequently, for most applications this region is preferred.

Current automotive radars are classified according to their maximum detectable range: short-range radar (SRR), medium-range radar (MRR) and long-range radar (LRR). Key parameters of current automotive radars such as desired angular resolutions and allocated frequency bands are shown in Table 2.4. In terms of the utilised frequencies, LRR employs 76 - 77 GHz whereas 77 – 81 GHz is used for SRR and MRR. LRR provides the narrow FoV at the range up to 250 m and is used for applications such as adaptive cruise control (ACC). MRR is used for up to 100 m ahead of the vehicle and for applications such as rear collision warning and cross traffic alert. Regarding SRR, it intends for distances from a few centimetres up to 30 m and is employed for applications such as parking assistance and pre-crash warning. Figure 2.16 shows the automotive radar applications based on used radar types in terms of range.



Table 2.4: Automotive radar categories [39].

Type	LRR	MRR	SRR
Maximum transmit power	55 dBm	-9 dBm/MHz	-9 dBm/MHz
Frequency band	76 – 77 GHz	77 – 81 GHz	77 – 81 GHz
Bandwidth	600 MHz	600 MHz	4 GHz
Distance range	10 – 250 m	1 – 100 m	0.15 – 30 m
Velocity resolution	0.6 m/s	0.6 m/s	0.6 m/s
Angular accuracy	0.1°	0.5°	1°
3 dB beamwidth in azimuth	$\pm 15^\circ$	$\pm 40^\circ$	$\pm 80^\circ$
3 dB beamwidth in elevation	$\pm 5^\circ$	$\pm 5^\circ$	$\pm 10^\circ$

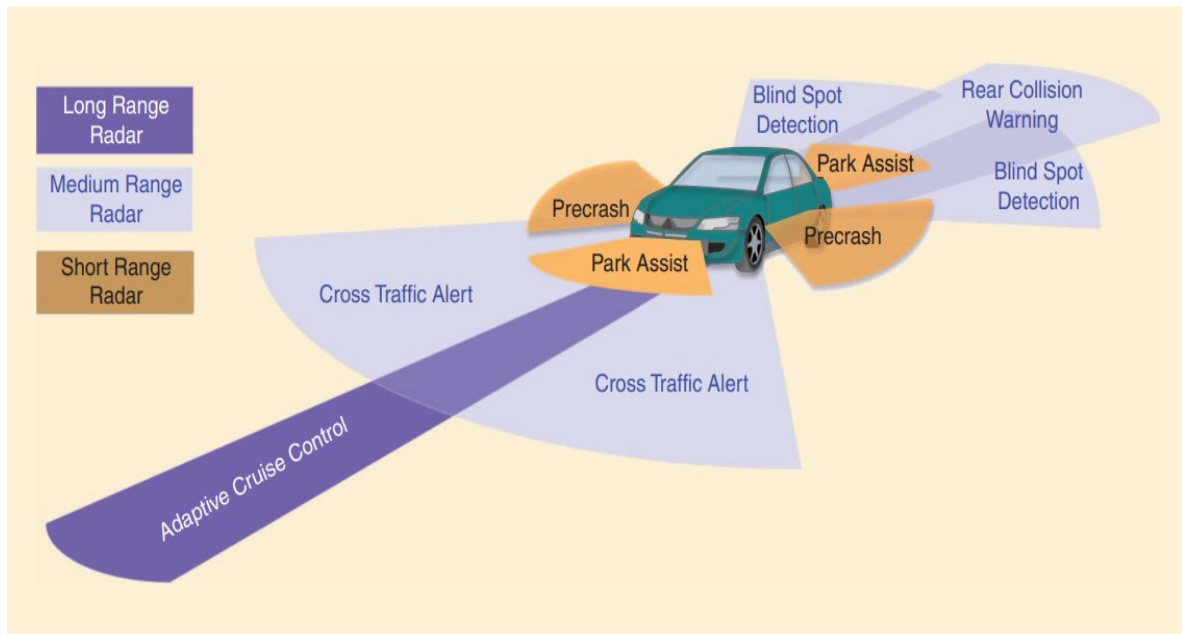


Figure 2.16: Automotive radar applications [42].

Frequency-modulated-continuous-wave (FMCW) radars are commonly used in automotive radars. The main challenge of FMCW is mutual interference which can become a severe issue, especially where there are a large number of vehicles in close proximity. This would exacerbate if several automotive radars are mounted around the vehicle to increase view of the sensed areas and thus improve journey safety by providing a warning to the driver or taking over the complete control of the driving task and in dense spatial and frequency co-existence environment, the interference problem becomes a major challenge. There is significant body of work on phenomenology and mitigation of interference [43], [44], [45], which is beyond the scope of this thesis.

## 2.2 Communication Basics

Communication systems designed to convey data or information from one user to another [46] can generally be of two types: *analog* and *digital communication*. Analog communication systems transmit analog continuous signals via amplitude modulation (AM), frequency modulation (FM), or phase modulation (PM). Digital communication systems transmit digital signals by encoding the information and modulating the signals through amplitude shift keying (ASK), frequency shift keying (FSK), phase shift keying (PSK) etc. [46].

Communication systems consist of three main parts: *transmitter*, *transmission channel*, and *receiver* as shown Figure 2.17. The transmitter converts information into a suitable format for transmission through the channel. The channel is the medium in which the signal propagates from the transmitter to the receiver. The channel could be a wire channel, such as coaxial cables or a wireless channel, such as air and seawater. Every channel introduces noise and attenuation which affects the reliability of the transmission [47]. The receiver receives the transmitted signal from the channel and performs signal processing to make sense of the received signal, in

other words, to obtain the transmitted information, through demodulation, decoding filters, etc. Communication systems typically rely on one-way propagation for the transfer of information from sender to receiver, in contrast to radar systems, which involve two-way propagation to detect targets.

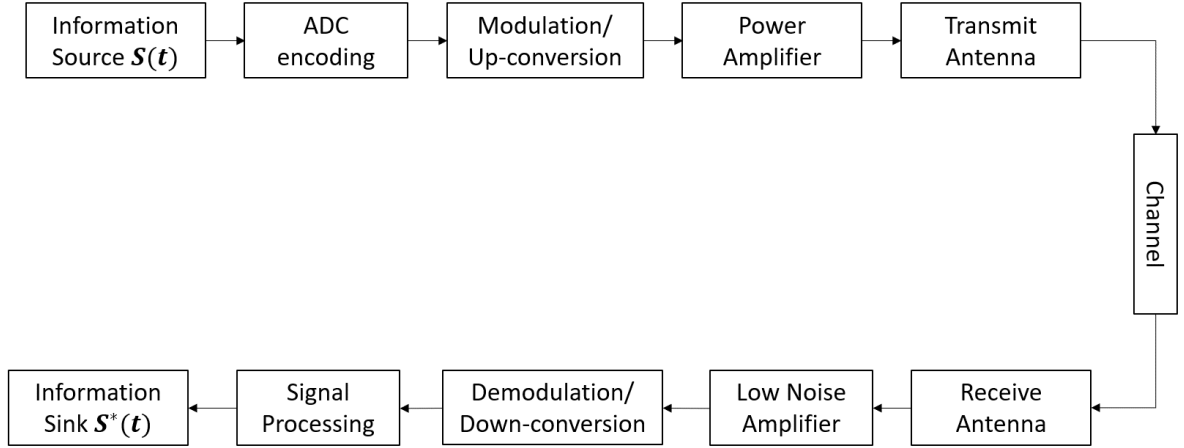


Figure 2.17: Digital communication system [47].

The amount of data that can be transferred over the channel is limited and this is known as channel capacity. The maximum channel capacity,  $C$ , expressed in bits per second was formulated by Shannon in 1948 [48] as shown in (2.37). It is apparent that the channel capacity is directly proportional to the bandwidth of the channel, so as the bandwidth increases, the maximum achievable data rate increases in the bandwidth-limited regime of signal-to-noise ratio larger than 0 dB:

$$C = B \log_2 \left( 1 + \frac{S}{N} \right) \quad (bits/s) \quad (2.37)$$

where  $B$  is channel bandwidth in Hertz,  $\frac{S}{N}$  is the signal-to-noise ratio of the received signal, expressed in absolute units.

The most crucial parameter in a communication system is how accurately the transmitted data is received at the receiver. This is because, until it reaches the receiver, the transmitted signal is exposed to unknown noise, interference, and attenuation – a loss of energy, caused by the distance between the transmitter and receiver. These could taint the signal, leading to errors in the data demodulation process. Therefore, the *probability of a bit error*, in other words *bit error rate* (BER), must be considered whilst modulating the signal, since each modulation type has its own BER response. The BER represents the number of bit errors per unit of time, so a lower BER means a higher level of accuracy in the received data.

## 2.2.1 Communication Waveforms

In digital communication, a digital signal can be modulated by altering the amplitude, frequency, and phase of the sine wave. These schemes are known as amplitude shift keying, frequency shift keying and phase shift keying, respectively. PSK, which is used extensively in this thesis, is explained in more detail and a brief explanation of ASK and FSK is provided in this sub-section.

In ASK modulation, the data is encoded by altering the amplitude of the carrier sine wave which has a constant transmission frequency and a constant phase. In other words, the waveform could be generated by switching the carrier as on and off, therefore it is also known as *on-off keying* and is shown in Figure 2.18(b). Although ASK is easy to generate and detect, which reduce the complexity and cost of both transmitter and receiver, it is highly prone to noise interference because noise distorts the signal's amplitude, which causes the error in the received data.

In FSK modulation, the transmission frequency is changed in such a way that each frequency represents a different component of digital data as shown in Figure 2.18(c). It is

possible to use two or more different frequencies. Although FSK has the advantage of being resistant to noise and is easy to modulate/demodulate, it requires a larger bandwidth, compared with other modulation types.

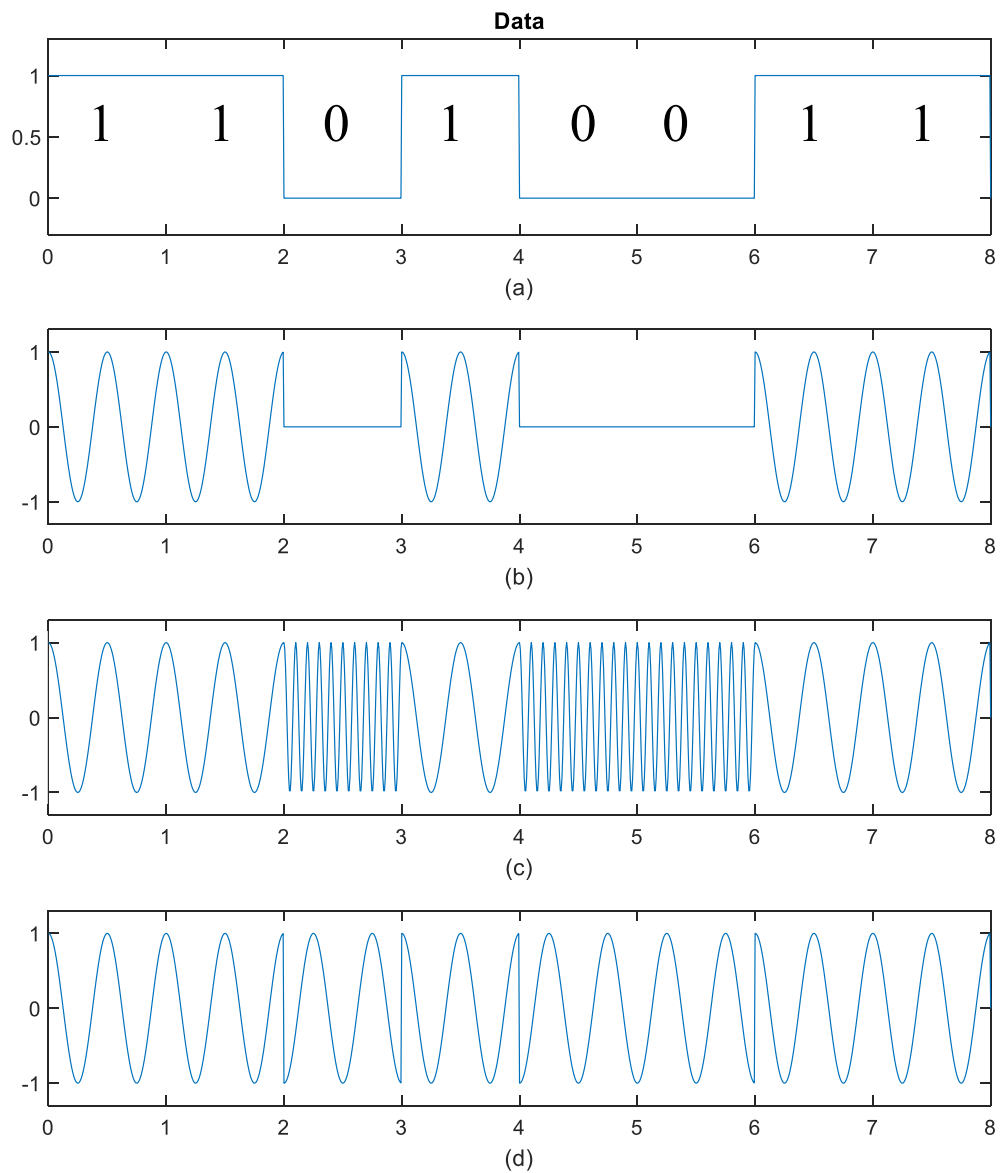


Figure 2.18: (a) The encoded binary data, (b) ASK modulated waveform, (c) FSK modulated waveform, (d) BPSK modulated waveform.

### 2.2.1.1 Phase Shift Keying

In phase shift keying data is encoded through alterations in the phase of the carrier sine wave whilst keeping the amplitude and transmission frequency constant, as depicted in Figure 2.18(d). The phase values utilized may vary, depending on the constellation diagram, but the number of phase states is usually a power of two, such as 2, 4, 8, and so on.

In *Binary phase shift keying* (BPSK), the phase of the carrier signal can take two values which can be 0 and  $\pi$  as shown in Figure 2.19(a). These express a binary “1” and “0”, respectively. Also,  $\pm\pi/2$  phase values can be also used. Crucially, the key parameter is the 180° phase difference between these two symbols. Hence, the general expression of the transmitted BPSK signal is given as below in [49].

$$s_{BPSK}(t) = \sqrt{\frac{2E_b}{T_b}} \cos(2\pi f_c t) \quad 0 \leq t \leq T_b \quad \text{for binary 1} \quad (2.38)$$

and

$$s_{BPSK}(t) = \sqrt{\frac{2E_b}{T_b}} \cos(2\pi f_c t + \pi) = -\sqrt{\frac{2E_b}{T_b}} \cos(2\pi f_c t) \quad \text{for binary 0} \quad (2.39)$$

where  $E_b$  is the energy per bit,  $T_b$  is the bit duration.

In *Quadrature Phase Shift Keying* (QPSK), four different phase values are assigned, each separated by 90°. In this modulation, each symbol is represented by two-bits, in contrast to one-bit in BPSK, so the data rate becomes twice that of BPSK. The constellation diagram of QPSK is illustrated in Figure 2.19(b), and the general form of the QPSK signal can be expressed by

$$s_{QPSK}(t) = \sqrt{\frac{2E_s}{T_s}} \cos\left(2\pi f_c t + (n-1)\frac{\pi}{2}\right) \quad 0 \leq t \leq T_s \quad n = 1, 2, 3, 4 \quad (2.40)$$

where  $E_s$  is the symbol energy and is equal to two times  $E_b$ , and  $T_s$  is the symbol duration and is equal to twice bit duration.

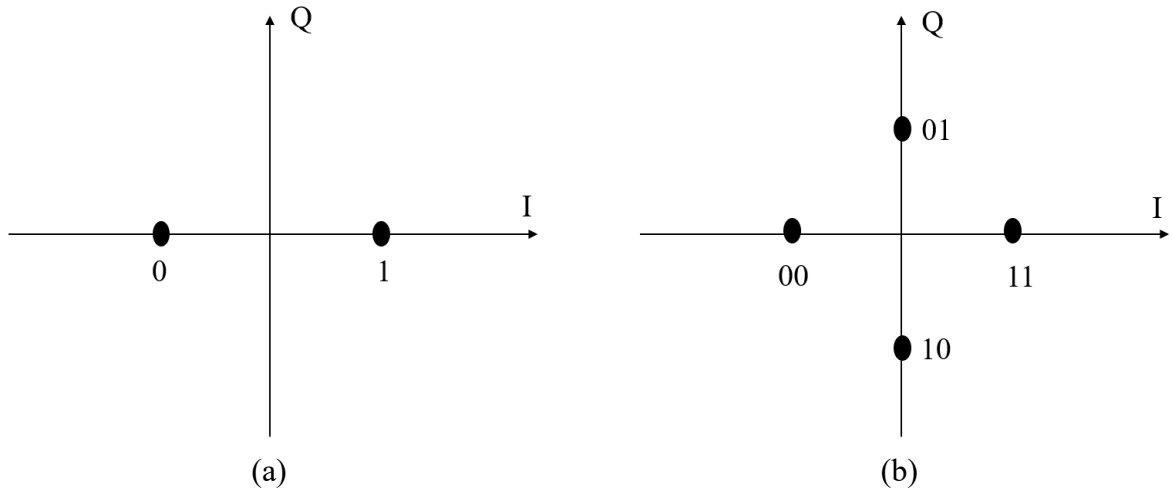


Figure 2.19: Constellation diagram of (a) BPSK, (b) QPSK.

Figure 2.20 displays the block diagram illustrating the process of modulation and demodulation for BPSK. As can be seen, the transmitted signal arrives at the receiver with added noise induced by the channel. To extract the data from the received signal, the first step is to apply matched filtering. This process maximises the signal-to-noise ratio, as explained in Section 2.1.2.1.1. Subsequently, the output of the matched filter undergoes thresholding to determine whether a bit or symbol corresponds to a '1' or a '0'. After obtaining the bits or symbols by thresholding, the transmitted data is encoded.

In Figure 2.21, the waveforms at various points, depicted in Figure 2.20, are plotted. The transmitted binary data is demonstrated in Figure 2.21(a). The modulated signal is shown in Figure 2.21(b) whereas the received signal at point C is illustrated in Figure 2.21(c). It is obvious that the received signal is distorted due to the AWGN, compared to the transmitted

signal. The received signal after the mixer, that is at point D, and after the integrator – that is at point E, are plotted in Figures 2.21(d) and 2.21(e), respectively. Finally, after thresholding, the received binary data is shown in Figure 2.21(f). It is seen that the transmitted binary data is received without any errors.

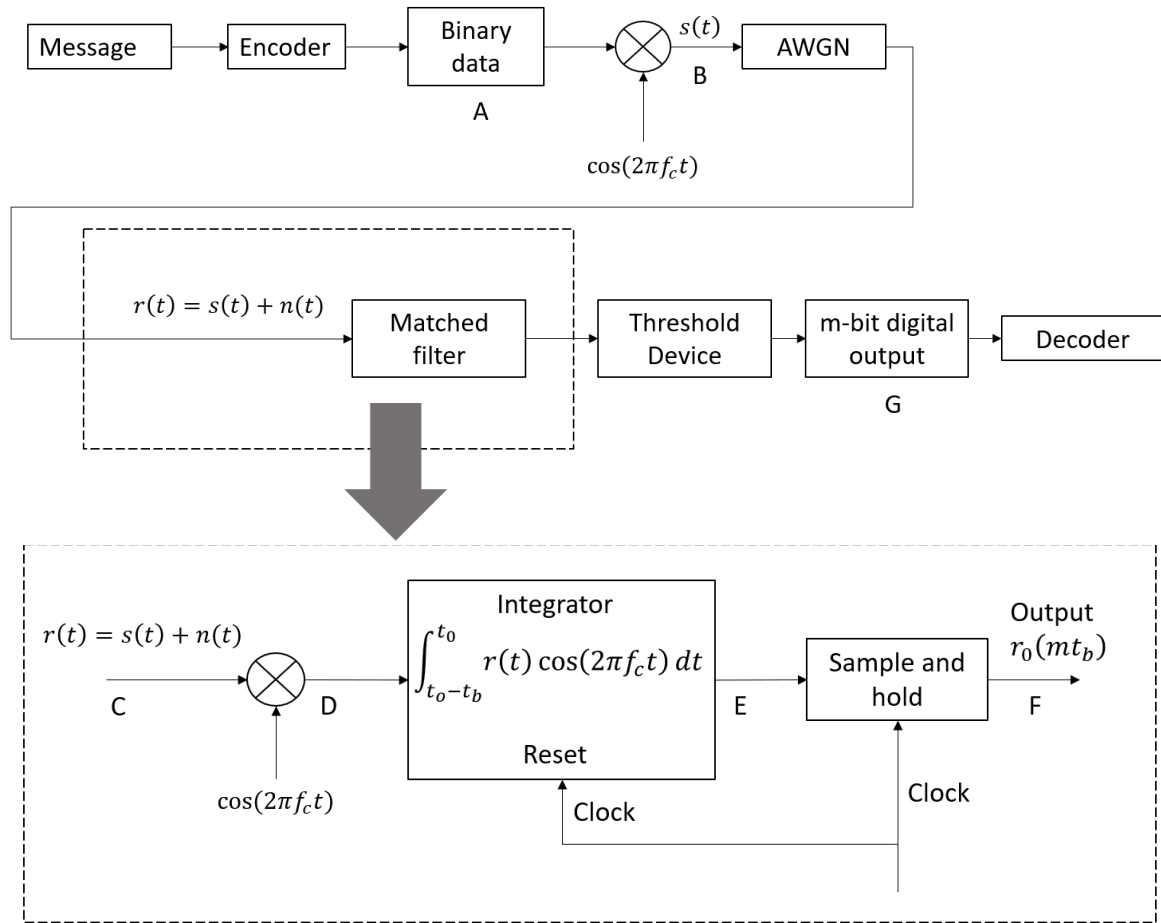


Figure 2.20: Block diagram of modulation and demodulation of BPSK.



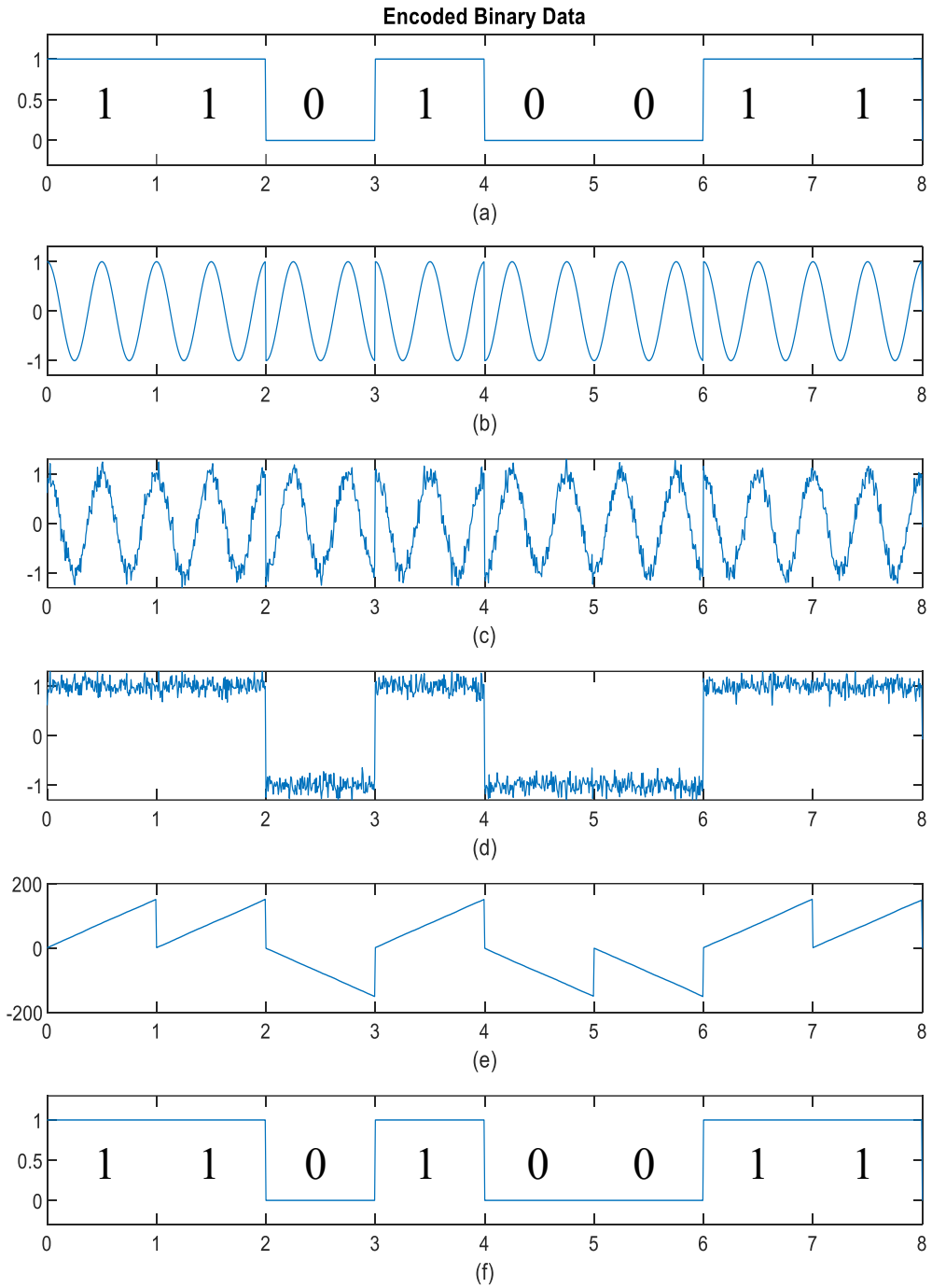


Figure 2.21: (a) The transmitted binary data at point A, (b) transmitted BPSK waveform at point B, (c) received signal at point C, (d) waveform after mixer – at point D, (e) waveform after the integrator – at E, (f) the received data after thresholding – at point F.

The BER of BPSK and QPSK under additive white Gaussian noise is given by [49]

$$BER = Q \sqrt{\frac{2E_b}{N_0}} \quad (2.41)$$

where  $Q(\cdot)$  is  $Q$ -function and  $N_0$  is the noise spectral density.

As the number of phase states increases, more bits per symbol and consequently higher data rates are achieved. For instance, each symbol represents 3-bits and 4-bits with 8-ary PSK and 16-ary PSK, respectively. However, the more phase states, the more susceptible the modulation is to noise and interference, thereby diminishing the performance and reliability of the system. The impact of higher phase states on the BER performance is shown in Figure 2.22. It is clear that although BPSK and QPSK have the same performance, this does not apply to the use of high phase states, which cause higher bit errors in the detection part than BPSK/QPSK. Therefore, there is a trade-off between the BER and the modulation type, and the optimal choice must be done based on the requirements and constraints of the communication system.

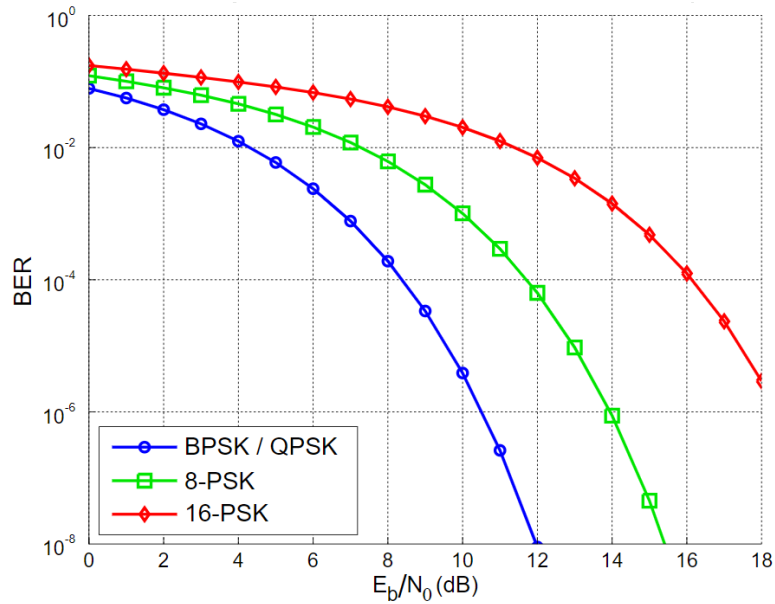


Figure 2.22: Bit error rate performance of BPSK, QPSK, 8-PSK and 16-PSK [50].

## 2.2.2 Multiple Access Schemes in Communication

Since the radio spectrum is limited, it needs to be used efficiently to enable communication simultaneously to/between large numbers of users. Multiple access schemes allow effective share of the available resources (bandwidth, time) between a number of uncoordinated users without causing interference or collision with each other. Commonly used multiple access schemes are demonstrated in Figure 2.23 and briefly explained below.

*Frequency Division Multiple Access (FDMA):* The available frequency spectrum is divided into multiple sub-bands, with each centre sub-frequency being allocated for the exclusive use of an individual user. The users can simultaneously communicate with each other without interfering with each other, provided required guard band is used to accommodate potential Doppler shift of mobile users. FDMA is commonly used in radio and television broadcasting, where different channels are allocated specific frequency bands.

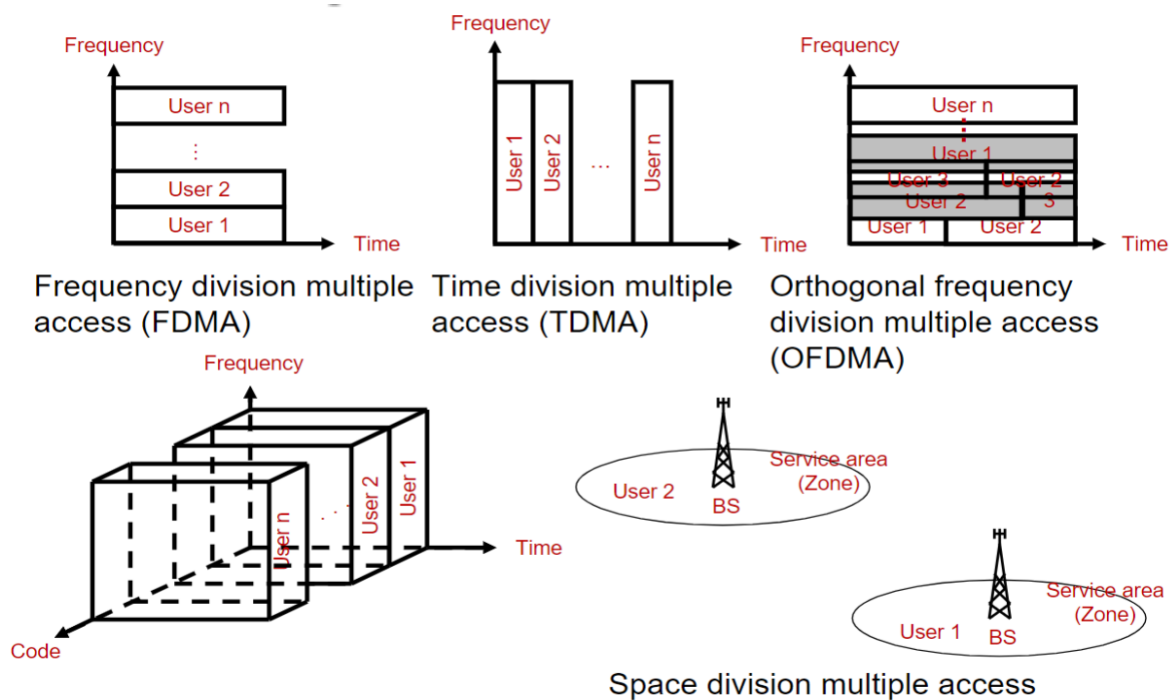


Figure 2.23: Multiple access schemes [51].

*Time Division Multiple Access (TDMA)*: The channel is divided into different time slots to enable multiple users to access the assigned full bandwidth. Therefore, at each time slot, only one user becomes active whereas others are passive. This method is used in mobile radio communication.

*Code Division Multiple Access (CDMA)*: To overcome the drawbacks of both FDMA and TDMA, CDMA assigns a unique code, generally a pseudo-random code to each user, in order to allow users to transmit simultaneously while using the full available bandwidth. This method provides good protection against jamming. Therefore, it is preferred in military usage.

*Orthogonal Frequency Division Multiple Access (OFDMA)*: OFDMA divides a channel into multiple closely spaced subcarriers, assigning them to different users. These subcarriers are orthogonal, so they can be active simultaneously using the same channel without causing inference among the users. It provides high-speed data transmission, so it is mainly used in modern wireless communication systems.

*Space Division Multiple Access (SDMA)*: This method gets the benefit of the spatial separation of users. If there is a reusable separation between the users at different locations, the same frequency sets can be shared by the users. By exploiting spatial separation and diversity, SDMA increases the capacity of wireless networks by activating multiple users who use the same frequency but are in different service zones. Microcell frequency re-use is based on that principle.

## 2.3 Summary

This chapter has provided a basic knowledge of the radar systems and communication used throughout the rest of this thesis. The radar section has introduced the fundamentals of radar, including the radar equation, operational frequencies, waveforms, ambiguity function, MIMO radar, and automotive radar. The communications section introduced main fundamental concepts in communications, such as communication system types, channel capacity, communication waveforms, and multiple access types.

# Chapter 3 - Waveform Design for Joint RadCom Systems

## 3.1 Introduction

The aim of the work presented in this chapter is to propose new techniques which enable communication data to be embedded into radar waveforms without significant degradation in the radar performance.

Advanced driver assistance systems (ADAS) have been developed by placing multiple sensors around vehicles in order to aid the human driver when driving and parking. ADAS applications, such as adaptive cruise control, automatic emergency braking, collision warning, increase the safety of journeys and make it more comfortable. Radar is a compulsory sensor in ADAS because it is the only sensor robust to weather and lighting conditions and which can directly measure a target's range, angle and radial velocity.

Sensors operate over a limited range, have a limited field of view and, at mm-wave frequency bands require line of sight, thus limited coverage may compromise vehicle safety [5]. It is, however, possible to enhance situational awareness of the vehicle through the communication of acquired information with other road users, infrastructure etc., within a V2X communication network. Therefore, the DSRC standard was developed to provide V2V, V2I or V2X communications as mentioned in Chapter 1. However, due to the limited bandwidth at

5.9 GHz, the maximum achievable data rate is 27 Mbps [52], inadequate for real-world operations.

Currently, there is strong interest in combining both radar sensing and communication capabilities within the same system in order to use the Electromagnetic spectrum more efficiently. Moreover, using one hardware chipset for two different functionalities is a desirable approach for vehicles with increasingly dense sensor packaging in order to provide higher levels of automation.

In this chapter, an LFM signal is used for radar sensing, and multiple PSK symbols or bit sequences are embedded into the LFM signal for communications. Such waveforms are subsequently used for radar sensing with MIMO beamforming. Orthogonality between transmitters is ensured using either a TDM or CDM approach. This chapter is focused on demonstration of these novel techniques and their validation through both simulation and experimentation.

In this chapter, firstly a literature review on joint radar and communication systems is presented in Section 3.2. Then, this is followed by a mathematical description of the proposed techniques. System parameters based on BER are explained in Section 3.4. The simulation results, including ambiguity functions, are presented in Section 3.5, and the experimental results are shown in Section 3.6, where results are also discussed. Finally, conclusions are formulated in Section 3.7.

To the knowledge of the author, the presented work is original and includes novel waveforms for joint RadCom systems. TDM PSK-LFM part of it was presented at the 2020 IEEE Radar Conference [53], and the extended work with CDM PSK-LFM was published in IEEE Sensors Journal [54].

## 3.2 State of the Art

The request to use mm-wave frequency levels is increasing day by day for both radar and communication applications due to the availability of wide bandwidths. Hence, radars can be designed to achieve finer range resolution whereas communication systems can increase their data rates. However, the frequency spectrum is extremely dense, and mm-wave band is commonly employed by radar systems [10], [11]. The solution for both radar and communication (RadCom) systems is to share the same frequency band to meet their high bandwidth demands. In this way, spectrum congestion can be substantially alleviated, and small size chipsets can be designed. Moreover, the front-end parts of both radar and communication systems become very similar to each other [55]. These reasons increase the motivation of researchers to work on joint RadCom systems.

The idea of a dual mode, single chipset started in the early 1960s. R. M. Mealey presented research in which modulated communications data was inserted into a radar pulse via pulse interval modulation. This enables both sensing and one-way connectivity to be achieved without any degradation in radar performance [56]. Then, in the mid-1990s, interest in combining radar and communication systems accelerated. The US Naval Research Office launched a project named, “Advanced Multifunction RF System” that aimed to enable the same antenna to be used for multiple functions, namely: communication, electronic warfare and sensing. The overall aim was to reduce the total number of antennas required on-board ships [57].

Several methods have been proposed to combine both the radar and communication functions. The first method proposed for automotive applications was the use of spread spectrum techniques [58]. In such an approach, the host vehicle transmits its own pseudo-noise



code (PN-code), and the target vehicle re-transmits the signal by multiplying the received signal from the host vehicle with the communication message. Hence, the host vehicle can simultaneously measure the distance between the host and target vehicle and receive the message by demodulating the received signal from the target vehicle. In [59], [60], [61], a single transceiver platform which operates in both the radar and communication modes allocating different time slots for each modality was proposed in order to prevent interference between the systems. However, in such an arrangement the radar cannot detect targets during the communication mode, so radar performance may be affected negatively. In the SLIMSENS project [62], [63], a combination of simultaneous 76 GHz long and short-range radar mode and 63 GHz communication mode using a common aperture was considered. In [64], [65], [66], [67], the authors suggested sending data via modulation of antenna sidelobes, whereas radar detection was via the main lobe. The main drawback of this method is that communication receivers must be always in the sidelobe direction which is not always possible for automotive sensing. Recently a number of research papers were published on dual-function systems where communication waveforms are utilized for joint radar and communication operations. For instance, in [68] IEEE 802.11p standard, allocated for vehicular communication was used in experiments to demonstrate the performance of the targets' range and velocity estimation in two different environments: urban and highway. In [69], [70], [71], [72] orthogonal frequency-division multiplexing (OFDM) waveforms are used for joint radar and communication purposes. Although use of this waveform does not result in range-Doppler coupling, it requires complex signal processing. In [73], [74], [75], spread spectrum techniques were employed, but the system design and implementation in terms of time/frequency synchronization is complex and expensive and utilization of spectrum is inefficient. Interest has been shown in using PMCW (Phase Modulated Continuous Wave) for joint radar and communication purposes due

to advantages such as a thumbtack-like ambiguity function that has a single sharp at the origin and almost zero level everywhere else, robustness to interference and simplicity of implementation [76], [77], [78]. However, automotive radars require high range resolution as well as high unambiguous range and velocity. In order to satisfy such requirements, the bit duration must be short, and the code length must be large in PMCW.

The majority of automotive radars use chirp signals, and extensive research has been done, where an LFM waveform was used as a signal for encoding communication information. Saddik et al. [79] proposed that each transmitted pulse carries one symbol via phased shift keying. In [80] this was extended into the MIMO radar concept by embedding one PSK symbol in each orthogonal waveform. However, this technique achieves very low data rates. In order to increase the data rate, [81], [82], [83] suggested embedding a sequence of bits into the LFM pulse with the BPSK m-sequence, the minimum shift keying and BPSK respectively. However, in [81] and [83] only communication aspects were considered. In [84], [85], communication sequences were modulated using continuous phase modulation and phase-attached to a polyphase coded frequency-modulated radar waveform. In [86], two different message channels were employed where the binary PSK m-sequence was used to encode a single LFM pulse, and the effect of the code embedding on the radar performance was investigated in terms of the ambiguity function. MIMO beamforming for LFM radar however was not considered in either [81], [82], [83], [84], [85], [86]. Yet, MIMO beamforming is one of the powerful tools to provide improved angular resolution and improved beam control of modern imaging radar systems designed to deliver situational awareness for semi- and fully-autonomous driving [87].

In this thesis, I investigate, analytically and experimentally, the feasibility of MIMO PSK modulated LFM waveform dual-function system, where vehicular communication data are embedded into radar waveforms using PSK symbols without significant degradation of

radar detection or beamforming performance. To achieve this, the sweep time of the LFM signal is divided into smaller sub-units, and within each sub-units the signal carries a PSK symbol. Hence, multiple symbols are embedded into each chirp. Also, PSK communication data can be coded using either an m-sequence or Barker code. In this way, orthogonality of multiple transmitted signals can be maintained so MIMO transmitters can operate simultaneously. The achievable data rate depends on the sub-unit duration, the sweep time, the pulse repetition interval (PRI), the size of the PSK constellation and the number of transmitters operating, which in its turn depends on waveform orthogonality. Importantly, the proposed technique is used in a MIMO configuration in order to gain improved angular resolution. In this chapter, orthogonality between MIMO transmitters is provided by TDM and CDM techniques, where each transmitter sends a different message from the others. A message is embedded into an LFM signal using PSK in a TDM implementation and an m-sequence or Barker code is utilized to embed signals into an LFM waveform in a CDM case. These methods are compared, through both simulation and experimentation to assess their radar and communication performance.

To demonstrate the viability of the concept, experiments were conducted at a frequency of 2 GHz, due to available laboratory equipment. However, without loss of generality the results are scalable to automotive radar frequencies (24 GHz, 77 GHz and 79 GHz) and beyond.

### 3.3 Proposed Techniques

In this section, specific methods to embed communication data into a radar waveform are presented with the aim of obtaining an enhanced data rate consistent with the needs of vehicular communications. The orthogonality between transmitters in MIMO is provided by using TDM or CDM. The proposed joint radar and communication scenario is demonstrated in Figure 3.1. It is assumed that the radar transmitter and receiver antenna elements are co-located,

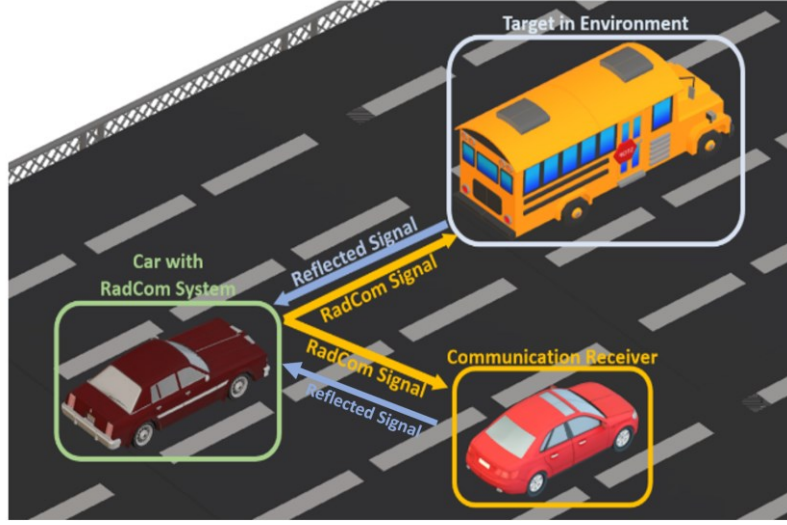


Figure 3.1: The proposed joint radar and communication scenario.

the radar waveform carries communication data, and the communication receiver is located in the far-field.

### 3.3.1 Time Division Multiplexing (TDM)

Here, LFM is used as a radar waveform, with sweep time divided into a number of sub-units as shown in Figure 3.2(a). The phase of each sub-signal is defined within each sub-unit as illustrated in Figure 3.2(b) according to the chosen phase shift keying modulation such as BPSK, QPSK etc.

The up-chirp LFM signal and MIMO beamforming principle are described in Section 2.1.2.1, but for the sake of completeness it will be given again here, so the complex form of an up-chirp LFM signal is given by:

$$s(t) = e^{j(\phi + 2\pi f_c t + \pi \frac{B}{T_m} t^2)}, \quad 0 < t \leq T_m \quad (3.1)$$

where  $\phi$  is the initial phase,  $f_c$  is the center frequency,  $B$  is the bandwidth,  $T_m$  is the sweep time.

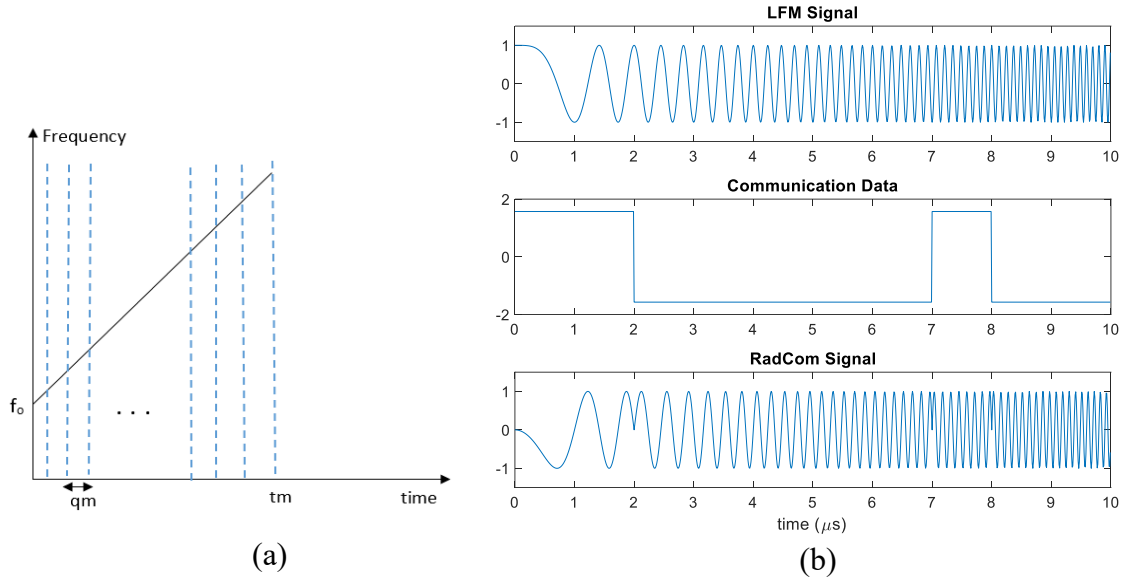


Figure 3.2: (a) The demonstration of dividing sweep time into multiple sub-units and (b) an example of embedded data into the radar signal.

The initial phase,  $\phi$ , is constant in a pure LFM signal. However, the phase can be near instantaneously switched at the start of sub-unit segments according to the phase shift modulation sequence of the communication signal. The PSK-LFM signal becomes

$$s_{radcom}(t) = e^{j(\phi_{data}(t) + 2\pi f_c t + \pi \frac{B}{T_m} t^2)}, \quad 0 < t \leq T_m \quad (3.2)$$

where  $\phi_{data}(t)$  is the phase shift keying data which is embedded into LFM signal, and it contains  $N_{sym}$  different symbols.  $N_{sym}$  is equal to  $\frac{T_m}{t_{sub}}$ ,  $t_{sub}$  is the sub-unit which expresses the symbol period.

$$\phi_{data}(t) = \begin{cases} \phi[t - i \cdot t_{sub}] \in [0, 2\pi], & i \cdot t_{sub} < t \leq (i + 1)t_{sub} \\ 0, & otherwise \end{cases} \quad (3.3)$$

where  $i = 0, 1, \dots, N_{sym} - 1$ , and  $\phi_{data}(t)$  depending on PSK constellation will have a finite number of discrete phases: two for BPSK and four for QPSK. The dimension of  $\phi_{data}(t)$  in

discrete time is  $(1 \times N_{sample})$ , where  $N_{sample}$  is the number of samples per pulse and defines the number of range bins.

When a co-located MIMO array is used, orthogonality of transmitted signals must be ensured to avoid mutual interference and here, TDM is utilized. Assuming a MIMO array with  $N_T$  transmit and  $N_R$  receive antenna elements, the transmit and receive steering vectors,  $\mathbf{a}(\theta)$  and  $\mathbf{b}(\theta)$  respectively, are given by

$$\mathbf{a}(\theta) = [1 \ e^{jkd_T \sin \theta} \dots e^{jk(N_T-1)d_T \sin \theta}]^T_{N_T \times 1} \quad (3.4)$$

and

$$\mathbf{b}(\theta) = [1 \ e^{jkd_R \sin \theta} \dots e^{jk(N_R-1)d_R \sin \theta}]^T_{N_R \times 1} \quad (3.5)$$

where  $\theta$  is the azimuth angle of the target,  $k$  is the wave number  $(2\pi/\lambda)$ ,  $[\cdot]^T$  stands for transpose,  $d_T$  and  $d_R$  are the transmitter and receiver element spacings, respectively.

Each transmitter sends different symbols from the other, and the transmitted data per frame,  $\tilde{\Phi}_{data_f}(t)$ , can be represented as:

$$\tilde{\Phi}_{data_f}(t) = [\phi_{data_1}(t) \ \phi_{data_2}(t) \dots \phi_{data_{N_T}}(t)]^T \quad (3.6)$$

where  $\phi_{data_n}(t)$  is the transmitted data from  $n^{th}$  transmit element,  $n = 1, 2, \dots, N_T$ . The dimension of  $\tilde{\Phi}_{data_f}(t)$  is  $(N_T \times N_{sample})$  in discrete time.

Hence, the transmitted signals per frame,  $\mathbf{s}_{radcom_f}(t)$ , can be expressed as

$$\mathbf{s}_{radcom_f}(t) = [s_{radcom_1}(t) \ s_{radcom_2}(t) \dots s_{radcom_{N_T}}(t)]^T \quad (3.7)$$

where  $s_{radcom_n}(t)$  is the transmitted PSK-LFM signal from  $n^{th}$  transmit element,  $n = 1, 2, \dots, N_T$ . The dimension of  $\mathbf{s}_{radcom_f}(t)$  is  $(N_T \times N_{sample})$  in discrete time.

### 3.3.1.1 Radar Receiver Part in TDM

In a co-located MIMO radar, the signal reflected by  $L$  targets are input in the receiver as:

$$\mathbf{x}_{rad}(t) = \sum_{l=1}^L \beta_l \mathbf{b}^c(\theta_l) \mathbf{a}^*(\theta_l) e^{j(\tilde{\Phi}_{data_f}(t-\tau_l) + 2\pi f_c(t-\tau_l) + \pi \frac{B}{T_m}(t-\tau_l)^2)} + \boldsymbol{\varepsilon}(t) \quad (3.8)$$

where  $\beta_l$  is the reflection coefficient of the  $l^{th}$  target,  $\mathbf{a}(\theta_l)$  and  $\mathbf{b}(\theta_l)$  are transmit and receive steering vectors of the  $l^{th}$  target,  $\tau_l$  is the delay time of  $l^{th}$  target and  $\boldsymbol{\varepsilon}(t)$  is zero-mean white Gaussian noise. Symbols  $[\cdot]^c$  and  $[\cdot]^*$  denote the complex conjugate and the conjugate transpose, respectively. Discrete version of equation (3.8) will result in of  $\mathbf{x}_{rad}(t)$  being an array of  $(N_T N_R \times N_{sample})$ .

Each received signal is match filtered using corresponding transmitted signal as in (3.9). When a pure LFM signal is used, both matched filtering and stretch processing can be applied to the received signal. However, in the case of PSK-LFM signal only MF gives the correct range information.

$$\mathbf{y}(t) = \int_0^{T_m} \mathbf{x}_{rad}(t) \mathbf{s}_{radcom_f}^c(t) d\tau \quad (3.9)$$

The size of the range compressed data is  $(N_T N_R \times N_{sample})$ , where  $N_T N_R$  is, again, the number of virtual array elements and  $N_{sample}$  defines the number of range bins. Finally, a range-angle map is generated by taking a Fourier transform along the azimuth direction.

### 3.3.1.2 Communication Receiver Part in TDM

It is assumed that communication receiver is positioned in the far-field of the radar transceiver and contains just one receive element. The received signal from the  $n^{th}$  transmit element at the communication receiver is the time delayed version of the transmitted signal sent and is given by

$$\mathbf{x}_{com_n}(t) = \mathbf{a}_n^*(\theta_c) e^{j(\phi_{data_n}(t-\tau_c) + 2\pi f_c(t-\tau_c) + \pi \frac{B}{T_m}(t-\tau_c)^2)} + w(t) \quad (3.10)$$

where  $\tau_c$  is the time delay between the transmit antenna and the communication receiver,  $\theta_c$  is the azimuth angle of the receiver with respect to the transmitter;  $w(t)$  is zero-mean white Gaussian noise.

The received signal is demodulated, using a reference signal as shown in (3.11). Here, it is assumed that the communication receiver ‘knows’ the transmitter steering vector, so the reference signal contains the steering vector in order to compensate the phase shifts between the received signals from the MIMO antenna. Assuming that the receiver knows the steering vector is not always practical. To overcome this challenge, channel estimate approaches based on pilot signals may be used. However, this is out of the scope of this thesis.

$$refsig_{com_n}(t) = e^{j(2\pi f_c t + \pi \frac{B}{T_m} t^2)} \mathbf{a}_n^*(\theta_c) \quad (3.11)$$

In order to demodulate the transmitted data sent from the  $n^{th}$  transmit element, a matched filter is used as below:

$$y_n(t) = \int_0^{T_m} x_{com_n}(t) refsig_{com_n}^c(t) d\tau \quad (3.12)$$



(3.12) is a matched filter operation presented as a correlation processing. As a result of correlation processing and synchronization the modulation envelope  $\phi_{data_n}$  is extracted. Here,  $\phi_{data_n}$  takes discrete constant values depending on the size of PSK constellation. For instance, if a BPSK modulation is applied,  $\phi_{data_n}$  contains  $\pm\pi/2$  values corresponding to each bit. Hence, the resulting term consists of  $\pm j$  with a rectangular carrier. The transmit data is recovered by using comparator after the integration.

Finally, received data from each transmit element is combined in a vector

$$D = [d_1 \ d_2 \ \cdots \ d_{N_T}] \quad (3.13)$$

where  $d_n$  is the bit stream from  $n^{th}$  transmit element recovered after comparator, and the dimension of  $D$  is  $(1 \times N_T N_{sym} N_{cons})$ .  $N_{cons}$  represents the bit number per PSK symbol.

It is an important to note that when a single-input single-output (SISO) antenna configuration is used, the equations above are still valid, but  $\mathbf{a}(\theta)$  and  $\mathbf{b}(\theta)$  are equal to one.

### 3.3.2 Code Division Multiplexing (CDM)

Orthogonality of transmit signals can be easily achieved by using TDM, but the data rate is lower than in case of simultaneous transmission. Therefore, I will use CDM approach where quasi-orthogonal signals can be transmitted simultaneously and demodulated in the receiver. Hence, the data rate can be increased by the number of transmitters. Moreover, this provides faster MIMO radar response than TDM.

In CDM, the communication message is embedded into the LFM signal by using different bit sequences for each transmitter. Each sub-unit contains a bit sequence which represents one symbol. To clarify this further, an example is shown in Figure 3.3. By using 7-bit m-sequence, the binary symbols are embedded into an LFM signal. The transmitted signals

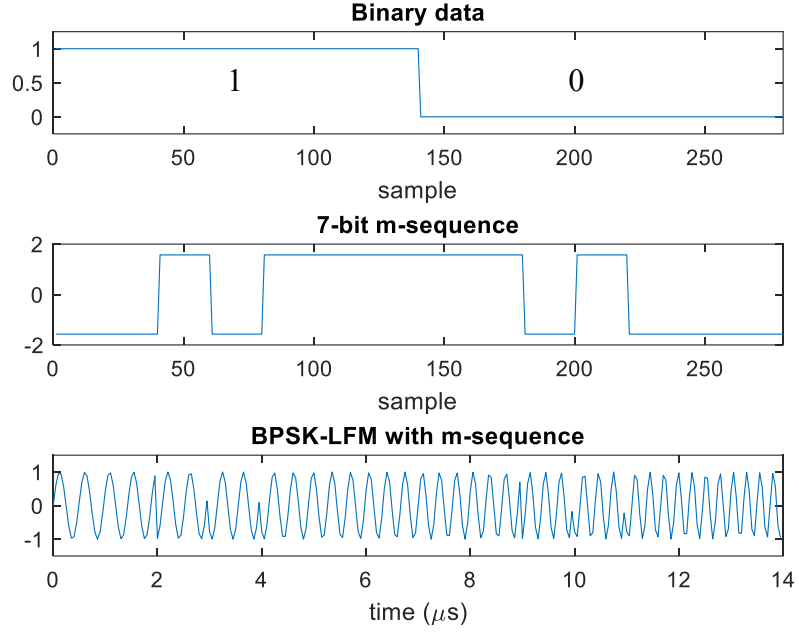


Figure 3.3: An example of embedded data into LFM signal by using 7-bit m-sequence.

in CDM are given by (3.14)

$$s_{radcom_n}(t) = e^{j(\phi_{data_n}(t) \cdot \Lambda_n(t) + 2\pi f_c t + \pi \frac{B}{T_m} t^2)}, \quad 0 < t \leq T_m \quad (3.14)$$

where  $\Lambda_n(t)$  is the bit sequence of  $n^{th}$  transmitter and it consists of  $\pm\pi/2$  and it is repeated each sub-unit time ( $t_{sub}$ ).  $\phi_{data_n}(t)$  is 1 for '1' and  $-1$  for '0' each sub-unit time.

The transmitted data and transmitted signals per frame can be expressed as in (3.6) and (3.7) respectively.

### 3.3.2.1 Radar Receiver Part in CDM

As all transmitters are active at the same time in CDM, the received signals can be written as

$$\mathbf{x}_{rad}(t) = \sum_{l=1}^L \mathbf{b}^c(\theta_l) \sum_{n=1}^{N_T} \beta_l \mathbf{a}^*(\theta_l) e^{j(\phi_{data_n}(t-\tau_l) \cdot \Lambda_n(t-\tau_l) + 2\pi f_c(t-\tau_l) + \pi \frac{B}{T_m}(t-\tau_l)^2)}$$

$$+ \varepsilon(t) \quad (3.15)$$

where all symbols have the same meaning as in (3.8). The dimension of  $\mathbf{x}_{rad}(t)$  is  $(N_R \times N_{sample})$  in discrete time.

Each received signal is matched filtered using each transmitted signal, so the range response is obtained  $((N_T N_R \times N_{sample})$  in discrete time). Then, range-angle map is created by taking a second Fourier transform in azimuth direction.

### 3.3.2.2 Communication Receiver Part in CDM

The communication received signal in CDM is summation of the time delayed versions of all transmitted signals, and it is given by

$$x_{com}(t) = \sum_{n=1}^{N_T} \mathbf{a}_n^*(\theta_c) e^{j(\phi_{data_n}(t-\tau_c) \cdot \Lambda_n(t-\tau_c) + 2\pi f_c(t-\tau_c) + \pi \frac{B}{T_m}(t-\tau_c)^2)} + w(t) \quad (3.16)$$

where all symbols have the same meaning as in (3.10).

The received signal is demodulated, using reference signals as shown below. Here the bit sequences used by the transmitters are assumed to be known by the communication receiver. Also, the transmitter steering vector is known from the communication receiver, and the reference signal contains the steering vector as a multiplier so as to compensate phase shifts between received signals coming from different transmitters.

$$refsig_{com_n}(t) = e^{j(\Lambda_n(t) + 2\pi f_c(t) + \pi \frac{B}{T_m}(t)^2)} \mathbf{a}_n^*(\theta_c) \quad (3.17)$$

In order to obtain message from received signal, matched filters are utilized as in (3.12). Moreover, received message from each transmitter is combined as in (3.13).

### 3.4 System Parameters Based On BER

The BPSK-LFM signal is examined in [83] in terms of its bit error rate (BER) performance. It is shown that the BER for BPSK-LFM is exactly the same as that for the BPSK signal. This means that the carrier waveform does not affect the communication performance in terms of BER. In the TDM case, transmitters emit BPSK-LFM signals in different time slots. Therefore, in the BER calculation, the TDM system can be thought as a single transmitter. Hence, it can be assumed that multiple transmitter usage with TDM does not change the BER performance of the signal.

With regards to CDM, [49] demonstrates that when one symbol is expressed with a bit sequence, the BER is still the same as for BPSK in the case of single transmitter usage. However, when the number of transmitters increases, the BER response becomes worse. In [49], it is illustrated that there is a trade-off among number of transmitters, code length, energy per bit to noise ( $E_b/N_0$ ) ratio and BER. The system design can be chosen by trading these parameters. The relationship between these parameters is given in [49] as

$$P_e = Q\left(\frac{1}{\sqrt{\frac{N_T - 1}{3N} + \frac{N_0}{2E_b}}}\right) \quad (3.18)$$

where  $P_e$  is the average probability of bit error,  $Q(\cdot)$  is Q-function,  $N_T$  is the number of transmitter and  $N$  is the code length.

In vehicular communication systems, a  $10^{-6}$  BER or less is required. Using this criterion, equation (3.18) enables  $E_b/N_0$  versus number of transmitters to be plotted as shown in Figure 3.4. The graph shows the usable maximum number of transmitters and their required  $E_b/N_0$  for

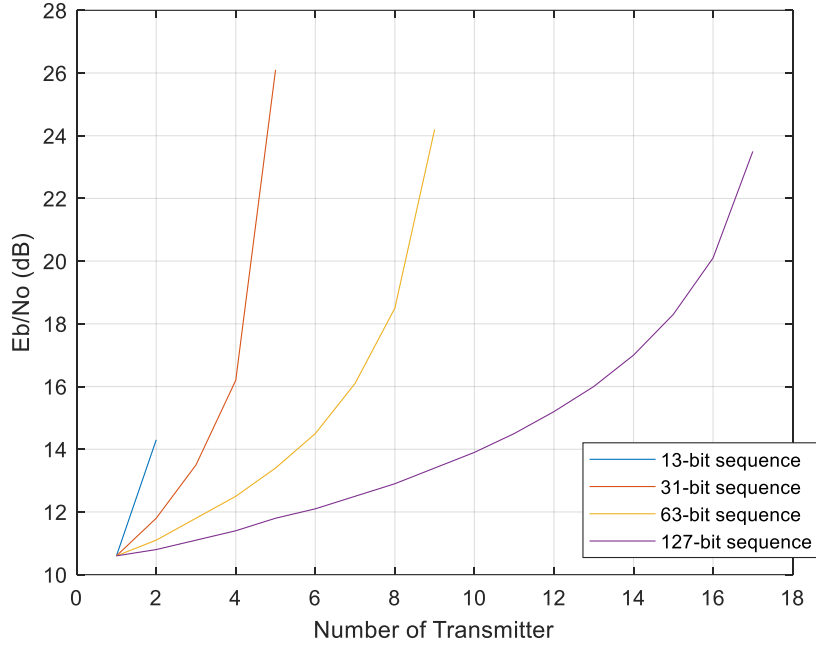


Figure 3.4: Number of transmitter vs  $E_b/N_0$  for different code lengths under a  $10^{-6}$  BER or less criterion.

each code lengths. For instance, when a 63-bit code length is used, a maximum of 9 transmitters can be used with minimum  $E_b/N_0$  of 24 dB to obtain the required BER. However, 13 dB  $E_b/N_0$  is enough for 4 transmitters to ensure the BER criterion. Obviously, the longer is the code length, the higher number of transmitters can be used to improve radar performance. In the following sections, case of only two transmitters will be considered, so 13-bit and 31-bit sequences are used in order to prove the CDM concept.

### 3.5 Simulation Results

In this section, the radar and communication performance of both TDM and CDM methods using an example scenario is presented in order to demonstrate the viability of the proposed concept. The radar and communication waveform parameters are shown in Table 3.1. The modulation type used is BPSK, and each LFM pulse contains 500 binary symbols. In this

Table 3.1: Radar parameters

Parameters	Value
Frequency	2 GHz
LFM Bandwidth	200 MHz
Sampling frequency	6.25 Gsps
Sweep time	50 $\mu$ s*
PRI	100 $\mu$ s*
Modulation	BPSK
Sub-unit	0.1 $\mu$ s*
Number of embedded data per pulse	500
Achieved data rate	5 Mbps (in TDM) 10 Mbps (in CDM)
Number of transmitters	2
Number of receivers	4
Spacing between Rx	$\lambda/2$
Spacing between Tx	$4 \cdot \lambda/2$
Angular resolution	$\sim 14.41^\circ$
Orthogonality	TDM or CDM

Note: \* Here, slightly different sweep time, pulse repetition interval and sub-unit are used in order that the sample number is an integer to design a bit.

way, data rates of 5 Mbps and 10 Mbps rate are achieved by using TDM and CDM respectively. The data rate can be increased by decreasing the sub-unit duration and/or the PRI, or using a higher order PSK modulation. Also, increasing the number of transmitters in CDM provides for a higher data rate.

In TDM, a BPSK-LFM signal is used as discussed above. For the CDM case, 13-bit Barker code and 31-bit m-sequences with their cyclic phase-shifted versions are utilized. In the case of a 13-bit Barker code, the first transmitter uses  $[1, 1, 1, 1, 1, -1, -1, 1, 1, -1, 1, -1, 1]$  to embed data onto the LFM signal whereas the second transmitter uses its phase-shifted version,  $[1, 1, 1, 1, -1, -1, 1, 1, -1, 1, -1, 1, 1]$ . A 31-bit m-sequence is obtained by using a polynomial  $f(x) = x^5 + x^3 + 1$ . In order to understand the impact of embedding data into an LFM signal, ambiguity functions (AF) of pure LFM, BPSK-LFM, 13-bit Barker and 31-bit m-sequence are

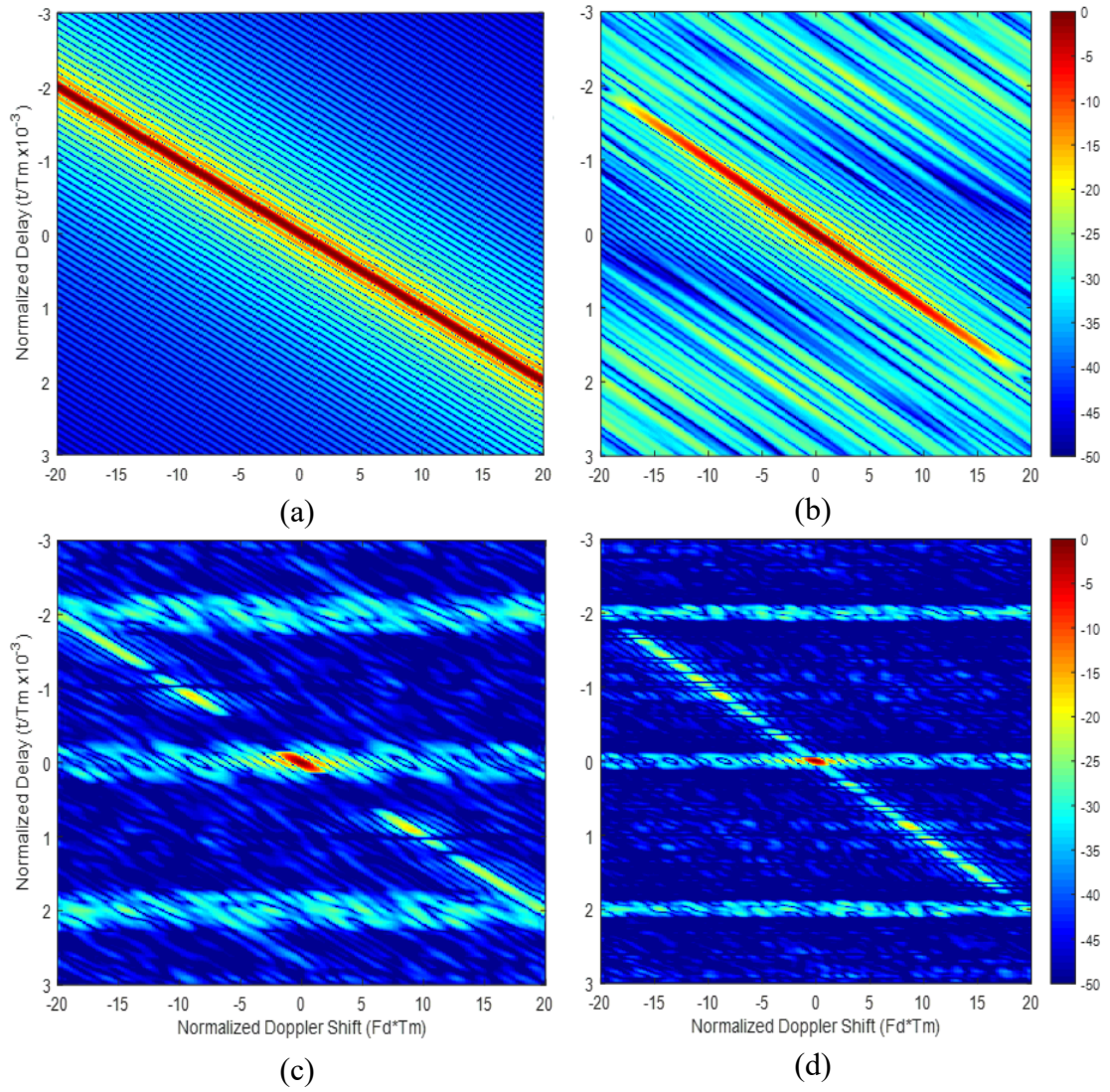


Figure 3.5: Ambiguity function of (a) pure-LFM, (b) BPSK-LFM, (c) 13-bit Barker code and its phase-shifted version, (d) 31-bit m-sequence and its phase-shifted version.

computed. As seen from the ambiguity function diagram in Figure 3.5, embedding data into LFM signal reduces range-Doppler coupling. As the higher number of sequences are used, AF becomes closer to a thumbtack shape. However, it is use of both 13-bit Barker and 31-bit m-sequences lead to appearance of the grating lobes at around  $0.1 \mu\text{s}$  which corresponds to the distance around 15 m.

Simulation scenario. A point target is placed 7.2 m away from the MIMO antenna at a  $10^\circ$  azimuth angle with respect to boresight. A communication receiver is located at an angle of  $30^\circ$ . Note that both transmitters send different messages from each other. However, the same communication data is used in all simulations to compare the radar responses. Range-angle maps are shown in Figures 3.6 – 3.8 for each of the proposed signals. When all range cuts are examined, it may be seen that there is no difference in the azimuth responses where the 4 dB beamwidth is  $14.8^\circ$ . Although the target's positions are obtained correctly, the range resolutions, defined by different roll-offs from the maximum, are different. The 3 dB range resolutions are approximately 0.72 m, 0.52 m and 0.32 m for BPSK-LFM, 13-bit Barker code and 31-bit m-sequence cases respectively. The data bandwidth depends on the bit duration. When the null-to-null bandwidths are examined, it can be seen that the data bandwidth can extend the LFM bandwidth. Naturally, the null-to-null bandwidth is close to twice of the total

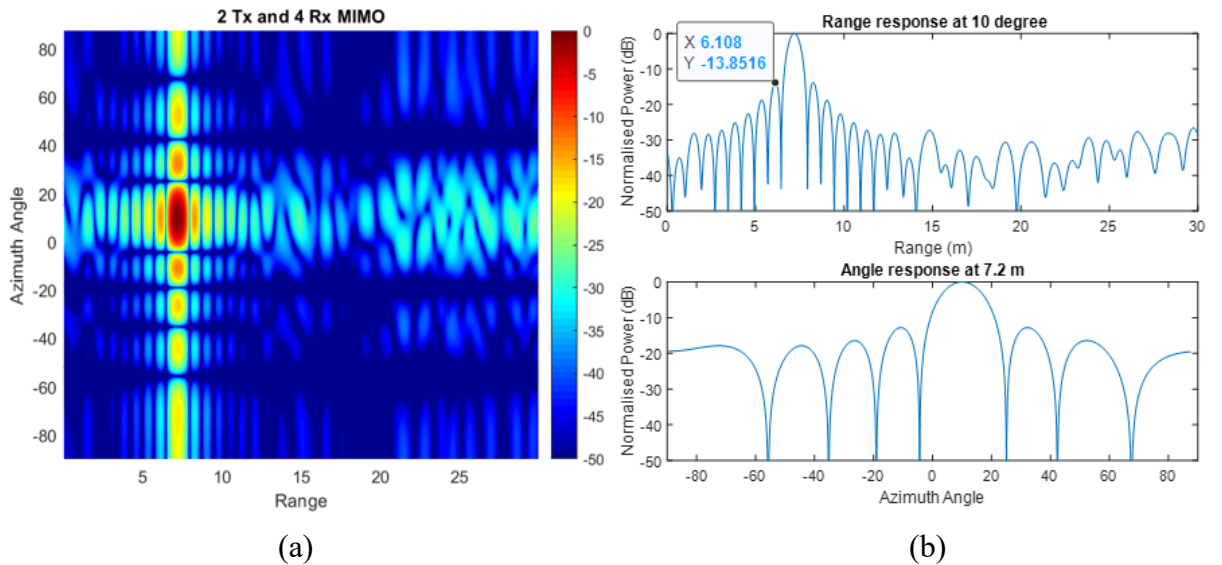


Figure 3.6: (a) Range-angle map by using BPSK-LFM, (b) range and azimuth angle cuts.



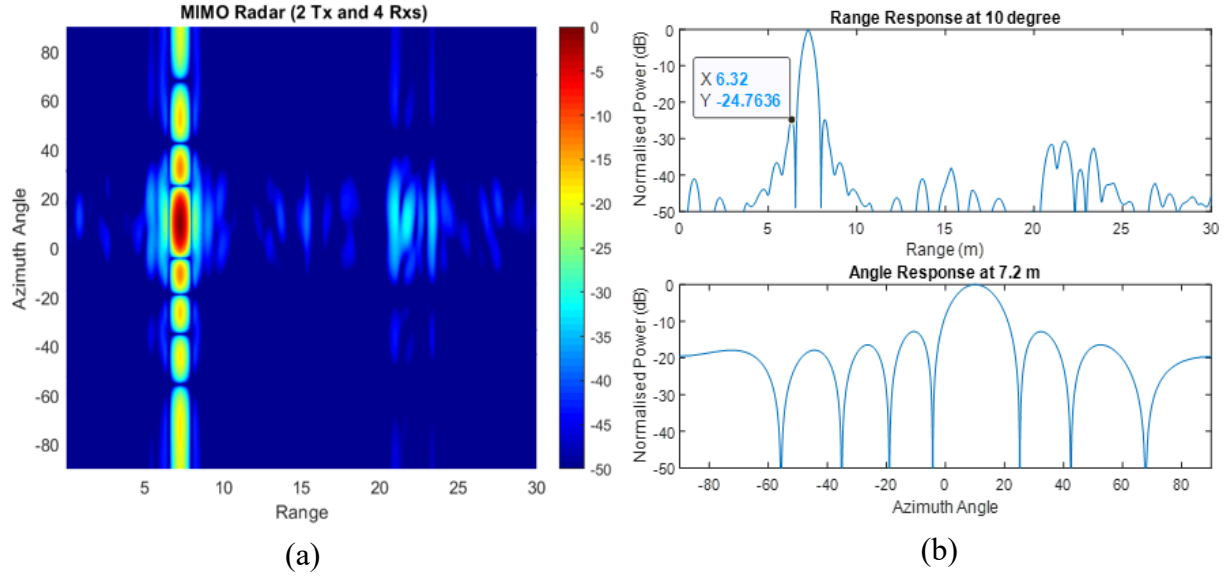


Figure 3.7: (a) Range-angle map by using 13-bit Barker code and its shifted version, (b) range and azimuth angle cuts.

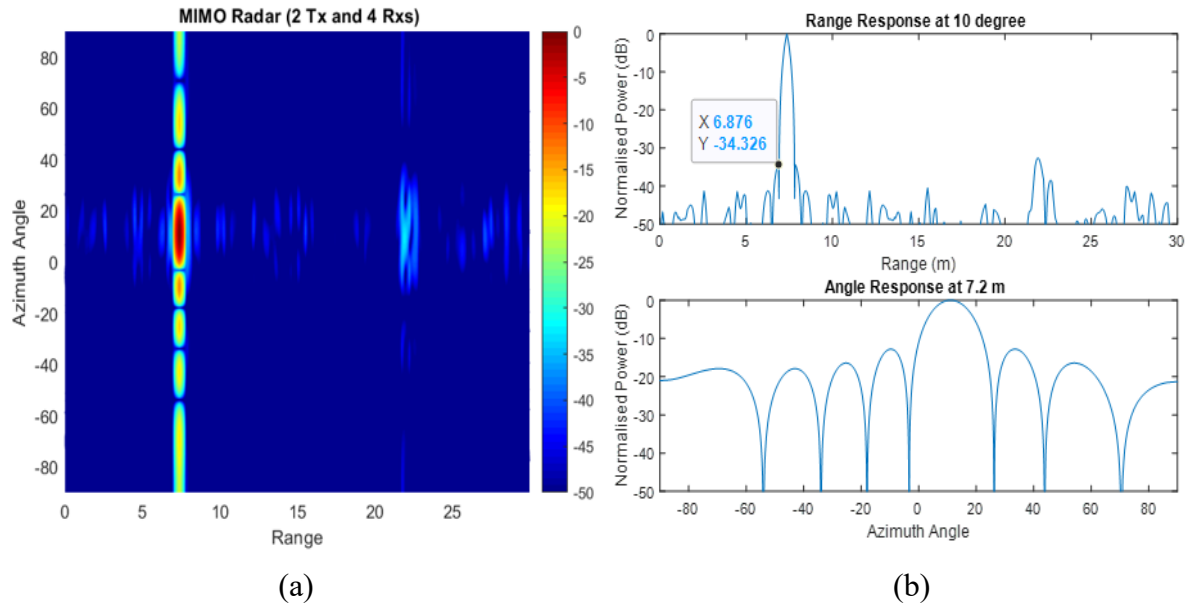


Figure 3.8: (a) Range-angle map by using 31-bit m-sequences, (b) range and azimuth angle cuts.

signal bandwidth. For instance, 3.2 ns bit duration is used in 31-bit m-sequence, and this results in a bandwidth of 312.5 MHz. A null-to-null bandwidth of nearly 640 MHz is obtained in the case of 31-bit m-sequence because the data bandwidth is greater than the LFM bandwidth (200 MHz).

On the other hand, the sidelobe level dramatically decreases when using a higher number of bit sequences as seen from the Figures 3.6 – 3.8. BPSK-LFM produces the highest sidelobe levels in range response whereas 31-bit m-sequence and its shifted version experience the lowest sidelobe level, compared with others. Also, when  $0.1 \mu\text{s}$  is used as a sub-time unit, a grating lobe is seen every 15 m. Although the power level of the grating lobe is low, it could result in appearance of false targets. With regards to the communication part, all proposed methods have been examined, and the transmitted message has been received without any distortion (error) in the communication receiver in each case. Therefore, only an example result where signal coded by 13-bit Barker code is transmitted by the first transmitter illustrated in Figure 3.9.

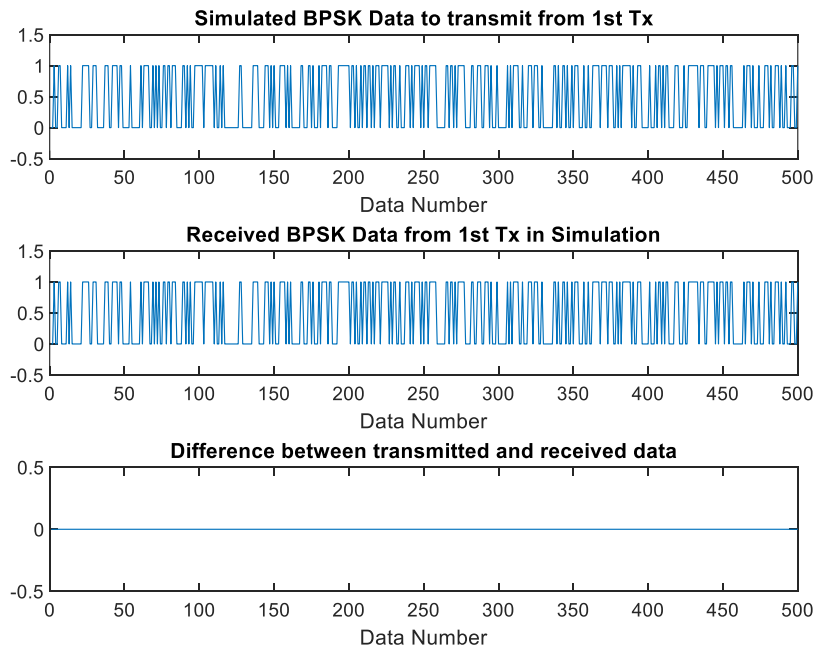


Figure 3.9: Simulation result of transmitted data from the first transmitter by using 13-bit Barker code and demodulated data in communication receiver.

### 3.6 Experimental Results

To generate and receive modulated signals a Tektronix AWG7102 arbitrary waveform generator (AWG) and a Tektronix DPO 72004 digital oscilloscope (DPO) are used. The oscilloscope sampling rate is limited by 6.25 Gsps, so a 2 GHz carrier was chosen for a signal with a bandwidth of 200 MHz. The parameters of the set-up and signals are given in Table 3.1. Two broadband horn antennas (Q-par WBH1-18S) operating over a range of 1-18 GHz were used, with a physical aperture size of 96 x 90 mm<sup>2</sup> [88]. A rectangular corner reflector of 29 x 29 x 29 cm<sup>3</sup> size, made of copper, is used as a calibration target.

The transmitted signals with the parameters given above are simulated in Matlab, then the designed waveform is imported to the AWG. For a full control, a reference signal is provided by cable from the AWG to DPO Channel-1 whereas the target reflected signal is received by DPO Channel-2. The recorded reference and received signals are transferred to a laptop for processing and analysis. The schematic experimental setup is illustrated in Figure 3.10. The cable length is 1 m for the reference signal and 4 m cables are used to connect the transmitter and receiver antennas to AWG and DPO respectively.

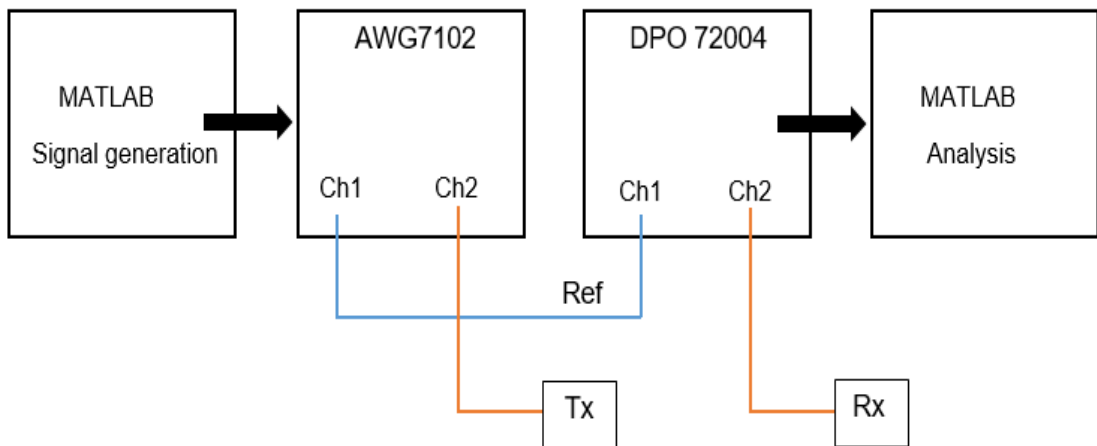


Figure 3.10: The configuration of experimental setup.

### 3.6.1 SISO Case

The transmit and receive antennas are placed as close as possible to represent the quasi-monostatic radar, and a target is placed 3.1 m away from the antennas on the boresight as shown in Fig. 3.11(a). Due to availability of only two antennas, radar detection and the communication link were done separately. Hence, the radar receiver antenna position was changed to be a communication received antenna after radar detection was completed. The communication receiver is placed almost 3 m away at an angle of  $30^\circ$  with respect to the transmitter as shown in Figure 3.11(b).

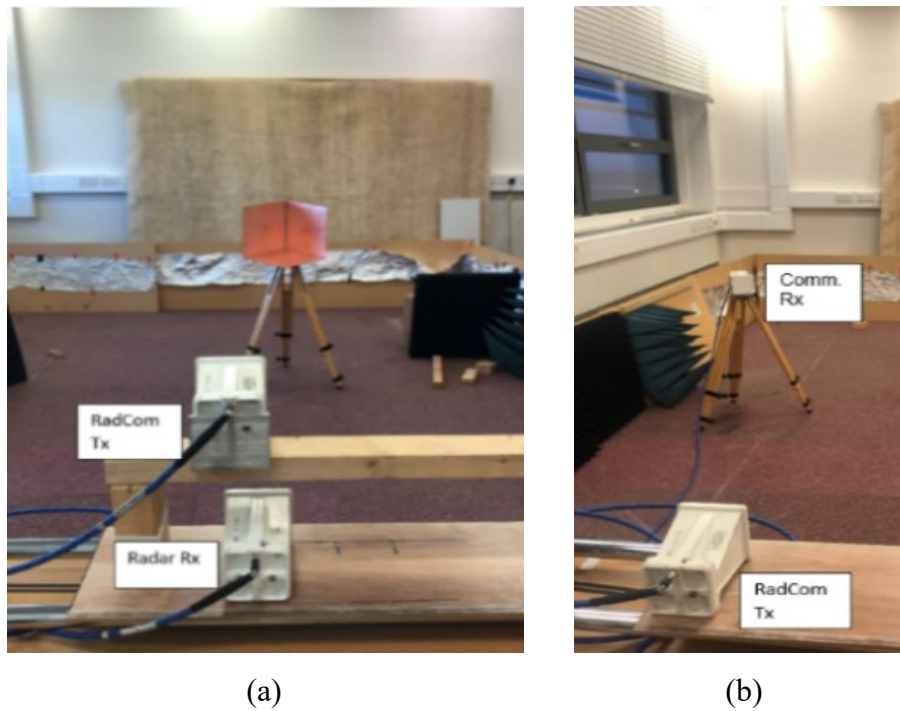


Figure 3.11: In SISO case (a) Setup for target detection, (b) communication setup.

Experimental results for the SISO case are shown in Figures 3.12 and 3.13. Due to the difference in the cable length (as mentioned above) the target's range is approximately 6.6 m ( $((4+4-1)/2) \text{ m} + 3.1 \text{ m}$ ). When the radar results are examined, the target appears at a range of 6.7 m. At 3.9 m one can see the direct coupling and the laboratory wall is seen at 9.7 m, which correspond to actual wall position at 6.1 m from the radar with additional cable paths. With regard to communication part, the message is obtained by compensating the delay between the reference and received signals as in the simulated case as seen in Figure 3.13(b).

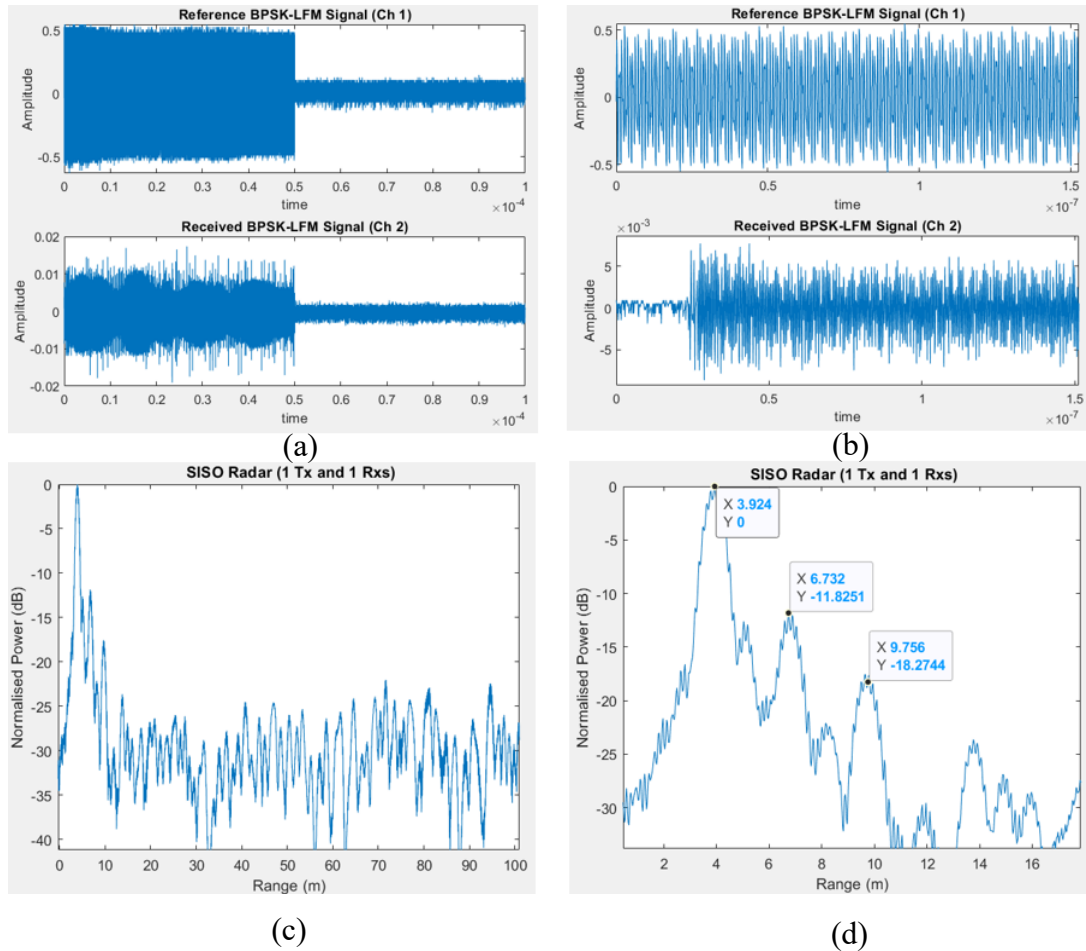


Figure 3.12: In radar part, (a) captured reference (BPSK-LFM) and received (BPSK-LFM) signals, (b) zoomed version of (a), (c) range response after matched filtering, (d) zoomed version of the range response.

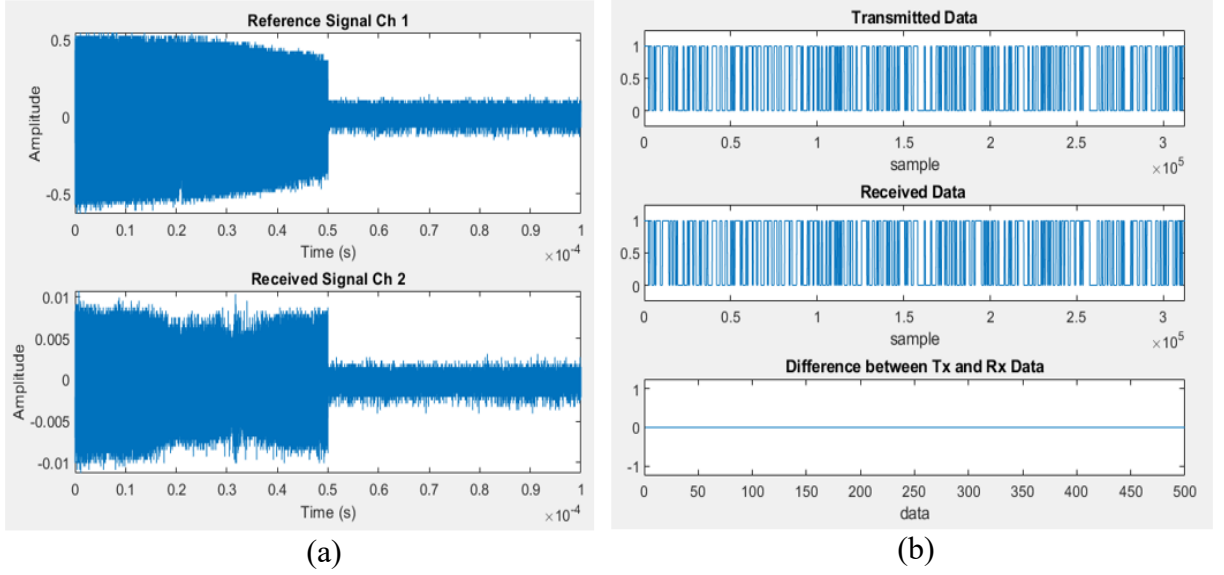


Figure 3.13: In communication part, (a) captured reference (LFM) and received (BPSK-LFM) signals, (b) embedded data into radar emission in simulation and received data from communication receiver in the experiment.

### 3.6.2 MIMO Case

To emulate  $2 \times 4$  MIMO array as shown in Figure 3.14, the signals were recorded when physical  $T_x$  and  $R_x$  antennas were positioned at each node of MIMO array sequentially. Orthogonality between received signals is achieved by using TDM and CDM as explained above. Moreover, each transmitted signal contains different messages. The MIMO array configuration in Figure 3.14 is used. Transmit and receive antennas are off-set in elevation to accommodate large size antennas with respect to the signal wavelength. The actual MIMO antenna length of this configuration is  $N_R \cdot \frac{\lambda}{2} + 0.09$  m, that is  $2\lambda + 0.09 = 0.39$  m where 9 cm relates to the physical antenna size. Hence, the far field distance  $d_{far} = \frac{2D^2}{\lambda}$  is 2.028 m. Such MIMO array would yield a beamwidth of approximately  $14.4^\circ$ , according to  $\theta_{4dB} = 0.88 \frac{\lambda}{D}$

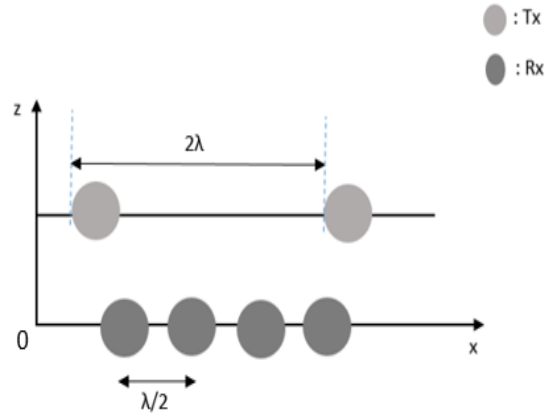


Figure 3.14: MIMO array configuration.

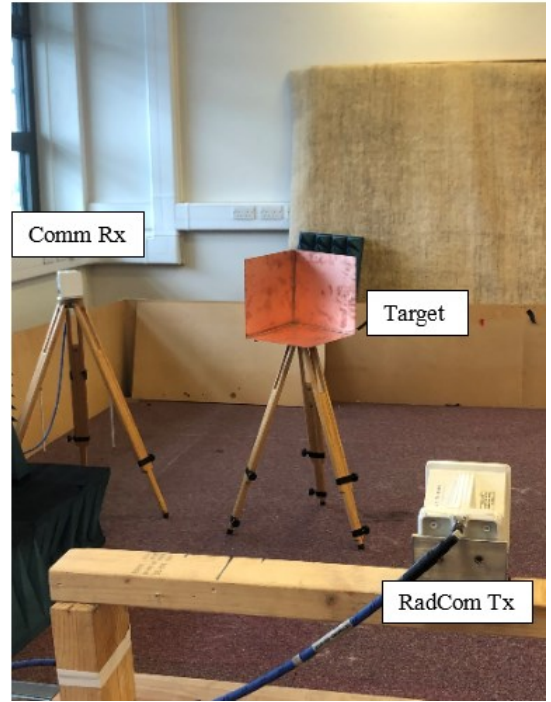
where  $D$  is the length of virtual antenna. The target is located at 7 m which includes cable length as illustrated in Figure 3.15 (a) at the angle of  $10^\circ$  with respect to the boresight of the antenna array. The communication receiver is placed almost 3.5 m away from the radar antennas at an angle of  $30^\circ$  as shown in Figure 3.15 (b). As the experiments with different nodes and CDM and TDM techniques have been conducted in consecutive days, the target position could be slightly different.

During the experiment, one transmit and one receive antenna was used for each measurement simulating one virtual element signal. In order to implement the complete MIMO configuration, for each position of transmit antenna the receive antenna position was shifted by precisely one half-wavelength along the x-axis. After recording the received signal in each receiver position, the transmit antenna position was changed by two wavelengths and the same steps were repeated. This method can be applied when using TDM. For CDM, the received signals at each receiver coming from both transmitters can be summed in the signal processing part. Hence, it can be assumed that transmitters are active simultaneously. As only two antennas were available, radar detection and the communication link were done separately as in SISO case. Hence, the radar receiver antenna position was changed to be a communication received





(a)



(b)

Figure 3.15: In MIMO case (a) Setup for target detection, (b) communication setup.

antenna after radar detection was completed. It is note that coupling effect between the transmitted and received signals is not considered in this method.

The target appears at 7.2 m in Figure 3.16 whereas it appears at around 7.4 m in Figure 3.17 – Figure 3.18 because it was put in a slightly different position. The range-azimuth angle map is plotted for the range between 5.7 m and 9.4 m. 4-dB azimuth beamwidth is obtained as roughly  $15.5^\circ$  in all experimental results. Range resolutions, however, are different from each other. In the BPSK-LFM, a 0.72 m range resolution is obtained, whereas resolutions of 0.69 m and 0.46 m are obtained from the 13-bit Barker code and 31-bit m-sequence, respectively. Moreover, it is clear that when sequences are used to embed symbols into an LFM signal, the sidelobe levels are less than in case of BPSK-LFM waveform, corresponding to simulation results. Note, the sidelobe patterns are not the same as in the simulation possibly due to multipath/multibounce effects or some inaccuracy in equipment positioning. When the



communication part is examined, all data from all transmitters are received by the receiver without any error. Therefore, the example results are shown only for 13-bit Barker code in Figure 3.19.

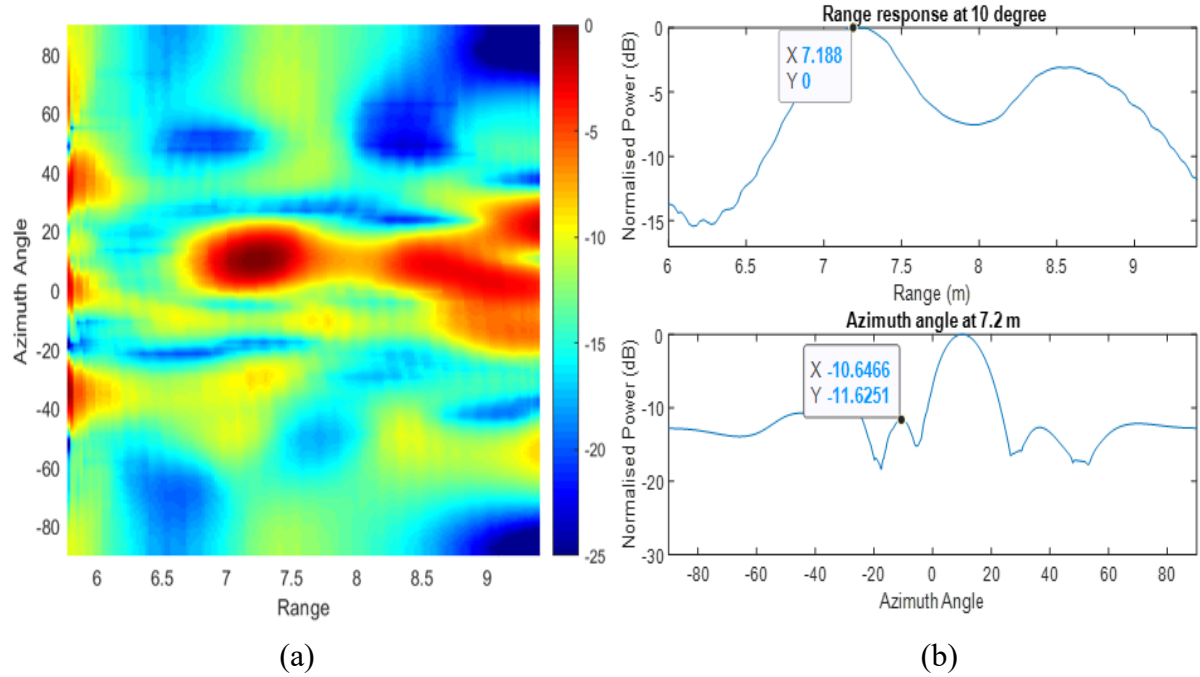


Figure 3.16: Experimental result of BPSK-LFM, (a) Range-azimuth angle map, (b) range and azimuth cuts.

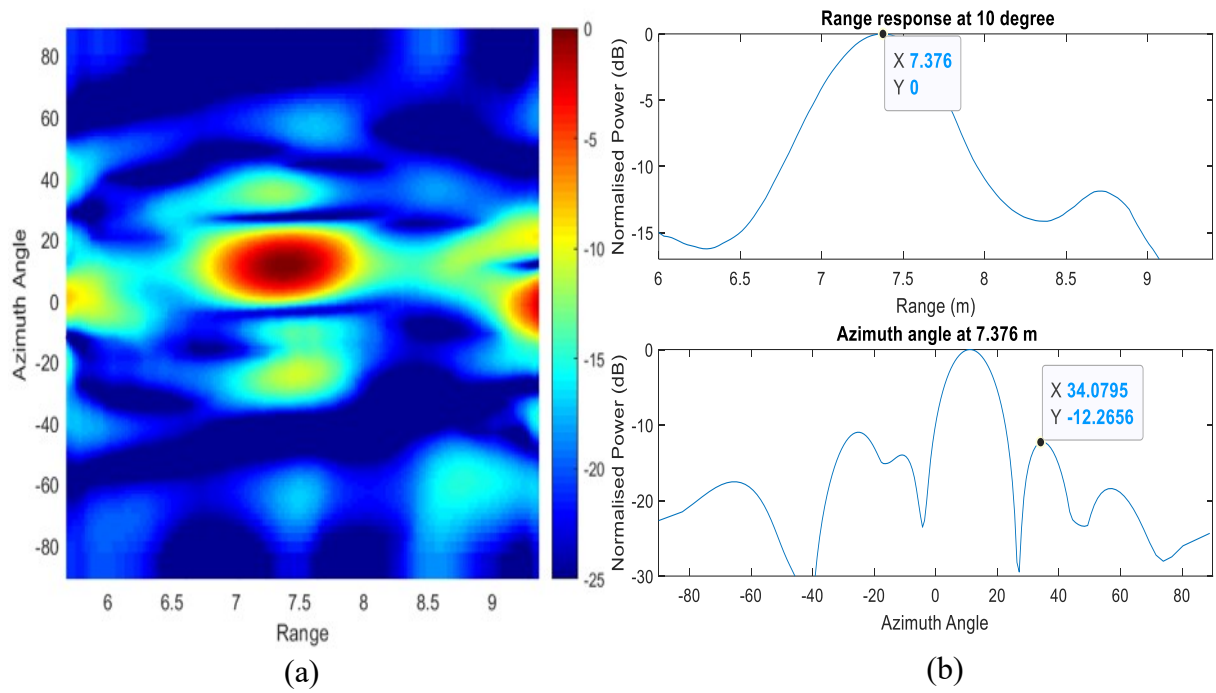


Figure 3.17: Experimental result of 13-bit Barker code, (a) Range-azimuth angle map, (b) range and azimuth cuts.

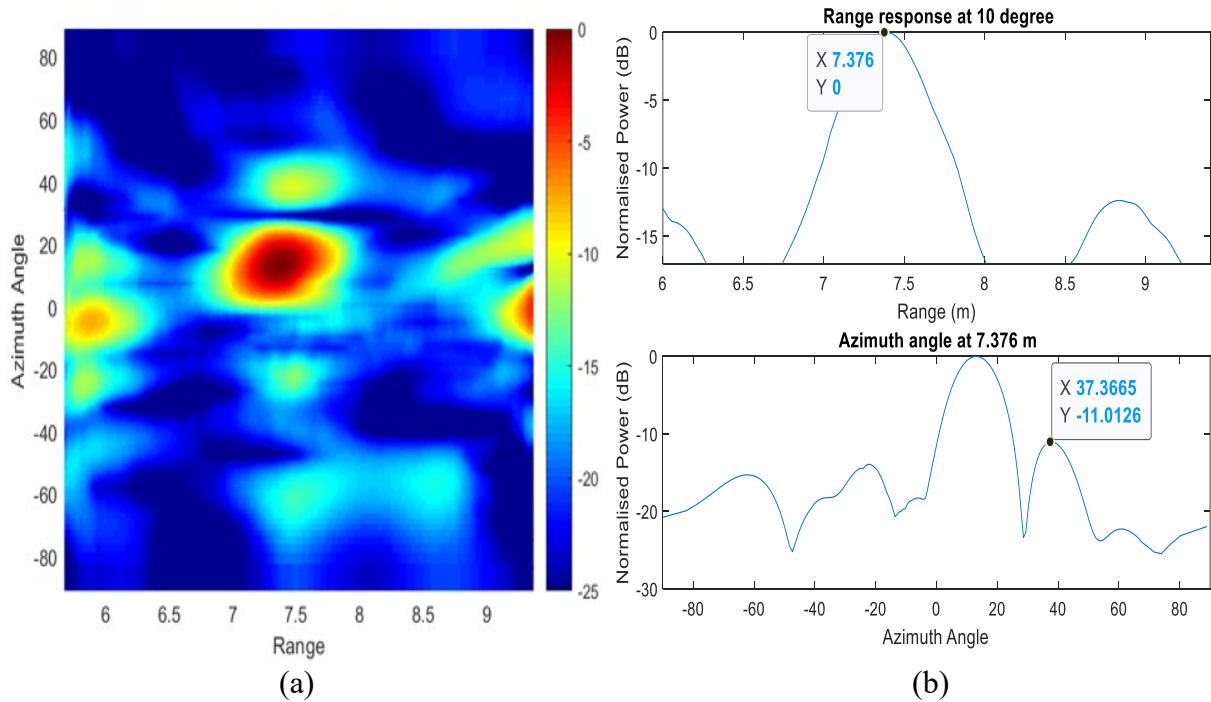


Figure 3.18: Experimental result of 31-bit m-sequence, (a) Range-azimuth angle map, (b) range and azimuth cuts.

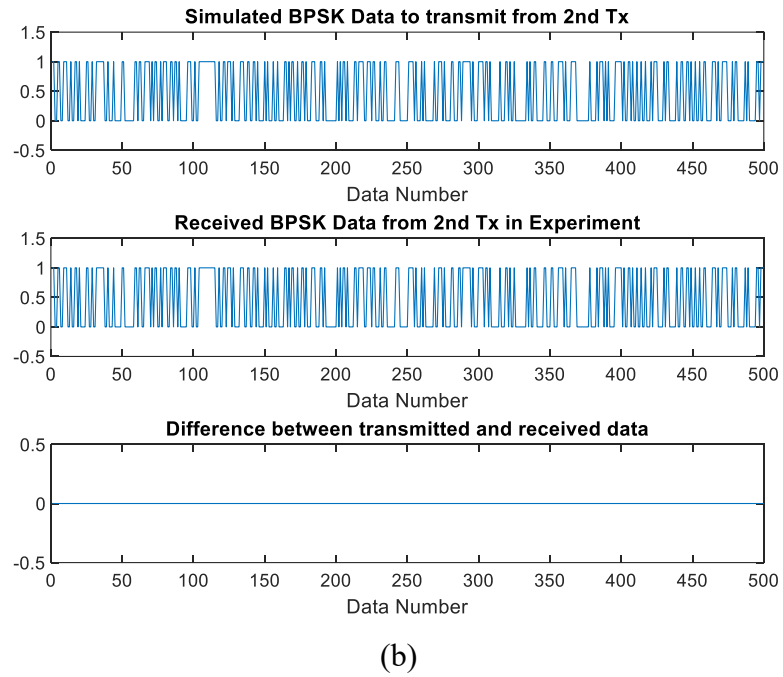
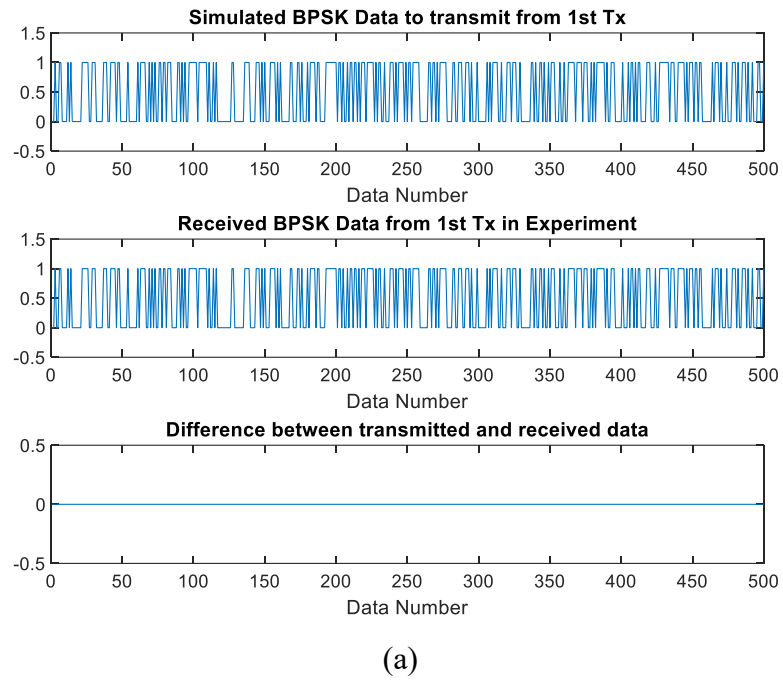
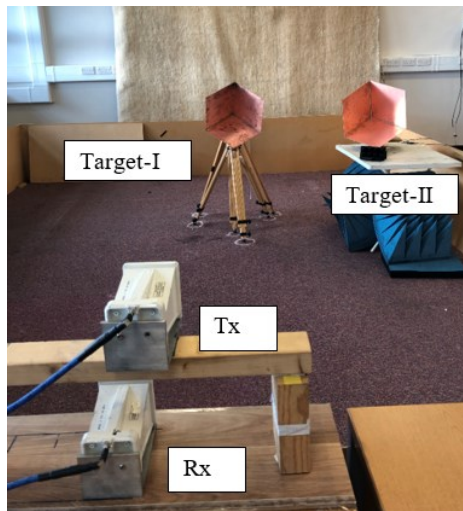


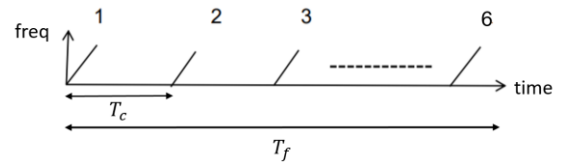
Figure 3.19: In experiment (a) transmitted data from the first transmitter by using 13-bit Barker code and demodulated data in communication receiver, (b) transmitted data from the second transmitter by using 13-bit Barker code and the demodulated data in communication receiver.

### 3.6.3 Doppler Effect

Another radar setup with the same MIMO antenna array as shown in Figure 3.14 uses a 13-bit Barker code PSK-LFM in order to examine radar performance in terms of velocity estimation. In this case, two targets are used as shown in Figure 3.20 (a). Target-I is stationary whereas Target-II has a 12 m/s velocity, and their ranges are both 8.5 m (including cable lengths). Further, the azimuth angle of Target-I and Target-II are approximately  $-5^\circ$  and  $-20^\circ$ , respectively. During the experiment, one transmitter and one receiver antenna were again used, so all received signals for MIMO configuration, realized as stop and go, are recorded. The experiment is repeated for each change of antenna position and each movement of the target. In order to decrease the effort, the chirp duration ( $T_c$ ) is chosen as 1.25 ms (causes 1.5 cm movement of Target-II due to its 12 m/s velocity), and, in total, each transmitter sends 6 chirps, as illustrated in Figure 3.20 (b). Therefore, the total frame time ( $T_f$ ) is 7.5 ms, resulting in a total movement of 9 cm for Target-II. Target-II is moved by using a linear positioner. Initially, Target-II is shifted by 1.5 cm to a new position. Once it reached this point, radar signals are



(a)



(b)

Figure 3.20: (a) Radar setup for velocity estimation, (b) chirp and frame durations.

transmitted, and the reflected echoes are captured. Following the receiving of these echoes, Target-II is relocated, and the radar operation is resumed when Target-II settles at the subsequent position.

As it is well known, the duration of the chirp affects the maximum detectable speed which can be measured ( $v_{max} = \frac{\lambda}{4T_c}$ ) and the frame duration determines velocity resolution ( $v_{res} = \frac{\lambda}{2T_f}$ ). Hence, depending on chirp and frame durations, the velocity resolution and maximum measurable velocity are calculated as 10 m/s and 30 m/s, respectively. It is noted that different information was embedded into LFM signals in each frame.

Experimental results are presented in Figure 3.21. In the range-velocity-angle plot, the direct signal, the two targets and the wall can all be seen clearly. When the angle-velocity cut is examined at a range of 8.5 m as shown in Figure 3.21(b), the targets' angles and velocities are correctly derived. As expected, the measured angular and velocity resolutions are  $15.5^\circ$  and 9.4 m/s, respectively. Although the corner reflectors were made of the same material and have

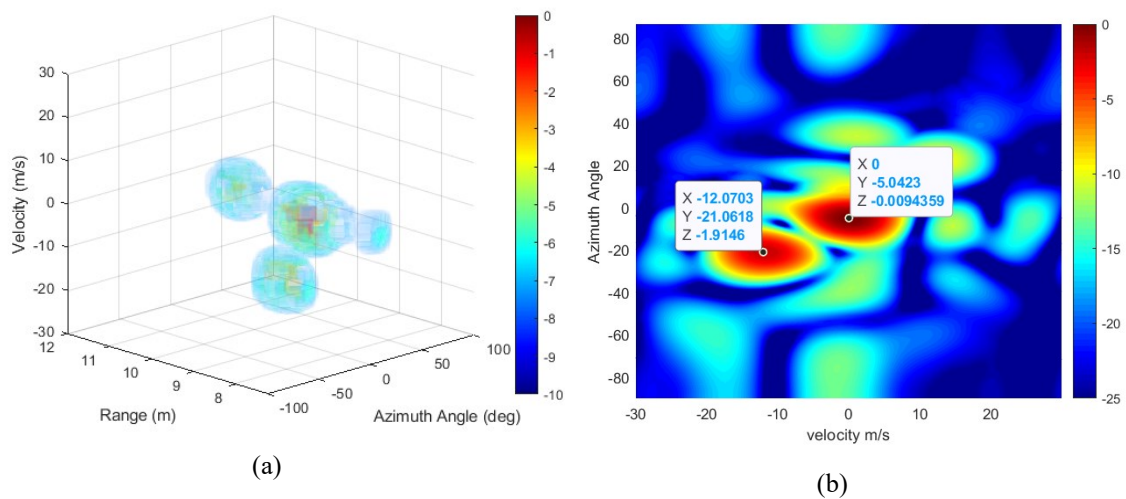


Figure 3.21: (a) Experimental result of range-velocity-angle. (b) Azimuth angle-velocity cut when range is 8.5 m.

the same size, there is roughly a 2 dB power difference between their echo responses. It is not clear why this might be so but could be related to manufacturing differences.

### 3.7 Conclusion

In this chapter, I have shown that a dual-mode MIMO waveform can be designed consistent with the parameters anticipated for the future automotive radar systems whilst simultaneously providing high data rate. However, data rate can be varied as a function of the sub-unit duration, sweep time, PRI, the size of the PSK constellation and the number of transmitters operating, which in its turn depends on waveform orthogonality. CDM is better in terms of data rate, though orthogonality is not as good as in TDM and gives rise a slightly higher background level as can be observed in the range-Doppler maps. The radar and communication performances of the methods have been investigated by simulation and experiments. It was shown that the range and angular resolution in both simulation and experiments agree well, though the range-angle map results differ mostly in terms of sidelobe positions potentially due to multipath effects in small laboratory setting. Additionally, moving target detection was experimentally implemented using a 13-bit Barker code PSK-LFM in a MIMO configuration where all the transmitters were active simultaneously, and the targets' positions and relative velocities were obtained with high accuracy.

# Chapter 4 – Sparse MIMO Antenna Designs

## 4.1 Introduction

A two-dimensional MIMO radar allows estimation of azimuth and elevation angular positions of separate targets or individual scatterers of extended targets within the imaged radar scene. Typically, the physical array elements in the Tx and Rx arrays are distributed in a way to provide a half-wavelength distance between adjacent virtual elements in MIMO beamforming process. The main issue for a 2-D MIMO consisting of a uniform virtual planar array, is that it requires a very high number of antenna elements when high angular resolutions are needed. Therefore, it is desirable to reduce the number of elements by thinning the array, yet keeping the aperture dimension the same by retaining the edge elements and reducing and repositioning inner elements within the array. Ultimately, the thinning of the array reduces power consumption, cost and weight of the antenna. The sparse/thinned phased arrays and 1-D MIMO concepts have been extensively studied in the literature, but sparsity in 2-D MIMO has been little explored.

Whilst retaining the extreme edge elements, thinning the other antenna elements provides the required angular resolution, but randomly positioned antenna elements may lead to grating lobes that drastically limit the detection capability. Hence, the positions of the antenna elements must be chosen carefully. The exhaustive search can be performed when there are few

potential solutions for the available positions of the antenna elements. However, it is nearly impossible to look through all potential solutions when the search space is large. This kind of problems can be approached using a heuristic approach. The heuristic approach allows derivation of acceptable solutions without going through all possible solutions for the given problem. In this way, the approach does not guarantee to give the best solution, but it reaches a good solution faster than a trial and error method.

In this chapter a methodology for optimizing the positions of the elements of sparse MIMO arrays is proposed and examined. This methodology is based on stochastic optimisation techniques and has the goal of minimizing the sidelobe level (SSL) whilst keeping the beamwidth constant and consistent with the size of the virtual receive array. The fundamentals of genetic algorithms and simulated annealing together with the implementation of these algorithms in order to optimise the position of the antenna elements are explained.

For the sake of the completeness, this chapter begins with a sparse 1-D MIMO and moves on to a sparse 2-D MIMO array. The computational benefits of pre-defined initial positions of the array are discussed and results are presented to illustrate performance potential.

The rest of this chapter is organised as follows. A literature review for sparse/thinned antenna is presented in Section 4.2 and the mathematical description of thinned 1-D and 2-D MIMO antenna operation is included in Section 4.3. Both simulated annealing and genetic algorithm with their steps are explained in Section 4.4, and the results using a simulation are shown in Section 4.5. Discussion and conclusions are in Section 4.6.

It is noted that part of this work has been presented at the 2023 EURAD conference in Berlin, Germany [89].



## 4.2 State of the Art

Even though the idea of array thinning can be traced back to the 1960s [90], [91], [92], [93], the challenge related to the inherent increase of the sidelobes, the appearance of grating lobes and the potential worsening of angular resolution should still be addressed and different solutions assessed. Several heuristic approaches such as genetic algorithm [94], [95], [96], particle swarm optimisation [97], [98], [99], simulated annealing [100], [101], differential evolution [102], [103], ant colony optimization [104], and hybrid algorithms [105], [106] have been reported in the literature to find suitable positions of antenna elements for designing thinned linear, planar arrays and 1-D MIMO antennas. In the research presented here, genetic algorithms and simulated annealing, commonly used among such approaches, are also used.

Simulated annealing was proposed by Kirkpatrick et. al in [100] and has been used in a variety of problems such as the travelling salesman problem, scheduling, and digital image processing. In [101] simulated annealing has been used for an unequally spaced linear phased array antenna positions to reduce the peak sidelobe level. Another example with optimisation of antenna positions and their amplitude weightings was implemented for an asymmetrical linear array [107]. In [108], thinned linear and planar arrays with low peak sidelobe levels were designed. In a symmetrical linear array, the optimisation was done over a uniform linear array of 200 elements with  $\lambda/2$  spacing, and as a result, -23.1 dB peak sidelobe levels were obtained [108]. With regard to a symmetrical 2-D thinned array, a uniform 10 x 20 planar array with half-wavelength spacing was thinned, and -24.4 dB peak sidelobe level was achieved [108]. Simulated annealing has also been used to optimise amplitude and phase distributions of the remaining antenna elements in the case of failure of a single element in the uniform linear array [109].

Simulated annealing has been applied in the design of thinned MIMO arrays. In [110], the authors aimed to reduce the number of matched filters of 1-D MIMO with 4 Tx x 16 Rx elements. Simulated annealing was applied to decide both the antenna positions and the amplitude weightings. In [111], cyclic difference sets were inserted to the searching part of the simulated annealing in order to obtain the optimal positions of elements in a 1-D thinned MIMO antenna. The optimal thinned 1-D MIMO antenna positions were determined as a function of the required beamwidth and acceptable sidelobe levels using a hybrid method based on a combination of a genetic algorithm and simulated annealing in [106].

With regard to the genetic algorithm (GA), Holland [112] proposed that the antenna element positions of aperiodic linear arrays are optimised using a GA in order to suppress grating lobes and reduce overall SLLs in [94], [96], [113], [114]. R. L. Haupt et. al. has used a GA to thin a 50-element linear array, achieving -21.98 dB peak sidelobe level [94]. In [95], a 20x10 element planar array has been thinned using a GA, and with just 108 elements (54% filled), -20.07 dB and -19.76 dB peak SLLs have been obtained in  $\phi = 0^\circ$  and  $\phi = 90^\circ$  angles, respectively. Optimal antenna configurations and weights of planar array elements have been found using an enhanced GA in [115], whereas antenna thinning has been done in a planar array to get lower sidelobe using a modified GA in [116]. In [117], a Hadamard matrix and a GA have been combined to achieve the lowest sidelobe level in a thinned planar array. It was decided which antenna elements are active by using the Hadamard matrix, whereas the inter-element spacings have been optimised in both the  $x$ - and  $y$ - axes using the GA. Both linear and planar antenna arrays have been thinned using a GA [118].

In [119], the excitation coefficient values of an 8-elements uniform linear array with half-wavelength spacing antenna have been determined using a GA. By holding the spacing between the antenna elements to a half-wavelength, either amplitude or amplitude & phase

weighting have been applied to both linear and circular arrays [120]. As a result, -36.02 dB and -29.16 dB relative SLLs were achieved by amplitude weighting whereas -23.82 dB at  $60^\circ$  and -24.88 dB at  $11.25^\circ$  was obtained via both amplitude and phase weightings for a 30-element linear array and circular array, respectively. Amplitude weighting coefficients have been obtained for different uniform linear arrays using a GA, and it has been found that the GA creates better relative SLLs than, say, a Chebyshev weighting [121]. Both amplitude and phase weighting values have been found via application of a GA in the case of failure of single or multiple antenna elements in a linear array [122].

In some applications, it is required to place nulls into the antenna pattern, in the direction of sources of interference. In order to reach this aim, the optimal phase weighting vector of the adaptive antenna has been found by applying a GA [123]. On the other hand, in [124], researchers have claimed that the null points may prevent the detection of pedestrians or obstacles. To overcome this issue, a null-filling antenna for automotive radar has been proposed. Here, the amplitude weightings using a GA have been determined in order to design an array pattern which does not include any nulls between  $\pm 40^\circ$  [124]. In [64], [125], [126], the number of active elements and their weights (over time) have been found by applying a GA to obtain different sidelobe levels, whereas the main lobe of the array remains stable. Each sidelobe level represents a specific type of data. For example, communication data can be sent via sidelobes on a broadcast basis, while radar detection was achieved using the main lobe of the antenna pattern [64], [125], [126], as mentioned in Chapter 3.

GAs have also been used in thinned MIMO array antenna configurations. 15 transmitters and 16 receivers have been located in one dimension using multiple GAs, and -28.36 dB relative SLL were obtained at  $90^\circ$  angles [127]. Optimal antenna configurations have been achieved using a GA applied to the design of a 1-D thinned MIMO with 2 transmitters

and 3 receivers. The designed antenna configuration has been fabricated and tested at 77 GHz [128] and [129]. In [130], the antenna positions of a conformal MIMO radar antenna, consisting of 3 transmitters and 8 receivers has been determined via a GA. Simulated and experimental results at 76.5 GHz with 2 GHz bandwidth show good agreement. GAs have been applied in the optimisation of the positions of 3 transmitters and 4 receivers in a sparse 1D MIMO array [131]. In [132], only amplitude weights have been optimised but for a T-shaped MIMO antenna, where an average SLL of -33.7 dB was obtained using a GA and -41.5 dB using a chaotic GA with 10 transmitters and 10 receivers. In [133] 4 transmitters and 8 receivers have been placed in a 2-D MIMO using a GA at 76.5 GHz. Peak SLL, azimuth and elevation resolutions have been obtained as -6.75 dB, 8° and 5.9°, respectively. Moreover, comparison between simulation and measured ambiguity functions have been made, and it can be seen that there is very good agreement.

As it can be seen from the literature review above, while the thinned/sparse linear and planar phased arrays and thinned/sparse 1-D MIMO arrays have been extensively examined, sparsity in 2-D MIMO array has received less attention. In this chapter, for the sake of the completeness, firstly optimisation of a thinned 1-D MIMO array is considered, followed by the optimisation of a thinned 2-D MIMO array. The main aim of this chapter is to investigate the effect of optimal choice of initial parameters on the convergence of the optimization methods in thinned 2-D MIMO arrays with an acceptable sidelobe level and the desired angular resolutions. Hence, the allowable antenna positions can be arranged instead of searching all the planar positions, so that the required time to find the optimal antenna positions in the thinned MIMO can be decreased. To show the performance of the proposed approach, multiple 2-D MIMO arrays are designed by using different number of transmitters and receivers but keeping the total number of antenna elements same in each case.

## 4.3 Thinned MIMO Array

A sparse MIMO array is an antenna that uses fewer elements than a conventional MIMO array to achieve the same angular resolution. In this section, a mathematical description of both thinned 1-D and thinned 2-D MIMO arrays is given, which explains the conventional MIMO concepts building on the MIMO fundamentals presented in Chapter 2.

### 4.3.1 Thinned 1-D MIMO Array

Assume a thinned 1-D MIMO array has  $N_T$  transmit and  $N_R$  receive antenna elements where the antenna elements are positioned on the  $x$ -axis, as illustrated in Figure 4.1(a). The transmit and receive steering vectors,  $\mathbf{a}_{1-D}(\theta)$  and  $\mathbf{b}_{1-D}(\theta)$  respectively, for a far field target at azimuth angle  $\theta$  are given by equations (4.1) and (4.2).

$$\mathbf{a}_{1-D}(\theta) = \left[ e^{-jkx_{T_1}\sin\theta} \ e^{-jkx_{T_2}\sin\theta} \ \dots \ e^{-jkx_{T_{N_T}}\sin\theta} \right]^T \quad (4.1)$$

and

$$\mathbf{b}_{1-D}(\theta) = \left[ e^{-jkx_{R_1}\sin\theta} \ e^{-jkx_{R_2}\sin\theta} \ \dots \ e^{-jkx_{R_{N_R}}\sin\theta} \right]^T \quad (4.2)$$

where  $k = 2\pi/\lambda$  is the wavenumber,  $x_{T_n}$  and  $x_{R_n}$  are the  $x$ - coordinates of  $n$ th transmit and receive antenna element.

The steering vector of the virtual array is the Kronecker product of the transmit and receive steering vectors and can be written as below in equation (4.3).

$$\mathbf{v}_{1-D}(\theta) = \begin{pmatrix} e^{-jk(x_{T_1}+x_{R_1})\sin\theta} \\ e^{-jk(x_{T_1}+x_{R_2})\sin\theta} \\ \vdots \\ e^{-jk(x_{T_1}+x_{R_{N_R}})\sin\theta} \\ e^{-jk(x_{T_2}+x_{R_1})\sin\theta} \\ \vdots \\ e^{-jk(x_{T_{N_T}}+x_{R_{N_R}})\sin\theta} \end{pmatrix}_{N_T N_R \times 1} \quad (4.3)$$

and the positions of the virtual array elements are given by

$$\mathbf{l}_{1-D} = \begin{pmatrix} x_{T_1} + x_{R_1} \\ x_{T_1} + x_{R_2} \\ \vdots \\ x_{T_1} + x_{R_{N_R}} \\ \vdots \\ x_{T_{N_T}} + x_{R_{N_R}} \end{pmatrix}_{N_T N_R \times 1} \quad (4.4)$$

The virtual array dimension of the thinned 1-D MIMO is calculated as

$$l_x = \max(\mathbf{l}_{1-D}) - \min(\mathbf{l}_{1-D}) \quad (4.5)$$

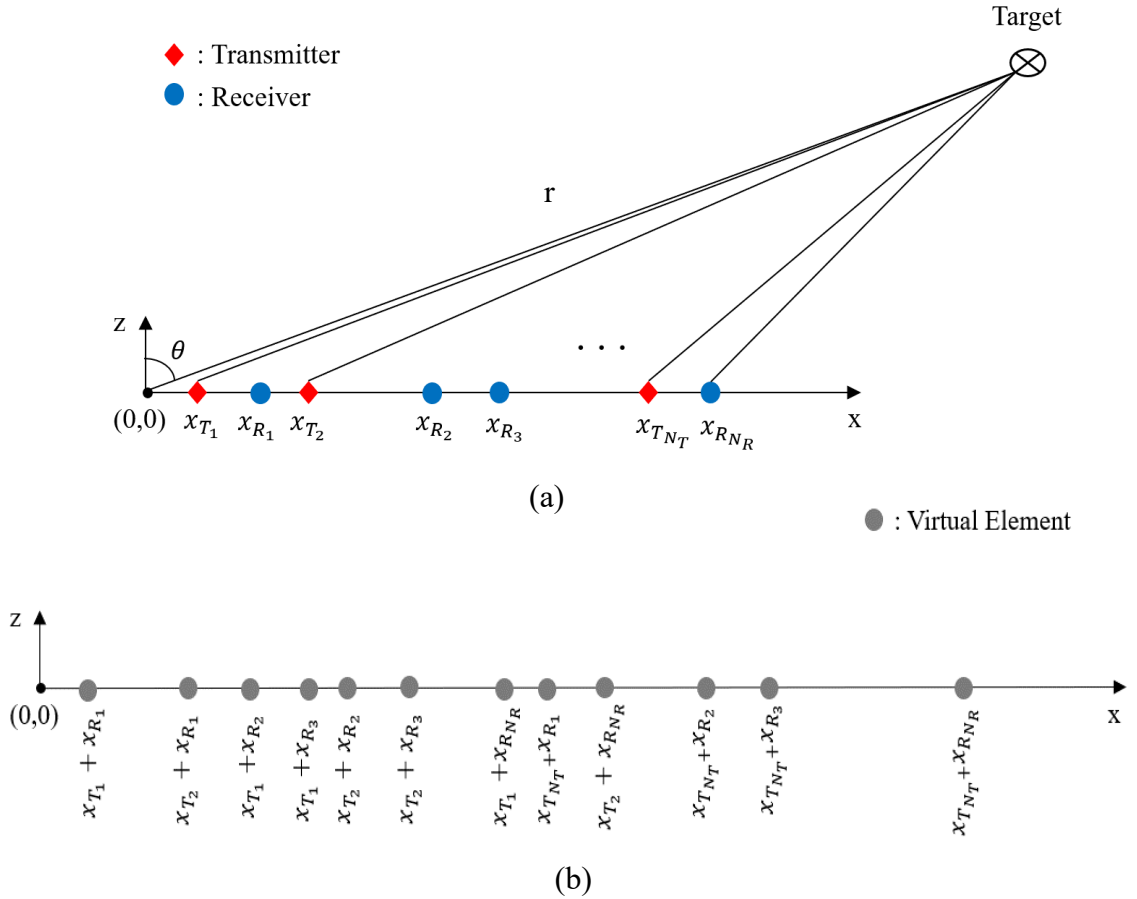


Figure 4.1: (a) An example of thinned 1-D MIMO array configuration, (b) virtual array of (a).

### 4.3.2 Thinned 2-D MIMO Array

A target coordinate is assumed to be  $(r, \theta, \varphi)$  as shown in Figure 4.2(a), where  $\theta$  is the elevation angle,  $\varphi$  is the azimuth angle and  $r$  is the range. It is assumed that target is in the far-field of the antenna, so that the angle to the target for the antenna elements can be considered constant across the co-located MIMO array. The number of transmitter and receiver elements are  $N_T$ , and  $N_R$ , respectively and each antenna element is located in the  $xz$  – plane as shown in Figure 4.2(b). The transmitted signal and the echo signal, from the target, follow slightly different trajectories from each other. Both steering vectors of the transmitted and received signals depend on  $\theta$  and  $\varphi$  as well as the relevant antenna element positions on the  $x$ - and  $z$ -axes. The transmit and receive steering vectors -  $\mathbf{a}_{2-D}(\theta, \varphi)$  and  $\mathbf{b}_{2-D}(\theta, \varphi)$  – can be written as [133]

$$\mathbf{a}_{2-D}(\theta, \varphi) = \begin{pmatrix} e^{-jk(x_{T,1}\sin\theta\cos\varphi+z_{T,1}\cos\theta)} \\ e^{-jk(x_{T,2}\sin\theta\cos\varphi+z_{T,2}\cos\theta)} \\ \vdots \\ e^{-jk(x_{T,N_T}\sin\theta\cos\varphi+z_{T,N_T}\cos\theta)} \end{pmatrix}_{N_T \times 1} \quad (4.6)$$

$$\mathbf{b}_{2-D}(\theta, \varphi) = \begin{pmatrix} e^{-jk(x_{R,1}\sin\theta\cos\varphi+z_{R,1}\cos\theta)} \\ e^{-jk(x_{R,2}\sin\theta\cos\varphi+z_{R,2}\cos\theta)} \\ \vdots \\ e^{-jk(x_{R,N_R}\sin\theta\cos\varphi+z_{R,N_R}\cos\theta)} \end{pmatrix}_{N_R \times 1} \quad (4.7)$$

where  $x_{T,n}$  and  $z_{T,n}$  are  $x$  and  $z$  coordinates of the phase centre of  $n$ th transmit antenna element, respectively and  $n$  is from 1 to  $N_T$ . Similarly,  $x_{R,u}$  and  $z_{R,u}$  are the  $x$  and  $z$  coordinates of the phase centre of the  $u$ th received antenna element, respectively, and  $u$  is from 1 to  $N_R$ .

The steering vector of the virtual array is the Kronecker product of  $\mathbf{a}_{2-D}(\theta, \varphi)$  and  $\mathbf{b}_{2-D}(\theta, \varphi)$ , and can be written as:

$$\mathbf{v}(\theta, \varphi) = \begin{pmatrix} e^{-jk((x_{T,1}+x_{R,1})\sin\theta\cos\varphi+(z_{T,1}+z_{R,1})\cos\theta)} \\ e^{-jk((x_{T,1}+x_{R,2})\sin\theta\cos\varphi+(z_{T,1}+z_{R,2})\cos\theta)} \\ \vdots \\ e^{-jk((x_{T,1}+x_{R,N_R})\sin\theta\cos\varphi+(z_{T,1}+z_{R,N_R})\cos\theta)} \\ \vdots \\ e^{-jk((x_{T,N_T}+x_{R,1})\sin\theta\cos\varphi+(z_{T,N_T}+z_{R,1})\cos\theta)} \\ \vdots \\ e^{-jk((x_{T,N_T}+x_{R,N_R})\sin\theta\cos\varphi+(z_{T,N_T}+z_{R,N_R})\cos\theta)} \end{pmatrix}_{N_T N_R \times 1} \quad (4.8)$$

Hence, the positions of the virtual antenna elements on the  $x$ - and  $z$ - axis are written as [133]

$$\mathbf{l}_{2-D,x} = \begin{pmatrix} x_{T,1} + x_{R,1} \\ x_{T,1} + x_{R,2} \\ \vdots \\ x_{T,N_T} + x_{R,N_R} \end{pmatrix}_{N_T N_R \times 1} \quad (4.9)$$

and

$$\mathbf{l}_{2-D,z} = \begin{pmatrix} z_{T,1} + z_{R,1} \\ z_{T,1} + z_{R,2} \\ \vdots \\ z_{T,N_T} + z_{R,N_R} \end{pmatrix}_{N_T N_R \times 1} \quad (4.10)$$

The dimensions of the virtual aperture in both  $x$ - and  $z$ - directions can be found as [133]

$$l_x = \max(\mathbf{l}_{2-D,x}) - \min(\mathbf{l}_{2-D,x}) \quad (4.11)$$

$$l_z = \max(\mathbf{l}_{2-D,z}) - \min(\mathbf{l}_{2-D,z}) \quad (4.12)$$

The angular resolution – -3 dB beamwidth – of the MIMO array is defined by the effective length,  $L$ , of virtual array,  $\theta_{3dB} \cong 0.88\lambda/L$ . In a thinned 2-D MIMO array, the azimuth and elevation angular resolutions depend on  $l_x$  and  $l_z$ , respectively.



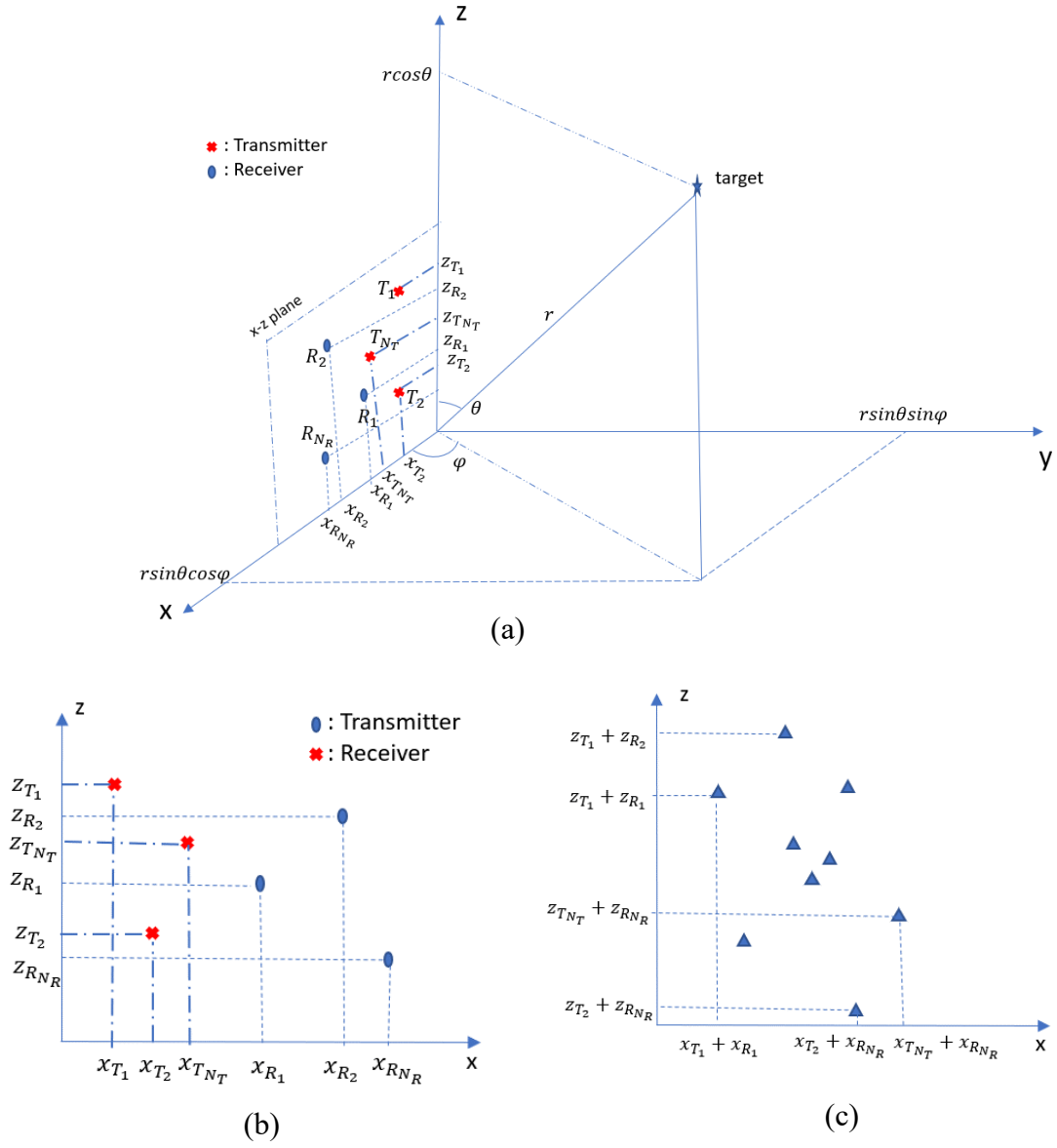


Figure 4.2: (a) Demonstration of 2-D MIMO in spherical coordinate system, (b) an example of thinned 2-D MIMO antenna configuration, (c) the virtual array of (b).

## 4.4 Optimisation Algorithms

### 4.4.1 Simulated Annealing

The principle of the algorithm is analogous to annealing of materials in thermodynamics. While the material is cooling, the temperature should be reduced very slowly to obtain perfect crystals, in other words, crystals with zero entropy. A similar approach is followed in simulated annealing. The simulated annealing (SA) algorithm is an iterative algorithm, and it yields two solutions at each iteration: the current solution and the best solution. For the latter if a solution is accepted as a best solution, it must have a better fitness value than the previous best solution. However, this rule is not valid for the current solution, and a solution may be accepted even if its fitness value is worse than the previous one. In the case of a worse fitness value, the acceptance in the current solution depends on the current temperature ( $T_{current}$ ) and the difference of the current and new fitness values ( $\Delta$ ). If the randomly chosen number between 0 and 1 is lower than  $e^{-\frac{\Delta}{T_{current}}}$ , the solution is accepted as a current solution. When the temperature is high, the acceptance probability in the current solution is high. As the temperature decreases, the probability decreases as well. Therefore, the algorithm mostly accepts the best configurations as it nears its end. Choosing the worse fitness value solution as a current solution can help the algorithm to find the global maxima/minima. Hence, the algorithm cannot be stuck in local maxima/minima.

In this thesis, the antenna configurations are optimised by considering the desired beamwidth, peak-to-sidelobe level and the spacing between the antenna elements. The steps of simulated annealing to obtain the optimal antenna configuration of a thinned 1-D and 2-D MIMO array are explained below. A flow chart of these steps is shown in Figure 4.3.

- 1- Set the number of transmitters and receivers, the allowable antenna positions, the required beamwidths in both azimuth and elevation, acceptable peak-to-sidelobe level (PSLL), desired PSLL, minimum allowable distance between adjacent elements and the cost for each unsuitable element placement. Also, define the initial and final temperatures, temperature step whilst cooling, maximum iteration number at which the code execution is terminated.
- 2- Create, randomly, initial Tx/Rx element positions in the allowed antenna region depending on whether optimising a 1-D or a 2-D MIMO array and calculate the PSLLs at each steering angle.
- 3- Evaluate the fitness value depending on PSLL and the antenna element spacing. The fitness value is evaluated by the following equation

$$fitness_{value} = \sum_{q=1}^{q=N_{scan}} PSLL_{desired} - PSLL_{obtained,q} + penalties \quad (4.13)$$

and

$$penalties = penalty_{HSL} + penalty_{spacing} \quad (4.14)$$

where  $N_{scan}$  is the number of the steering angle,  $PSLL_{desired}$  and  $PSLL_{obtained,q}$  are the desired PSLL and the PSLL of the created antenna positions at the  $q^{th}$  steering angle, respectively.  $penalty_{HSL}$  is given when the obtained PSLL is higher than the acceptable PSLL.  $penalty_{spacing}$ , is given in the case of each inappropriate antenna positions.

- 4- Save the antenna positions as a current and best solution as well as the fitness value as the current fitness value ( $fitness_{current}$ ) and best fitness value ( $fitness_{best}$ ).
- 5- Create a new Tx/Rx antenna configuration by following procedure

- Spin the wheel which has  $N$  sections, the position of one of antenna elements in the current solution is mutated with the probability of  $1 - \frac{1}{N}$ . Otherwise, multiple antenna positions will be changed.
  - The decision as to which type of antenna is mutated – transmitter or receiver - is made by spinning the wheel a second time. Both the transmitter element(s) and receiver element(s) are relocated with an  $N/2$  probability.
  - The selection of antenna element(s) and its/their new position(s) is made randomly.
- 6- Check the spacing between antenna elements. If it is less than the minimum allowable antenna element spacing, give the penalty,  $penalty_{spacing}$ , for each undesired spacing.
  - 7- Check the beamwidth(s) of the new antenna positions at  $0^\circ$  azimuth angle for the 1-D MIMO array and at  $(0^\circ, 0^\circ)$  azimuth and elevation angles, respectively for the 2-D MIMO array. If two or one of them is bigger than the required one, go step 5.
  - 8- Generate the patterns to determine the PSLLs at each scan angle.
  - 9- Evaluate the fitness value of the new antenna positions ( $fitness_{new}$ ) depending on the PSLLs and spacing between antenna elements as in (4.13).
  - 10- Calculate the difference between the current fitness value and the new fitness value ( $\Delta = fitness_{new} - fitness_{current}$ ).
- If  $\Delta < 0$ , then
- The new antenna configuration is accepted as the current solution, and the new fitness value is accepted as the current fitness value.
  - Calculate the difference between the best fitness value and the current fitness value  $\Delta_2 = fitness_{current} - fitness_{best}$ . If  $\Delta_2 < 0$ , accept the current fitness value as best fitness value, and save the antenna elements' positions as a best solution. Otherwise, keep the best solution and its fitness value as it is.

- Repeat steps from 5 with reduced current temperature and increased iteration number until temperature reaches the final value, or the iteration number is larger than the maximum allowed, at which point the algorithm stops.
- If the difference ( $\Delta$ ) is equal to or bigger than 0,
- Calculate  $e^{-\frac{\Delta}{T_{current}}}$  and choose randomly a number between 0 and 1.
    - If the random number is less than the value of exponential expression, the new antenna configuration is accepted as current solution, and the new fitness value is accepted as the current fitness value. Reduce the current temperature and increase the iteration number.
    - Otherwise, keep the current solution and the current temperature as they are. Then, increase the iteration number.
  - If the current temperature is less than the final temperature or current iteration number is bigger than the maximum iteration number, stop the algorithm. Otherwise, go to step 5.

## 4.4.2 Genetic Algorithm

The main inspiration behind the genetic algorithm (GA) comes from the process of natural evolution. Fundamentally, the GA which is an iteration-based algorithm produces multiple solutions at each iteration called a *generation*. These solutions are referred to as a *population* whereas each solution is called an *individual*. Each individual in the population has a unique *cost/fitness value* based on its *gene* sequence, and this *cost/fitness value* indicates how suitable it is for the problem, in our case the design of an antenna. *Genes* of each individual are expressed using binary codes, where "1" denotes "on" and "0" denotes "off" in the design of the antenna.

**Flow chart of Simulated Annealing**

```

graph TD
    Start([Start]) --> Determine[Determine  
• Radar parameters (fc, baw etc.)  
• Transmitter/Receiver numbers  
• Minimum spacing between antenna elements (d_min)  
• Desired beamwidths (θ_3dB, φ_3dB)  
• Initial and finish temperature with steps  
• Maximum iteration number (different from T_length)]
    Determine --> CreateFirst[Create first Tx/Rx antenna positions and calculate Δ_new]
    CreateFirst --> SaveCurrent[Save Δ_new as current solution  
Δ_new as best solution  
its antenna positions]
    SaveCurrent --> CreateNew[Create a new antenna positions]
    CreateNew --> CalculateBeam[Calculate the obtained beamwidths]
    CalculateBeam --> CheckBeam{θ_new = θ_3dB  
φ_new = φ_3dB}
    CheckBeam -- Yes --> GivePenalty[Give penalty for each unallowed  
spacing and high sidelobe levels]
    GivePenalty --> CalculateFitness[Calculate the new fitness value (Δ_new)]
    CalculateFitness --> CheckDelta{Δ = Δ_new - Δ_current ≤ 0}
    CheckDelta -- Yes --> SaveNew[Save the Δ_new as Δ_current  
the antenna pos. as current pos.]
    CheckDelta -- No --> CheckTemp1{Δ_current - Δ_best < 0}
    CheckTemp1 -- Yes --> SaveBest[Save the Δ_current as Δ_best  
the antenna pos. as best pos.]
    CheckTemp1 -- No --> ReduceTemp1[Reduce the temperature  
Increase the iteration number]
    SaveNew --> CheckTemp2{e^(-Δ/T_current) > rand(1)}
    CheckTemp2 -- Yes --> SaveCurrentPos[Save the Δ_new as Δ_current  
the antenna pos. as current pos.]
    CheckTemp2 -- No --> CheckTemp3{T_current > T_finish  
Or N_itea > N_itea_max}
    CheckTemp3 -- Yes --> Finish1([Finish])
    CheckTemp3 -- No --> CheckDelta
    ReduceTemp1 --> CheckTemp3
    
```

The flow chart illustrates the Simulated Annealing process for antenna position optimization. It begins with determining radar parameters, transmitter/receiver numbers, minimum spacing, desired beamwidths, initial/finish temperatures, and maximum iterations. The process then creates the first Tx/Rx antenna positions and calculates the initial fitness value  $\Delta_{new}$ . This value is saved as the current solution and the best solution. A new antenna position is created, and its beamwidths are calculated. If the new position satisfies the beamwidth constraints ( $\theta_{new} = \theta_{3dB}$  and  $\phi_{new} = \phi_{3dB}$ ), a penalty is given for unallowed spacing and high sidelobe levels. The new fitness value  $\Delta_{new}$  is calculated, and if it is less than or equal to the current fitness value  $\Delta_{current}$ , it is saved as the current solution. If not, the process checks if the current fitness value is less than the best fitness value  $\Delta_{best}$ . If yes, it is saved as the best solution. If no, the temperature is reduced, and the iteration number is increased. The process then checks if the new position is accepted based on the Metropolis criterion ( $e^{-\Delta/T_{current}} > rand(1)$ ). If yes, it is saved as the current solution. If no, it checks if the temperature is greater than the finish temperature  $T_{finish}$  or the iteration number is greater than the maximum iteration number  $N_{itea\_max}$ . If yes, the process finishes. If no, it continues to calculate the new fitness value.

106

The GA seeks to produce better individuals at each generation through cross-over, mutations, and in the selection part it aims to select fitted individuals to enhance the average cost value of the population. *Crossover* is a combination of two individuals in the current population called *parents*. The genes of the parents are exchanged after the crossover point to produce new individuals referred to as *offspring*. The crossover point is usually a single point, but there may be more than one. A representation of the single-point crossover is demonstrated in Figure 4.4(a). *Mutation* causes a random change in the sequence of the gene after the crossover as illustrated in Figure 4.4(b). The mutation of each bit (gene) depends on probability, so one or more multi-bits can be mutated, or none of them are mutated. Mutations can help to escape from local optimal solutions and reach a global optimal solution, whereas crossover increases the diversity in the population. With regard to the *selection* part, some of the individuals from the current population are selected and passed to the next generation whereas the remaining individuals in the current population are discarded. The selected individuals may include best fitted individuals in the population to obtain better ones compared to previous generation.

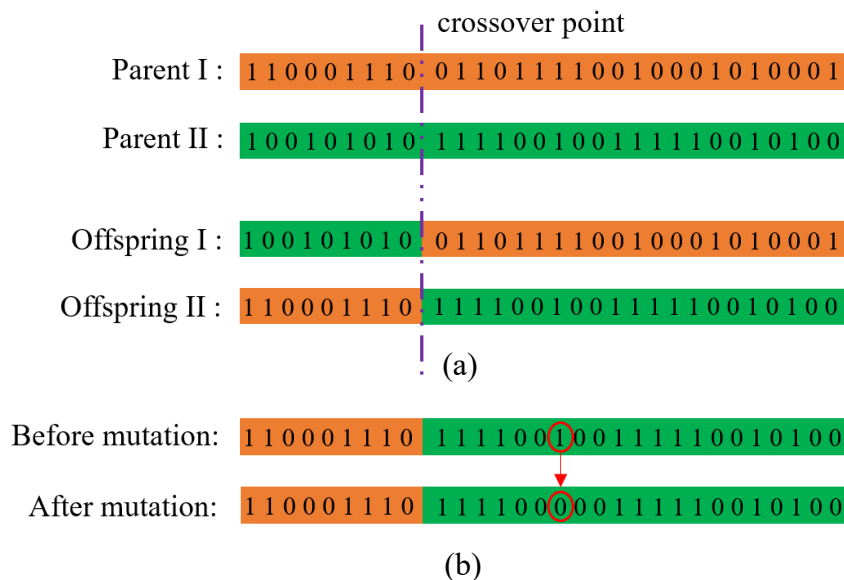


Figure 4.4: A representation of (a) crossover operator, (b) mutation operator.

When there is no restriction in the number of antenna elements, in other words, their number is not stable, the crossover and mutation operators can be implemented as illustrated in Figure 4.4. However, when a stable number of antenna elements are required in the antenna design, the methods in Figure 4.4 may not work because it is almost impossible to hold the number of antenna elements stable in this way. To keep the number of antenna elements stable, a slightly different method for crossover and mutation is proposed in this thesis. A matrix is created whose size is equal to the total number of antenna elements. If the designed antenna is a 1-D array, the matrix size is  $(1 \times N_{tot})$  where  $N_{tot}$  is the total number of antenna elements whereas if the antenna is a 2-D array, the matrix size becomes  $(2 \times N_{tot})$ . In the matrix, incrementation from 1 to  $N_T$  includes the positions of the transmitters and from  $N_T + 1$  to  $N_{tot}$  indicates the positions of the receive elements. Each potential element position has a unique number, and the position of each element is indicated using the assigned unique number. Regarding mutation, the mutated antenna element is randomly allocated in a new position. Hence, the number of antenna elements becomes stable in both the crossover and the mutation parts.

The steps taken by the genetic algorithm for optimising the element positions in both of the thinned 1-D and 2-D MIMO arrays are explained below.

- 1- Set the number of transmitters and receivers, the allowable range of element positions, the required beamwidths in both azimuth and elevation, acceptable peak-to-sidelobe level (PSLL), desired PSLL, minimum allowable distance between adjacent elements and the cost for each unsuitable element placement. Also, define the maximum allowable generation number, the total number of individuals in the population for each generation ( $p$ ), the number of crossovers at each generation ( $c$ ) and mutation rate for each gene ( $P_m$ ).



- 2- Create, randomly, element positions for each individual in the initial population, and evaluate the cost/fitness value of each individual based on their spacing and the PSLLs at each steering angle. The fitness value can be calculated as below.

$$fitness_{value} = \sum_{q=1}^{q=N_{scan}} PSLL_{desired} - PSLL_{obtained,q} + penalties \quad (4.15)$$

and

$$penalties = penalty_{HSL} + penalty_{spacing} \quad (4.16)$$

where  $N_{scan}$  is the number of the steering angle,  $PSLL_{desired}$  and  $PSLL_{obtained,q}$  are the desired PSLL and the PSLL of the created element positions at the  $q^{th}$  steering angle, respectively.  $penalty_{HSL}$  is given when the obtained PSLL is higher than the acceptable PSLL.  $penalty_{spacing}$ , is given in the case of each inappropriate antenna positions.

- 3- Select the individuals from the current population as parents for crossover, and produce offspring by deciding the single or multi crossover points.
- Check that the antenna positions of the offspring are the same as any individual in the current population. If there is an individual who has the same element position, choose new parents and apply crossover. If not, move to the next step.
- 4- Send the whole created (2c) offspring to the mutation part and apply mutation with a probability of  $P_m$ .
- Check that the antenna positions of the mutated individual are the same as any individual in the current population. Apply a new mutation till you get a different element position from the existing population if there is an individual with the same element positions.

- 5- Check the beamwidth(s) of the new individuals at  $0^\circ$  azimuth angle for 1-D MIMO and at  $(0^\circ, 0^\circ)$  azimuth and elevation angles, respectively for 2-D MIMO array. If two or one of them is bigger than that required, go to step 3.
- 6- Check the spacing between antenna elements. If it is less than the minimum allowable antenna element spacing, give the penalty,  $penalty_{spacing}$ , for each undesired spacing.
- 7- Generate the patterns to determine the PSLs at each scan angle, and then evaluate the cost/fitness value of new individuals using (4.15).
- 8- At this stage, the current population has  $p + 2c$  individuals, and it needs to be reduced to  $p$  for the next generation. Therefore, select the individuals from the grown-population as a new population. Most of the individuals are selected according to their fitness values, but a few individuals are selected randomly in order to not ignore the possibility of obtaining better individuals from them. It is noted that unselected individuals are discarded, so the total number of individuals in the new population is same as the initial population.
- 9- If there is at least one acceptable individual from the new population or the generation number reaches the maximum, finish the algorithm. Otherwise, go step 3 by increasing the generation number.

## 4.5 Simulation Results

### 4.5.1 Optimisation results of 1-D Thinned MIMO

In this subsection, the optimal thinned 1-D MIMO array configurations which have been obtained via the simulated annealing and genetic algorithm are examined. In both optimisation techniques, 5 transmitters (Tx) and 8 receivers (Rx) are used with the aim of achieving, roughly, a  $1.2^\circ$  beamwidth at 77 GHz. The maximum aperture length for both Tx and Rx antenna

positions is set at  $32\lambda$ , and the available positions are adjusted based on a  $\lambda/8$  spacing. The minimum allowed spacing between the antenna elements is  $\lambda/2$ . The desired and highest acceptable sidelobe levels are -12 dB and -6 dB, respectively. After generating the pattern, the value of peak SLL is evaluated at every angle between  $\pm 30^\circ$ . It is noted that the same optimisation is used to analyse different angles. The penalties that were empirically chosen and applied in both optimisation techniques are the same – “5” for each inadequate antenna element spacing and “10” when the radiation pattern of the thinned MIMO has an unacceptable PSLL.

In simulated annealing, the initial temperature should be chosen high and should be reduced very slowly as mentioned above, so the initial and finish temperatures are 3000 °C and 20 °C, respectively. The temperature rise is chosen as 0.995, so there are 1000 temperature levels, allowing for a maximum of 1000 acceptable antenna configurations. The maximum number of iterations is set as 15k. It means that the code will terminate after reaching either 1000 acceptable solutions or 15k iterations.

In Figure 4.5, the optimisation outcomes of applying simulated annealing are shown. Figure 4.5(a) illustrates the obtained fitness function (FF) values for each accepted current solution. There are 524 acceptable current solutions when the algorithm completes its maximum iteration number – 15k, and it is clear that the value of the FF enhances as the algorithm gets closer to the end of the available solutions. The optimal antenna configuration obtained at the end of the iterations and its virtual array configuration are demonstrated in Figure 4.5(b). The positions of the thinned MIMO antenna elements are written in Table 4.1. The size of the corresponding virtual array on the  $x$ -axis is  $42.25\lambda$  which gives angular resolution of  $1.3^\circ$  on boresight. Example radiation patterns of the thinned MIMO at  $0^\circ$  and  $-30^\circ$  scan angles are shown in Figure 4.5(c) and (d), respectively. The obtained PSLLs are approximately -11.5 dB

in both cases. Furthermore, when the radiation patterns at other scan angles between  $\pm 30^\circ$  were analysed, it was found that the PSLL value varies from -10.5 dB to -11.89 dB.

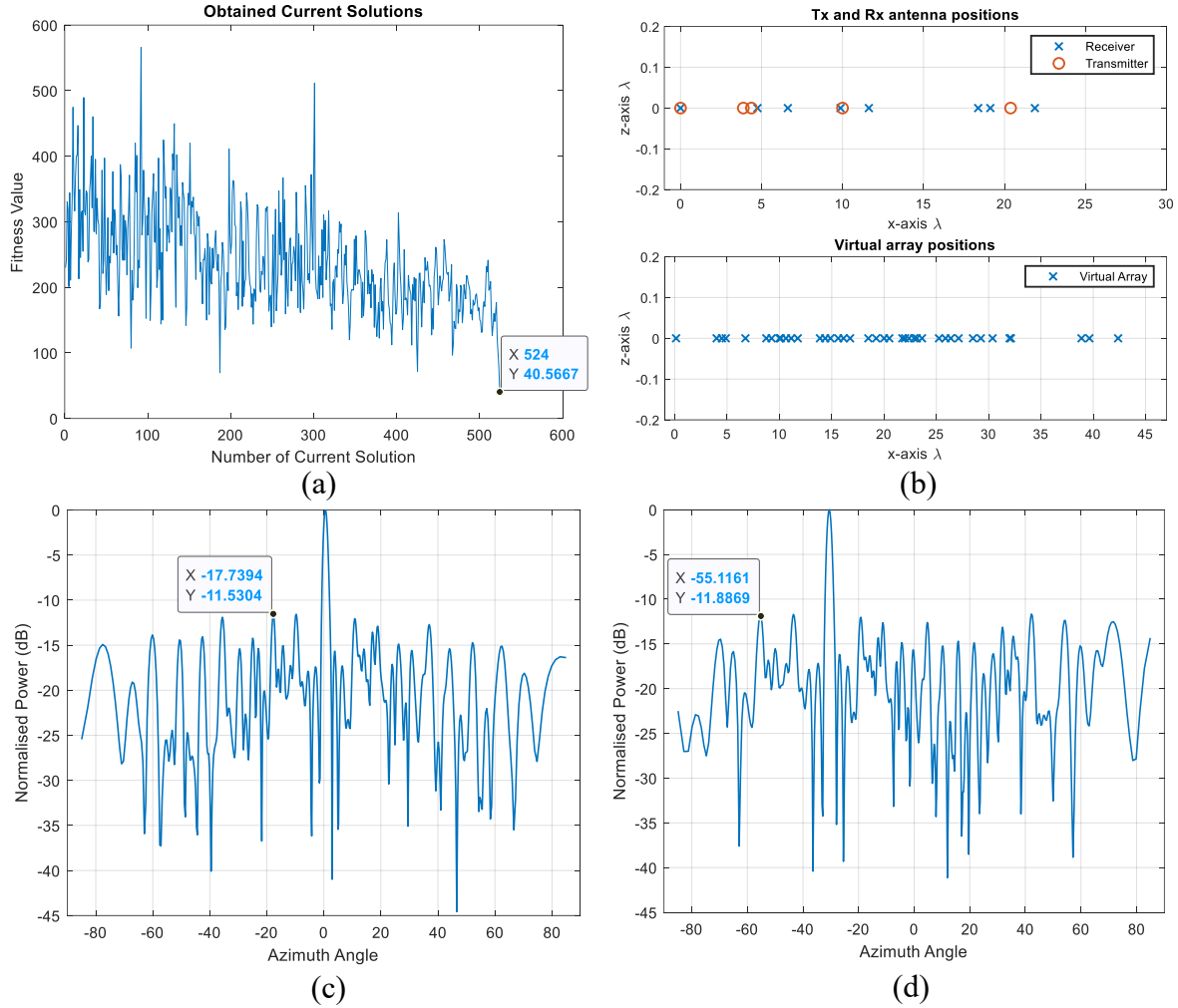


Figure 4.5: The simulated annealing results (a) fitness function response versus number of current solutions, (b) configuration of optimised thinned 1-D MIMO array, (c) the radiation pattern at  $0^\circ$  scan angle, (d) radiation pattern at  $-30^\circ$  scan angle.

Table 4.1: Optimised 1-D MIMO array using simulated annealing

	Value(s)
Transmitter positions	$[0, 3.875, 4.375, 10, 20.375] * \lambda$
Receiver positions	$[0, 4.75, 6.625, 9.875, 11.625, 18.375, 19.125, 21.875] * \lambda$
Peak sidelobe level	-11.5 dB
Obtained -3 dB beamwidth	$1.3^\circ$

In applying the genetic algorithm, the initial population number and maximum generation (iteration) number are empirically chosen as 24 and 1200, respectively. The cross-over number is 15 at each generation, which means that 30 different offspring are obtained, and then these offspring are mutated with a 0.05 probability in the mutation part. At this stage, the population number reaches to 54. After calculating the new individuals' fitness function values, whole population is sent to selection part. Here, depending on their FF values the 14 best individuals are selected and 10 individuals are randomly selected from the rest of the population with other individuals discarded. Hence, the number of individuals in the population remains stable at each generation whereas the best individuals are kept over the generations.

Figure 4.6 shows the optimisation results of the genetic algorithm applied to determine the optimal positions of the thinned 1-D MIMO antenna with 5 Tx and 8 Rx elements. The FF values obtained at each generation are shown in Figure 4.6(a). As can be observed there are two FF values for each generation with the red value representing the best FF value at that generation and the blue value being the mean FF value for the entire population at that generation. The improvement in the average FF value over the generations is obvious – the value starts at about 360 and continues to about 80 after 200 generations. The same trend is also followed by the FF value of best individual at each generation. The best individual at the first generation has an approximate value of 140 FF and its FF value improves to 40 after around 160 generations. This FF value is the best during the entire generation process – 1200 generations. The optimal antenna configuration obtained via the genetic algorithm and its virtual array configuration are shown in Figure 4.6(b). The positions of the thinned MIMO antenna elements are shown in Table 4.2. The radiation patterns of the thinned MIMO at  $0^\circ$  and  $10^\circ$  scan angles are shown in Figure 4.6(c) and (d), respectively. This antenna

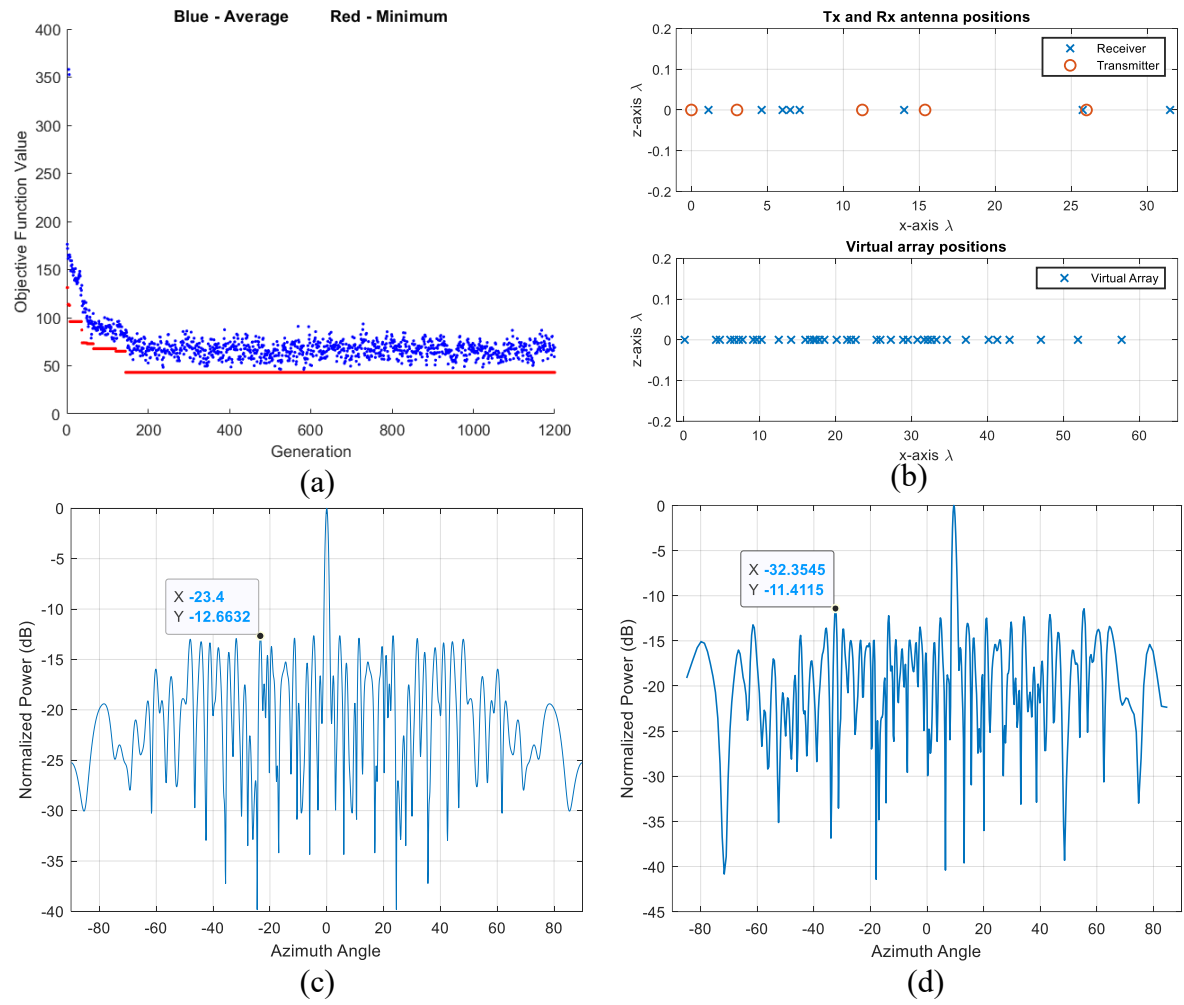


Figure 4.6: The genetic algorithm results (a) fitness function response versus generation, (b) configuration of optimised thinned 1-D MIMO array, (c) the radiation pattern at 0° scan angle, (d) radiation pattern at 10° scan angle.

Table 4.2: Optimised 1-D MIMO array using genetic algorithm

	Value(s)
Transmitter positions	$[0, 3, 11.25, 15.375, 26] * \lambda$
Receiver positions	$[1.125, 4.625, 6, 6.5, 7.125, 14, 25.75, 31.5] * \lambda$
Peak sidelobe level	-12.6 dB
Obtained -3 dB beamwidth	1.2°

configuration gives PSLLs of approximately -11 dB at each scan angle between  $\pm 30^\circ$  while providing an angular resolution of  $1.2^\circ$  on the boresight.

The outcomes from the optimized antenna configurations, obtained through the utilization of simulated annealing and genetic algorithms, exhibit notable similarity in the PSLLs achieved, despite variations in the position of the antenna elements. However, the initial population in the genetic algorithm has a significant impact on subsequent generations. In other words, if the initial population consists of individuals which have finer fitness values, the optimum solution may be achieved faster. These individuals give the algorithm a good start and help the algorithm converge faster towards the optimal solution. On the other hand, if the fitness values of the initial population are poorer, the algorithm may take more time to reach the optimal solution. This means that the algorithm will need more time and generations to search and improve solutions, as it has to overcome the disadvantageous starting point. Therefore, the initial population should be carefully chosen when applying a genetic algorithm. To generate an initial population that increases the algorithm's efficiency and quality of solutions, a diverse population may be created, or one of the heuristic approaches may be applied, as in [106]. On the other hand, simulated annealing typically operates on a single solution at a time, unlike genetic algorithms that maintain a population of individuals. Therefore, the convergence to the acceptable solution may be reached faster. Moreover, the algorithm has the capability to overcome local maximas and minimas by accepting worse solutions as current solutions during the search process. This allows it to eventually converge to the best solution, providing a favourable outcome at the end of the method.

The choice between SA and GA depends on the nature of the optimisation problem. SA is advantageous when the search space is rugged, containing many local optima, or when finding a global optimum is essential. SA's ability to escape local optima and explore a wide range of

solutions makes it suitable for such problems. On the other hand, GA is advantageous when the search space is complex, with discrete or combinatorial variables, or when maintaining diversity in solutions is critical. GA's population-based approach allows it to explore a diverse range of solutions and potentially find a global optimum.

Consequently, in the subsequent section, only simulated annealing is utilised for the reasons mentioned above.

## 4.5.2 Optimisation results of 2-D Thinned MIMO

In this section, optimal 2-D MIMO antenna configurations are examined to determine if there are better initial positions for the antenna elements, which would lead to faster convergence for the thinned MIMO array design. This is especially in the case of a larger number of elements. In this specific case considered here, the required angular resolutions in both azimuth and elevation angles is 5 degrees, and the total number of antenna elements is 24. Multiple antenna designs are examined using different numbers of Tx and Rx, but the total antenna number is 24. The Tx number is changing from 2 to 12, and accordingly, the Rx number is decreasing from 22 to 12.

To produce a 5 degree beamwidth in both dimensions the 22 Tx x 22 Rx an L-shaped MIMO array with half-wavelength spacing is used. Here, the same angular resolutions within the acceptable sidelobe levels are obtained by using almost half of the antenna elements of the L-shaped MIMO configuration. The simulated annealing approach will be used to find optimal configurations with all the potential ratios of numbers of Tx and Rx elements: 2 Tx x 22 Rx, 3 Tx x 21 Rx and 4 Tx x 20 Rx antennas and so on, until 12 Tx x 12 Rx due to a reciprocity in MIMO pattern for the same ratio of Tx/Rx and Rx/Tx.



The choice of the starting temperature is made to improve the convergence rate to the optimal solution. The increment should be small enough to avoid significant fluctuations during the annealing. I have used a starting temperature of  $T=5000$  °C and finishing temperature of  $T=1.5$  °C, and the temperature increment is chosen as 0.998. Hence, there are 4050 temperature levels, which means, a maximum of 4050 acceptable antenna positions can be obtained. The maximum iteration number is chosen as 50000. In other words, the code will stop when it reaches either 4050 acceptable results or 50000 iterations.

The maximum aperture size is chosen as  $6\lambda \times 6\lambda$  for the transmitters and receivers. Moreover, the available positions are adjusted based on a  $\lambda/8$  spacing, so the antennas can be placed on  $49 \times 49$  available points in a 2-D plane. The minimum spacing in both  $x$ - and  $z$ -directions between the antenna elements is set to  $\lambda/2$ , and a penalty of “5” is applied for unallowed spacing.

The initial antenna positions are chosen randomly, all the antenna elements can be located anywhere in the  $xz$ -plane except for 2 of the transmitters and 4 of the receivers. Each corner has at least one receiver element, and two transmitters are located at the diagonal corners as shown in Figure 4.7. This ensures the virtual array provides the required beamwidths. If the position of one of these two transmitters is changed in the code, the position of the second transmitter should also be changed and placed on the opposite corner of the first transmitter. Hence, each antenna configuration gives the required angular resolutions in both directions.

The desired PSLL and acceptable PSLL are chosen as -20 dB, -7 dB, respectively. In the evaluation part, the PSLL is examined at each scan angle, and when it is higher than the acceptable, there is a penalty of “10” in order to reduce its acceptance probability as a solution. Generating the pattern and check the PSLL at every angle slows down the code’s speed. For this reason, instead of every angle, combinations of every 10 degrees of both azimuth and

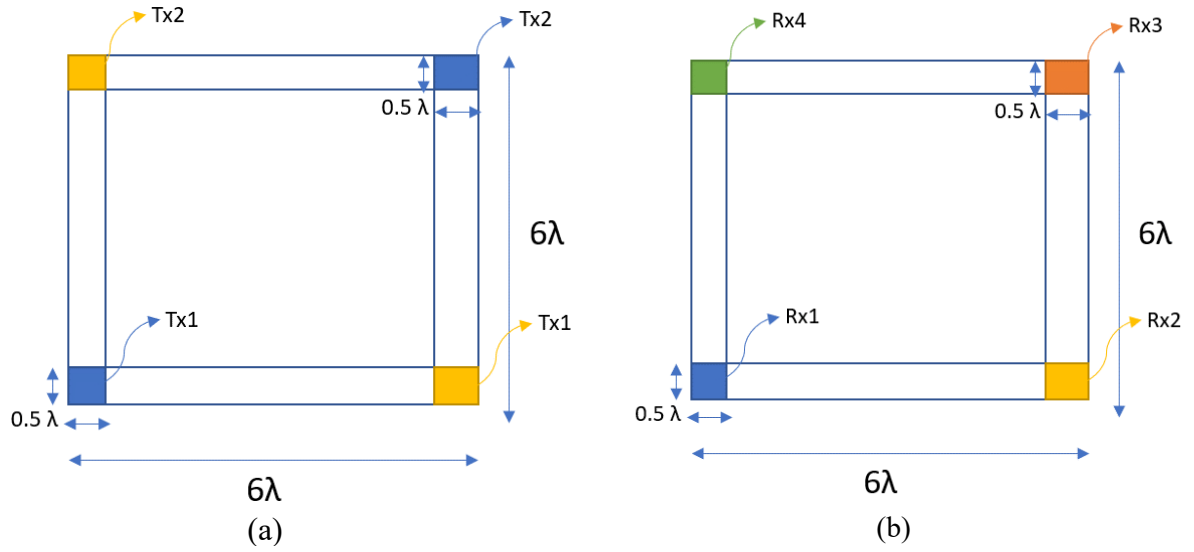


Figure 4.7: The available areas (a) for two restricted transmit elements, (b) for four restricted receive elements.

elevation within a range of  $\pm 40^\circ$  are examined. If the antenna configuration has the desired PSLR at each scan angle, the code will stop itself.

In Figure 4.8, 8 Tx and 16 Rx case - one of the optimized antenna configurations - is examined in detail. Figure 4.8(a) shows the fitness function values for each accepted current solution. It is seen that roughly 1600 current solutions are accepted, and the fitness function value improves towards the end of the existing solutions. The best antenna configuration obtained is shown in Figure 4.8(c), where the blue circles are the transmitters' positions and the orange crosses are the receivers' positions. When examining the configuration, it can be observed that the transmitters are located close to the edges. The virtual array of the thinned MIMO configuration is illustrated in Figure 4.8(d). The dimensions of the virtual apertures in the  $x$ - and  $z$ - directions are both  $11.75\lambda$ , so an angular resolution of 5-degrees is achieved. In Figure 4.8(b), the radiation pattern of the thinned MIMO array for the target at  $(0^\circ, 0^\circ)$  in azimuth and elevation is shown. The obtained PSLR is approximately -14.5 dB for this configuration. When other scan angles are examined, this antenna configuration gives roughly

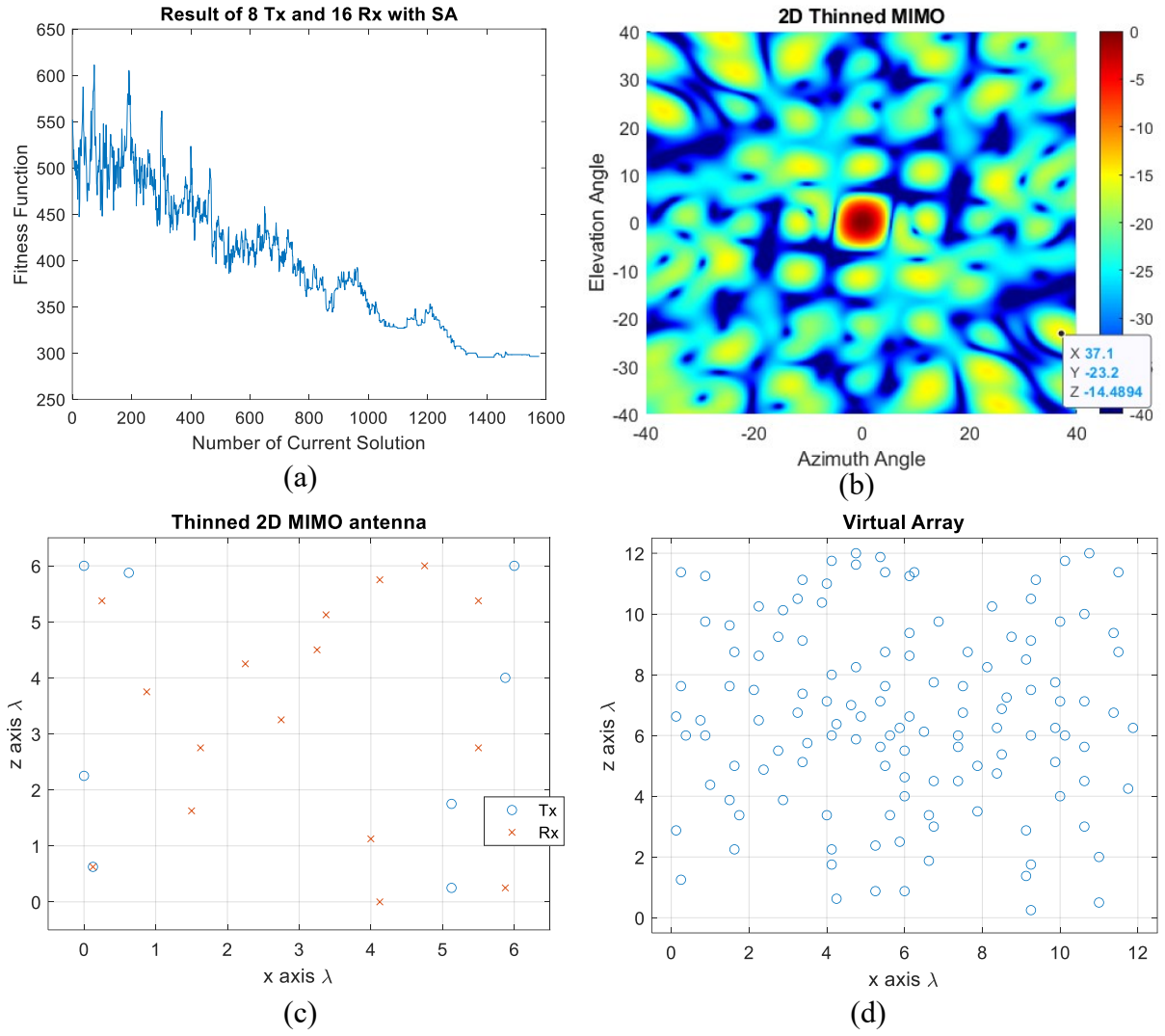


Figure 4.8: The case of 8 Tx and 16 Rx MIMO (a) fitness function response versus number of current solutions, (b) radiation pattern of the thinned 2D MIMO, (c) optimized 2D thinned MIMO array, (d) the corresponding virtual array.

a -14 dB PSL at each scan angle whereas the fully populated L-shaped MIMO with  $\lambda/2$  spacing gives a -13 dB PSL.

Figure 4.9 shows three other antenna configurations optimized with the SA code containing different numbers of Tx and Rx elements and their antenna responses. Figure 4.9(a), for example, shows an optimized design with 4 Tx and 20 Rx elements, with approximately a -12.5 dB PSL when there is a target at  $5^\circ$  in azimuth and  $20^\circ$  in elevation. The antenna positions

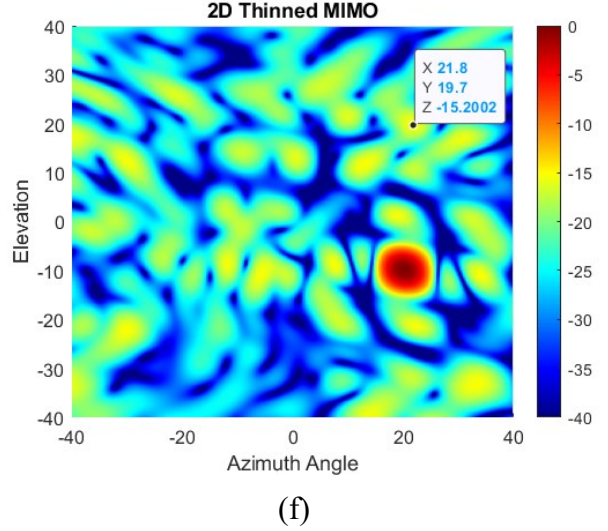
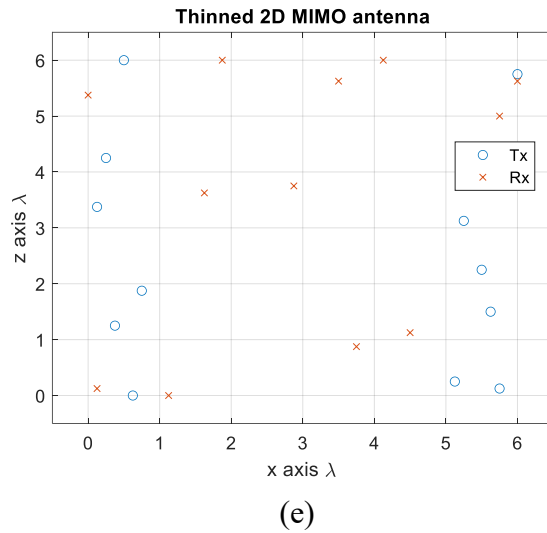
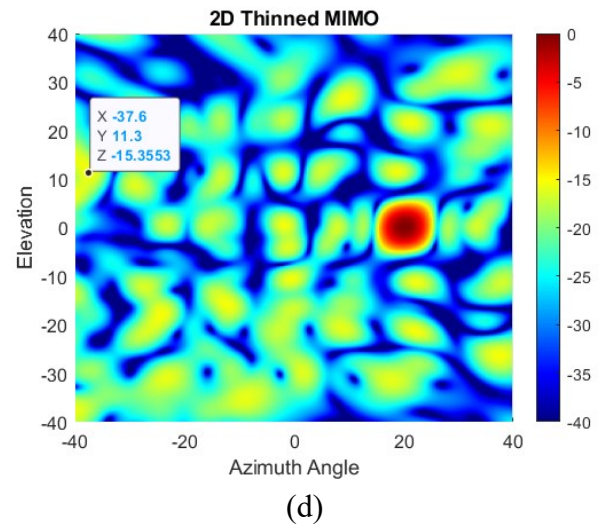
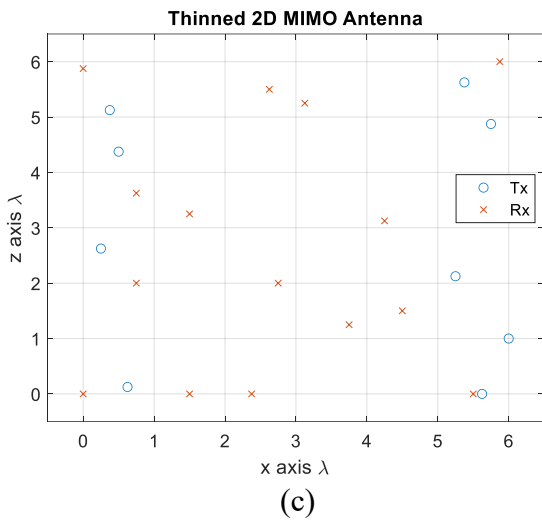
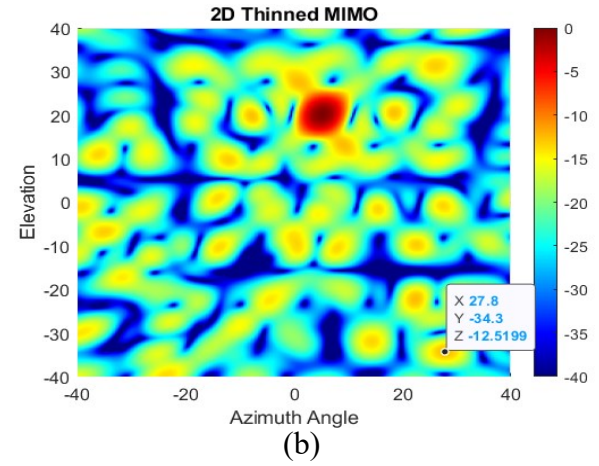
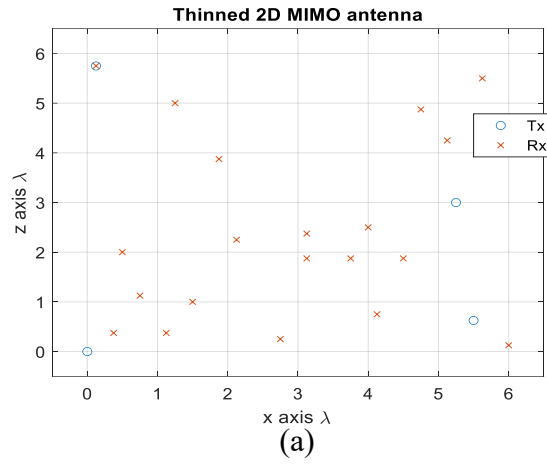


Figure 4.9: The optimized 2-D thinned MIMO antennas, (a) with 4 Tx and 20 Rx, (b) the pattern of (a) when target is at  $(5^\circ, 20^\circ)$ , (c) with 9 Tx and 15 Rx, (d) the pattern of (c) when target is at  $(20^\circ, 0^\circ)$ , (e) with 12 Tx and 12 Rx, (f) the pattern of (e) when target is at  $(20^\circ, -10^\circ)$  in azimuth and elevation, respectively.

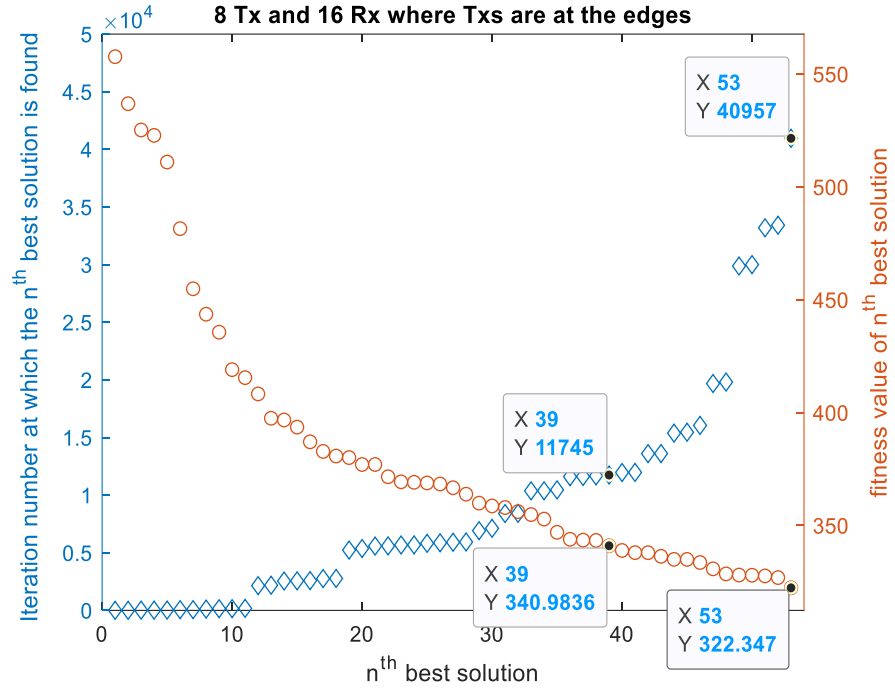
provides roughly a -15.3 dB PSLL. The antenna positions of the optimized 2D MIMO using 12 Tx and 12 Rx are demonstrated in Figure 4.9(e), and the MIMO provides -15.2 dB PSLL when a target appears at (20°, -10°) in azimuth and elevation, respectively.

The simulated annealing code is run approximately 70 times for each Tx/Rx ratio. It means roughly 770 (70x11) SA codes are run to find the best antenna configurations based on their fitness function values. Regardless of the number of transmitters, when each of the antenna configurations is examined, it is seen that all the transmitter elements are located at the edge region within the margin of  $\lambda$  with more than 80% probability, while the receivers are typically located at positions closed to diagonal, anti-diagonal or both.

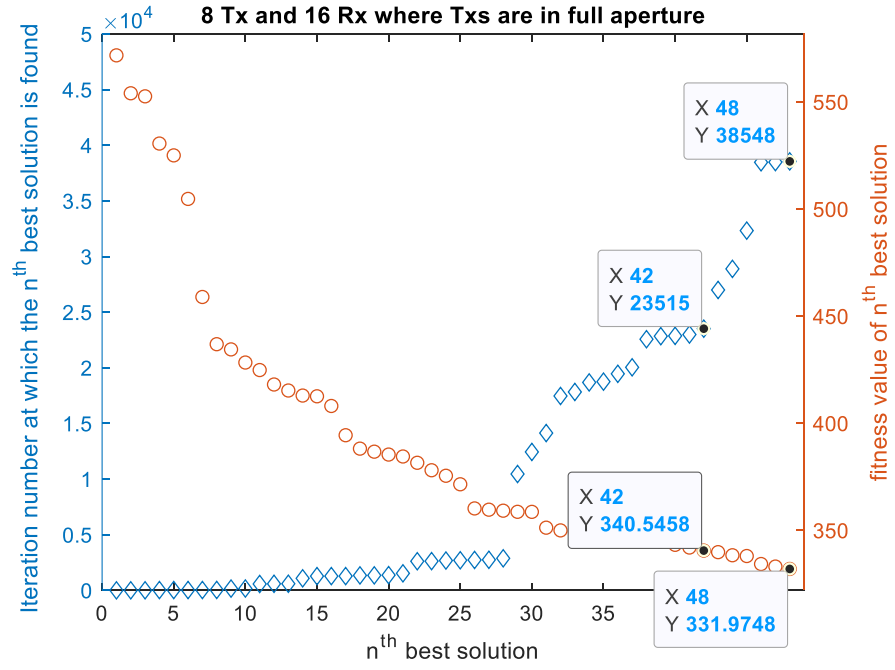
To enhance the code performance and find suitable antenna positions in a faster time, the definition area of the transmitters could be adjusted. The definition area of the transmitters can be decreased by more than 40% in the specific case considered here. Alternatively, the definition region of the transmitters can be left as it is, and it can be arranged that the transmitters are placed at the edges with a very high probability.

To validate the improvement in the algorithm, 14 additional MATLAB codes have been run. The Tx definition region is modified in 7 of them in order for the Tx elements to be located at the edge region within a  $\lambda$  margin (modified code) and the other 7 codes keep the Tx definition region as is (unmodified code). It is noted that the only changing parameter in the code is the transmitter's definition region. When the results are examined, it is seen that the modified code outperforms the unmodified code. In other words, the code which defines the Tx locations in the limited region reaches the desired solution faster than the other. As a typical response curve is shown in Figure 4.10. The figure illustrates that the obtained the fitness values and the number of iterations where the  $n^{\text{th}}$  best solution is obtained versus  $n^{\text{th}}$  best solution. The results for the modified and unmodified cases are shown in Figure 4.10(a) and 4.10(b),

respectively. It can be clearly seen that modifying the Tx definition region gives a better fitness value – 322.35 – for the same iteration number, compared with the unmodified code – 331.97. More crucially when the same fitness value is examined, say 340, the modified code obtains it after roughly 11.75k iterations whereas the unmodified code reaches this value after more than 23.5k iterations. Similar results for the other 12 codes are obtained. This indicates strongly that the performance of the algorithm whose Tx definition region is at the edge region within a  $\lambda$  margin can obtain the similar response twice as fast as the algorithm using the full planar area as the Tx definition region.



(a)



(b)

Figure 4.10: Fitness values and the number of iteration at which the  $n^{\text{th}}$  best solution is obtained versus the  $n^{\text{th}}$  best solution in the case of 8 Tx x 16 Rx (a) when the Tx's are located at the edges within  $\lambda$  margin, (b) Tx's could be anywhere in the planar aperture.

## 4.6 Summary

In this chapter sparse 1-D MIMO arrays are optimised using optimisation techniques based on simulated annealing and genetic algorithmic approaches. Subsequently, multiple sparse 2-D MIMO antenna configurations have been optimized using SA with the aim of minimizing the SLL whilst retaining a constant beamwidth. A novel methodology that aims to optimize the positions of the elements comprising the MIMO array, has been proposed. It is important to note that during the optimization process, the PSLL is taken into account, rather than the shape of the sidelobes. Repeated optimization simulations show that the Tx elements are located at the edge region, to within a wavelength margin, with more than an 80% probability. With the Tx locations predefined in this way, the performance of the virtual MIMO aperture is validated via simulation. The simulations show that the computational time required is subsequently reduced dramatically.



## Chapter 5

# Burg-Aided MIMO Array Extrapolation for Improved Spatial Resolution

### 5.1 Introduction

Using mm-waves radar can achieve high range resolution thanks to the high available bandwidth. In addition to high range resolution, most modern radar applications require high angular resolution in both the azimuth and elevation dimensions in order to resolve closely located targets within the radar field-of-view. As presented in Chapters 2 and 4, the angular resolution, for a given transmission frequency, is defined by antenna effective aperture size, and in the case of a MIMO array the same angular resolution can be achieved with significantly fewer antenna elements, compared with a fully populated phased array with half-wavelength element spacing [33], [42]. Nonetheless, both the total number of antenna elements in a MIMO configuration and the size of the antenna can still be large when high angular resolutions are required, which would limit its suitability for applications where the space available for sensors is limited, such as vehicle infrastructure. Additionally, when transmitters in MIMO are

activated at different time slots in TDM mode, the radar response time increases depending on the number of transmitters, which cause an unwanted reduction of Doppler unambiguous range, critical in MIMO-SAR applications [134]. Therefore, a further reduction in the total number of antenna elements, especially in the number of transmitters, is a desirable approach to reduce the cost, size, and weight but also to decrease the radar response time in TDM MIMO.

This chapter presents the proposed extrapolation of a 2-D MIMO array using the Burg algorithm (BA) with the goal of achieving a higher angular resolution algorithmically beyond that of the equivalent 2-D MIMO virtual array so that both the physical size and the number of antenna elements of the MIMO antenna array stay the same while resolution can be improved by several fold. The performance of the proposed Burg-aided MIMO as well as associated limitations are analysed using both 1-D and 2-D MIMO arrays through simulation and experimentation at 77 GHz. The general rule of designing a compact physical MIMO array allowing extrapolation in both regular and sparse element positioning is presented and demonstrated with several design realisations. Also, for experimental verification, a methodology to generate 3-D data, including range, azimuth, and elevation information using a commercially available 1-D MIMO array is described. By using this approach, the effectiveness of the proposed array can be empirically evaluated, particularly at frequencies where it is desired to evaluate the antenna's response before constructing it.

In this chapter, firstly, a literature review on how to achieve higher angular resolutions beyond that of the corresponding antenna is presented (Section 5.2). This section is followed by the mathematical explanation of the proposed compact 2-D MIMO configurations. Section 5.4 explains the Burg algorithm in detail whereas the proposed Burg-aided MIMO method is described in Section 5.5. Simulation and experimental results are presented and discussed in

Section 5.6 and 5.7, respectively. Conclusions are formulated and further steps are outlined in Section 5.8.

It is noted that a part of this work was presented at the 2023 EURAD conference in Berlin, Germany [135].

## 5.2 State-of-the-art

The angular resolution and sensitivity of a conventional MIMO antenna is defined by an array factor and can be expressed as a sinc function with approximately -13 dB for the highest sidelobe level without applying weightings [17]. When the number of antenna elements in MIMO is reduced by retaining the edge elements and repositioning the inner elements within the array, the same angular resolutions are achieved whereas grating lobes and high sidelobe levels which limit the performance of the radar detection may occur. In such context, finding the antenna positions in thinned MIMO to achieve the required angular resolution with acceptable sidelobe levels represents an optimization problem [136]. An exhaustive search can be performed when there are few potential solutions for the available positions of the antenna elements. However, it is nearly impossible to look through all potential solutions when search space is large. Several optimization techniques were reported in the literature, such as simulated annealing, genetic algorithm, particle swarm optimization, and ant colony optimization to find the suitable configurations of antenna elements positions to design thinned linear, planar and MIMO antennas [90], [94], [100], [102], [104], [133], [137]. All such techniques require a very high number of iterations. Moreover, as demonstrated in Chapter 4, the achieved antenna pattern may give irregular sidelobe levels in the background.

Another approach to achieve higher angular resolution is to use super-resolution techniques such as multiple signal classification (MUSIC) algorithm [138], but this method

requires multiple snapshots of the scene as well as prior knowledge of the number of targets. Also, radar data can be extrapolated through the matrix pencil method [139] and by machine learning [140], [141] to improve the resolution without expanding the physical antenna aperture or using multiple snapshots. However, the number of singular values in the matrix pencil method must be chosen carefully to avoid having false targets whereas machine learning techniques require a large quantity of training data and can be computationally expensive. To extrapolate radar data autoregressive (AR) methods can be employed [142], [143], [144], [145]. Several methods are reported to predict the coefficients of the AR model such as Yule-Walker, Burg algorithm (BA) and covariance method. In [145], the performance of these AR methods has been compared, and it is stated that BA has a better performance in terms of the image quality in noise environment and makes more reliable and stable estimation, compared to other methods [146], [147].

The performance of the BA has been well-studied and presented in the literature. For instance, in [148], the missing data in synthetic aperture radar (SAR) imaging was predicted using the BA, and the results demonstrated a significant improvement in the image quality. In [149], the BA was used with the DBS technique for side-looking radar geometry to enhance cross-range resolution. The BA was also used in a 1-D MIMO concept with the aim to both interpolate antenna elements positions where data is missing and to extrapolate where super resolution is needed in [150]. An exhaustive search suggests that, previously, the Burg Algorithm has been only applied to 1-D arrays.

To achieve higher angular resolution beyond that of the equivalent MIMO virtual array (VA), the virtual array elements are extrapolated towards both azimuth and elevation directions by applying an autoregressive method. In this way, it is shown that the size and number of elements of MIMO physical arrays can be significantly reduced. In this thesis, the Burg

algorithm is applied to extrapolate and/or interpolate the VA elements so that high resolution in both azimuth and elevation is achieved retaining initial compact 2-D MIMO array in a fast and easy to implement approach to retrieve the target's positional information without a requirement of additional input from the user or use of optimization techniques, whilst giving a stable prediction filter [151], [152], [153], [154].

Additionally, this approach can address an issue of missed experimental data due to manufacturing or experimental failure. Instead of re-manufacturing the antenna and repeating the experiment, the missing data can be estimated through the proposed method here.

The performance of the reconstructed MIMO array using the Burg algorithm is demonstrated here in both 1-D and 2-D configurations and the limitations of the algorithm are explained in detail. The validation of the 1-D MIMO concept as in [150] is presented in this chapter for the sake of integrity of material, alongside new analyses and results. The validation and analysis of the proposed approach to enhance performance of the 2-D MIMO array is made through both simulation and experiment at 77 GHz. The experimental methodology used to acquire 3-D data (range, azimuth and elevation information) using a 1-D MIMO radar is described. Using this approach, the antenna configuration can be tested experimentally using off-the-shelf 1-D MIMO chipset where it is desired to observe the antenna response prior to fabricating the antenna.

It is noted that throughout this chapter, MIMO array, virtual array of the MIMO array, and the Burg-aided MIMO array are called *physical array*, *virtual array* and *extrapolated array*, respectively.

### 5.3 MIMO Antenna

Mathematical explanations of both 1-D and 2-D MIMO arrays are presented in Chapters 2 and 4 in detail. Therefore, here, only the configurations of the proposed compact 2-D MIMO arrays are presented.

Physical MIMO elements can be arranged in L-shaped or T-shaped configurations to produce a rectangular VA as in [155], [156], where transmit and receive elements positioned separately along orthogonal axes. Another way could be placed the Tx and Rx antennas at the edges of a rectangle as in [157], [158]. Rectangular VA is the most compact form resulting in smaller area, therefore, in this chapter, the rectangular VA is formed with two different approaches, and both will be used in Section 5.6.2 with examples of several designs.

**1<sup>st</sup> approach:** Assuming  $xz$ - is the plane of 2-D MIMO array, both transmit and receive sub-arrays are also two-dimensional with  $N_{R_x} \times N_{R_z}$  receive and  $N_{T_x} \times N_{T_z}$  transmit elements, respectively. The positions of each receive and transmit element on  $x$ - and  $z$ - axes can be formulated as

$$Rx_{pos_{w,t}} = [(w - 1)dx; (t - 1)dz] \quad (5.1)$$

and

$$Tx_{pos_{e,s}} = [(e - 1)N_{R_x}dx; (s - 1)N_{R_z}dz] \quad (5.2)$$

where  $dx$  and  $dz$  are the spacing between the receive elements on the  $x$ - and  $z$ -axes, respectively,  $w = 1, 2, \dots, N_{R_x}$ ,  $t = 1, 2, \dots, N_{R_z}$ ,  $e = 1, 2, \dots, N_{T_x}$ , and  $s = 1, 2, \dots, N_{T_z}$ .

This antenna configuration gives us a uniform rectangular VA with  $dx$  and  $dz$  spacings along  $x$ - and  $z$ -axes, respectively without producing overlapped virtual elements. When the

$\pm 90^\circ$  unambiguous field of view is needed in both azimuth and elevation directions, the spacing between the receive antenna elements can be chosen as  $dx = dz = \lambda/2$ .

**2<sup>nd</sup> approach:** Under the same assumptions as above and the same locations of each receive element as in (5.1), the position of transmit elements can be determined by the following equation:

$$Tx_{pos_{e,s}} = [1.5(e - 1)dx; 1.5(s - 1)dz] \quad (5.3)$$

In such a case, a uniform rectangular array with spacings of  $dx/2$  and  $dz/2$  on the  $x$ - and  $z$ -axes, respectively, is obtained within the inner area of the VA. However, this 2-D MIMO arrangement generates sparse elements with  $dx$  and  $dz$  spacing on the  $x$ - and  $z$ -axes at the edges of the VA. Therefore, to obtain  $\lambda/2$  spacing between elements inner array of the VA elements in this configuration, spacings among receivers and transmitters are  $\lambda$  and  $1.5\lambda$ , respectively.

It is worth stressing, that following this procedure, as can be seen from either (5.1) and (5.2), or (5.1) and (5.3), the first Rx and Tx physical elements are co-located at the origin [0;0]. One possible solution would be a design of such elements as a transceiver, though a more straightforward solution would be separation of the transmitter and receiver areas, as will be demonstrated in Section 5.6.2. The latter will apparently increase the physical dimension at least in one direction, however retaining the radar's performance as in more elegant case of colocated transmitter/receiver element.

## 5.4 The Burg Algorithm

For the target detection by the phased array, based on the evolution of phases of the actual signals into the receive elements, it is possible to predict the phases of signals for extrapolated, or reconstructed, receive elements, and the problem should actually include

estimation of boundaries of applicability after which the prediction is not any more accurate. Autoregressive methods can predict, or extrapolate, future values of a sequence of  $\{\mathbf{u}\}$  by examining past values, and the AR model can be defined as [147]

$$\mathbf{u}[p] = - \sum_{q=1}^M a_q \mathbf{u}[p - q] \quad (5.4)$$

where  $M$  is the model order,  $a_q$  is the  $q^{th}$  model coefficient,  $p = M + 1, \dots, N_x$ , and  $N_x$  is the total number of elements in the sequence after extrapolation is done.

The Burg Algorithm can be used to estimate the values of coefficients,  $a_q$ , of the AR model or, in other words, AR filter. The same algorithm can also be used for interpolation. In radar applications this will be the case when experimental data are missing e.g., due to antenna manufacturing or experimental failures, so that the antenna pattern can still be reconstructed. The principle of the iterative-based BA operation is to minimize the combined estimation error,  $E_i$ , through forward and backward prediction:

$$E_i = \mathbf{f}_i^* \mathbf{f}_i + \mathbf{b}_i^* \mathbf{b}_i \quad (5.5)$$

where  $i$  is the iteration number,  $(\cdot)^*$  is the conjugate transpose,  $\mathbf{f}_i$  and  $\mathbf{b}_i$  are forward and backward prediction error vectors, respectively.

The algorithm steps to compute  $M$  model, or filter coefficients, whose maximum number is limited by the number of available virtual antenna elements consists of follows [150], [159]:

- 1- At the first iteration ( $i = 0$ ), the initial forward and backward prediction error vectors ( $\mathbf{f}'_0$  and  $\mathbf{b}'_0$ ) are assumed to be equal to  $\mathbf{u}$ :

$$\mathbf{u} = [u_0, u_1, u_2, \dots, u_{N-1}]^T \quad (5.6)$$



where  $\mathbf{u}_n$  denotes the input signal coming from the  $n^{th}$  element ( $0 \leq n \leq N - 1$ ) and the first finite impulse response (FIR) filter coefficient,  $a_0$ , is equal to 1.

- 2- The first element is then removed from the  $\mathbf{f}'_i$ , and the last element is removed from  $\mathbf{b}'_i$  in each iteration so that

$$\mathbf{f}_i = \mathbf{f}'_i(1:N-i-1) \quad \& \quad \mathbf{b}_i = \mathbf{b}'_i(0:N-i-2) \quad (5.7)$$

- 3- At each next iteration  $i$ , the reflection coefficient ( $k_i$ ) is calculated as

$$k_i = -\frac{2\mathbf{b}_i^* \mathbf{f}_i}{\mathbf{f}_i^* \mathbf{f}_i + \mathbf{b}_i^* \mathbf{b}_i} \quad (5.8)$$

- 4- The updated prediction vectors are calculated as

$$\mathbf{f}'_{i+1} = \mathbf{f}_i + k_i \mathbf{b}_i \quad \& \quad \mathbf{b}'_{i+1} = \mathbf{b}_i + k_i^c \mathbf{f}_i \quad (5.9)$$

where  $(\cdot)^c$  denotes complex conjugate.

- 5- The updated FIR coefficients are calculated as

$$\mathbf{a}_{i+1} = \begin{bmatrix} \mathbf{a}_i \\ 0 \end{bmatrix} + k_i \mathbf{Y} \begin{bmatrix} \mathbf{a}_i^c \\ 0 \end{bmatrix}, \quad \mathbf{Y} = \begin{bmatrix} 0 & \cdots & 0 & 1 \\ \vdots & & 1 & 0 \\ 0 & & & \vdots \\ 1 & 0 & \cdots & 0 \end{bmatrix} \quad (5.10)$$

where  $\mathbf{Y}$  is the square antidiagonal matrix of the size  $(i+1) \times (i+1)$ . The iterations are repeated (steps 2 to 5) until the number of iterations is reached  $M$ .

## 5.5 Burg-Aided MIMO

In this section, the proposed method to achieve higher angular resolution beyond that of the virtual array of MIMO by applying the BA is described. It requires a uniform array configuration to extrapolate and/or interpolate the array aperture. The spacing between the virtual elements can be any multiples of wavelength such as  $0.5\lambda$ ,  $\lambda$ ,  $2\lambda$ , but regular spacing between elements is required though the spacing between the virtual elements along two

orthogonal dimensions could be different. These spacings will define the unambiguous resolvable angular field of view, but they do not limit the performance of the BA. It is also worth mentioning that the number of virtual elements along both dimensions do not need to be equal and that the algorithm gives a more accurate estimation with the increase of the number of virtual array elements. Importantly, if the VA is sparse, interpolation must be performed first to fill the missing data of the sparse elements in the VA to make the extrapolation possible.

The block diagram of the processing chain is shown in Figure 5.1. To reconstruct the virtual elements of MIMO by interpolating or extrapolating the radar data using the BA, initially the range compression is done to the acquired data in the case of the FMCW signal. Then, for each range bin, the BA steps described in Section 5.4 are performed along the angular dimension. For the clarity, the  $\mathbf{u}$  in (5.6) consists of the virtual array data of the related range bin, and the filter coefficients in (5.4) are found as in steps 1-5, followed by the data extrapolation/interpolation through the angular dimension calculating (5.4). In the case of 2-D MIMO, this must be done along both azimuth and elevation dimensions. As a final step, angular FFT is taken to obtain either the range–azimuth map (1-D MIMO) or a 3-D map (range,

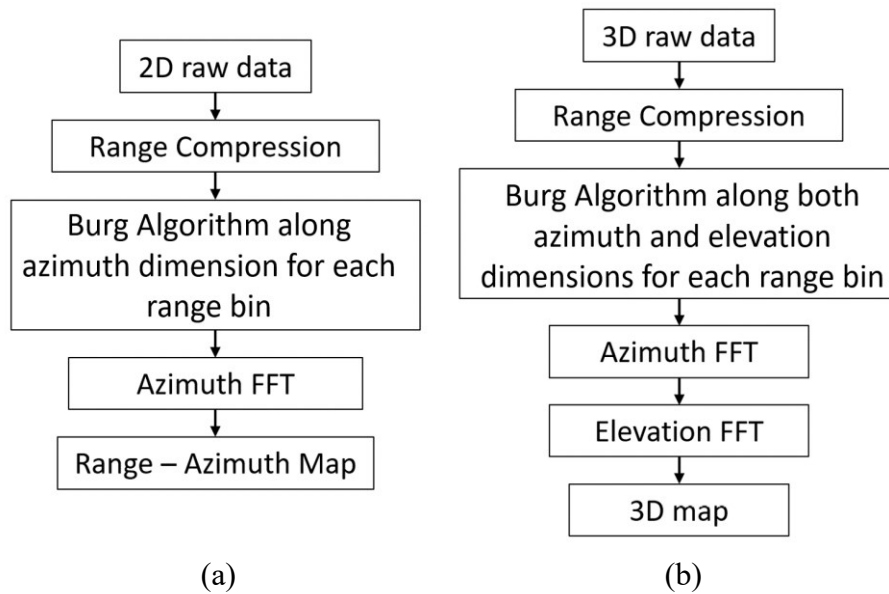


Figure 5.1: Processing chain of the Burg-aided 1-D MIMO (a), and 2-D MIMO (b).

azimuth, and elevation) in 2-D MIMO. The Burg-aided MIMO steps for both 1-D and 2-D MIMO arrays are shown in Figure 5.1.

## 5.6 Simulation Results

In this section, the performance of the Burg algorithm to interpolate and/or extrapolate the available data is analysed. The operational frequency used in the simulation is 77 GHz with a bandwidth of 2 GHz, which corresponds to experimental results later in this chapter.

### 5.6.1 Burg-Aided 1-D MIMO

#### 5.6.1.1 Estimation of Missing Data (Interpolation)

While the principle described above is generic and applicable for an arbitrary number of transmit and receive elements, for simplicity of analysis here I use a conventional MIMO radar comprising 2 transmitters and 9 receivers with the spacing between the transmitters and the receivers of  $9(\lambda/2)$  and  $\lambda/2$  respectively, as shown in Figure 5.2(a). The corresponding VA consists of uniformly distributed 18 linear elements with a  $\lambda/2$  spacing, which provides approximately  $6^\circ$  angular resolution in the direction along array extent. If one of the physical elements of MIMO array is missing, owing to a hardware failure or experimental data being corrupted, the MIMO can be considered as a thinned MIMO. For instance, if the 6-*th* physical receiver element is absent, as shown in Figure 5.2(b), the VA will miss the 6-*th* and 15-*th* virtual elements, which would result in a degradation of performance in terms of the sidelobes of the array pattern, as demonstrated in Figure 5.3(a), 5.3(b) and 5.3(c) for a single, separated two targets and closely located two targets, respectively. The angular resolution is not deteriorated, as the extreme edge elements, and hence the dimension of array, are retained. After

interpolation with the BA, the response is an exact match to that of the fully populated MIMO array (Figure 5.3(a), 5.3(b) and 5.3(c) green lines).

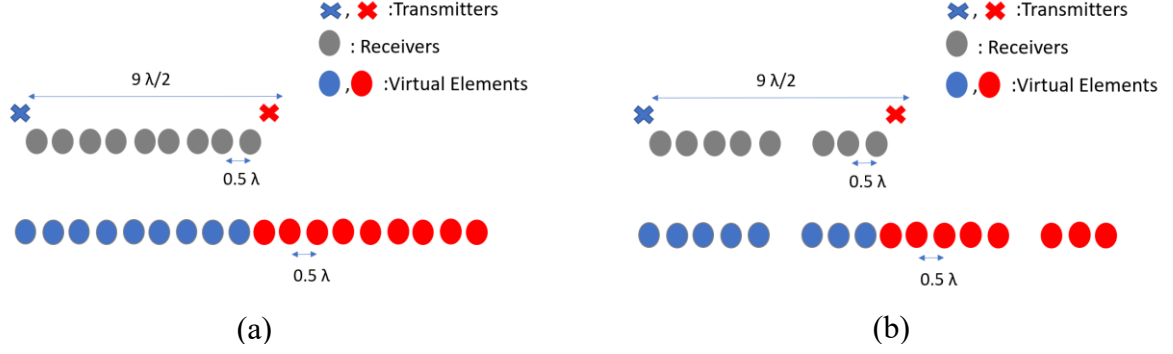


Figure 5.2: (a) MIMO antenna configuration, and its positions of VA elements, (b) the positions of the VA elements when the 6<sup>th</sup> receiver is missing/failed.

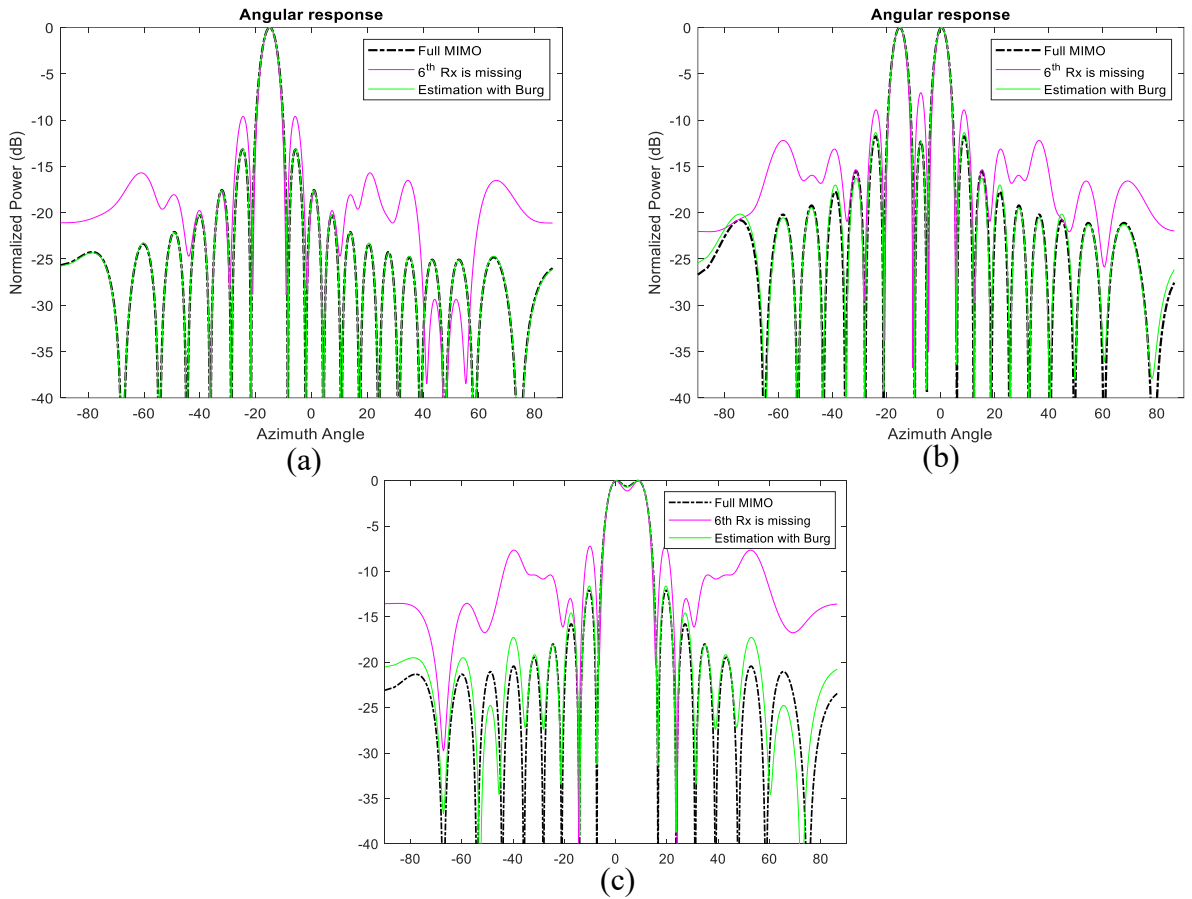


Figure 5.3: The azimuth cut at 15 m range in the case of (a) a single target at -15° azimuth angle, (b) two targets at -15° and 0° azimuth angles, (c) targets at 0° and 9° azimuth angles.

### 5.6.1.2 Estimation of Forward Data (Extrapolation)

This section evaluates the performance of the Burg algorithm to extrapolate 1-D MIMO radar data and the limitation to which an extrapolation is expedient is analyzed and discussed with supporting simulation results.

The ability to distinguish targets at the same range but at different angular positions depends on wavelength and effective antenna aperture length. When the Burg algorithm is applied to extrapolate the number of uniformly spaced virtual array elements, the angular resolution can be estimated as:

$$\varphi_{3dB_{Burg}} \cong \frac{0.88\lambda}{(\varepsilon_f N_{VA} - 1)d_{VA}} \frac{180}{\pi} \quad (in \ degrees) \quad (5.11)$$

where  $\varepsilon_f$  is extrapolation factor,  $N_{VA}$  is the number of virtual elements corresponding to actual MIMO array, and  $d_{VA}$  is the spacing between the virtual elements.

In this subsection, I will demonstrate the performance of the extrapolation by BA with an example of multiple targets (12 targets) which are placed at various azimuth angles and ranges. The simulated scenario is shown in Figure 5.4(a), where blue circles indicate the positions of targets. Targets are located at the ranges of [12, 12, 15, 15, 18, 18, 20, 20, 21, 22, 22, 22] m at azimuth angles of [0°, -4.5°, 15°, -30°, 0°, 3°, -20°, -25°, 30°, 0°, 5.5°, 11°], respectively.

The simulated MIMO range-angle map for the scene in Figure 5.4(a) is demonstrated in Figure 5.4(b). All closely positioned targets at the range of 12 m, 18 m, 20 m, and 22 m are not resolved with this array resolution of 6°. However, extrapolated by factor of two and three arrays with 36 and 54 equally spaced virtual elements refine angular resolution by the same factor, so it becomes ~2.9° and 1.9°, respectively and all targets are resolved as shown in Figure

5.5(a, c) and 5.5(b, d). The range cuts corresponding to 21 m and 15 m are shown in Figure 5.6 respectively to demonstrate improvement in terms of resolution refinement for a single target at 21 m and two targets at 15 m. The azimuth cuts of the relevant ranges which include closely positioned targets are demonstrated in Figure 5.7, and it is evident that the enhancement in angular resolution with Burg-aided MIMO applies not only to single or widely separated targets, but also to closely located targets that cannot be separated by the physical MIMO array.

These simulation results demonstrate that the BA is able to improve the angular resolution regardless of the number of targets and their positions. However, when the signal contains noise or when the model order selected for the Burg algorithm is too high, line splitting may occur, and the algorithm may produce spurious peaks in the estimated spectrum, leading to inaccuracies. Therefore, one should be cautious that when the extrapolation factor is more than three, the Burg algorithm may not work properly in all possible target positions due to the bias effect as detailed in [142], [160]. It should be noted that far field region may change after the extrapolation, so the range assumed as far-field for the physical MIMO array may be near-field in the extrapolated array.

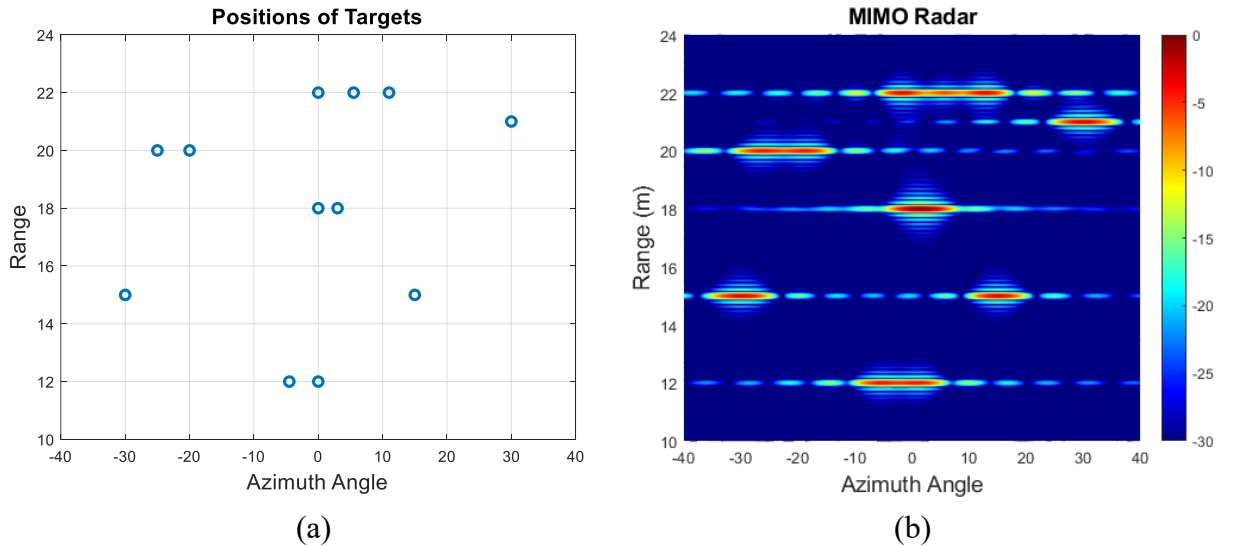


Figure 5.4: (a) The positions of the multiple targets, (b) the range – azimuth response of 2 Tx and 9 Rx MIMO.

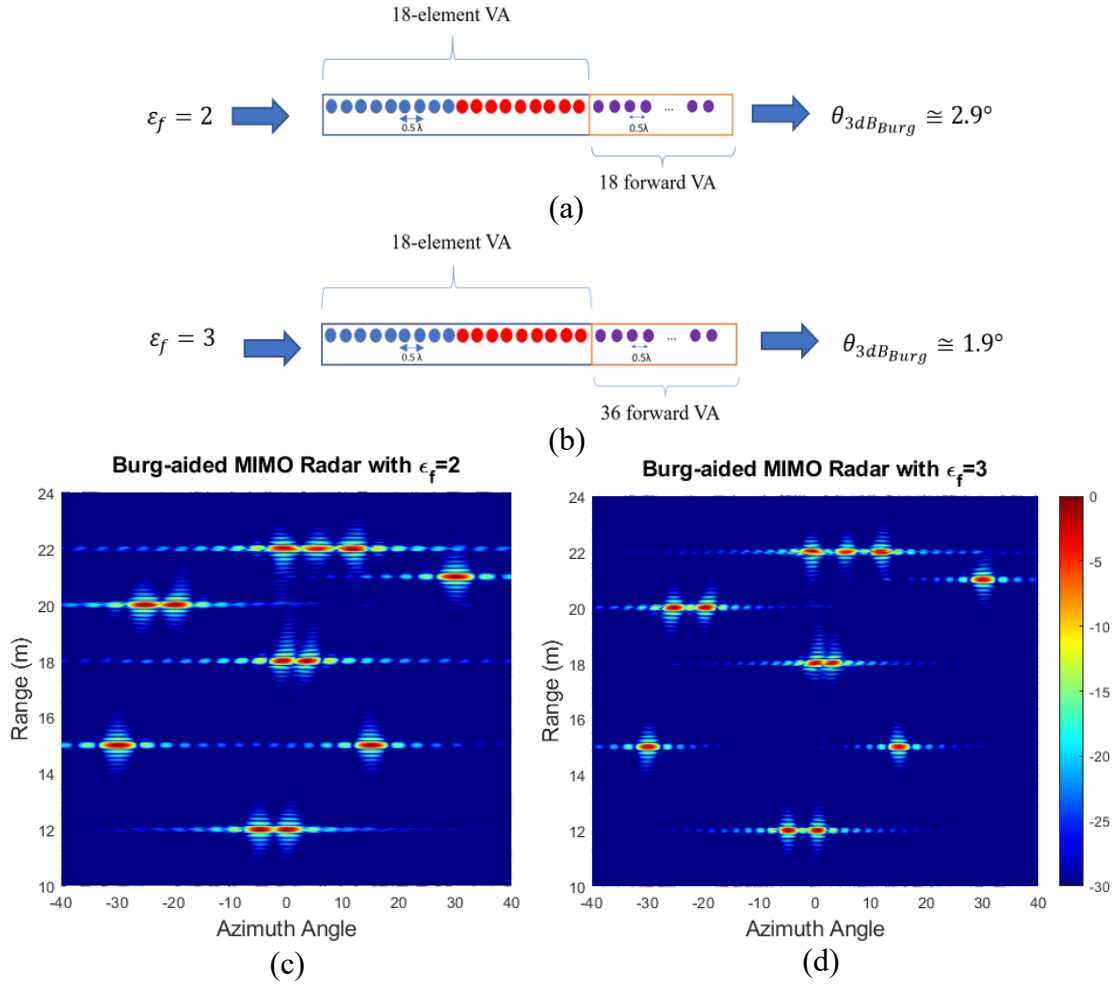


Figure 5.5: The extrapolated VA element and its angular resolution for 2 Tx and 9 Rx based on (a)  $\epsilon_f$  is 2, (b)  $\epsilon_f$  is 3, and the range – azimuth angle response of Burg-aided MIMO with (c)  $\epsilon_f$  of two, (d)  $\epsilon_f$  of three.

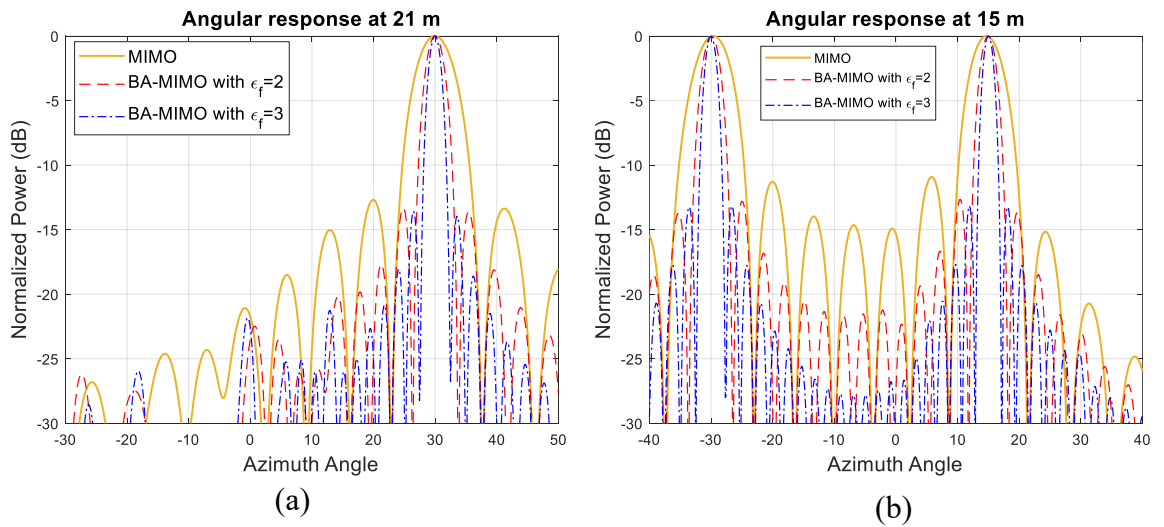


Figure 5.6: The angular response of the MIMO antenna, Burg-aided MIMO antenna with  $\epsilon_f = 2$ , and  $\epsilon_f = 3$  at the range of (a) 21 m, (b) 15 m.

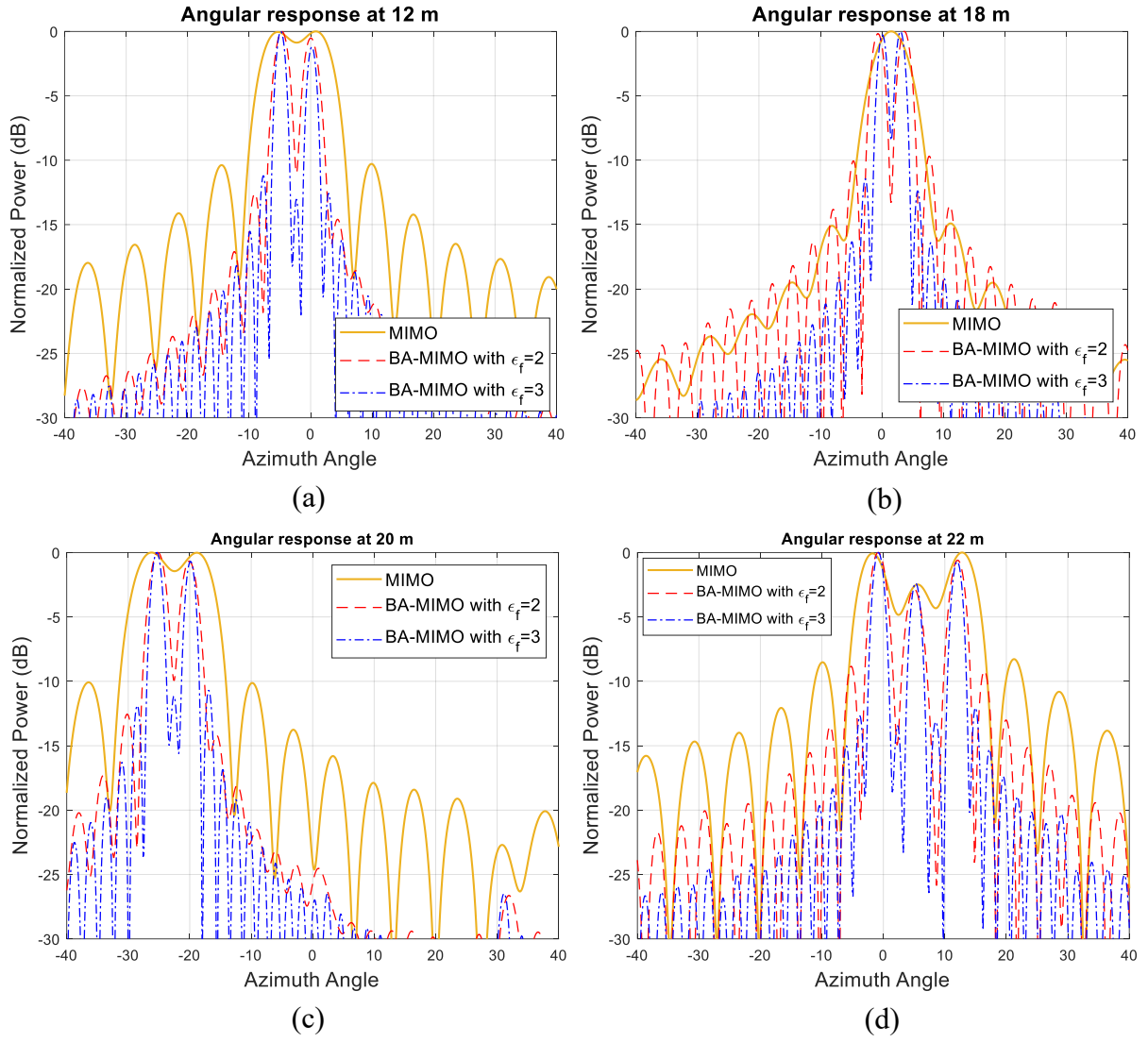


Figure 5.7: The angular response of the MIMO antenna, Burg-aided MIMO antenna with  $\epsilon_f = 2$ , and  $\epsilon_f = 3$  at the range of (a) 12 m, (b) 18 m, (c) 20 m, (d) 22 m.

Figure 5.8 illustrates the Burg-aided resolution improvement by factor 2 in comparison with the VA.



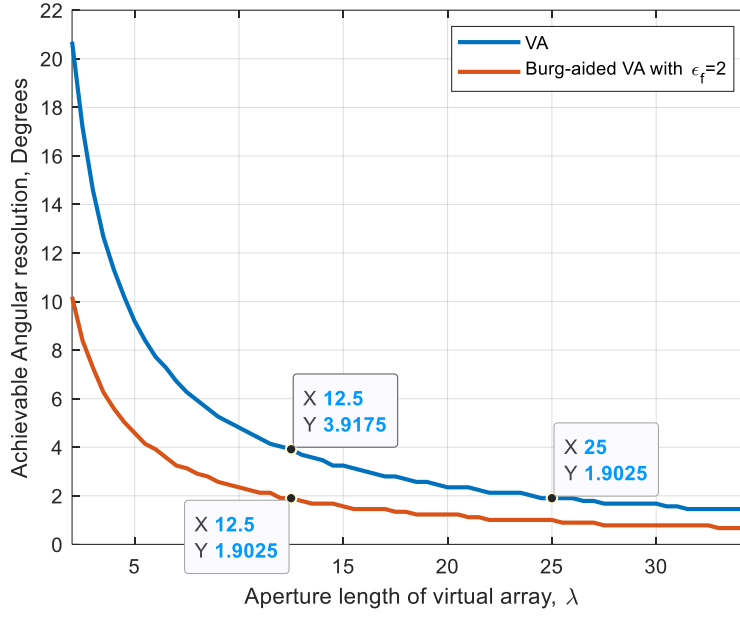


Figure 5.8: The achievable angular resolution versus the aperture length of the Burg-aided VA with  $\epsilon_f = 2$  in comparison to VA.

## 5.6.2 Burg-Aided 2-D MIMO

Assume the required azimuth and elevation resolutions are  $\theta_{AZ}$  and  $\theta_{EL}$ , respectively. This requires the size of the aperture in both dimensions to be  $l_{AZ}$  and  $l_{EL}$ , regardless of whether it is made by a fully populated array, or a MIMO virtual array. For instance, in the case of a conventional uniform L-shaped MIMO, the dimension of the MIMO physical array size must be  $(l_{AZ} \times l_{EL})$ .

In this section several compact designs will be considered illustrating the advantages of the Burg-based approach. In particular it will be shown that equivalent angular resolutions can be achieved by use of 2-D MIMO array of  $\left(\frac{l_{AZ}+0.5\lambda}{4} \times \frac{l_{EL}+0.5\lambda}{4}\right)$  size, by use of the first approach described in Section 5.3. It is worth stressing that the reduction of the physical aperture by almost a factor of 4 whilst ensuring the required performance can bring dramatic advantage of

applications, where miniature size of sensors is a requirement due to dense packaging within the infrastructure as in the case of automotive radars.

As an illustrative example here, I will consider initial conventional L-shaped 20 Tx and 20 Rx MIMO array with  $\lambda/2$  spacing giving  $5.2^\circ$  angular resolution in both dimensions. Here it will be shown that a number of MIMO configurations with significant reduction of both (i) number of physical elements and (ii) physical size of the array can be designed to achieve the same resolution using the proposed approach.

First, 4 Tx and 25 Rx are arranged in a compact design as shown in Figure 5.9(a) by determining Rx positions via (5.1) and Tx positions via (5.2). This decreases the number of antenna elements by 27.5%, but more importantly the radar response time in case of TDM is decreased dramatically by 80% due to fewer transmit elements. The corresponding virtual array includes  $10 \times 10$  virtual elements with  $\lambda/2$  spacing as shown in Figure 5.9(b). This gives roughly a  $10.5^\circ$  angular resolution in both dimensions. In order to attain a  $5.2^\circ$  beamwidth, the MIMO virtual aperture is extrapolated to twice its original size by use of the BA. This is first applied to each row and each column of the virtual elements, and the extrapolated data are shown as red crosses in Figure 5.9(c). Then, to populate the upper-right corner (shown in green cross sign in Figure 5.9(c)), the previously extrapolated data – shown as red crosses – are used in a similar way, and the extrapolated data of the upper right corner elements is done by taking the mean of new extrapolated data. In this way, the reconstructed virtual aperture resembles the virtual array configuration of the L-shaped MIMO of 4 times larger size in each dimension with respect to the original physical aperture. However, as seen in Figure 5.9(a), a Tx and a Rx are colocated at (0,0) m, necessitating the use of a transceiver at this point. If this is not desired, the positions of the Rx antennas can be shifted by  $\lambda/4$  in both the x- and z- axes as shown in Figure 5.10(a). Although it does not change the physical size of the 2-D MIMO antenna, the challenge could

be to provide  $\lambda/4$  spacing at high frequencies during the fabrication of such an antenna configuration. Another option could be to separate the Tx and Rx arrays as shown in Figure 5.11(a), but this makes the MIMO array physically larger, yet still twice more compact than conventional MIMO with advantage of easier manufacturing and avoiding coupling between elements. Each design would have  $10 \times 10$  virtual elements with  $\lambda/2$  spacing.

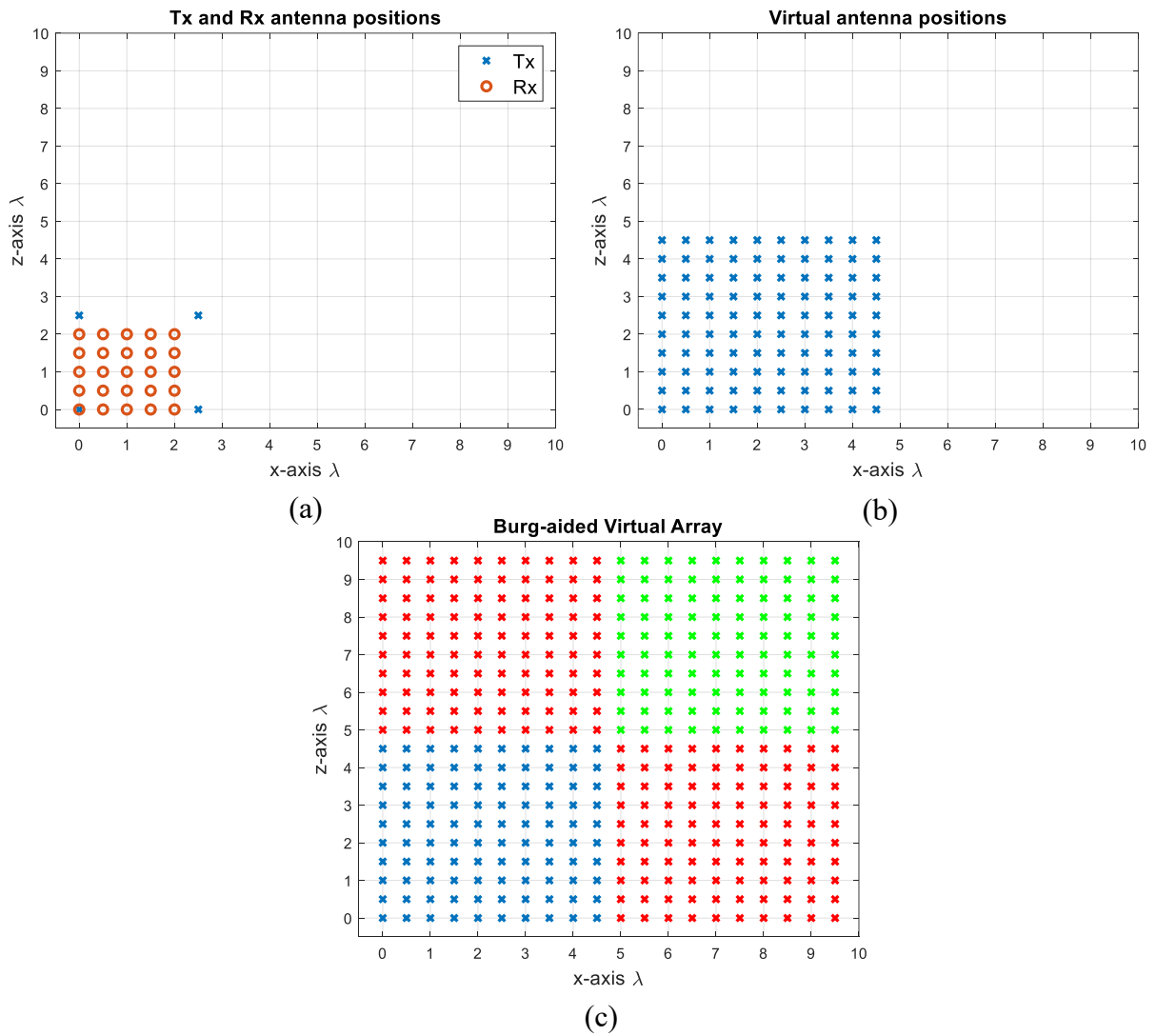


Figure 5.9: (a) The proposed 2-D MIMO array one single transmit/receive element, (b) Virtual array of the antenna configuration of (a), (c) Extrapolated virtual elements via the BA (extrapolation along each dimension is shown in red with further extrapolation shown in green).

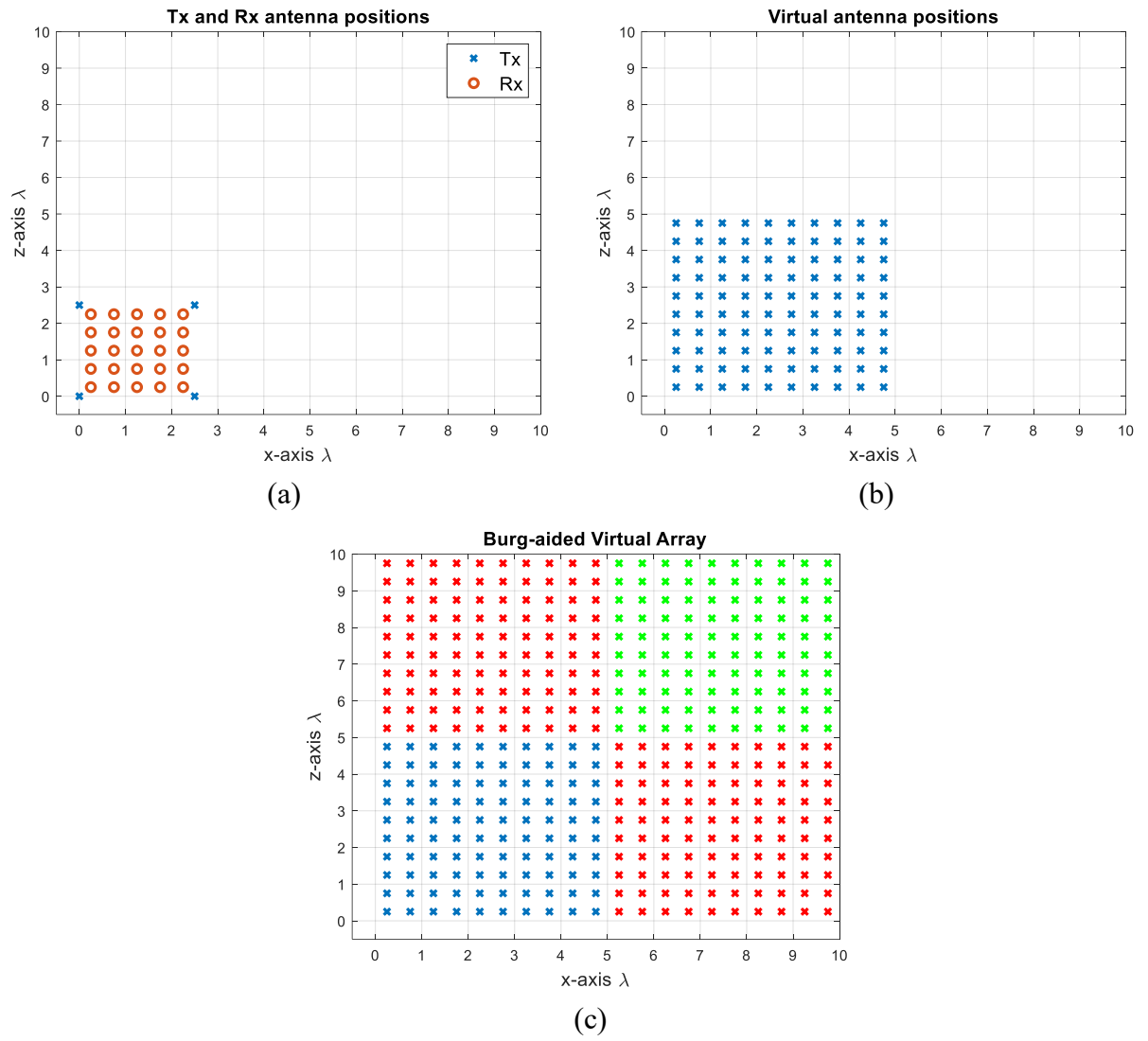


Figure 5.10: (a) Proposed MIMO with separated Tx and Rx (b) VA of the antenna configuration of (a), (c) Extrapolated virtual elements via the BA.

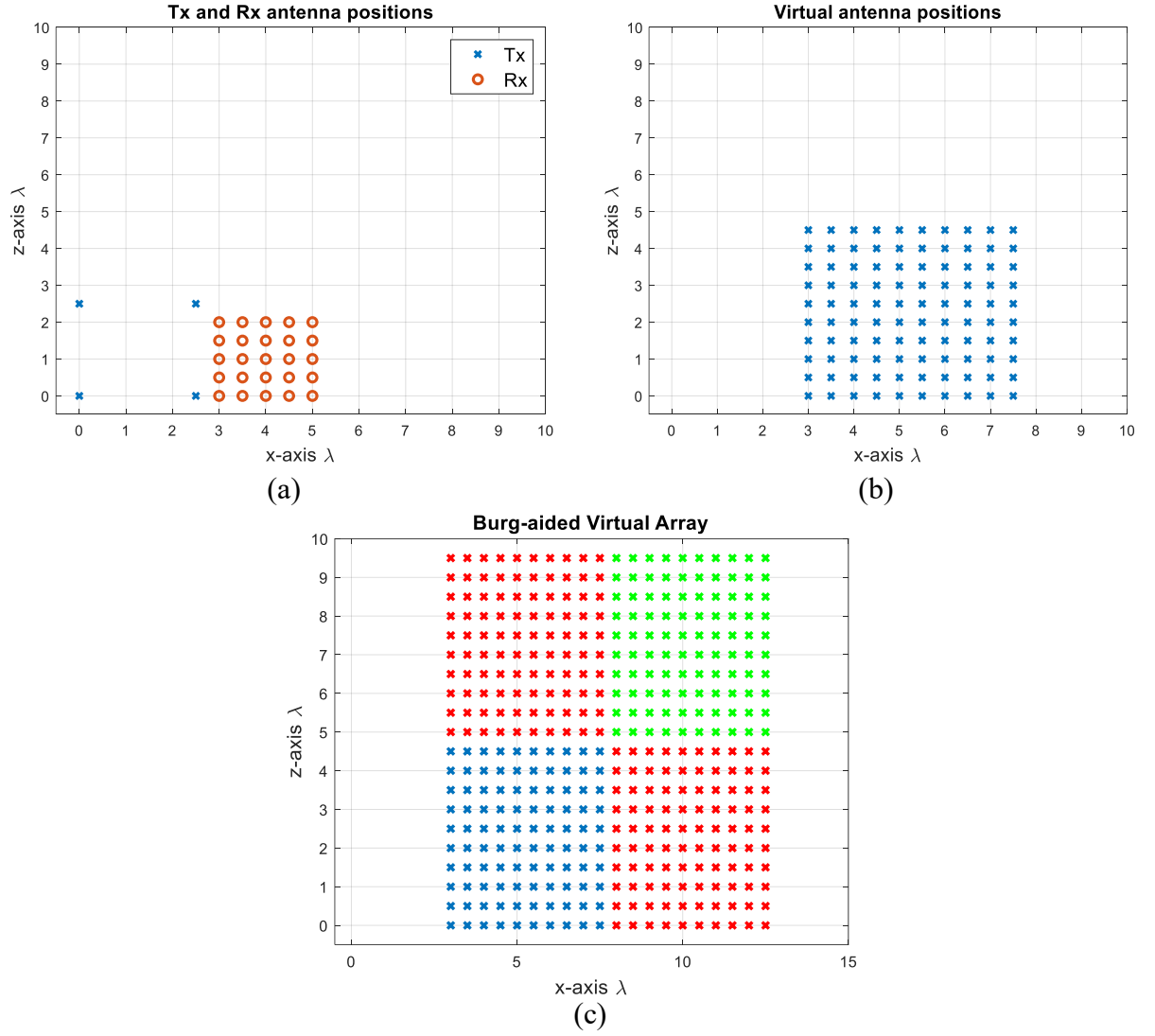


Figure 5.11: (a) When Tx and Rx packs are separated, (b) VA of the antenna configuration of (a), (c) Extrapolated virtual elements via the BA.

The angular response of the proposed compact size 2-D MIMO antenna in Figure 5.9(a) and 5.10(a) for a single target at a range of 15 m on boresight at  $(0^\circ, 0^\circ)$  is illustrated in Figure 5.12(a) and the Burg-aided extrapolation result is shown in Figure 5.12(b). For the latter the angular resolutions in both dimensions are improved by a factor of approximately two, as expected, without degradation in sidelobe level. The response of the configuration in Figure 5.11 to the same scenario with the single target is shown in Figure 5.13. It is seen that the change

in the phase centre of the array does not have an impact on the radar response. Therefore, the remaining analyses are done by considering the MIMO antenna configuration in Figure 5.9(a).

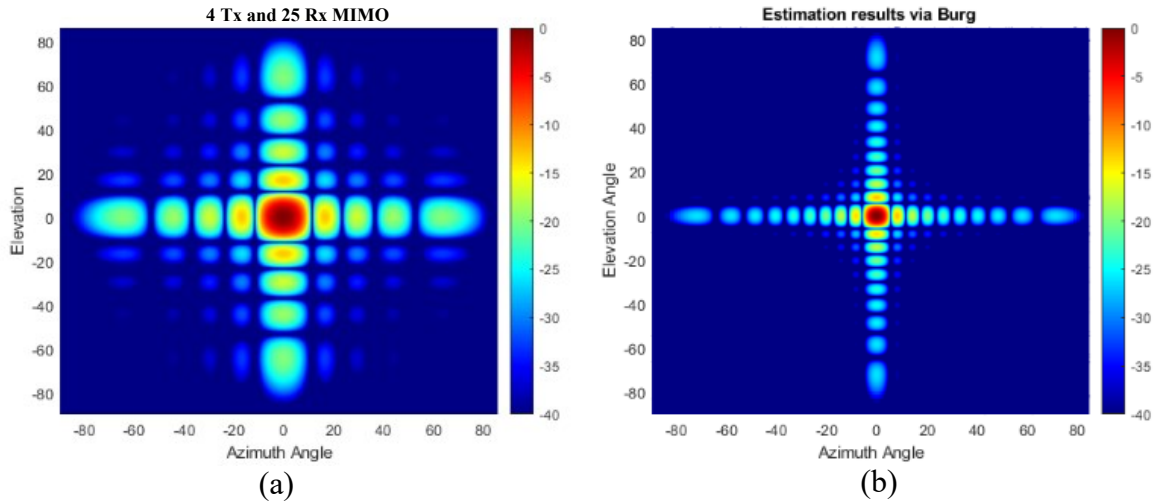


Figure 5.12: The angular response for a boresight target (a) the compact size 2-D MIMO, (b) Burg-aided 2-D MIMO.

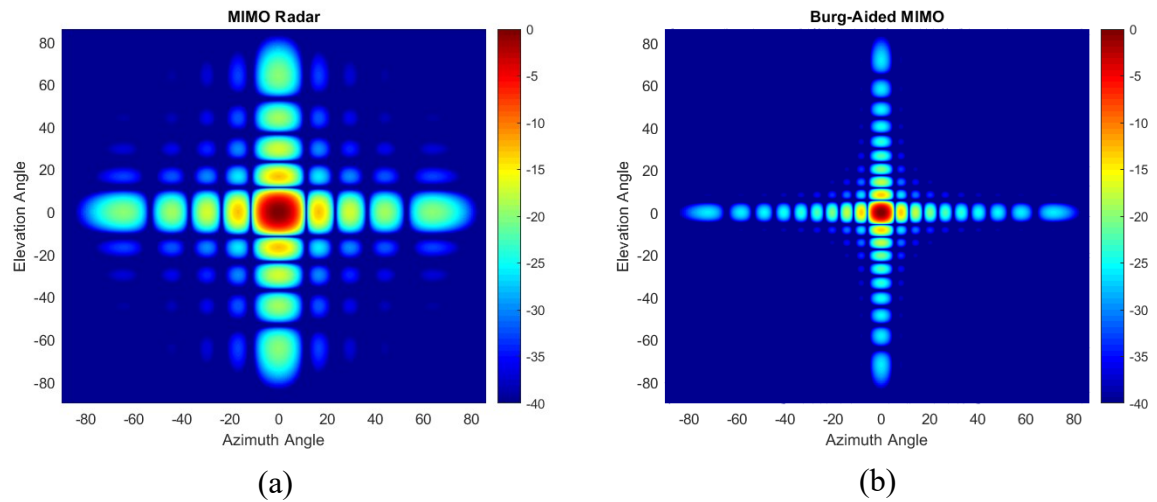


Figure 5.13: The angular response for a boresight target (a) the antenna configuration in Figure 5.11(a), (b) Burg-aided 2-D MIMO.

The performance of the proposed method in the case of multiple targets of the same radar cross section (RCS) positioned at the same range is also examined. An example of 9 targets arranged within  $(\pm 6^\circ, \pm 6^\circ)$  area in azimuth and elevation angles is used in simulation. Conventional beamforming with physical 4 Tx and 25 Rx elements of 2-D MIMO, does not allow to resolve all targets shown in Figure 5.14(a), while in case of Burg-aided MIMO targets are resolved without sacrificing the signal to background ratio, as illustrated in Figure 5.14(b).

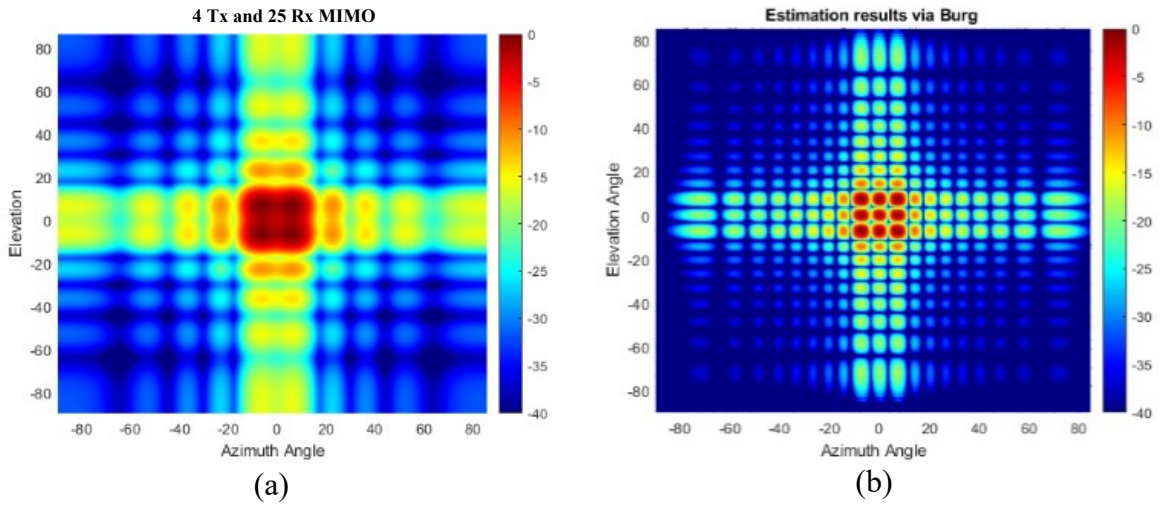


Figure 5.14: The angular response for multiple targets (a) the compact size 2-D MIMO, (b) Burg-aided 2-D MIMO.

In the next multi-target scenario, the performance of the algorithm is examined when the targets have different RCSs. In this case, four targets are located at 15 m with  $[-8^\circ 0^\circ 5^\circ 10^\circ]$  in elevation and  $[10^\circ 0^\circ -10^\circ 15^\circ]$  in azimuth, respectively. The RCSs of the targets are  $[1 \ 1 \ 0.7 \ 0.5]$  in normalized units, that is, targets III and IV have 3 and 6 dB less reflectivity w.r.t. first two targets. The Burg-aided MIMO determines positions and reflections of all four targets correctly as illustrated in Figure 5.15(b), but has a slightly higher background level, compared to the fully populated L-shaped 20 Tx by 20 Rx MIMO shown in Figure 5.15(c).

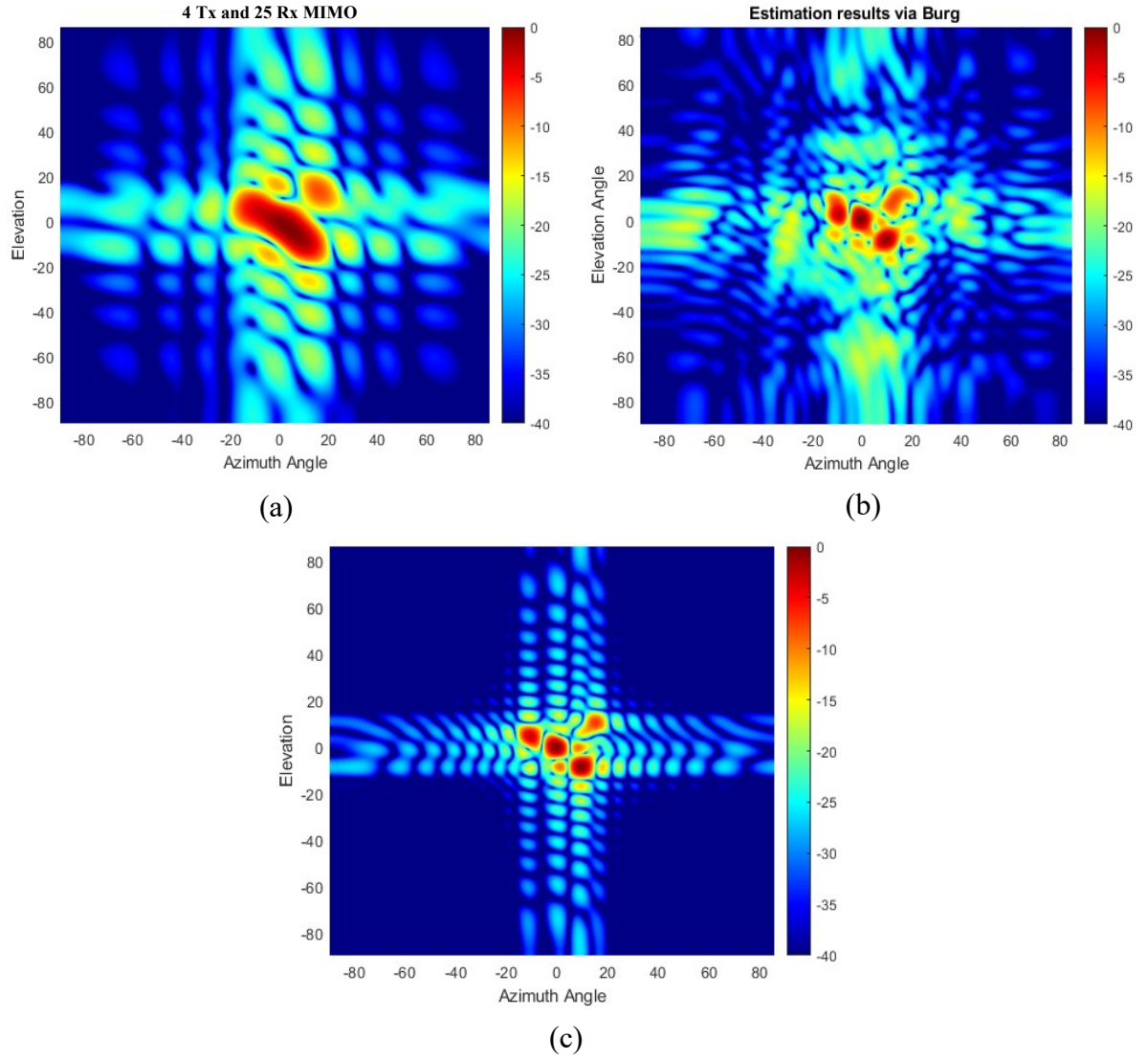


Figure 5.15: The angular response when targets have different RCSs (a) the compact size 2-D MIMO, (b) Burg-aided 2-D MIMO, (c) L-shaped 20 Tx by 20 Rx MIMO radar.

The second design approach from Section 5.3 has been used to come up with the configuration shown in Figure 5.16(a). Whilst keeping the number of antenna elements the same as in the previous designs, the spacing between the transmitter elements is chosen to be  $1.5\lambda$  whereas the spacing between the receiver elements is  $\lambda$  leading to a sparsity of virtual array (Figure 5.16(b)). In this design, to achieve the  $5.2^\circ$  angular resolutions in both directions, initially the interpolation is done to populate the missing virtual array elements, followed by



the extrapolation towards right, up, and upper-right directions, respectively, so that fully populated 20 by 20 extrapolated array is shown in Figure 5.16(c). This proposed 2-D MIMO antenna configuration can be particularly useful when higher frequencies, potentially in sub-THz region with mm-order wavelengths, [161], [162], are desired. This is because it is difficult to fabricate antennas with mm-level. Therefore, it is desired to have larger space between the antenna elements to achieve the required angular resolutions without encountering grating lobes. In the proposed MIMO with one wavelength as the minimum spacing the fabrication will be less challenging.

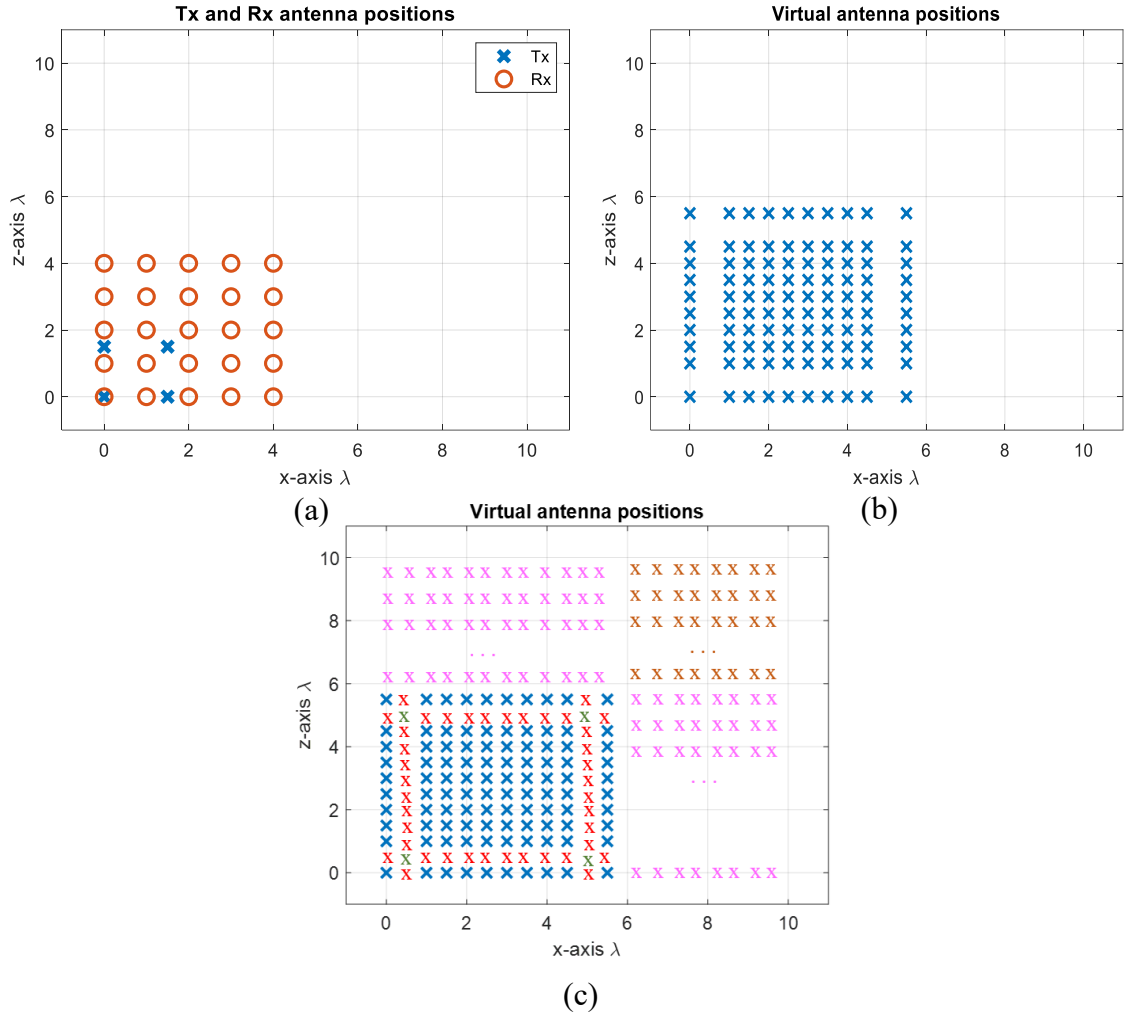


Figure 5.16: (a) The second proposed 2-D MIMO array, (b) Virtual array of the antenna configuration of (a), (c) Extrapolated virtual elements via the BA.

Regarding the performance of the BA in such antenna configuration, the angular responses of the original VA and Burg-aided MIMO in the case of single-target and multi-target scenarios are illustrated in Figure 5.17 and Figure 5.18, respectively. Due to the sparsity in the virtual array of the 2-D MIMO, the angular responses contain high sidelobes, but after applying the proposed method, the response improves dramatically due to interpolation of thinned array, as well as ensuring the desired angular resolutions.

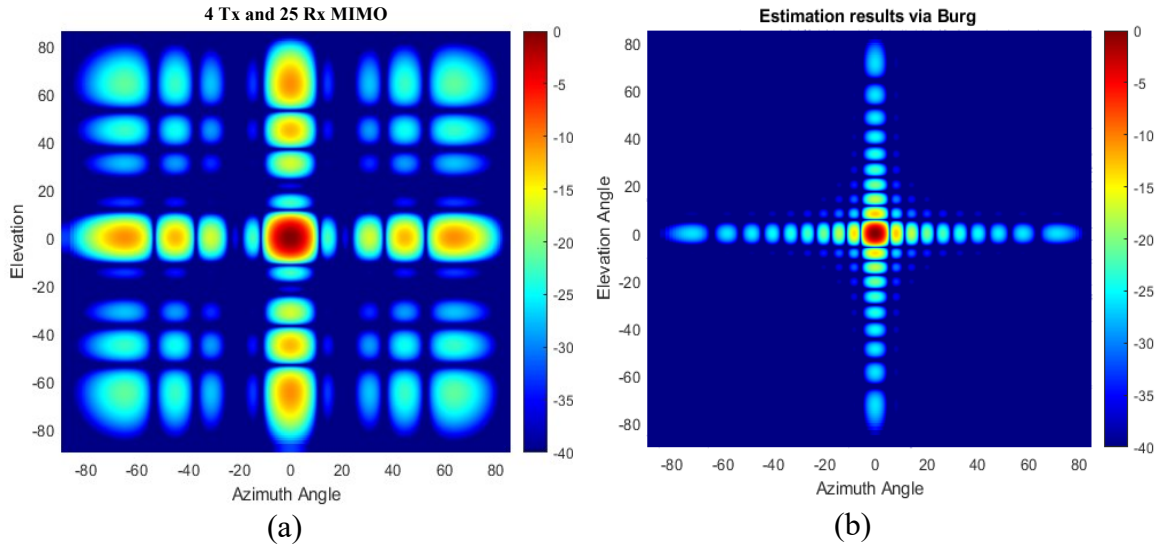


Figure 5.17: The angular response for a boresight target (a) the second proposed 2-D MIMO, (b) After the BA is applied to the 2<sup>nd</sup> configuration.

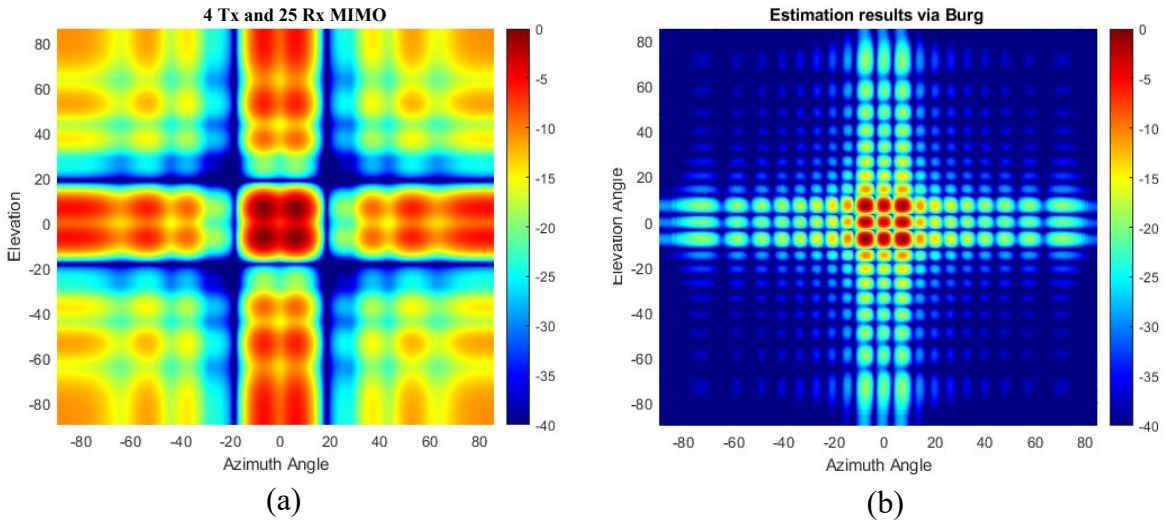


Figure 5.18: The angular response for multi-target scenario (a) the 2<sup>nd</sup> proposed 2-D MIMO, (b) After the BA is applied to the 2<sup>nd</sup> configuration.

It is worth to stress here, that specific design of array where Burg-aided interpolation and extrapolation is expected would be driven by intended application requirements and limitations of the fabrication, but there are no fundamental limitations of the approach to improve resolution in 2-D MIMO.

## 5.7 Experimental Setup and Results

For the experimental verification of the proposed technique, INRAS Radarbook MIMO radar operating at 77 GHz has been used with 2 GHz bandwidth, giving a range resolution of 7.5 cm [163]. INRAS Radarbook frontend is a 1-D MIMO with 4 transmitters and 8 receivers aligned in azimuth, giving 32 virtual linear elements [163]. Three of the elements overlap, resulting in a 29 elements linear array with half-wavelength spacing.

The experimental set-up in the Microwave Systems Laboratory of the School of Engineering at the University of Birmingham is shown in Figure 5.19. Six triangular corner reflectors have been used as point targets of known RCS during the experiment. The corner reflector with 7 cm edges of 8.21 dBsm RCS has been placed at 1.7 m range at  $(0^\circ, 0^\circ)$  with respect to the phase center of the antenna as shown in Figure 5.19(c). Two corner reflectors with edges of 10 cm of 14.41 dBsm RCS were placed at a range of 2.5 m at  $15^\circ$  in azimuth with a difference of 0.36 m in elevation, as shown in Figure 5.19(d). Other three corner reflectors with 15 cm edge (RCS of 21.45 dBsm) are positioned at a range of 3.7 m and 0.25 m in elevation at the distances between them of 0.7 m and 0.65 m, respectively, in azimuth, as shown in Figure 5.19(e). The corner reflector on the right-hand side is on the boresight of the radar antenna. It is noted that direct coupling between transmitters and receivers may occur at very close detections due to the experimental setup.

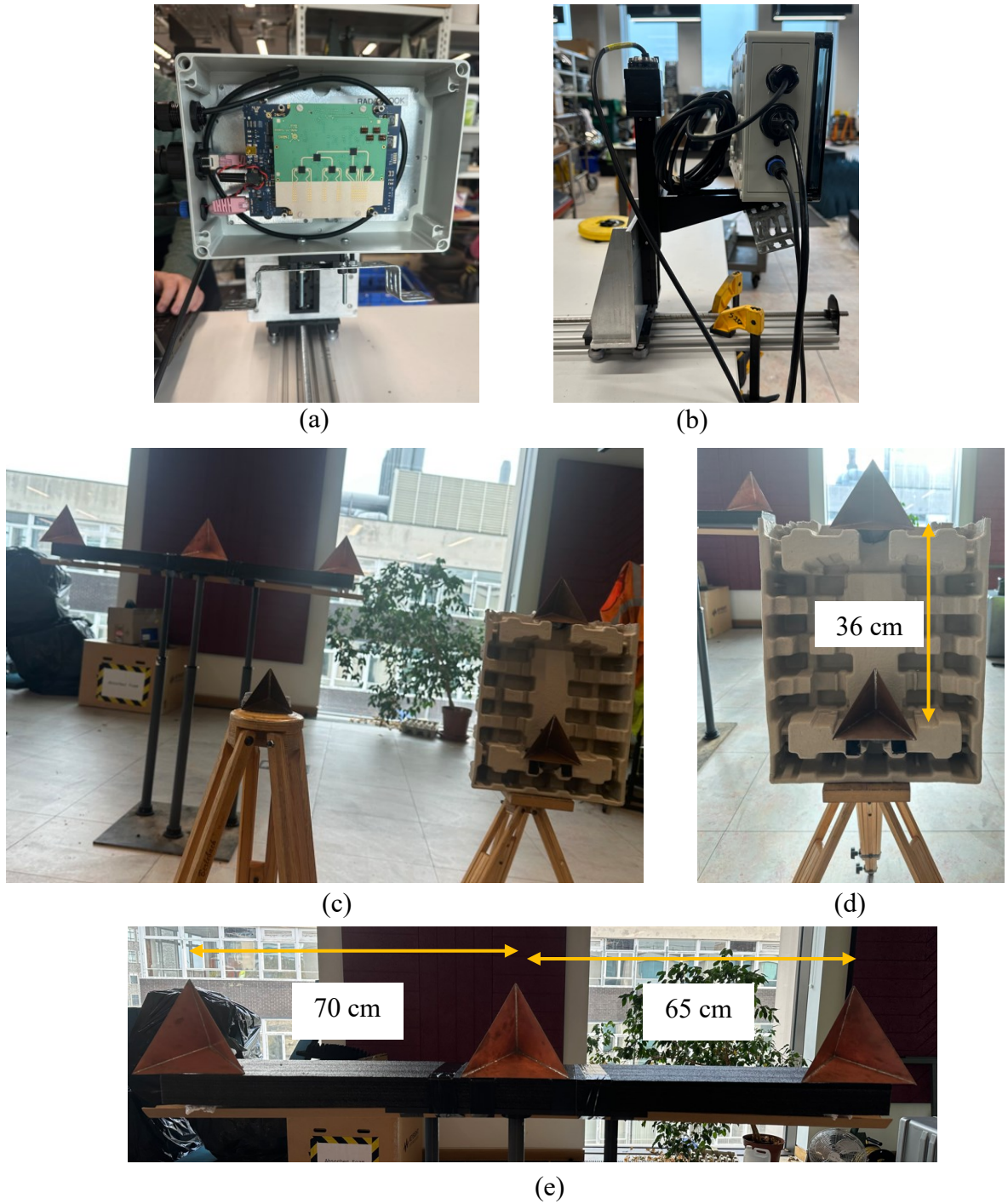


Figure 5.19: (a) INRAS MIMO radar with 77 GHz frontend, (b) the vertical positioner used with the radar, (c) photograph from the experimental site, (d) two corner reflectors at 2.5 m, (e) three corner reflectors at 3.7 m.

For 3-D scene mapping in range, azimuth and elevation the third dimension was added by consecutive changes of the position of the 1-D MIMO radar in elevation using an 8MT175 Standa vertical positioner with minimum displacement steps of  $2.5\mu\text{m}$  [164]. The geometry used for the data collection process is shown in Figure 5.20. Considering a monostatic radar configuration, while the radar is at the 1<sup>st</sup> position, the distance between the transceiver and target is  $r + d_R \sin\theta$ , so the total signal travelling distance is  $2r + 2d_R \sin\theta$ . When the transceiver is moved to the 2<sup>nd</sup> position by  $d_R/2$  towards the z- axis, the total distance becomes  $2r + d_R \sin\theta$ . It is therefore clear that a  $d_R/2$  movement of the transceiver results in a  $d_R$  path difference between data collected at each consecutive position.

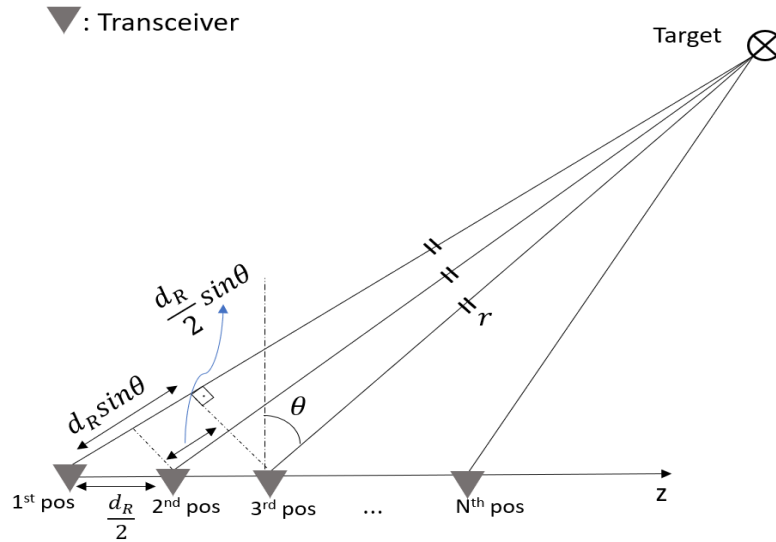


Figure 5.20: The geometrical explanation of the followed direct path of the signal at each transceiver's position.

In the experiment to collect the 3-D data using 1-D MIMO radar, the position of the radar was moved each time by  $\lambda/4$  in elevation, so that the spacing between the virtual elements in elevation is  $\lambda/2$  as both transmitters and receivers are moved simultaneously in this method. For the experimental validation of the proposed method with the first 2-D MIMO antenna configuration given in Section 5.6.2 as an example, the radar was moved in elevation 20 times,

and the 3-D data cube of  $(N_{range}, 29, 20)$  size was formed, where  $N_{range}$  is the number of range bins, and 29 and 20 are the numbers of the array elements in the azimuth and in the elevation dimensions, respectively. To achieve a virtual array of an L-shaped  $20 \times 20$  MIMO configuration, the data of the first 20 elements of the 1-D MIMO in azimuth were used, and data collected from 21 to 29 virtual elements on the 1-D MIMO azimuth were discarded. Hence, a fully populated 20 by 20 virtual array is obtained and its radar response serves as an experimentally reference response for our proposed method.

To compare the proposed method and the L-shaped  $20 \times 20$  2-D MIMO experimental responses, the data cube is reduced from  $(N_{range}, 20, 20)$  to  $(N_{range}, 10, 10)$  which corresponds the virtual array configuration in Figure 5.9(b), and the remaining data is estimated by applying the BA as in Section 5.5.

Figure 5.21 shows the range-azimuth map of (a) L-shaped  $20 \times 20$  MIMO, (b) 4 Tx and 25 Rx 2-D MIMO, (c) extrapolated virtual array of 4 Tx and 25 Rx 2-D MIMO using the BA without the use of any averaging or weightings. The azimuth response of the compact sized 2-D MIMO as in Figure 5.21(b) is wider because there are 10 virtual elements in each row, hence it cannot resolve the corner reflectors at a range of 3.7 m. However, the Burg-aided MIMO estimation enhances the azimuth response and obtains range-azimuth response very close to that of the L-shaped full MIMO as seen in Figure 5.21(c). To highlight the improvement in angular resolutions in Burg-aided MIMO, both zero-azimuth and zero-elevation cuts of experimental response from the corner reflector at 1.7 m are shown in Figures 5.22(a) and 5.22(b). Although the elevation response is a sinc function, the azimuth response exhibits some irregularities in the sidelobes, which is potentially caused by the multipath reflections in the lab as the INRAS radarbook has a wider beam in azimuth of  $51^\circ$  [163].



The azimuth-elevation cut of 3-D data at the range of 2.5 m is shown in Figure 5.23. Whilst the compact size 2-D MIMO can detect the two corner reflectors as just one target as seen in Figure 5.23(b), Burg-aided MIMO separates targets, as expected, which is seen in Figure 5.23(c). The corner reflector at roughly  $-4^\circ$  elevation angle has slightly higher reflection, compared to the reflector at around  $4^\circ$  elevation angle although they are identical. The reason could be slight orientation differences of the corner reflectors, or the cardboard apparatus used to mount the corner reflector. Also, it is clear that Burg-aided responses are very close to the L-shaped MIMO response shown in the 3-D plots of Figure 5.24.

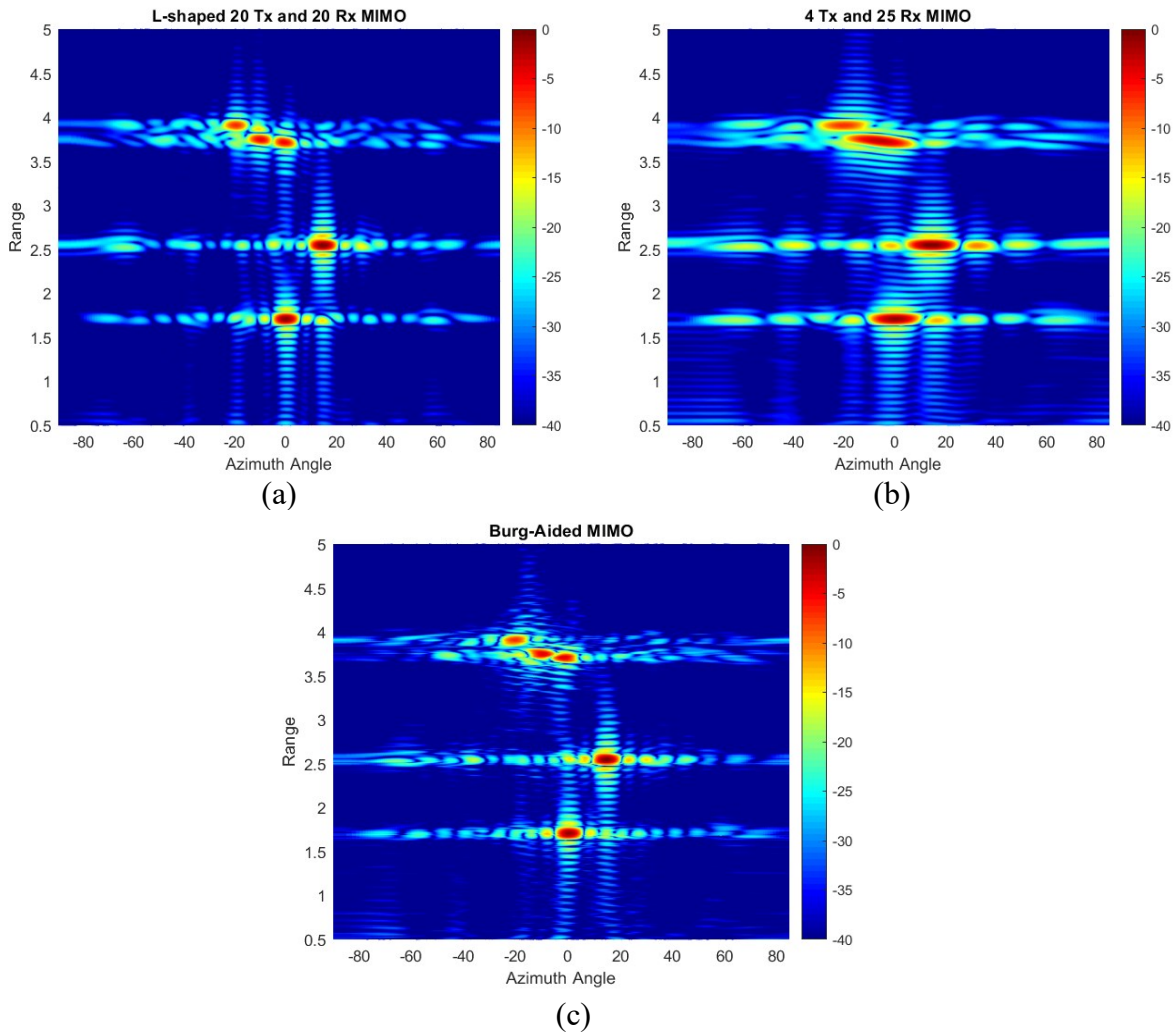


Figure 5.21:Range – Azimuth angle responses of (a) L-shaped 20x20 MIMO radar, (b) compact size 2-D MIMO radar with 4 Tx and 25 Rx, (c) Burg estimation is applied to compact size 2-D MIMO.

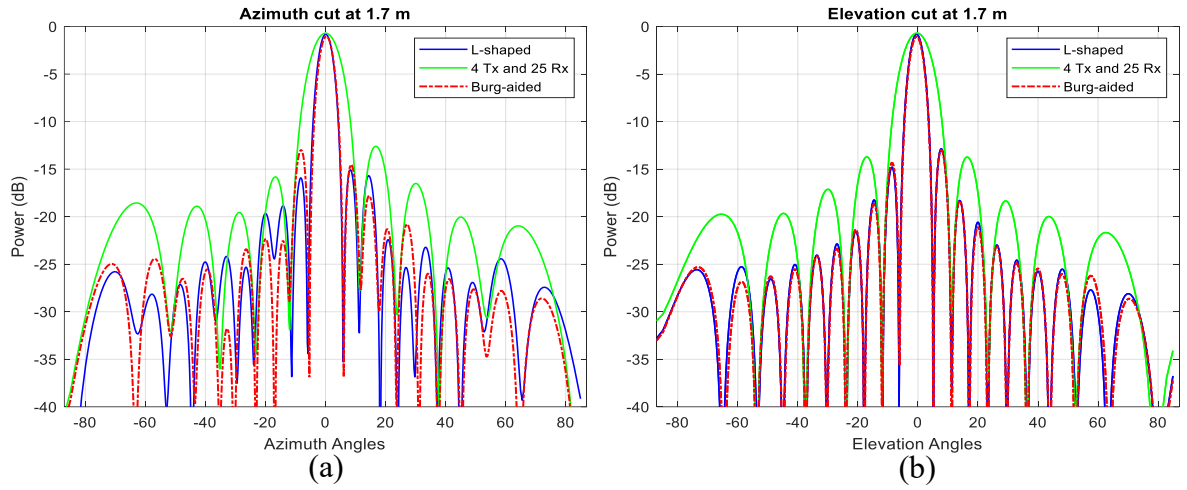


Figure 5.22: The responses of the L-shaped MIMO, compact size MIMO and Burg-aided MIMO for (a) azimuth cut of the corner reflector on the boresight at 1.7 m, (b) elevation cut of the corner reflector on the boresight at 1.7 m.

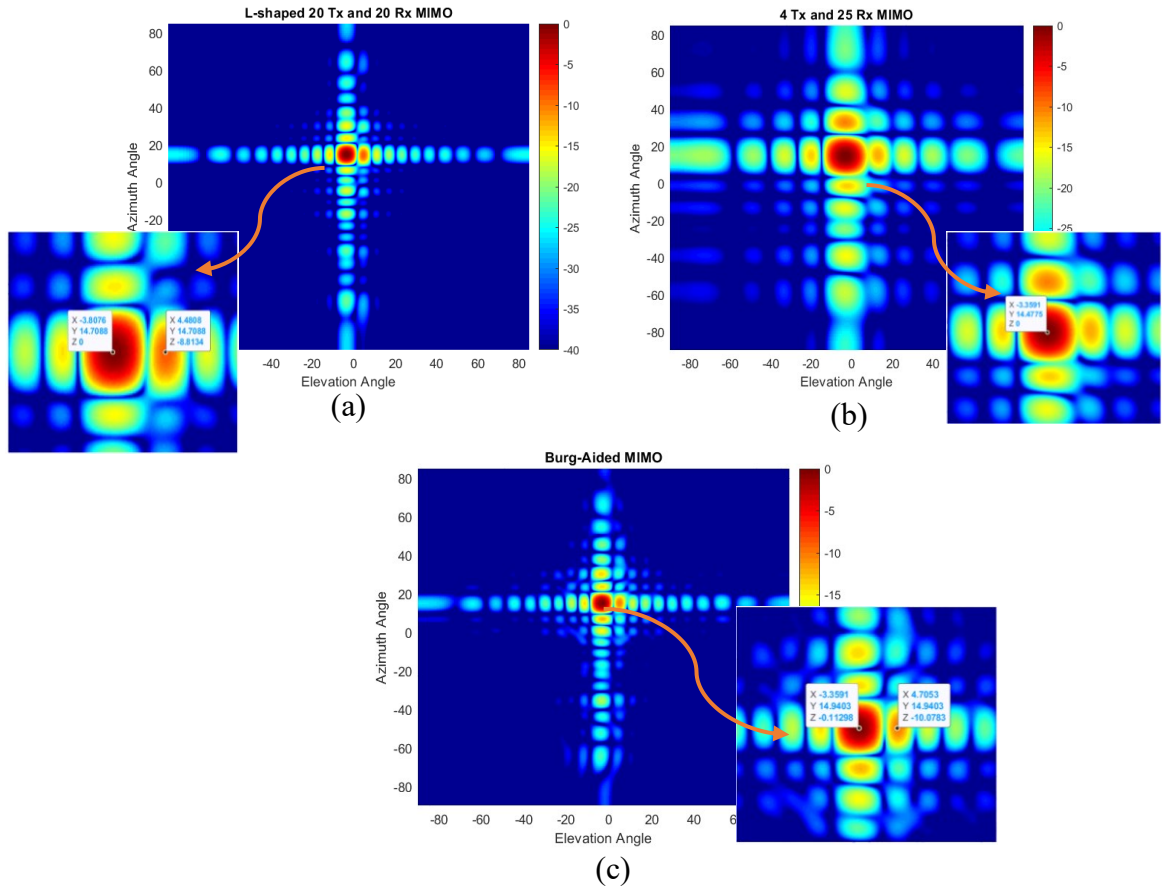


Figure 5.23: 2-D MIMO azimuth - elevation angle maps of two corner reflectors at 2.5 m (a)L-shaped 20x20 MIMO radar, (b) compact size 2-D MIMO radar, (c)Burg-aided MIMO.



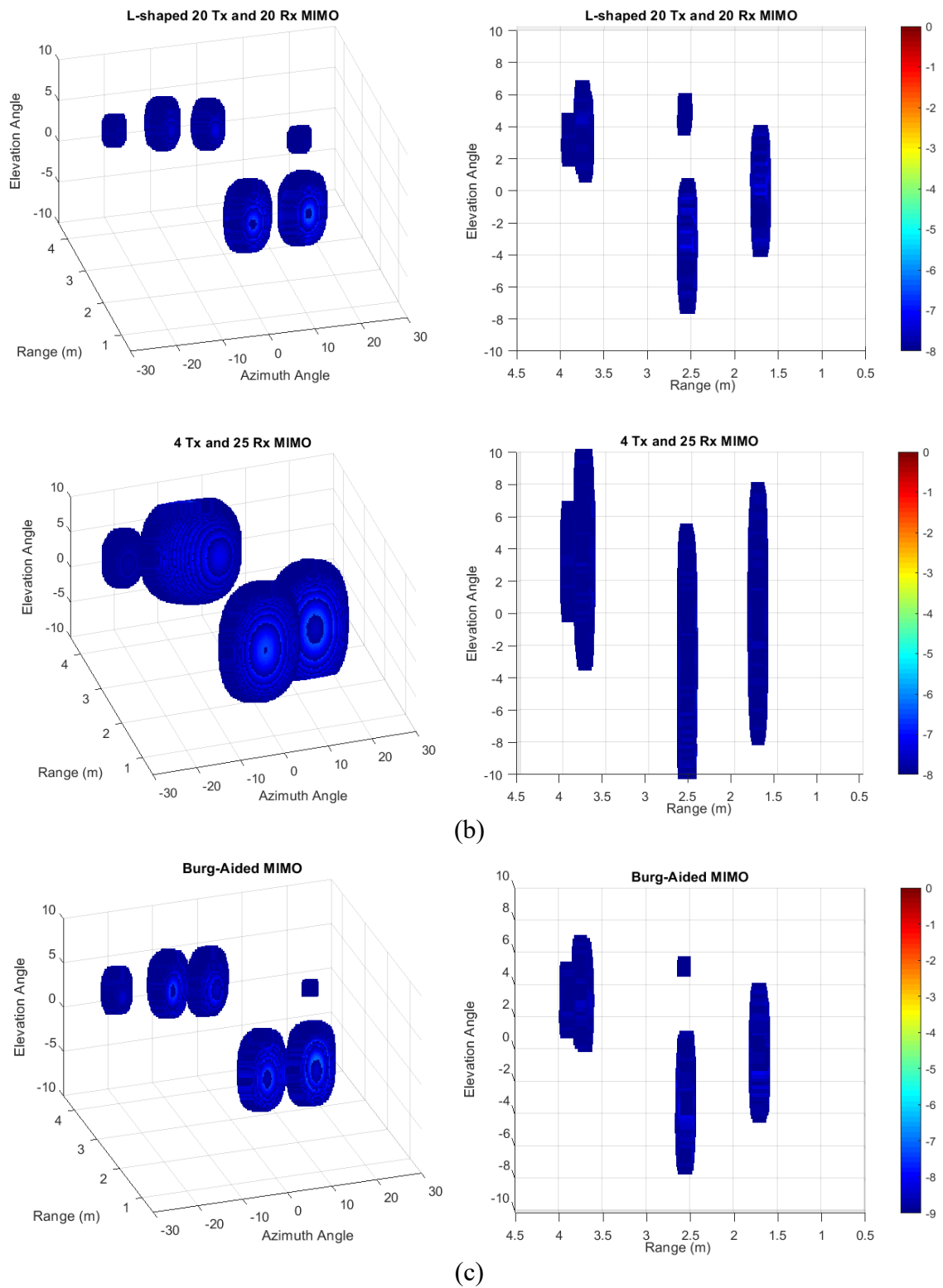


Figure 5.24: 3-D plots of (a) L-shaped 20x20 MIMO radar, (b) compact size 2-D MIMO radar, (c) Burg-aided MIMO.

In Table 5.1, the sensitivity of the proposed method (the Burg-aided 2-D MIMO) to position precision and power accuracy, as compared to a reference MIMO array (L-shaped 20 Tx and 20 Rx 2-D MIMO) is evaluated using measurement results. It is apparent that the difference in the obtained power values is not higher than  $\pm 1.3$  dB whereas the azimuth and elevation estimations differ by no more than  $\pm 0.5^\circ$ , which is within 5% of the boresight beamwidth of actual, non-extrapolated MIMO. Moreover, Burg-aided MIMO gives values closer to that of ground truth. Given that both azimuth and elevation angular resolutions of a compact-sized 2-D MIMO are enhanced by a factor of two via the proposed method, regardless of the number of targets, their RCS values, and their positions, can be determined and these accuracies agree very well with some discrepancy corresponding to expected measurement error.

Table 5.1: Comparison of L-Shaped MIMO and Burg-aided MIMO in terms of power and positional accuracy of targets

		L- Shaped 20 Tx and 20 Rx MIMO			Burg-Aided MIMO			Changes		
Target	Range	Power ( $P_L$ )	Azimuth ( $Az_L$ )	Elevation ( $El_L$ )	Power ( $P_B$ )	Azimuth ( $Az_B$ )	Elevation ( $El_B$ )	$\Delta P = P_L - P_B$	$\Delta Az = Az_L - Az_B$	$\Delta El = El_L - El_B$
Target I	1.7 m	-0.81 dB	$0^\circ$	$-0.448^\circ$	-1.063 dB	$0^\circ$	$-0.448^\circ$	0.253 dB	$0^\circ$	$0^\circ$
Target II	2.5 m	0 dB	$14.709^\circ$	$-3.808^\circ$	-0.113 dB	$14.940^\circ$	$-3.359^\circ$	0.113 dB	$-0.231^\circ$	$-0.449^\circ$
Target III	2.5 m	-8.813 dB	$14.709^\circ$	$4.481^\circ$	-10.078 dB	$14.940^\circ$	$4.705^\circ$	1.265 dB	$-0.231^\circ$	$-0.224^\circ$
Target IV	3.711 m	-4.90 dB	$-0.671^\circ$	$2.911^\circ$	-4.078 dB	$-0.895^\circ$	$2.911^\circ$	-0.822 dB	$0.224^\circ$	$0^\circ$
Target V	3.743 m	-4.630 dB	$-9.897^\circ$	$3.359^\circ$	-4.052 dB	$-9.670^\circ$	$3.135^\circ$	-0.578 dB	$-0.227^\circ$	$0.224^\circ$
Target VI	3.903 m	-6.808 dB	$-19.867^\circ$	$2.687^\circ$	-7.047 dB	$-20.106^\circ$	$2.686^\circ$	0.029 dB	$0.239^\circ$	$0.01^\circ$

## 5.8 Conclusion

The main benefit of using extrapolation offered by BA is an opportunity to obtain fine resolution by use of compact hardware with small number of physical elements and occupied area. This would offer not only a cost-effective solution but allow use of such sensor in applications where allocation of space is under severe constraints, as, for instance, in case of densely packed vehicle internal infrastructure. Moreover, fewer transmit elements in TDM MIMO array would mean larger and therefore more favourable unambiguous Doppler, which would make a radar to be better suitable for use from moving platform and with moving targets. In this chapter, the performance of the Burg algorithm to both interpolate and extrapolate data for improved spatial resolution as well as associated limitations have been examined in both 1-D and 2-D MIMO arrays. Also, in the experiment part, the authors have described methodology to generate 3-D data (range, azimuth and elevation information) using a 1-D MIMO array.

The general rule of how to design an initial compact MIMO allowing extrapolation in cases of both regular and sparse element positioning has been presented and discussed with several design realizations. It has been shown that even extrapolation factor 3 can deliver expected super-resolution performance, though the linearity of algorithm response at higher factors as well as transition to near-field zone of the larger virtual antenna put constraints on the viability of extrapolation with higher factors. The proposed method has been validated through both simulation and experimentation at 77 GHz with targets of the different RCSs.

Importantly while point-like targets have been considered to validate the simulation results, the value of this approach is that in the case of extended targets, the Burg-aided MIMO resolution would define more image-like extended target representation within the radar map, also thanks to the sensitivity of mm-wave radar to surface texture. Based on that, in the next

chapter, the performance of the Burg algorithm is evaluated with the aim of producing enhanced imagery of an automotive real-world road environment using an off-the-shelf automotive MIMO radar carried by a moving vehicle.

# Chapter 6 – Burg-aided MIMO-DBS

## 6.1 Introduction

To achieve higher levels of autonomous driving, imaging radar that is robust, regardless of lighting and weather conditions, is required in order to provide reliable, accurate and precise situational awareness. Spatial resolution is one of the important parameters enabling detection, differentiation and recognition of closely positioned targets. Doppler beam sharpening (DBS) is a technique which achieves cross-range resolution beyond that of antenna aperture by exploiting the motion of the radar platform. Furthermore, in the literature, the motion of the MIMO radar platform has been exploited using Doppler beam sharpening, named as MIMO-DBS, to obtain higher cross-range resolution in the off-boresight while suppressing high sidelobe levels inherent in MIMO. However, there have been no improvements made in the boresight direction which is the most crucial for path planning.

This chapter proposes a technique that applies the Burg algorithm to MIMO radar data collected along path formed by the platform's motion to enhance the cross-range resolution in the boresight direction and to achieve further enhanced cross-range resolution in the off-boresight directions. The performance of the proposed method is evaluated through simulation as well as both lab-based and real-world environment experiments at 77 GHz.

The remainder of this chapter is organised as follows. Section 6.2 provides a review of the key literature and Section 6.3 describes in detail the DBS technique and MIMO-DBS. The proposed method and the simulation and experimental results are presented and discussed in Sections 6.4 and 6.5 respectively. Finally, conclusions are formulated and presented in Section 6.6.

The part of this work has been presented at the 2023 EURAD conference in Berlin, Germany [165].

## 6.2 State of the Art

Angular resolution is defined by antenna effective aperture size, and in the case of a MIMO array, the same angular resolution can be achieved with significantly fewer antenna elements, compared with the uniform phased array as demonstrated in Chapter 2. However, unlike mechanically scanned radars but similar to electronically scanned phased arrays, the length of the effective aperture decreases when the target is off-boresight, which worsens the angular resolution in the off-boresight directions, in other words there is an increase in the -3 dB beamwidth (half-power) of the main lobe.

Alternatively, the cross-range resolution can be made finer by taking advantage of the motion of the radar platform. Doppler beam sharpening (DBS) is a technique, primarily utilized in airborne radar applications [166], [167], [168], [169], [170] that has been adapted for automotive radar. Experimental validation has been achieved using a side-looking frequency-modulated continuous-wave (FMCW) radar operating within the range of frequencies from mm-wavelengths to sub-THz frequencies in [171], [172], [173], [174]. Due to the motion of the radar, each stationary target is viewed at different angles and hence has different relative Doppler shifts during motion of the platform. DBS exploits this shift in order to enhance the angular resolution beyond that of the physical aperture. However, when using the DBS

technique with forward-looking radars, the direction to the target cannot be determined unambiguously since it appears at either side of the boresight axis. To resolve such ambiguity, the Doppler beam sharpening (DBS) technique can be used in combination with a MIMO array, as proposed in [175], [176]. This takes advantage of both techniques on a moving platform to improve the achievable angular resolution in both the forward (defined by MIMO) and side looking (defined by DBS) directions. Both simulation and real-world experimental results have demonstrated that DBS not only effectively improves angular resolution in the off-boresight but also enables a significant reduction in the sidelobe levels.

However, the cross-range resolution in the forward-looking direction, which is the most important region in automotive radar for path planning, is defined by the MIMO array in the MIMO-DBS technique, so there is no improvement in angular resolution caused by the DBS technique in such region. It is also important to reduce the physical size of the MIMO radar to meet the requirements of dense packaging within a vehicle's infrastructure and associated costs. Although a MIMO array has fewer antenna elements (compared with the phased array), the number of antenna elements in a conventional MIMO still remains very large. Another important consideration is that automotive radars typically use FMCW waveforms, and to provide orthogonality among the transmitted signals, transmitters are activated in different time slots using TDM. Hence, if the number of transmitters is increased, the radar response time increases in TDM, and this reduces the Doppler unambiguous range because it is inversely proportional with MIMO frame interval. Therefore, to reduce the cost and size of the MIMO array, a further reduction in the number of antenna elements is desirable but the challenge is to still maintain acceptable sidelobe levels for a desired beamwidth.

One further critical issue regarding MIMO-DBS is that the improvement in the angular resolution in the off-boresight direction depends on the total coherent processing interval (CPI).

As the CPI increases, the relevant angular resolution is enhanced. However, increasing the CPI may result in significant range cell migration (RCM), especially when both high range resolution and high platform speed are required. More explanation on RCM is given in Section 6.3.1.

Here, the use of autoregressive methods is proposed to interpolate and/or extrapolate the data gathered through the motion of a MIMO radar in two dimensions – Doppler and angular across virtual array elements. Thus, the total number of antenna elements and, accordingly the size of the antenna, can be decreased and the required CPI time is reduced whilst achieving higher angular resolution in both the boresight and lateral directions, compared to MIMO-DBS. As an autoregressive method, the Burg algorithm (BA) is chosen in this study as it is fast, easy to implement, yields a prediction filter, and is capable of improving the resolution by up to a factor of three [151], [152], [153], [154] as demonstrated in Chapter 5. The performance of BA has been analysed in the literature as stated in Chapter 5. However, in terms of SAR and DBS, BA was only applied to either missing SAR data to enhance the image quality by estimating the missing data [148] or the DBS data to enhance the cross-range resolution [149]. To the best of our knowledge, no one has so far implemented the autoregressive method to the MIMO-DBS data in order to enhance angular resolution in both boresight and lateral directions.

In this chapter, the Burg algorithm is combined with MIMO-DBS in order to enhance angular resolution in the boresight direction and to achieve further enhanced angular resolution in the off-boresight direction. The validation and analysis of the proposed approach are conducted via evaluation of the performance of a 1-D MIMO antenna array through simulations and both lab-based and real-world experiments carried out using a close-to-market off-the-shelf 77 GHz radar.



## 6.3 Background

For the integrity of the description of the proposed approach, the algorithms and methods used are explained in detail in this section. However, since the MIMO radar concept and the Burg algorithm are described in Chapters 2 and 5, respectively, they will not be repeated here.

### 6.3.1 Doppler Beam Sharpening

The motion of the radar platform causes relatively different Doppler shift of the stationary targets at different angles. By exploiting this shift, Doppler beam sharpening (DBS) enhances the angular resolution beyond that of the real or virtual aperture. Figure 6.1 illustrates the DBS geometry. Doppler frequency of the target depending on its radial velocity,  $v_r$ , is given as [171], [175]

$$f_d = \frac{2v_r}{\lambda} = \frac{-2|\mathbf{v}_p|\cos\alpha}{\lambda} \quad (6.1)$$

where  $\mathbf{v}_p$  is the platform velocity vector and  $\alpha$  is the angle between the target velocity vector and platform velocity vector.

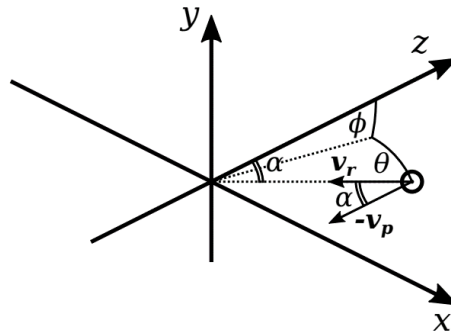


Figure 6.1: Geometry of DBS and relative velocity vector of a single stationary point target [175].

It is important to note that when the target is not stationary, the movement of the target must be distinguished from the motion of the radar platform to process the DBS technique. To compensate the motion of the target, adaptive systems may be used because the velocity of the radar platform is known, but this is out of the scope of this thesis.

Although the improvement in the cross-range resolution via the DBS technique is stated in [171], it is detailed here for the sake of completeness. Assuming that the radar antenna has a -3 dB beamwidth of  $\theta_{ant}$  and a look angle of  $\theta_{look}$  which is the angle between the antenna phase centre and the platform's velocity vector, the radar can detect targets at angles ranging from  $(\theta_{look} - \frac{\theta_{ant}}{2})$  to  $(\theta_{look} + \frac{\theta_{ant}}{2})$  as shown in Figure 6.2(a). Therefore, the obtainable highest and lowest Doppler frequencies are given by

$$f_d^h = \frac{2v_p}{\lambda} \cos\left(\theta_{look} - \frac{\theta_{ant}}{2}\right) \quad (6.2)$$

and

$$f_d^l = \frac{2v_p}{\lambda} \cos\left(\theta_{look} + \frac{\theta_{ant}}{2}\right) \quad (6.3)$$

As a result, the Doppler spread caused by the platform's motion across the antenna beam may be written as

$$\Delta f = f_d^h - f_d^l = \frac{2v_p}{\lambda} \left( \cos\left(\theta_{look} - \frac{\theta_{ant}}{2}\right) - \cos\left(\theta_{look} + \frac{\theta_{ant}}{2}\right) \right) \quad (6.4)$$

Also, the Doppler bin width is dependent on the total coherent processing interval (CPI),  $T$ , and given by

$$\Delta f_{-3dB} = \frac{1}{T} \quad (6.5)$$

Hence, the number of Doppler bins in the Doppler spread can be calculated as [171]

$$\begin{aligned}
n &= \frac{\Delta f}{\Delta f_{-3dB}} = \frac{2Tv_p}{\lambda} \left( \cos \left( \theta_{look} - \frac{\theta_{ant}}{2} \right) - \cos \left( \theta_{look} + \frac{\theta_{ant}}{2} \right) \right) \\
&= \frac{4Tv_p}{\lambda} \sin(\theta_{look}) \sin \left( \frac{\theta_{ant}}{2} \right)
\end{aligned} \tag{6.6}$$

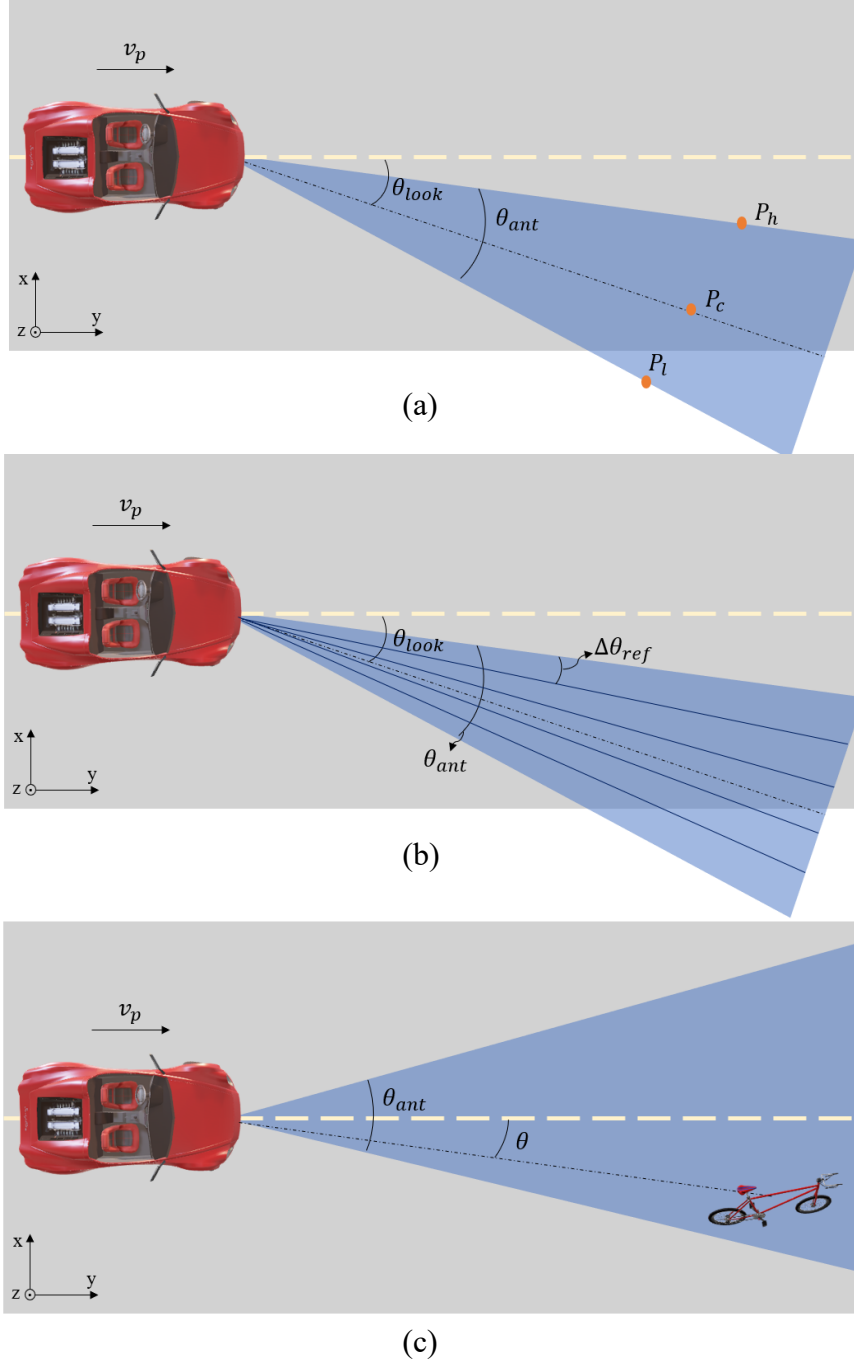


Figure 6.2: (a) Side looking DBS scenario, (b) improvement in the angular resolution via DBS, (c) forward looking DBS.

The  $n$  is the refinement factor, and if  $n$  is not greater than 1, it can be said that there is no refinement in the angular resolution. After the DBS technique, the obtained refined angular resolutions are depicted in Figure 6.2(b), and the average angular resolution for the antenna beam following DBS refinement can be determined by [171]

$$\Delta\theta_{ref} = \frac{\theta_{ant}}{n} \quad (6.7)$$

If  $\theta_{look}$  is equal to 0 degree, it is called as forward looking. The geometry is shown in Figure 6.2(c). In this case, the highest and lowest Doppler frequencies of the target differ from those shown in (6.2) and (6.3). In forward looking scenario, these Doppler frequencies vary depending on the target's relative angle to the radar,  $\theta$ . For example, there is no angular refinement for targets centred on boresight since the target's Doppler frequency remains constant during the platform's motion. However, improvement in the angular resolution is observed as the target moves away from boresight. The relationship between the angular resolution and the target's angle in the DBS technique is given by [175]

$$\theta_{DBS\_FL} \cong \frac{0.9 \lambda}{2Tv_p \sin \theta} \quad (6.8)$$

where  $\theta$  is the angle of the target relative to the radar antenna boresight axis and  $T$  is the total coherent processing interval. The scaling factor of 0.9 used here is just a rounding of the 0.88 in the angular resolution equation.

It is obvious that the angular resolution becomes enhanced as the  $\theta$  angle increases due to the sine relationship. It should be noted that the forward-looking DBS technique is not able to decide the direction of the angle of the target since the cosine relationship in Doppler frequency in (6.1) omits the  $(\mp)$  sign of the angle. This is the main disadvantages of the forward-looking DBS technique.

Due to the motion of the radar platform and the data collection geometry of the DBS, targets in the scene may appear in different range bins during the data acquisition time. This is called range cell migration (RCM) and is calculated by the following equation.

$$N_{RC} = \frac{\text{total travelled distance by the radar}}{\text{range resolution}} \cos\alpha = \frac{Tv_p}{(c/2B)} \cos\alpha \quad (6.9)$$

where  $N_{RC}$  is the number of range cell and  $B$  is the radar bandwidth. If  $N_{RC}$  is bigger than 1 for a target at  $\alpha$  angle, there is a range cell migration. In this case, the collected energy is spread across different range bins instead of concentrating in one range bin, which causes a smearing and defocussing effect on the radar results. When the  $N_{RC}$  is high, the effect of RCM becomes significant. To prevent these issues, range cell migration correction (RCMC) should be done so that the spreading energy can be concentrated in one range bin. However, the RCMC methods are beyond the scope of this thesis. Further, the usage of weightings may reduce smearing and blurring effects of the RCM by sacrificing resolution.

### 6.3.2 MIMO-DBS

The combination of MIMO and DBS improves angular resolution in the off-boresight direction and reduces sidelobes inherent in MIMO [175]. Furthermore, the angular ambiguity of the forward-looking DBS technique is also handled by the combined MIMO-DBS technique, allowing determination of the direction of the target. Briefly, in MIMO-DBS processing, a 3-D radar data cube is reduced to a 2-D data by selecting the intersecting samples in both the MIMO and DBS dimensions. The DBS angle  $\alpha$  in a 2-D array is

$$\cos\alpha = \cos\theta\cos\phi \quad (6.10)$$

where  $\theta$  and  $\phi$  are azimuth and elevation angles, respectively. In the case of employing a 1-D array,  $\alpha$  is equal to  $|\theta|$  by assuming the target's elevation angle is close to 0.

The approximately -3 dB beamwidth achieved using the combination of MIMO-DBS technique is given by [175]

$$\theta_{3dB\_MIMO-DBS} \approx \frac{0.9}{\sqrt{\left(\frac{(N-1)d_v}{\lambda} \cos\theta\right)^2 + \left(\frac{2Tv_p \sin\theta}{\lambda}\right)^2}} \quad (6.11)$$

where  $N$  is the number of virtual array elements, and  $d_v$  is the spacing between virtual array elements. It is noteworthy that when the platform velocity,  $v_p$ , is equal to 0, equation (6.11) gives the angular resolution of the MIMO antenna whereas when  $N = 1$ , the equation gives the angular resolution of the DBS.

An improvement in angular resolution is obtained for targets positioned at angles greater than  $\theta'$  as stated in [175]. The farther the target's angular position is from  $\theta'$ , the higher is improvement in the resolution:

$$\theta' = \arctan\left(\frac{(N-1)d_v}{2Tv_p}\right) \quad (6.12)$$

It is obvious from eq. (6.11) and (6.12) that as the total coherent processing interval,  $T$ , increases, the angular resolution improves. This increase in  $T$  also improves the velocity resolution,  $\Delta v$ , since  $\Delta v \cong \lambda/(2T)$ . However, increasing  $T$  too much may lead to RCM as expected from (6.9), hence, it should be noted that there is always a trade-off between resolutions and range cell migration whilst deciding the value of  $T$ .

It is worth noting that when the orthogonality among the transmitted waveforms in the MIMO array is achieved by time-division-multiplexing, a phase error induced by the motion of the platform occurs, and this phase error should be compensated before beamforming. The phase error is given, assuming the velocity is constant, by [175]

$$\Delta\beta = \frac{4\pi v_r T_{chirp} u}{\lambda} \quad (6.13)$$

where  $T_{chirp}$  is the pulse repetition interval and  $u$  is the  $u^{\text{th}}$  transmitter.

## 6.4 Proposed Algorithm and Simulation Results

Here the proposed method, referred as Burg-aided MIMO-DBS, is described. It allows achievement of higher angular resolutions in both the boresight and off-boresight directions of front-looking radar beyond that of the standard MIMO-DBS technique. At first, after the range-compression, the Burg algorithm is applied to extrapolate the data in the Doppler domain. A Doppler FFT is taken and phase shifts in MIMO nodes arising due to the motion of the radar platform are compensated. Secondly, Burg algorithm is applied in the angular dimension to increase the number of virtual array elements. After that, the 3-D data cube is obtained by taking an FFT along the angular dimension. Finally, to form a range-angle map of the scene, samples are selected from the data cube at points where MIMO and DBS angles are equivalent, as described in Section 6.3.2. The flow chart of the data processing of the Burg-aided MIMO-DBS is illustrated in Figure 6.3.

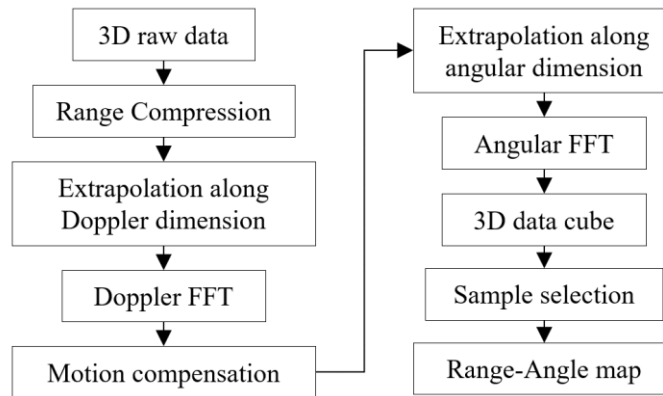


Figure 6.3: Flow chart of the proposed algorithm.

The equation of the acquired angular resolution in the Burg-aided MIMO-DBS technique can be rewritten as follows.

$$\theta_{3dB\_Burg-aided\_MIMO-DBS} \approx \frac{0.9}{\sqrt{\left(\frac{\varepsilon_{f\_a}(N-1)d_v}{\lambda} \cos\theta\right)^2 + \left(\frac{2\varepsilon_{f\_d}Tv_p \sin\theta}{\lambda}\right)^2}} \quad (6.14)$$

where  $\varepsilon_{f\_a}$  is extrapolation factor along the virtual array number whereas  $\varepsilon_{f\_d}$  is the extrapolation factor along the Doppler dimension.

The simulation results of modelling of achievable -3 dB beamwidths obtained by DBS, MIMO, MIMO-DBS, and Burg-aided MIMO-DBS methods are shown in Figure 6.4 using radar parameters shown in the Table 6.1. As an example, the velocity of the radar platform is taken as 2 m/s and the total coherent integration time is chosen to be 128 ms. Here, a bandwidth of 500 MHz is used to understand the performance of the proposed method with no-range cell migration. In Figure 6.4, it is shown that as the angle to the target moves away from zero degrees, the angular resolution in case of MIMO beamforming decreases while it improves in the case of DBS. As expected from (6.12), the transition point  $\theta'$  of MIMO-DBS technique is  $12.9^\circ$  for a given speed of the platform and other parameters, indicated by a dashed vertical line

Table 6.1: Radar parameters in Simulation

Parameters	Value
Modulation	FMCW
Centre frequency	77 GHz
Bandwidth	0.5 GHz
Sample rate	10 MSa/s
Samples per chirp	2048
Chirp interval	230 $\mu$ s
MIMO frame interval	1 ms
Frame interval	128 ms
Beamwidth	$1.7^\circ$



in Figure 6.4. After  $12.9^\circ$ , MIMO-DBS technique improves the angular resolutions, compared to MIMO. Moreover, the additional angular improvement is obvious in Figure 6.4 when the Burg algorithm is applied to both the Doppler and angular dimensions using MIMO-DBS. Further, since the extrapolation factor 2 is used in both dimensions, the on- and off-boresight resolutions are also refined by a factor of two.

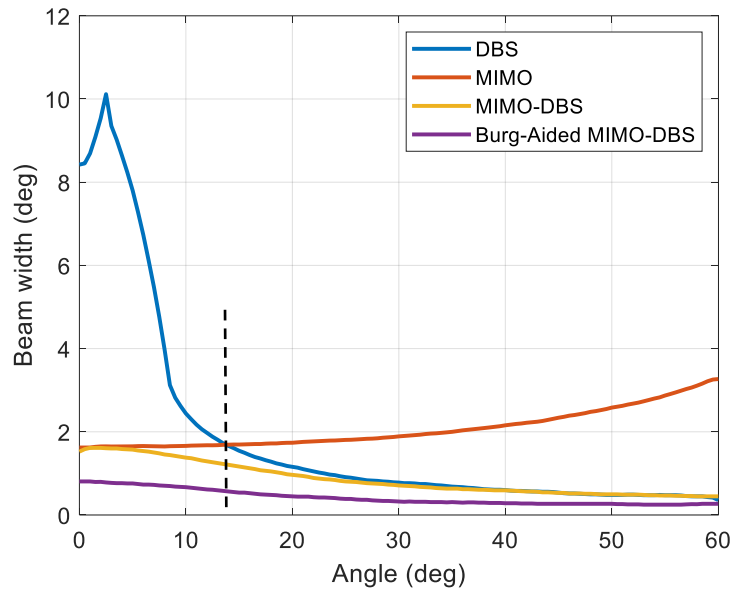


Figure 6.4: Angular resolutions for DBS, MIMO, MIMO-DBS, Burg-aided MIMO-DBS.

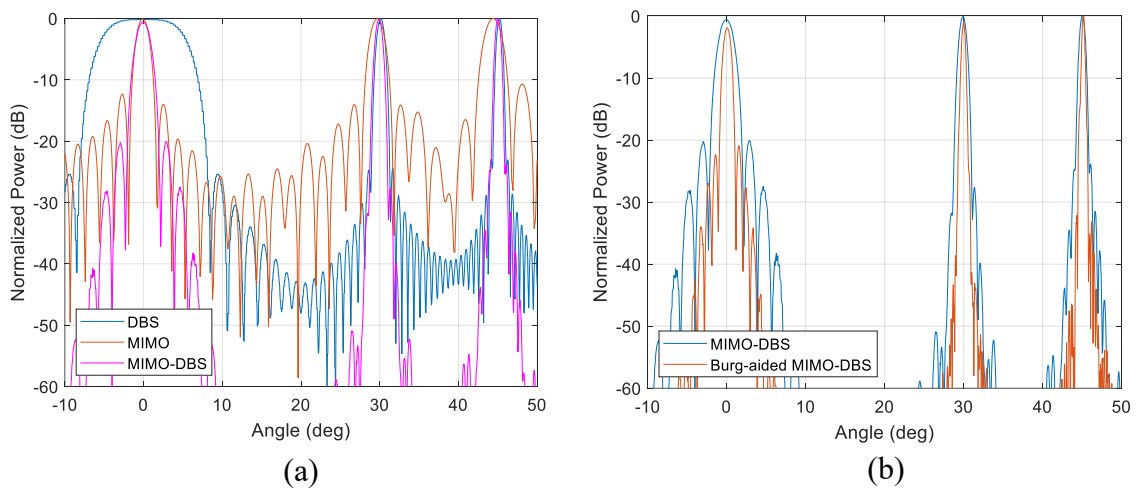


Figure 6.5: (a)Azimuth cut of DBS, MIMO, and MIMO-DBS, (b) azimuth cut of MIMO-DBS and Burg-aided MIMO-DBS.

In the second simulation scenario, there are three targets located at  $0^\circ$ ,  $30^\circ$ , and  $45^\circ$  at the same range in the far field region of the radar. The angular responses of each method are plotted in Figure 6.5(a) and 6.5(b), using the same radar parameters as in the first simulation. The angular resolution of the MIMO-DBS technique is equal to the MIMO's resolution at  $0^\circ$ , and higher resolution is attained by implementing Burg algorithm in both Doppler and angle. Similarly, there is an angular resolution improvement for targets located off-boresight in the Burg-aided MIMO-DBS technique, compared to the MIMO-DBS technique in Figure 6.5(b).

In the next simulation, 42 point-like targets are regularly placed with a separation of 3 m from -9 m to 9 m in cross-range and with a separation of 5 m in range in the region from 20 m to 45 m. It is assumed that all targets have the same elevation of 0 m and the radar parameters (Table 6.1), and platform velocity (2 m/s) are the same as in previous scenarios. The MIMO response in Figure 6.6(a) shows very high sidelobe levels. Figure 6.6(b) shows the range – cross-range map of the MIMO-DBS technique after compensating for the phase error caused by platform speed. It is clear that the MIMO-DBS technique not only improves the angular resolution off-the-boresight, but also suppresses the sidelobe levels. The impact of the Burg algorithm is examined in Figure 6.6(c) and (d) in the case of extrapolating only Doppler data using MIMO-DBS and extrapolating only the angular data of the MIMO-DBS, respectively. In both cases an extrapolation factor of two is used. Although the angular resolution in both cases generally improves at all-angles, extrapolating data towards angular dimension enhances the on-boresight whereas extrapolating the Doppler data has a significant impact on the off-boresight. Hence, when the MIMO-DBS data is extrapolated in both azimuth and Doppler dimensions twice via the BA, angular resolutions in both forward and lateral directions enhance twice as shown in Figure 6.6(e).

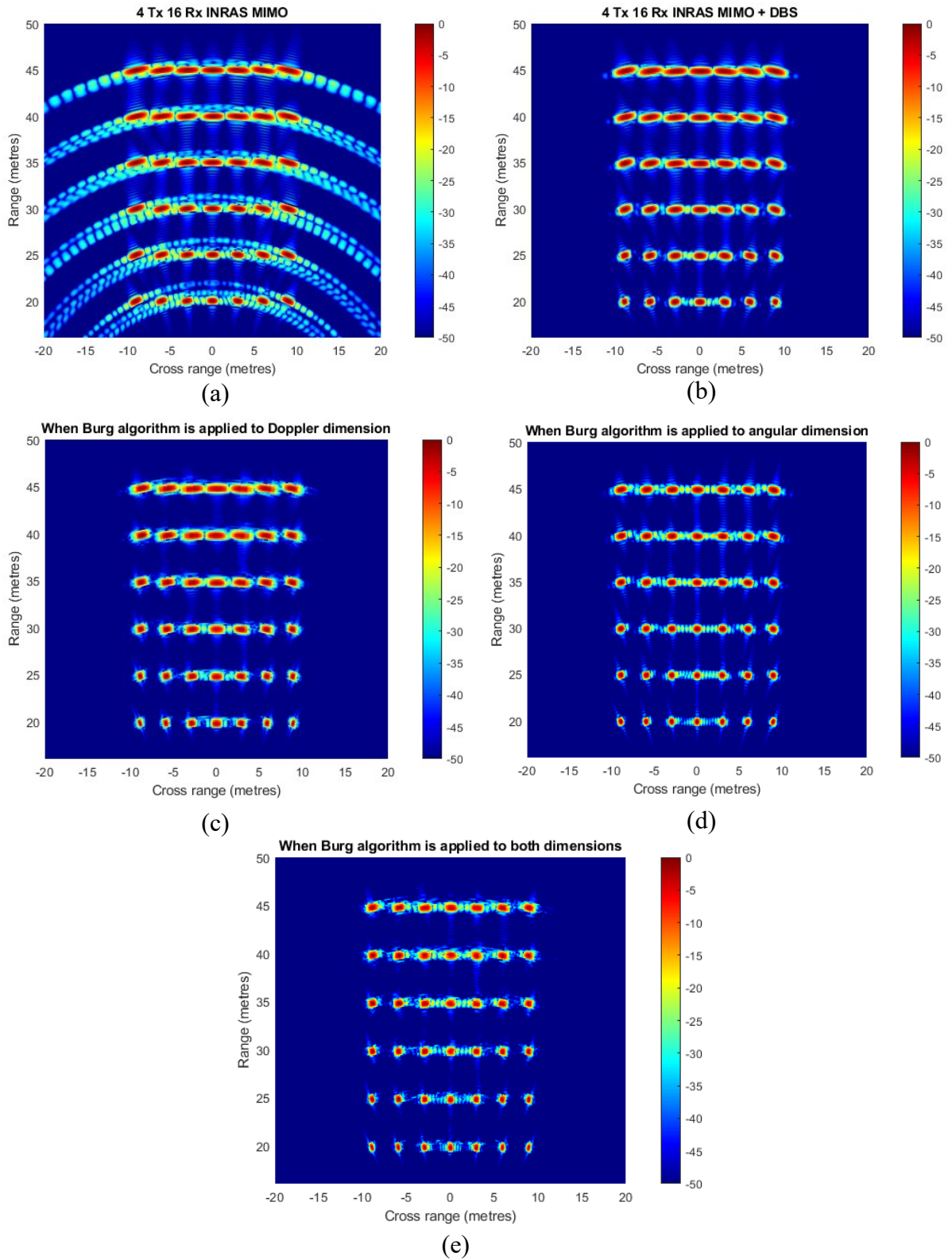


Figure 6.6: Range – cross range responses of (a) MIMO, (b) MIMO-DBS, (c) only Doppler data is extrapolated via the BA, (d) only angular data is extrapolated via the BA, (e) the BA is applied towards both azimuth and Doppler dimensions.

## 6.5 Experimental Results

In this section, both laboratory-based and real-world experimental results are presented to validate the proposed Burg-aided MIMO-DBS method.

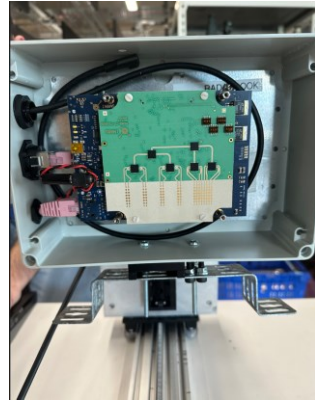
The experimental setup is the same as the experimental setup in Section 5.7, but with the addition of a rectangular target positioned at 2.5 m along the ground range and 0.8 m in the cross-range, as depicted in Figure 6.7. The experimental data has been collected using an INRAS Radarbook radar operating at 77 GHz. It has 4 transmitters and 8 receivers aligned in azimuth as shown in Figure 6.8(a) [163]. Due to the overlapping of three elements, the 1-D MIMO configuration provides 29 virtual elements with half-wavelength spacing. A bandwidth of 500 MHz was used, which provides a nominal range resolution of 30 cm. The radar parameters used during the lab-based experiment are detailed in Table 6.2.



Figure 6.7: The lab-based experimental setup.

Table 6.2: Radar parameters used in lab-based experiment

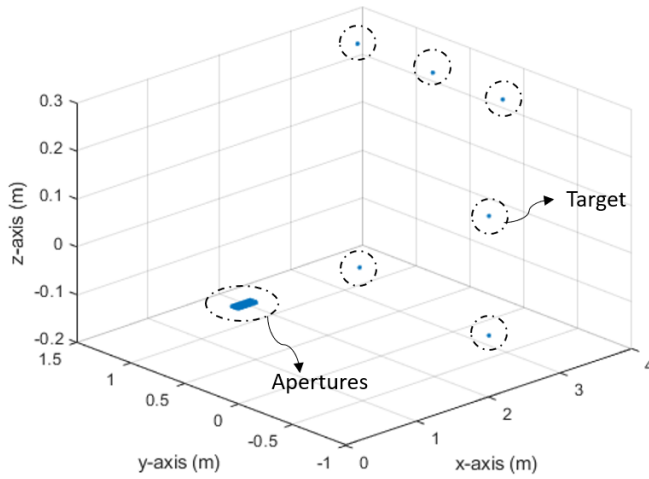
Parameters	Value
Modulation	FMCW
Centre frequency	77 GHz
Bandwidth	500 MHz
Transmitter Number	4
Receiver Number	8
Virtual array number	29
Chirp interval	256 $\mu$ s
MIMO frame interval	1.25 ms
Frame interval	137.5 ms
Velocity of the radar	1.6 m/s
Step of data collection	2 mm



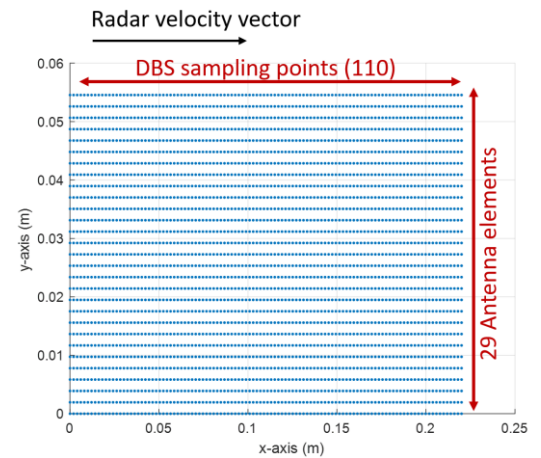
(a)



(b)



(c)



(d)

Figure 6.8: (a) INRAS MIMO radar with 77 GHz frontend, (b) the linear positioner used with the radar, (c) the experimental scenario, (d) collected data points during the experiment.

The radar platform's forward motion was ensured using a precise linear positioner. The velocity of the platform is 1.6 m/s and allows the radar to collect data at 2 mm intervals. With 110 sweeps, the total aperture length is 22 cm which is smaller than the range resolution and mitigates any RCM. The collected data points allow formation of the aperture through the motion of the platform. This is illustrated in Figure 6.8(c) and 6.8(d).

The experimental responses of INRAS MIMO, MIMO-DBS and Burg-aided MIMO-DBS are shown in Figure 6.9. The position of the rectangular target is unclear due to high sidelobe levels inherent in MIMO. However, when MIMO-DBS technique is applied, not only are the angular responses on the off-boresight enhanced but also the rectangular target becomes

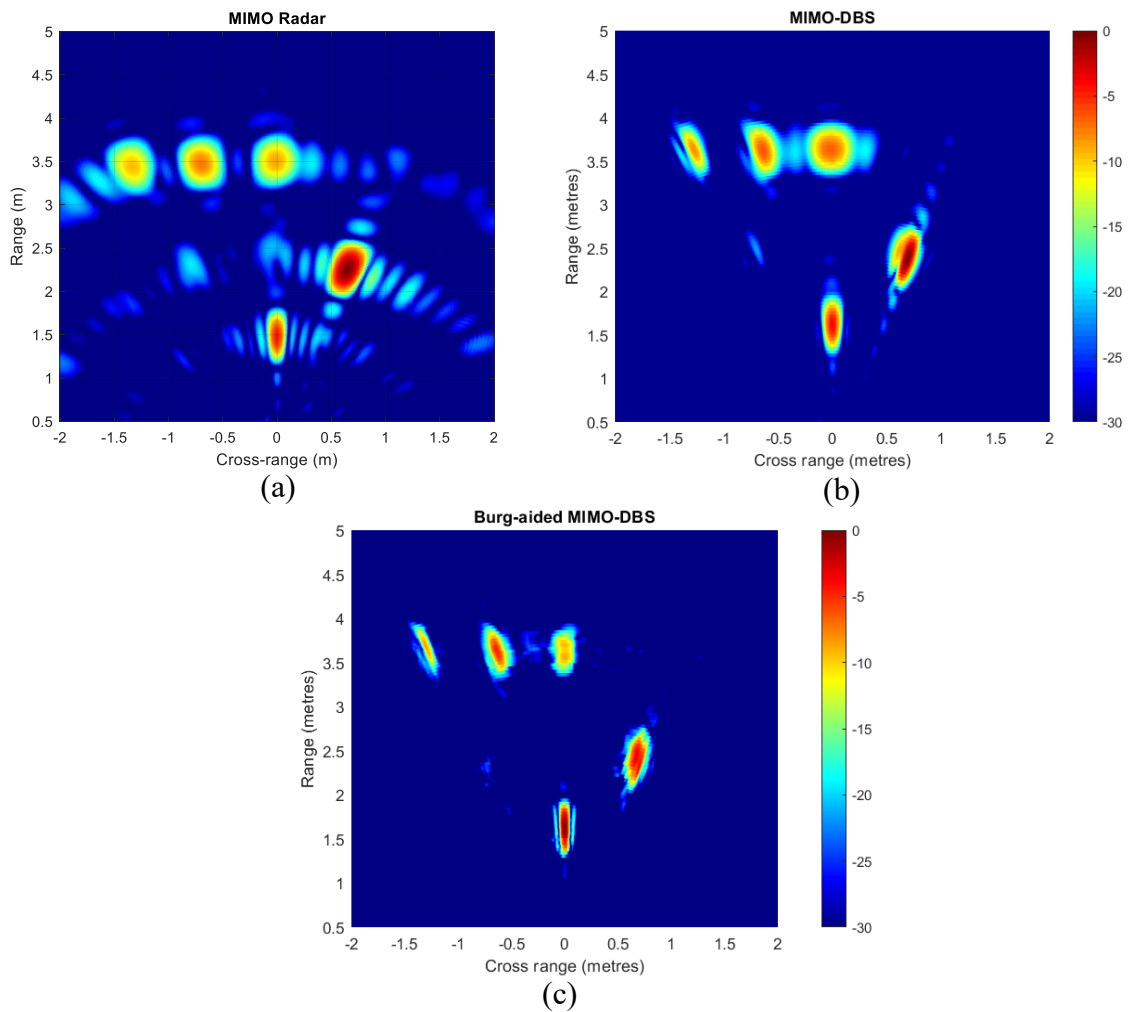


Figure 6.9:(a) MIMO radar result, (b) MIMO-DBS result, (c) Burg-aided MIMO-DBS result

visible due to suppression of the sidelobes. Regarding the proposed method, Burg-aided MIMO-DBS, the collected data is extrapolated by a factor of two in both the Doppler and azimuth dimensions. Specifically, the number of sweeps is increased from 110 to 220, and the number of virtual array elements is extrapolated from 29 to 58 via the Burg algorithm. The range cross-range map obtained is shown in Figure 6.9(c). As expected, the cross-range resolution improves in both the on- and off-boresight directions.

In the real-world experiment, an existing experimental dataset at the University of Birmingham (UoB) is used to examine the performance of the proposed method [177]. The experimental data has been collected on campus at the UoB using INRAS RadarLog MIMO radar with its 77 GHz frontend as shown in Figure 6.10(a) (alongside UoB mechanically scanning 77 GHz radar POLARAD for benchmark comparison). The radar has 4 transmitters and 16 receivers, which gives 64 virtual linear elements in azimuth and 3 of them overlapped [178]. The vehicle's speed was 3.87 m/s (8.65 mph) during data acquisition. The radar parameters provided in Table 6.3 were used.

Table 6.3: Radar parameters used in real-world experiment

Parameters	Value
Modulation	FMCW
Centre frequency	77 GHz
Bandwidth	2 GHz
Sample rate	10 MSa/s
Samples per chirp	2048
Chirp interval	230 $\mu$ s
MIMO frame interval	1 ms
Frame interval	128 ms
Transmitter Number	4
Receiver Number	16
Overlapped Virtual Element	3
Beamwidth	1.7°

The experimental scene is shown in Figure 6.10(b). The orthogonality among the transmitted signals in INRAS RadarLog is achieved using TDM. The RadarLog MIMO response after compensating the phase error induced by the platform movement using  $e^{-j4\beta}$  is illustrated in Figure 6.10(c). Regularly spaced posts of the railings visible on the left side (at - 3.5 m in cross-range) of the photo in Figure 6.10(b), as well as the support pillars and back wall of the covered parking area on the right side produce significant scattering as shown in Figure 6.10(c). However, any structural details are not observable due to the low angular resolution and the high interfering sidelobes, resulting in the significant background floor level.

With the MIMO-DBS technique, a significant reduction in the sidelobe levels and an improvement in the angular resolution at the off-boresight are seen in Figure 6.10(d). It is noted that during the recording of the data, the DBS aperture length is achieved through the motion of the radar. This length is given by the velocity of the platform multiplied by the total frame interval, that is, 3.57 m/s x 128 ms, resulting in a length of 0.457 m. In this experiment, a 2 GHz bandwidth was used, which provides a 7.5 cm range resolution. Hence, the aperture length is larger than the range resolution, and targets appear in multiple range bins. The number of RCM bins according to (6.9) – is equal to  $0.457/0.075 \cong 6$ . To reduce RCM effects in this experiment, a Blackman-Harris weighting in the range dimension and a Hanning weighting in both the Doppler and azimuth dimensions is implemented. The reason of employing two different weighting in different directions is the superior sidelobe suppression capability of the Blackman-Harris weighting compared to the Hanning weighting. However, while the Blackman-Harris weighting provides better sidelobe suppression, it also results in lower resolution. Hence, in the range direction, the Blackman-Harris weighting is used to address the RCM issue, while in the cross-range direction, the Hanning weighting is used to minimize



sidelobes without significantly degrading resolution, in contrast to the Blackman-Harris weighting.

Next, the proposed method, the Burg-aided MIMO-DBS, is applied to extrapolate the data two times in both Doppler and angle. Thus, the number of sweeps is increased from 128 real samples to 256 extrapolated samples and the number of virtual elements is increased from 61 to 122. The resulting map is shown in Figure 6.10(e). As expected, the cross-range resolutions in the both the forward looking and lateral directions are now enhanced as compared to MIMO-DBS. This improvement can be seen in the zoomed area in the red circle. Furthermore, an additional reduction in the background level is achieved.

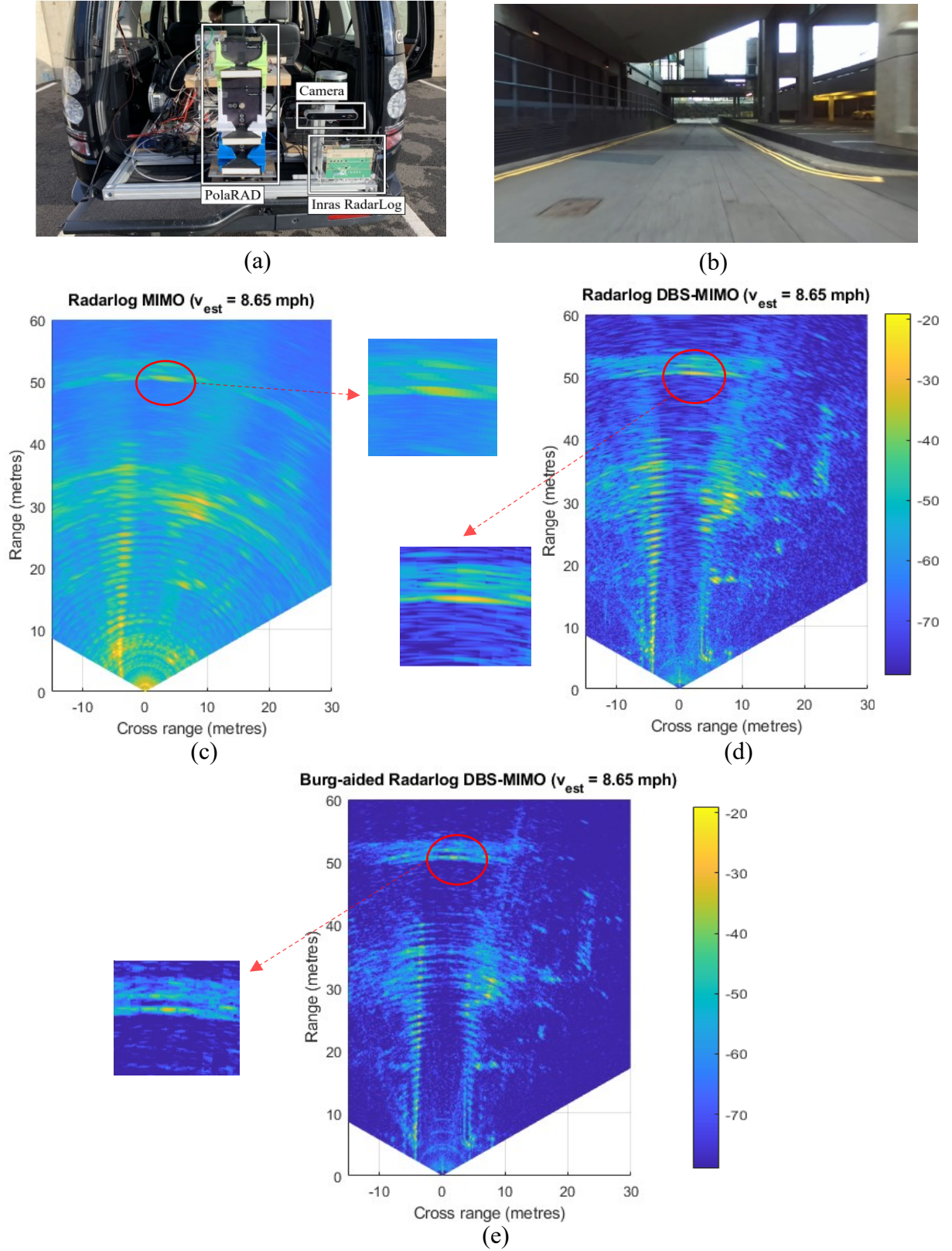


Figure 6.10: (a) Experimental setup on the vehicle [175], (b) Photograph of the scene, (c) MIMO result after motion compensation, (d) MIMO-DBS result, (e) results with Burg algorithm applied to both Doppler and angular dimensions (factor 2) to extrapolate the data.

## 6.6 Conclusion

In this chapter, it has been demonstrated that higher angular resolutions in both on- and off-boresight directions of a forward-looking MIMO radar, together with a reduction in sidelobe levels, can be achieved by extrapolating MIMO-DBS data along both the Doppler and angular dimensions using the Burg algorithm. The proposed method has been validated through simulations, laboratory-based experiments, and real-world trials at 77 GHz with the improved performance clearly demonstrated. The importance of this approach is first of all related to improved detection and secondly improved radar imaging performance where the whole scene response (clutter map) must be retained for effective path planning within the road infrastructure.

# Chapter 7 – Conclusion and Future Work

## 7.1 Summary and Outcomes

This thesis presents detailed research studies on development of radar combined with the communication capability and techniques allowing improved resolution with thinned and extrapolated arrays for use in automotive applications. The developed techniques, simulation and experimental methodologies represent an original research and are applicable to the wide range applications, where the imaging radar for the platform navigation and path planning combined with ability to share collected data are required.

These research strands include:

- i) The design of novel waveforms that enable the use of both radar and communication systems simultaneously,
- ii) Optimisation of both sparse 1-D and 2-D MIMO arrays to reduce the total number of antenna elements,
- iii) The design a new form of 2-D MIMO antenna configuration that keeps the antenna size compact while allowing significant enhancement of resolution by interpolating and extrapolating virtual elements using Burg algorithm,
- iv) Implementation and practical evaluation of Burg algorithm to achieve higher angular resolution than implied by the physical size of an antenna,

- v) Application of the Burg algorithm to the data obtained via radar platform motion in a MIMO configuration to enhance angular resolution in both the on- and off-boresight directions while suppressing the high sidelobe levels inherent in MIMO arrays.

Following the presentation of fundamentals of both radar and communication systems, novel waveforms were proposed for joint radar and communication systems. The main concept for the designed waveforms was to embed the communication data into an LFM signal by changing the phase of the LFM signal, thus leading to the creation of the PSK-LFM hybrid waveform. Moreover, in order to activate all the transmitters at the same time, CDM PSK-LFM waveforms were designed using codes such as Barker code and m-sequences. The performance of the proposed waveforms for both radar and communication capabilities assessment was analysed, discussed and demonstrated with the number of simulations and experiments, with the set-ups and methodologies developed and demonstrated within this original work. Good agreement between simulated and experimental results was demonstrated, defining the framework of further developments in the area of joint radar and communication systems development.

In the second part of the thesis, the optimisation of sparse MIMO arrays was investigated where the aim was to achieve high angular resolution with low sidelobe levels whilst reducing the total number of antenna elements. After evaluating two optimisation methods – simulated annealing and genetic algorithms, for the optimisation of thinned 1-D MIMO arrays, multiple sparse 2-D MIMO antenna configurations were proposed and optimised using simulated annealing.

In the sparse 2-D MIMO antenna configuration, the total number of antenna elements was almost halved compared to the conventional MIMO to achieve the same resolution. During

the sparse 2-D MIMO optimisation, the number of total physical antenna elements were fixed while the number of transmit and receive elements was changed to analyse the trends of resolution improvement of corresponding MIMO arrays. It has been shown that when the number of virtual elements increases, the PSLR decreases with achieved -15.5 dB level, compared to -13 dB in conventional MIMO. It has also been demonstrated that in the optimized configuration the Tx elements are likely to be positioned within the edge region, with a margin of one wavelength, with a probability exceeding 80%. When the Tx locations were predefined in this way, the simulations showed dramatic decrease of the optimization time.

Apart from the use of sparse antenna configurations, an autoregressive algorithm implementation was studied to deliver more compact hardware with a smaller number of physical elements. Specifically, the Burg Algorithm was used to interpolate or extrapolate the radar data to achieve very fine resolution within a compact antenna size. The performance of the Burg algorithm for improved spatial resolution together with associated limitations were examined for both 1-D and 2-D MIMO array configurations. Research has demonstrated that with the use of extrapolation factor of up to 3 the corresponding super-resolution performance is achievable without the degradation of extrapolated array performance, however higher factors would not be led to further improvement due to different factors related to the performance of autoregression and transfer of operational scenario to the near-field region. The proposed approach has been verified using both simulation and experiments at a frequency of 77 GHz, with targets of varying RCS. Also, in the experiment a methodology to generate 3-D data (range, azimuth, and elevation information) using a 1-D MIMO array was proposed, and this methodology made it feasible to experimentally evaluate the performance of the proposed method prior to the fabrication of 2-D antenna.

Finally, the combination of Burg-aided MIMO beamforming was combined with the Doppler Beam Sharpening (unfocused SAR) by exploiting the motion of the vehicle to further improve the angular resolution and reduce the background level of the imaged scene. Here BA was used to extrapolate MIMO-DBS data along both the Doppler and the angular dimensions, resulting in finer angular resolutions in both on- and off-boresight directions of a forward-looking MIMO radar. The validity of the proposed method has been confirmed through simulations, laboratory-based experiments and real-world experiments conducted at 77 GHz on the campus of the University of Birmingham.

## 7.2 Future Work

The PSK-LFM waveforms that are transmitted by several vehicles simultaneously in a realistic scenario may cause interference effects. The proposed CDM-based waveforms offer a solution to this problem, as they enable simultaneous transmissions by multiple transmitters. However, as mentioned in Chapter 3, the maximum number of transmitters that can be used simultaneously is limited per requirements, such as the energy per bit to noise ratio and BER in communication links. Hence, additional research is needed to analyse the performance in dense co-existence scenarios and mitigate potential interferences with increase of number of users.

As demonstrated in Chapter 3, the angular response of the antenna configuration is independent of the waveform. Therefore, the antenna configurations designed in Chapters 4-6 are compatible with both TDM PSK-LFM and CDM PSK-LFM waveforms, so while enabling the dual functionality using a compact-sized chipset, higher spatial resolutions can be achieved. However, further analyses are required to fully demonstrate the performance of system.

During the optimisation of thinned MIMO arrays, the PSLL of the antenna configuration optimised in Section 4 can be anywhere in the radiation pattern. However, depending on the

application, more constraints might be applied, such as the shape of the sidelobes or that the first SLL has the highest SLL. Therefore, further analyses can be performed in the future.

In Chapter 6, it was shown that Burg-aided MIMO-DBS technique can be used to achieve higher resolution with lower sidelobes beyond that of the MIMO antenna can provide. Nevertheless, this work included only two-dimensional maps – range and cross-range map. Along with range and angle information, autonomous vehicles must also have accurate height data of objects around them for full situational awareness. So, adding target shape reconstruction to this technique is crucial and will be a subject of further work. This in particular can be achieved by using the Burg-aided MIMO-DBS technique with one of the 2-D MIMO antenna configurations proposed in Chapter 5. In this way, not only improved azimuth resolution but also improved elevation resolution in both boresight and off-boresight can be obtained with low sidelobes. As an alternative method, interferometry can be employed to estimate the height of the targets. This is a well-known technique in SAR but, its application in automotive scenarios is less explored. Investigating the integration of interferometry with MIMO-DBS could be a future research topic.

In the future studies, the range cell migration mitigation techniques in the MIMO-DBS will be developed and tested to remove limitations, related to the use of small bandwidth and/or heavy windowing, ultimately degrading achievable range resolution. This exploration may involve examining various approaches, either range-cell migration correction techniques or the implementation of advanced imaging algorithms such as back-projection. Hence, the most suitable approach can be determined by evaluating the pros and cons of each method.



# References

- [1] P. Thomas, A. Morris, R. Talbot, and H. Fagerlind, ‘Identifying the causes of road crashes in Europe’, *Ann Adv Automot Med*, vol. 57, pp. 13–22, 2013.
- [2] ‘[https://cdn.oemoffhighway.com/files/base/acbm/ooh/document/2016/03/automated\\_driving.pdf](https://cdn.oemoffhighway.com/files/base/acbm/ooh/document/2016/03/automated_driving.pdf)’.
- [3] ‘SAE J3016 automated-driving graphic’. Accessed: Nov. 22, 2023. [Online]. Available: <https://www.sae.org/site/news/2019/01/sae-updates-j3016-automated-driving-graphic>
- [4] J. Hasch, ‘Driving towards 2020: Automotive radar technology trends’, in *2015 IEEE MTT-S International Conference on Microwaves for Intelligent Mobility (ICMIM)*, Heidelberg, Germany: IEEE, Apr. 2015, pp. 1–4. doi: 10.1109/ICMIM.2015.7117956.
- [5] J. Choi, V. Va, N. Gonzalez-Prelcic, R. Daniels, C. R. Bhat, and R. W. Heath, ‘Millimeter-Wave Vehicular Communication to Support Massive Automotive Sensing’, *IEEE Commun. Mag.*, vol. 54, no. 12, pp. 160–167, Dec. 2016, doi: 10.1109/MCOM.2016.1600071CM.
- [6] A. Frischen, J. Hasch, and C. Waldschmidt, ‘Performance degradation in cooperative radar sensor systems due to Uncorrelated Phase Noise’, in *2014 11th European Radar Conference*, Italy: IEEE, Oct. 2014, pp. 241–244. doi: 10.1109/EuRAD.2014.6991252.
- [7] J. Kenney, ‘Dedicated Short-Range Communications (DSRC) Standards in the United States’, *Proceedings of the IEEE*, vol. 99, pp. 1162–1182, Aug. 2011, doi: 10.1109/JPROC.2011.2132790.
- [8] ‘ETSI TS 102 792 - V1.2.1 (2015-06) – Intelligent transportation Systems (ITS); Mitigation techniques to avoid interference between European CEN dedicated short range communication (CEN DSRC) equipment and intelligent transport systems (ITS) operating

- in the 5 GHz frequency range’, [Online]. Available: [https://www.etsi.org/deliver/etsi\\_ts/102700\\_102799/102792/01.02.01\\_60/ts\\_102792v010201p.pdf](https://www.etsi.org/deliver/etsi_ts/102700_102799/102792/01.02.01_60/ts_102792v010201p.pdf).
- [9] L. Reichardt, C. Sturm, F. Grunhaupt, and T. Zwick, ‘Demonstrating the use of the IEEE 802.11P Car-to-Car communication standard for automotive radar’, *2012 6th European Conference on Antennas and Propagation (EUCAP)*, pp. 1576–1580, Mar. 2012, doi: 10.1109/EuCAP.2012.6206084.
  - [10] H. Griffiths, S. Blunt, L. Cohen, and L. Savy, ‘Challenge problems in spectrum engineering and waveform diversity’, in *2013 IEEE Radar Conference (RadarCon13)*, Ottawa, ON, Canada: IEEE, Apr. 2013, pp. 1–5. doi: 10.1109/RADAR.2013.6586140.
  - [11] H. Griffiths *et al.*, ‘Radar Spectrum Engineering and Management: Technical and Regulatory Issues’, *Proc. IEEE*, vol. 103, no. 1, pp. 85–102, Jan. 2015, doi: 10.1109/JPROC.2014.2365517.
  - [12] A. R. Chiriyath, B. Paul, and D. W. Bliss, ‘Radar-Communications Convergence: Coexistence, Cooperation, and Co-Design’, *IEEE Transactions on Cognitive Communications and Networking*, vol. 3, no. 1, pp. 1–12, Mar. 2017, doi: 10.1109/TCCN.2017.2666266.
  - [13] L. Zheng, M. Lops, Y. C. Eldar, and X. Wang, ‘Radar and Communication Coexistence: An Overview: A Review of Recent Methods’, *IEEE Signal Process. Mag.*, vol. 36, no. 5, pp. 85–99, Sep. 2019, doi: 10.1109/MSP.2019.2907329.
  - [14] J. A. Zhang *et al.*, ‘An Overview of Signal Processing Techniques for Joint Communication and Radar Sensing’, *IEEE J. Sel. Top. Signal Process.*, vol. 15, no. 6, pp. 1295–1315, Nov. 2021, doi: 10.1109/JSTSP.2021.3113120.

- [15] W. Zhou, R. Zhang, G. Chen, and W. Wu, ‘Integrated Sensing and Communication Waveform Design: A Survey’, *IEEE Open J. Commun. Soc.*, vol. 3, pp. 1930–1949, 2022, doi: 10.1109/OJCOMS.2022.3215683.
- [16] C. A. Balanis, *Antenna Theory: Analysis and Design*. Newark, UNITED STATES: John Wiley & Sons, Incorporated, 2016. Accessed: Nov. 18, 2023. [Online]. Available: <http://ebookcentral.proquest.com/lib/bham/detail.action?docID=7104469>
- [17] J. Li and P. Stoica, *MIMO Radar Signal Processing*. New York: Wiley, 2009.
- [18] B. Friedlander, ‘On the role of waveform diversity in MIMO radar’, *Digital Signal Processing*, vol. 23, no. 3, pp. 712–721, May 2013, doi: 10.1016/j.dsp.2012.12.008.
- [19] Y. Qu, G. Liao, S. Zhu, X. Liu, and H. Jiao, ‘Performance comparisons of MIMO and phased-array radar’, presented at the MIKON 2008 - 17th International Conference on Microwaves, Radar and Wireless Communications, 2008, pp. 1–4.
- [20] M. I. Skolnik, *Introduction to radar systems*, 2nd ed. New York: McGraw-Hill, 1980.
- [21] V. S. Chernyak and I. Ya. Immoreev, ‘A Brief History of Radar’, *IEEE Aerospace and Electronic Systems Magazine*, vol. 24, no. 9, pp. B1–B32, Sep. 2009, doi: 10.1109/MAES.2009.5282288.
- [22] H. Griffiths, C. J. Baker, and D. Adamy, *Stimson’s introduction to airborne radar*, Third edition. Raleigh, NC, USA: SciTech Publishing, 2016.
- [23] M. A. Richards, J. Scheer, and W. A. Holm, *Principles of modern radar. Volume 1, Basic principles*. Edison, N.J.: SciTech Publishing, 2010.
- [24] M. Jankiraman, *Design of Multi-Frequency CW Radars*. Institution of Engineering and Technology, 2007.
- [25] I. G. Cumming and F. H. Wong, *Digital Processing of Synthetic Aperture Radar Data: Algorithms and Implementation*, Illustrated edition. Boston London: Artech House, 2004.

- [26] D. V. Sarwate and M. B. Pursley, ‘Crosscorrelation properties of pseudorandom and related sequences’, *Proc. IEEE*, vol. 68, no. 5, pp. 593–619, 1980, doi: 10.1109/PROC.1980.11697.
- [27] S. W. Golomb, ‘Shift-register sequences and spread-spectrum communications’, in *Proceedings of IEEE 3rd International Symposium on Spread Spectrum Techniques and Applications (ISSSTA’94)*, Oulu, Finland: IEEE, 1994, pp. 14–15. doi: 10.1109/ISSSTA.1994.379622.
- [28] N. Levanon and E. Mozeson, *Radar Signals*. Newark, UNITED STATES: John Wiley & Sons, Incorporated, 2004. Accessed: Nov. 17, 2023. [Online]. Available: <http://ebookcentral.proquest.com/lib/bham/detail.action?docID=214304>
- [29] H. Sun, F. Briguei, and M. Lesturgie, ‘Analysis and comparison of MIMO radar waveforms’, in *2014 International Radar Conference*, Oct. 2014, pp. 1–6. doi: 10.1109/RADAR.2014.7060251.
- [30] J. J. M. de Wit, W. L. van Rossum, and A. J. de Jong, ‘Orthogonal waveforms for FMCW MIMO radar’, in *2011 IEEE RadarCon (RADAR)*, May 2011, pp. 686–691. doi: 10.1109/RADAR.2011.5960625.
- [31] A. Zwanetski, M. Kronauge, and H. Rohling, ‘Waveform design for FMCW MIMO radar based on frequency division’, in *2013 14th International Radar Symposium (IRS)*, Dresden, Jun. 2013, pp. 89–94.
- [32] L. Lo Monte, B. Himed, T. Corigliano, and C. J. Baker, ‘Performance analysis of time division and code division waveforms in co-located MIMO’, in *2015 IEEE Radar Conference (RadarCon)*, May 2015, pp. 0794–0798. doi: 10.1109/RADAR.2015.7131104.

- [33] W. L. Melvin and J. A. Scheer, *Principles of Modern Radar: Advanced Techniques*. Raleigh (N.C.): SciTech Publishing, 2013.
- [34] D. W. Bliss and K. W. Forsythe, ‘Multiple-input multiple-output (MIMO) radar and imaging: degrees of freedom and resolution’, in *The Thrity-Seventh Asilomar Conference on Signals, Systems & Computers, 2003*, Nov. 2003, pp. 54-59 Vol.1. doi: 10.1109/ACSSC.2003.1291865.
- [35] M. Schneider, ‘Automotive radar—Status and trends’, *Proc. German Microwave Conf. (GeMiC)*, pp. 144–147, 2005.
- [36] H. H. Meinel, ‘Evolving automotive radar — From the very beginnings into the future’, in *The 8th European Conference on Antennas and Propagation (EuCAP 2014)*, Apr. 2014, pp. 3107–3114. doi: 10.1109/EuCAP.2014.6902486.
- [37] R. Mende and H. Rohling, ‘New automotive applications for smart radar systems’, *Proc. German Radar Symp.*, pp. 35–40, 2002.
- [38] J. Wenger, ‘Automotive radar - status and perspectives’, in *IEEE Compound Semiconductor Integrated Circuit Symposium, 2005. CSIC '05.*, Palm Springs, CA, USA, Oct. 2005, pp. 21–24. doi: 10.1109/CSICS.2005.1531741.
- [39] J. Hasch, E. Topak, R. Schnabel, T. Zwick, R. Weigel, and C. Waldschmidt, ‘Millimeter-Wave Technology for Automotive Radar Sensors in the 77 GHz Frequency Band’, *IEEE Transactions on Microwave Theory and Techniques*, vol. 60, no. 3, pp. 845–860, Mar. 2012, doi: 10.1109/TMTT.2011.2178427.
- [40] C. Waldschmidt, J. Hasch, and W. Menzel, ‘Automotive Radar — From First Efforts to Future Systems’, *IEEE Journal of Microwaves*, vol. 1, no. 1, pp. 135–148, Jan. 2021, doi: 10.1109/JMW.2020.3033616.

- [41] K. Ramasubramanian and K. Ramaiah, ‘Moving from Legacy 24 GHz to State-of-the-Art 77-GHz Radar’, *ATZ Elektron Worldw*, vol. 13, no. 3, pp. 46–49, Jun. 2018, doi: 10.1007/s38314-018-0029-6.
- [42] S. M. Patole, M. Torlak, D. Wang, and M. Ali, ‘Automotive radars: A review of signal processing techniques’, *IEEE Signal Processing Magazine*, vol. 34, no. 2, pp. 22–35, Mar. 2017, doi: 10.1109/MSP.2016.2628914.
- [43] S. Alland, W. Stark, M. Ali, and M. Hegde, ‘Interference in Automotive Radar Systems: Characteristics, Mitigation Techniques, and Current and Future Research’, *IEEE Signal Process. Mag.*, vol. 36, no. 5, pp. 45–59, Sep. 2019, doi: 10.1109/MSP.2019.2908214.
- [44] G. M. Brooker, ‘Mutual Interference of Millimeter-Wave Radar Systems’, *IEEE Trans. Electromagn. Compat.*, vol. 49, no. 1, pp. 170–181, Feb. 2007, doi: 10.1109/TEMC.2006.890223.
- [45] F. Norouzian, A. Pirkani, E. Hoare, M. Cherniakov, and M. Gashinova, ‘Phenomenology of automotive radar interference’, *IET Radar, Sonar & Navigation*, vol. 15, no. 9, pp. 1045–1060, 2021, doi: 10.1049/rsn2.12096.
- [46] L. W. Couch, *Digital & Analog Communication Systems*, 8th, 8th ed. ed. NOIDA: Pearson Education UK, 2013.
- [47] A. B. Carlson, P. Crilly, and J. Rutledge, *Communication Systems*, 4th edition. Boston: McGraw-Hill Education, 2001.
- [48] C. E. Shannon, ‘A Mathematical Theory of Communication’, *Bell System Technical Journal*, vol. 27, no. 3, pp. 379–423, 1948, doi: 10.1002/j.1538-7305.1948.tb01338.x.
- [49] T. S. Rappaport, *Wireless Communications: Principles and Practice*, 2nd edition. Upper Saddle River, N.J: Prentice Hall, 2002.

- [50] ‘Phase-shift keying’, *Wikipedia*. Nov. 16, 2023. Accessed: Nov. 26, 2023. [Online]. Available: [https://en.wikipedia.org/w/index.php?title=Phase-shift\\_keying&oldid=1185411437#Quadrature\\_phase-shift\\_keying\\_.28QPSK.29](https://en.wikipedia.org/w/index.php?title=Phase-shift_keying&oldid=1185411437#Quadrature_phase-shift_keying_.28QPSK.29)
- [51] Peter Gardner, ‘Satellite, Mobile and Optical Communications, Lecture Notes’, University of Birmingham, UK, 2017.
- [52] P. Papadimitratos, A. La Fortelle, K. Evenssen, R. Brignolo, and S. Cosenza, ‘Vehicular communication systems: Enabling technologies, applications, and future outlook on intelligent transportation’, *IEEE Commun. Mag.*, vol. 47, no. 11, pp. 84–95, Nov. 2009, doi: 10.1109/MCOM.2009.5307471.
- [53] M. Bekar, C. J. Baker, E. Hoare, and M. Gashinova, ‘Realization of a Joint MIMO Radar and Communication System using a PSK-LFM Waveform’, in *2020 IEEE Radar Conference (RadarConf20)*, Florence, Italy: IEEE, Sep. 2020, pp. 1–6. doi: 10.1109/RadarConf2043947.2020.9266699.
- [54] M. Bekar, C. J. Baker, E. G. Hoare, and M. Gashinova, ‘Joint MIMO Radar and Communication System Using a PSK-LFM Waveform With TDM and CDM Approaches’, *IEEE Sensors J.*, vol. 21, no. 5, pp. 6115–6124, Mar. 2021, doi: 10.1109/JSEN.2020.3043085.
- [55] C. Sturm and W. Wiesbeck, ‘Waveform Design and Signal Processing Aspects for Fusion of Wireless Communications and Radar Sensing’, *Proc. IEEE*, vol. 99, no. 7, pp. 1236–1259, Jul. 2011, doi: 10.1109/JPROC.2011.2131110.
- [56] R. M. Mealey, ‘A Method for Calculating Error Probabilities in a Radar Communication System’, *IEEE Trans. Space Electron. Telemetry*, vol. 9, no. 2, pp. 37–42, 1963, doi: 10.1109/TSET.1963.4337601.

- [57] G. C. Tavik *et al.*, ‘The advanced multifunction RF concept’, *IEEE Trans. Microwave Theory Techn.*, vol. 53, no. 3, pp. 1009–1020, Mar. 2005, doi: 10.1109/TMTT.2005.843485.
- [58] K. Mizui, M. Uchida, and M. Nakagawa, ‘Vehicle-to-vehicle communication and ranging system using spread spectrum technique (Proposal of Boomerang Transmission System)’, in *IEEE 43rd Vehicular Technology Conference*, Secaucus, NJ, USA: IEEE, 1993, pp. 335–338. doi: 10.1109/VETEC.1993.507206.
- [59] K. Konno and S. Koshikawa, ‘Millimeter-wave dual mode radar for headway control in IVHS’, in *1997 IEEE MTT-S International Microwave Symposium Digest*, Denver, CO, USA: IEEE, 1997, pp. 1261–1264. doi: 10.1109/MWSYM.1997.596556.
- [60] K. Konno and S. Koshikawa, ‘60 GHz Millimeter-Wave Dual Mode radar for IVHS’, in *Proc. Top. Symp. Millim. Waves*, Kanagawa, Japan, Jul. 1997, pp. 159–161.
- [61] L. Han and K. Wu, ‘Multifunctional Transceiver for Future Intelligent Transportation Systems’, *IEEE Trans. Microwave Theory Techn.*, vol. 59, no. 7, pp. 1879–1892, Jul. 2011, doi: 10.1109/TMTT.2011.2138156.
- [62] E. G. Hoare, N. E. Priestley, R. I. Henderson, P. S. Hall, N. J. Clarke, and R. N. Foster, ‘SLIMSENS - A Single Aperture Automotive Radar and Communications-design & development’, in *Proc. JSAE Annu. Congr., Pacifico Conf. Centre*, Yokohama, Japan, May 2008.
- [63] R. I. Henderson, W. M. A. Qureshi, and B. Kumar, ‘A compact multifunction automotive antenna’, in *2nd European Conference on Antennas and Propagation (EuCAP 2007)*, Edinburgh, UK: Institution of Engineering and Technology, 2007, pp. 130–130. doi: 10.1049/ic.2007.1253.



- [64] J. Euziere, R. Guinvarc'h, M. Lesturgie, B. Uguen, and R. Gillard, 'Dual function radar communication Time-modulated array', in *2014 International Radar Conference*, Lille, France: IEEE, Oct. 2014, pp. 1–4. doi: 10.1109/RADAR.2014.7060416.
- [65] P. M. McCormick, S. D. Blunt, and J. G. Metcalf, 'Simultaneous radar and communications emissions from a common aperture, Part I: Theory', in *2017 IEEE Radar Conference (RadarConf)*, Seattle, WA, USA: IEEE, May 2017, pp. 1685–1690. doi: 10.1109/RADAR.2017.7944478.
- [66] P. M. McCormick, B. Ravenscroft, S. D. Blunt, A. J. Duly, and J. G. Metcalf, 'Simultaneous radar and communication emissions from a common aperture, Part II: Experimentation', in *2017 IEEE Radar Conference (RadarConf)*, Seattle, WA, USA: IEEE, May 2017, pp. 1697–1702. doi: 10.1109/RADAR.2017.7944480.
- [67] A. Hassanien, M. G. Amin, Y. D. Zhang, and F. Ahmad, 'Dual-Function Radar-Communications: Information Embedding Using Sidelobe Control and Waveform Diversity', *IEEE Trans. Signal Process.*, vol. 64, no. 8, pp. 2168–2181, Apr. 2016, doi: 10.1109/TSP.2015.2505667.
- [68] L. Reichardt, C. Sturm, F. Grunhaupt, and T. Zwick, 'Demonstrating the use of the IEEE 802.11P Car-to-Car communication standard for automotive radar', in *2012 6th European Conference on Antennas and Propagation (EUCAP)*, Prague, Czech Republic: IEEE, Mar. 2012, pp. 1576–1580. doi: 10.1109/EuCAP.2012.6206084.
- [69] D. Garmatyuk, J. Schuerger, Y. T. Morton, K. Binns, M. Durbin, and J. Kimani, 'Feasibility Study of a Multi-Carrier Dual-Use Imaging Radar and Communication System', in *Proc. Eur. Radar Conf.*, Munich, Germany, Oct. 2007, pp. 194–197.
- [70] D. Garmatyuk and J. Schuerger, 'Conceptual design of a dual-use radar/communication system based on OFDM', in *MILCOM 2008 - 2008 IEEE Military Communications*

- Conference*, San Diego, CA, USA: IEEE, Nov. 2008, pp. 1–7. doi: 10.1109/MILCOM.2008.4753063.
- [71] C. Sturm, T. Zwick, and W. Wiesbeck, ‘An OFDM System Concept for Joint Radar and Communications Operations’, in *VTC Spring 2009 - IEEE 69th Vehicular Technology Conference*, Barcelona, Spain: IEEE, Apr. 2009, pp. 1–5. doi: 10.1109/VETECS.2009.5073387.
- [72] P. Kumari, D. H. N. Nguyen, and R. W. Heath, ‘Performance trade-off in an adaptive IEEE 802.11AD waveform design for a joint automotive radar and communication system’, in *2017 IEEE International Conference on Acoustics, Speech and Signal Processing (ICASSP)*, New Orleans, LA: IEEE, Mar. 2017, pp. 4281–4285. doi: 10.1109/ICASSP.2017.7952964.
- [73] T. W. Tedesso and R. Romero, ‘Code shift keying based joint radar and communications for EMCON applications’, *Digital Signal Processing*, vol. 80, pp. 48–56, Sep. 2018, doi: 10.1016/j.dsp.2018.05.013.
- [74] W. Baxter, E. Aboutanios, and A. Hassanien, ‘Dual-Function MIMO Radar-Communications Via Frequency-Hopping Code Selection’, in *2018 52nd Asilomar Conference on Signals, Systems, and Computers*, Pacific Grove, CA, USA: IEEE, Oct. 2018, pp. 1126–1130. doi: 10.1109/ACSSC.2018.8645212.
- [75] I. P. Eedara, A. Hassanien, M. G. Amin, and B. D. Rigling, ‘Ambiguity Function Analysis for Dual-Function Radar Communications Using PSK Signaling’, in *2018 52nd Asilomar Conference on Signals, Systems, and Computers*, Pacific Grove, CA, USA: IEEE, Oct. 2018, pp. 900–904. doi: 10.1109/ACSSC.2018.8645328.

- [76] N. Levanon and B. Getz, ‘Comparison between linear FM and phase-coded CW radars’, *IEEE Proceedings - Radar, Sonar and Navigation*, vol. 141, no. 4, pp. 230–240, Aug. 1994, doi: 10.1049/ip-rsn:19941233.
- [77] S. H. Dokhanchi, M. R. B. Shankar, Y. A. Nijssure, T. Stifter, S. Sedighi, and B. Ottersten, ‘Joint automotive radar-communications waveform design’, in *2017 IEEE 28th Annual International Symposium on Personal, Indoor, and Mobile Radio Communications (PIMRC)*, Montreal, QC: IEEE, Oct. 2017, pp. 1–7. doi: 10.1109/PIMRC.2017.8292466.
- [78] S. H. Dokhanchi, M. R. Bhavani Shankar, K. V. Mishra, T. Stifter, and B. Ottersten, ‘Performance Analysis of mmWave Bi-static PMCW-based Automotive Joint Radar-Communications System’, in *2019 IEEE Radar Conference (RadarConf)*, Boston, MA, USA: IEEE, Apr. 2019, pp. 1–6. doi: 10.1109/RADAR.2019.8835577.
- [79] G. N. Saddik, R. S. Singh, and E. R. Brown, ‘Ultra-Wideband Multifunctional Communications/Radar System’, *IEEE Trans. Microwave Theory Techn.*, vol. 55, no. 7, pp. 1431–1437, Jul. 2007, doi: 10.1109/TMTT.2007.900343.
- [80] A. Hassanien, M. G. Amin, Y. D. Zhang, and B. Himed, ‘A dual-function MIMO radar-communications system using PSK modulation’, in *2016 24th European Signal Processing Conference (EUSIPCO)*, Budapest, Hungary: IEEE, Aug. 2016, pp. 1613–1617. doi: 10.1109/EUSIPCO.2016.7760521.
- [81] M. Kowatsch and J. Lafferl, ‘A Spread-Spectrum Concept Combining Chirp Modulation and Pseudonoise Coding’, *IEEE Trans. Commun.*, vol. 31, no. 10, pp. 1133–1142, Oct. 1983, doi: 10.1109/TCOM.1983.1095745.
- [82] X. Chen, X. Wang, S. Xu, and J. Zhang, ‘A novel radar waveform compatible with communication’, in *2011 International Conference on Computational Problem-Solving*

- (ICCP), Chengdu, China: IEEE, Oct. 2011, pp. 177–181. doi: 10.1109/ICCPS.2011.6092272.
- [83] Z. Zhang, M. J. Nowak, M. Wicks, and Z. Wu, ‘Bio-inspired RF steganography via linear chirp radar signals’, *IEEE Commun. Mag.*, vol. 54, no. 6, pp. 82–86, Jun. 2016, doi: 10.1109/MCOM.2016.7497771.
- [84] C. Sahin, J. Jakabosky, P. M. McCormick, J. G. Metcalf, and S. D. Blunt, ‘A novel approach for embedding communication symbols into physical radar waveforms’, in *2017 IEEE Radar Conference (RadarConf)*, Seattle, WA, USA: IEEE, May 2017, pp. 1498–1503. doi: 10.1109/RADAR.2017.7944444.
- [85] C. Sahin, J. G. Metcalf, A. Kordik, T. Kendo, and T. Corigliano, ‘Experimental Validation of Phase-Attached Radar/Communication (PARC) Waveforms: Radar Performance’, in *2018 International Conference on Radar (RADAR)*, Brisbane, QLD: IEEE, Aug. 2018, pp. 1–6. doi: 10.1109/RADAR.2018.8557302.
- [86] M. J. Nowak, Zhiping Zhang, Yang Qu, D. A. Dessources, M. Wicks, and Zhiqiang Wu, ‘Co-designed radar-communication using linear frequency modulation waveform’, in *MILCOM 2016 - 2016 IEEE Military Communications Conference*, Baltimore, MD, USA: IEEE, Nov. 2016, pp. 918–923. doi: 10.1109/MILCOM.2016.7795447.
- [87] A. Stroescu, M. Cherniakov, and M. Gashinova, ‘Classification of High Resolution Automotive Radar Imagery for Autonomous Driving Based on Deep Neural Networks’, in *2019 20th International Radar Symposium (IRS)*, Ulm, Germany: IEEE, Jun. 2019, pp. 1–10. doi: 10.23919/IRS.2019.8768156.
- [88] ‘Miniature Single Polarisation 1–18 GHz Horn Antenna’. Accessed: Nov. 23, 2023. [Online]. Available: [http://intermera.ru/files/docs/WBH1-18\\_Datasheetnew1\\_web.pdf](http://intermera.ru/files/docs/WBH1-18_Datasheetnew1_web.pdf)

- [89] M. Bekar, C. J. Baker, and M. Gashinova, ‘Sparse 2D MIMO Antenna Designs using Simulated Annealing’, in *2023 20th European Radar Conference (EuRAD)*, Berlin, Germany: IEEE, Sep. 2023, pp. 371–374. doi: 10.23919/EuRAD58043.2023.10289537.
- [90] H. Unz, ‘Linear Arrays with arbitrarily distributed elements’, *IRE Trans. Antennas Propag.*, vol. 8, no. 2, pp. 222–223, Mar. 1960, doi: 10.1109/TAP.1960.1144829.
- [91] R. Willey, ‘Space tapering of linear and planar arrays’, *IRE Trans. Antennas Propag.*, vol. 10, no. 4, pp. 369–377, Jul. 1962, doi: 10.1109/TAP.1962.1137887.
- [92] Y. Lo, ‘A mathematical theory of antenna arrays with randomly spaced elements’, *IEEE Trans. Antennas Propagat.*, vol. 12, no. 3, pp. 257–268, May 1964, doi: 10.1109/TAP.1964.1138220.
- [93] A. Moffet, ‘Minimum-redundancy linear arrays’, *IEEE Trans. Antennas Propagat.*, vol. 16, no. 2, pp. 172–175, Mar. 1968, doi: 10.1109/TAP.1968.1139138.
- [94] R. L. Haupt, J. J. Menozzi, and C. J. McCormack, ‘Thinned arrays using genetic algorithms’, in *Proceedings of IEEE Antennas and Propagation Society International Symposium*, Ann Arbor, MI, USA: IEEE, 1993, pp. 712–715. doi: 10.1109/APS.1993.385248.
- [95] R. L. Haupt, ‘Thinned arrays using genetic algorithms’, *IEEE Trans. Antennas Propagat.*, vol. 42, no. 7, pp. 993–999, Jul. 1994, doi: 10.1109/8.299602.
- [96] P. Brahma, P. Nandi, A. Senapati, and J. S. Roy, ‘Reduction of Side Lobe Level of Thinned Phased Array Antenna using Genetic Algorithm’, *International Journal of Computer Applications*, vol. 112, no. 8, pp. 13–15, Feb. 2015.
- [97] N. Jin and Y. Rahmat-Samii, ‘Particle Swarm Optimization for Antenna Designs in Engineering Electromagnetics’, *Journal of Artificial Evolution and Applications*, vol. 2008, pp. 1–10, Mar. 2008, doi: 10.1155/2008/728929.

- [98] M. M. Khodier and C. G. Christodoulou, 'Linear array geometry synthesis with minimum sidelobe level and null control using particle swarm optimization', *IEEE Trans. Antennas Propagat.*, vol. 53, no. 8, pp. 2674–2679, Aug. 2005, doi: 10.1109/TAP.2005.851762.
- [99] N. Jin and Y. Rahmat-Samii, 'Advances in Particle Swarm Optimization for Antenna Designs: Real-Number, Binary, Single-Objective and Multiobjective Implementations', *IEEE Trans. Antennas Propagat.*, vol. 55, no. 3, pp. 556–567, Mar. 2007, doi: 10.1109/TAP.2007.891552.
- [100] S. Kirkpatrick, C. D. Gelatt, and M. P. Vecchi, 'Optimization by Simulated Annealing', *Sci*, vol. 220, pp. 671–680, 1983, doi: DOI: 10.1126/science.220.4598.671.
- [101] V. Murino, A. Trucco, and C. S. Regazzoni, 'Synthesis of unequally spaced arrays by simulated annealing', *IEEE Trans. Signal Process.*, vol. 44, no. 1, pp. 119–122, Jan. 1996, doi: 10.1109/78.482017.
- [102] D. G. Kurup, M. Himdi, and A. Rydberg, 'Synthesis of uniform amplitude unequally spaced antenna arrays using the differential evolution algorithm', *IEEE Trans. Antennas Propagat.*, vol. 51, no. 9, pp. 2210–2217, Sep. 2003, doi: 10.1109/TAP.2003.816361.
- [103] S. K. Goudos, K. Siakavara, T. Samaras, E. E. Vafiadis, and J. N. Sahalos, 'Self-Adaptive Differential Evolution Applied to Real-Valued Antenna and Microwave Design Problems', *IEEE Trans. Antennas Propagat.*, vol. 59, no. 4, pp. 1286–1298, Apr. 2011, doi: 10.1109/TAP.2011.2109678.
- [104] O. Quevedo-Teruel and E. Rajo-Iglesias, 'Ant Colony Optimization in Thinned Array Synthesis With Minimum Sidelobe Level', *Antennas Wirel. Propag. Lett.*, vol. 5, pp. 349–352, 2006, doi: 10.1109/LAWP.2006.880693.

- [105] F. Grimaccia, M. Mussetta, and R. E. Zich, ‘Genetical Swarm Optimization: Self-Adaptive Hybrid Evolutionary Algorithm for Electromagnetics’, *IEEE Trans. Antennas Propagat.*, vol. 55, no. 3, pp. 781–785, Mar. 2007, doi: 10.1109/TAP.2007.891561.
- [106] A. Sayin, E. G. Hoare, and M. Antoniou, ‘Design and Verification of Reduced Redundancy Ultrasonic MIMO Arrays Using Simulated Annealing & Genetic Algorithms’, *IEEE Sensors J.*, vol. 20, no. 9, pp. 4968–4975, May 2020, doi: 10.1109/JSEN.2020.2964774.
- [107] A. Trucco and V. Murino, ‘Stochastic optimization of linear sparse arrays’, *IEEE J. Oceanic Eng.*, vol. 24, no. 3, pp. 291–299, Jul. 1999, doi: 10.1109/48.775291.
- [108] C. A. Meijer, ‘Simulated annealing in the design of thinned arrays having low sidelobe levels’, in *Proceedings of the 1998 South African Symposium on Communications and Signal Processing-COMSIG ’98 (Cat. No. 98EX214)*, Rondebosch, South Africa: IEEE, 1998, pp. 361–366. doi: 10.1109/COMSIG.1998.736983.
- [109] J. Redvik, ‘Simulated annealing optimization applied to antenna arrays with failed elements’, in *IEEE Antennas and Propagation Society International Symposium. 1999 Digest. Held in conjunction with: USNC/URSI National Radio Science Meeting (Cat. No.99CH37010)*, Orlando, FL, USA: IEEE, 1999, pp. 458–461. doi: 10.1109/APS.1999.789177.
- [110] X. Liu, C. Sun, Y. Yang, J. Zhuo, and Y. Han, ‘Low complexity MIMO sonar imaging using a virtual sparse linear array’, *J. of Syst. Eng. Electron.*, vol. 27, no. 2, pp. 370–378, Apr. 2016, doi: 10.1109/JSEE.2016.00038.
- [111] J. Dong, J. Yang, W. Lei, R. Shi, and Y. Guo, ‘Antenna array design in MIMO radar using cyclic difference sets and simulated annealing’, in *2012 International Conference*

- on *Microwave and Millimeter Wave Technology (ICMMT)*, Shenzhen, China: IEEE, May 2012, pp. 1–4. doi: 10.1109/ICMMT.2012.6229950.
- [112] J. H. Holland, ‘Genetic Algorithms’, *Scientific American*, vol. 267, no. 1, pp. 66–73, 1992.
- [113] W. C. Barott and P. G. Steffes, ‘Grating Lobe Reduction in Aperiodic Linear Arrays of Physically Large Antennas’, *Antennas Wirel. Propag. Lett.*, vol. 8, pp. 406–408, 2009, doi: 10.1109/LAWP.2008.2005364.
- [114] M. G. Bray, D. H. Werner, D. W. Boeringer, and D. W. Machuga, ‘Optimization of thinned aperiodic linear phased arrays using genetic algorithms to reduce grating lobes during scanning’, *IEEE Trans. Antennas Propagat.*, vol. 50, no. 12, pp. 1732–1742, Dec. 2002, doi: 10.1109/TAP.2002.807947.
- [115] M. Donelli, S. Caorsi, F. de Natale, D. Franceschini, and A. Massa, ‘A Versatile Enhanced Genetic Algorithm for Planar Array Design’, *Journal of Electromagnetic Waves and Applications*, vol. 18, no. 11, pp. 1533–1548, 2004, doi: 10.1163/1569393042954893.
- [116] K. Chen, X. Yun, Z. He, and C. Han, ‘Synthesis of Sparse Planar Arrays Using Modified Real Genetic Algorithm’, *IEEE Trans. Antennas Propagat.*, vol. 55, no. 4, pp. 1067–1073, Apr. 2007, doi: 10.1109/TAP.2007.893375.
- [117] J. S. Roy, B. B. Mishra, and A. Deb, ‘Design of thinned planar array using genetic algorithm and hadamard matrix arrangement’, *International Journal of Conceptions on Electrical and Electronics Engineering*, vol. 2, no. 1, pp. 6–9, 2014.
- [118] R. Jain and G. S. Mani, ‘Solving “Antenna Array Thinning Problem” Using Genetic Algorithm’, *Applied Computational Intelligence and Soft Computing*, vol. 2012, pp. 1–14, 2012, doi: 10.1155/2012/946398.



- [119] M. Shimizu, ‘Determining the excitation coefficients of an array using genetic algorithms’, in *Proceedings of IEEE Antennas and Propagation Society International Symposium and URSI National Radio Science Meeting*, Seattle, WA, USA: IEEE, 1994, pp. 530–533. doi: 10.1109/APS.1994.407697.
- [120] Keen-Keong Yan and Yilong Lu, ‘Sidelobe reduction in array-pattern synthesis using genetic algorithm’, *IEEE Trans. Antennas Propagat.*, vol. 45, no. 7, pp. 1117–1122, Jul. 1997, doi: 10.1109/8.596902.
- [121] S. A.Babale, D. D. Dajab, and K. Ahmad, ‘Synthesis of a Linear Antenna Array for Maximum Side-lobe Level Reduction’, *IJCA*, vol. 85, no. 16, pp. 24–28, Jan. 2014, doi: 10.5120/14925-3445.
- [122] Beng-Kiong Yeo and Yilong Lu, ‘Array failure correction with a genetic algorithm’, *IEEE Trans. Antennas Propagat.*, vol. 47, no. 5, pp. 823–828, May 1999, doi: 10.1109/8.774136.
- [123] Chao-Hsing Hsu, ‘Optimizing beam pattern of adaptive linear phase array antenna using local genetic algorithm’, in *2005 IEEE Antennas and Propagation Society International Symposium*, Washington, DC, USA: IEEE, 2005, pp. 315–318. doi: 10.1109/APS.2005.1551553.
- [124] Dong-Hun Shin, Ki-Beom Kim, Jong-Guk Kim, and Seong-Ook Park, ‘Design of Null-Filling Antenna for Automotive Radar Using the Genetic Algorithm’, *Antennas Wirel. Propag. Lett.*, vol. 13, pp. 738–741, 2014, doi: 10.1109/LAWP.2014.2316300.
- [125] J. Euziere, R. Guinvarc’h, I. Hinostroza, B. Uguen, and R. Gillard, ‘Time Modulated Array for dual function radar and communication’, in *2015 IEEE International Symposium on Antennas and Propagation & USNC/URSI National Radio Science Meeting*, Vancouver, BC, Canada: IEEE, Jul. 2015, pp. 806–807. doi: 10.1109/APS.2015.7304790.

- [126] J. Euziere, R. Guinvarc'h, B. Uguen, and R. Gillard, 'Optimization of Sparse Time-Modulated Array by Genetic Algorithm for Radar Applications', *Antennas Wirel. Propag. Lett.*, vol. 13, pp. 161–164, 2014, doi: 10.1109/LAWP.2014.2299285.
- [127] Jie He, Da-zheng Feng, N. H. Younan, and Xiao-ming Li, 'Optimizing thinned antenna array geometry in MIMO radar systems using multiple genetic algorithm', in *Proceedings of 2011 IEEE CIE International Conference on Radar*, Chengdu, China: IEEE, Oct. 2011, pp. 971–974. doi: 10.1109/CIE-Radar.2011.6159703.
- [128] C. Vasanelli, R. Batra, A. D. Serio, F. Boegelsack, and C. Waldschmidt, 'Assessment of a Millimeter-Wave Antenna System for MIMO Radar Applications', *Antennas Wirel. Propag. Lett.*, vol. 16, pp. 1261–1264, 2017, doi: 10.1109/LAWP.2016.2631889.
- [129] C. Vasanelli, R. Batra, and C. Waldschmidt, 'Optimization of a MIMO radar antenna system for automotive applications', in *2017 11th European Conference on Antennas and Propagation (EuCAP)*, Paris, France: IEEE, Mar. 2017, pp. 1113–1117. doi: 10.23919/EuCAP.2017.7928056.
- [130] C. Vasanelli *et al.*, 'Characterization of mm-Wave Conformal Antenna Arrays for a 3×8 MIMO Radar', in *2019 International Conference on Electromagnetics in Advanced Applications (ICEAA)*, 2019, pp. 0167–0171. doi: 10.1109/ICEAA.2019.8878980.
- [131] Z. Le, W. Wei, S. Song, and W. Xuetian, 'Optimisation of sparse array configuration using ambiguity function in automotive radar application', *The Journal of Engineering*, vol. 2019, no. 19, pp. 6152–6154, 2019, doi: 10.1049/joe.2019.0211.
- [132] X. Fu, X. Chen, Q. Hou, Z. Wang, and Y. Yin, 'An Improved Chaos Genetic Algorithm for T-Shaped MIMO Radar Antenna Array Optimization', *International Journal of Antennas and Propagation*, vol. 2014, pp. 1–6, 2014, doi: 10.1155/2014/631820.

- [133] A. Di Serio, P. Hügler, F. Roos, and C. Waldschmidt, ‘2-D MIMO Radar: A Method for Array Performance Assessment and Design of a Planar Antenna Array’, *IEEE Transactions on Antennas and Propagation*, vol. 68, no. 6, pp. 4604–4616, Jun. 2020, doi: 10.1109/TAP.2020.2972643.
- [134] M. E. Yanik, D. Wang, and M. Torlak, ‘Development and Demonstration of MIMO-SAR mmWave Imaging Testbeds’, *IEEE Access*, vol. 8, pp. 126019–126038, 2020, doi: 10.1109/ACCESS.2020.3007877.
- [135] M. Bekar, C. J. Baker, and M. Gashinova, ‘Reconstructed 2D MIMO Using Burg Algorithm’, in *2023 20th European Radar Conference (EuRAD)*, Berlin, Germany: IEEE, Sep. 2023, pp. 375–378. doi: 10.23919/EuRAD58043.2023.10289589.
- [136] Chun-Yang Chen and P. P. Vaidyanathan, ‘Minimum redundancy MIMO radars’, in *2008 IEEE International Symposium on Circuits and Systems*, Seattle, WA, USA: IEEE, May 2008, pp. 45–48. doi: 10.1109/ISCAS.2008.4541350.
- [137] J. Robinson and Y. Rahmat-Samii, ‘Particle swarm optimization in electromagnetics’, *IEEE Trans. Antennas Propagat.*, vol. 52, no. 2, pp. 397–407, Feb. 2004, doi: 10.1109/TAP.2004.823969.
- [138] R. Schmidt, ‘Multiple emitter location and signal parameter estimation’, *IEEE Trans. Antennas Propagat.*, vol. 34, no. 3, pp. 276–280, Mar. 1986, doi: 10.1109/TAP.1986.1143830.
- [139] Y. Hua and T. K. Sarkar, ‘Matrix pencil method for estimating parameters of exponentially damped/undamped sinusoids in noise’, *IEEE Trans. Acoust., Speech, Signal Process.*, vol. 38, no. 5, pp. 814–824, May 1990, doi: 10.1109/29.56027.
- [140] H.-W. Cho, W. Kim, S. Choi, M. Eo, S. Khang, and J. Kim, ‘Guided Generative Adversarial Network for Super Resolution of Imaging Radar’, in *2020 17th European*

- Radar Conference (EuRAD)*, Utrecht, Netherlands: IEEE, Jan. 2021, pp. 144–147. doi: 10.1109/EuRAD48048.2021.00046.
- [141] I. Roldan, F. Fioranelli, and A. Yarovoy, ‘Self-Supervised Learning for Enhancing Angular Resolution in Automotive MIMO Radars’, *IEEE Trans. Veh. Technol.*, vol. 72, no. 9, pp. 11505–11514, Sep. 2023, doi: 10.1109/TVT.2023.3269199.
- [142] I. J. Gupta, M. J. Beals, and A. Moghaddar, ‘Data extrapolation for high resolution radar imaging’, *IEEE Trans. Antennas Propagat.*, vol. 42, no. 11, pp. 1540–1545, Nov. 1994, doi: 10.1109/8.362783.
- [143] H. Chen *et al.*, ‘Cross-Range Resolution Enhancement for DBS Imaging in a Scan Mode Using Aperture-Extrapolated Sparse Representation’, *IEEE Geosci. Remote Sensing Lett.*, vol. 14, no. 9, pp. 1459–1463, Sep. 2017, doi: 10.1109/LGRS.2017.2710082.
- [144] M. Andres, W. Menzel, H.-L. Bloecher, and J. Dickmann, ‘Detection of slow moving targets using automotive radar sensors’, in *2012 The 7th German Microwave Conference*, Ilmenau, Germany, 2012, pp. 1–4.
- [145] B.-L. Cho and S.-G. Sun, ‘Cross-range resolution improvement in forward-looking imaging radar using autoregressive model-based data extrapolation’, *IET Radar, Sonar & Navigation*, vol. 9, no. 8, pp. 933–941, 2015, doi: 10.1049/iet-rsn.2014.0495.
- [146] M. J. L. De Hoon, T. H. J. J. Van Der Hagen, H. Schoonewelle, and H. Van Dam, ‘Why Yule-Walker should not be used for autoregressive modelling’, *Annals of Nuclear Energy*, vol. 23, no. 15, pp. 1219–1228, Oct. 1996, doi: 10.1016/0306-4549(95)00126-3.
- [147] I. A. Rezek, ‘Parametric model order estimation: a brief review’, in *IEE Colloquium on The Use of Model Based Digital Signal Processing Techniques in the Analysis of Biomedical Signals*, London, UK: IEE, 1997, pp. 3–3. doi: 10.1049/ic:19970061.

- [148] J. Salzman, D. Akamine, R. Lefevre, and J. C. Kirk, ‘Interrupted synthetic aperture radar (SAR)’, in *Proceedings of the 2001 IEEE Radar Conference (Cat. No.01CH37200)*, Atlanta, GA, USA: IEEE, 2001, pp. 117–122. doi: 10.1109/NRC.2001.922962.
- [149] H. Chen, M. Li, P. Zhang, G. Liu, L. Jia, and Y. Wu, ‘Resolution enhancement for Doppler beam sharpening imaging’, *IET Radar, Sonar & Navigation*, vol. 9, no. 7, pp. 843–851, 2015, doi: 10.1049/iet-rsn.2014.0384.
- [150] M. Hott, J. Mietzner, S. Lutz, M. Bockmair, and P. A. Hoeher, ‘Joint Super-Resolution and Array Interpolation for MIMO Radar Virtual Arrays’, in *2018 15th European Radar Conference (EuRAD)*, Madrid: IEEE, Sep. 2018, pp. 126–129. doi: 10.23919/EuRAD.2018.8546547.
- [151] B. Shakibi, F. Honarvar, M. D. C. Moles, J. Caldwell, and A. N. Sinclair, ‘Resolution enhancement of ultrasonic defect signals for crack sizing’, *NDT & E International*, vol. 52, pp. 37–50, Nov. 2012, doi: 10.1016/j.ndteint.2012.08.003.
- [152] J. Ning, R. Wang, Y. Deng, N. Li, H. Song, and W. Fei, ‘AET-IAA: A Novel Approach to Enhance Azimuth Resolution for ScanSAR Interferometry’, *IEEE J. Sel. Top. Appl. Earth Observations Remote Sensing*, vol. 10, no. 12, pp. 5674–5685, Dec. 2017, doi: 10.1109/JSTARS.2017.2741964.
- [153] Ning Li *et al.*, ‘Improved Full-Aperture ScanSAR Imaging Algorithm Based on Aperture Interpolation’, *IEEE Geosci. Remote Sensing Lett.*, vol. 12, no. 5, pp. 1101–1105, May 2015, doi: 10.1109/LGRS.2014.2384594.
- [154] T. G. Moore, B. W. Zuerndorfer, and E. C. Burt, ‘Enhanced Imagery Using Spectral-Estimation-Based Techniques’, vol. 10, no. 2, 1997.

- [155] Huaijun Wang and Yi Su, ‘Narrowband MIMO radar imaging with two orthogonal linear T/R arrays’, in *2008 9th International Conference on Signal Processing*, Beijing, China: IEEE, Oct. 2008, pp. 2513–2516. doi: 10.1109/ICOSP.2008.4697660.
- [156] M. Harter, T. Mahler, T. Schipper, A. Ziroff, and T. Zwick, ‘2-D antenna array geometries for MIMO radar imaging by Digital Beamforming’.
- [157] H. Cetinkaya, S. Kueppers, R. Herschel, and N. Pohl, ‘Comparison of near and far field focusing patterns for two-dimensional sparse MIMO arrays’, in *2016 10th European Conference on Antennas and Propagation (EuCAP)*, Davos, Switzerland: IEEE, Apr. 2016, pp. 1–4. doi: 10.1109/EuCAP.2016.7481127.
- [158] A. Ganis *et al.*, ‘A Portable 3-D Imaging FMCW MIMO Radar Demonstrator With a  $24 \times 24$  Antenna Array for Medium-Range Applications’, *IEEE Trans. Geosci. Remote Sensing*, vol. 56, no. 1, pp. 298–312, Jan. 2018, doi: 10.1109/TGRS.2017.2746739.
- [159] K. Vos, ‘A Fast Implementation of Burg’s Method’, *Signal Processing*, vol. 10, pp. 2–4, 2013.
- [160] Pei-Rin Wu, ‘A criterion for radar resolution enhancement with Burg algorithm’, *IEEE Trans. Aerosp. Electron. Syst.*, vol. 31, no. 3, pp. 897–915, Jul. 1995, doi: 10.1109/7.395248.
- [161] ‘Silicon radar’. Accessed: Nov. 25, 2023. [Online]. Available: <https://siliconradar.com/>
- [162] L. Daniel and M. Gashinova, ‘Sub-THz Radar Imagery for Automotive Application’, in *2022 19th European Radar Conference (EuRAD)*, Milan, Italy: IEEE, Sep. 2022, pp. 261–264. doi: 10.23919/EuRAD54643.2022.9924931.
- [163] Haderer, A, ‘MIMO-77-TX4RX8 Frontend (User Manual)’, 2015.

- [164] ‘Standa motorized linear positioner’. Accessed: Dec. 08, 2023. [Online]. Available: [https://www.standa.lt/products/catalog/motorised\\_positioners?item=60](https://www.standa.lt/products/catalog/motorised_positioners?item=60)
- [165] M. Bekar, C. Baker, and M. Gashinova, ‘Enhanced Angular Resolution in Automotive Radar Imagery Using Burg-Aided MIMO-DBS Approach’, in *2023 20th European Radar Conference (EuRAD)*, Berlin, Germany: IEEE, Sep. 2023, pp. 315–318. doi: 10.23919/EuRAD58043.2023.10289130.
- [166] C. Wiley, ‘Synthetic Aperture Radars’, *IEEE Trans. Aerosp. Electron. Syst.*, vol. AES-21, no. 3, pp. 440–443, May 1985, doi: 10.1109/TAES.1985.310578.
- [167] M. E. Radant, ‘The evolution of digital signal processing for airborne radar’, *IEEE Trans. Aerosp. Electron. Syst.*, vol. 38, no. 2, pp. 723–733, Apr. 2002, doi: 10.1109/TAES.2002.1009002.
- [168] T. Long, Z. Lu, Z. Ding, and L. Liu, ‘A DBS Doppler Centroid Estimation Algorithm Based on Entropy Minimization’, *IEEE Trans. Geosci. Remote Sensing*, vol. 49, no. 10, pp. 3703–3712, Oct. 2011, doi: 10.1109/TGRS.2011.2142316.
- [169] G. Pietrzyk, P. Samczynski, A. Gorzelanczyk, and K. Kulpa, ‘Real-time implementation of doppler beam sharpening technique with simple motion estimation’, *European Radar Conference*, 2004.
- [170] M. L. Williams, L. H. Bartlett, A. Britton, and H. A. Deadman, ‘Millimetre wave radar imaging’, *Proc. IEE Colloq. Radar Microw. Imaging*, p. 8/1-8/2, Nov. 1994.
- [171] L. Daniel *et al.*, ‘Application of Doppler beam sharpening for azimuth refinement in prospective low-THz automotive radars’, *IET Radar, Sonar & Navigation*, vol. 12, no. 10, pp. 1121–1130, 2018, doi: 10.1049/iet-rsn.2018.5024.

- [172] L. Daniel *et al.*, ‘Doppler Beam Sharpening for Angular Refinement at 150 GHz – Initial Experimentation’, in *2018 19th International Radar Symposium (IRS)*, Bonn, Germany: IEEE, Jun. 2018, pp. 1–7. doi: 10.23919/IRS.2018.8448091.
- [173] L. Daniel and M. Gashinova, ‘Sub-THz Radar Imagery for Automotive Application’, in *2022 19th European Radar Conference (EuRAD)*, Milan, Italy: IEEE, Sep. 2022, pp. 261–264. doi: 10.23919/EuRAD54643.2022.9924931.
- [174] A. Laribi, M. Hahn, J. Dickmann, and C. Waldschmidt, ‘A new height-estimation method using FMCW radar Doppler beam sharpening’, in *2017 25th European Signal Processing Conference (EUSIPCO)*, Kos, Greece: IEEE, Aug. 2017, pp. 1932–1936. doi: 10.23919/EUSIPCO.2017.8081546.
- [175] S. L. Cassidy, S. Pooni, M. Cherniakov, E. G. Hoare, and M. S. Gashinova, ‘High resolution automotive imaging using MIMO radar and Doppler beam sharpening’, *IEEE Trans. Aerosp. Electron. Syst.*, pp. 1–11, 2022, doi: 10.1109/TAES.2022.3203953.
- [176] S. L. Cassidy, S. Pooni, A. Pirkani, E. G. Hoare, M. Cherniakov, and M. S. Gashinova, ‘Doppler Beam Sharpening for High-Resolution Imaging in Dynamic Automotive Scenes’, in *2022 19th European Radar Conference (EuRAD)*, Milan, Italy: IEEE, Sep. 2022, pp. 325–328. doi: 10.23919/EuRAD54643.2022.9924919.
- [177] Scott Cassidy, Sukhjot Pooni, and Marina Gashinova, ‘University of Birmingham Campus Driving MIMO Dataset’. University of Birmingham, 2022. doi: <https://doi.org/10.25500/edata.bham.00000825>.
- [178] ‘Inras RadarLog’. Accessed: Aug. 25, 2022. [Online]. Available: <https://inras.at/en/radarlog/>